Towards Spin Squeezed ^{171}Yb Atomic Clock beyond the Standard Quantum Limit

by

Akio Kawasaki

B.S., The University of Tokyo (2010)

Submitted to the Department of Physics
in partial fulfillment of the requirements for the degree of

Doctor of Philosophy

at the

MASSACHUSETTS INSTITUTE OF TECHNOLOGY

September 2017

Author .....
Department of Physics
August 21, 2017

Certified by .....
Vladan Vuletić
Lester Wolfe Professor of Physics
Thesis Supervisor

Accepted by .....
Nergis Mavalvala
Curtis and Kathleen Marble Professor of Physics,
Associate Department Head for Education

Towards Spin Squeezed ^{171}Yb Atomic Clock beyond the Standard Quantum Limit

by

Akio Kawasaki

Submitted to the Department of Physics
on August 21, 2017, in partial fulfillment of the
requirements for the degree of
Doctor of Philosophy

Abstract

State-of-the-art atomic clocks have fractional frequency instability of 6×10^{-17} at 1 s averaging time, and are aiming for even higher stability. One of the main factors limiting this stability is the standard quantum limit (SQL) of quantum projection noise, which can be overcome by spin squeezing.

We constructed an apparatus to perform spin squeezing on an ytterbium optical lattice clock to demonstrate the enhancement of clock stability by spin squeezing. Using the spin 1/2 system of the ground state Zeeman sublevels of ^{171}Yb, two different methods are utilized to perform a spin squeezing via coupling to 6s6p$^3P_1$ excited state. One method is measurement-based squeezing, which gave 2.1 dB of spin squeezing. The latter method, cavity feedback squeezing, achieved 8.6 dB of inferred squeezing. The sequence is designed in such a way that the squeezing procedure is unitary, which is demonstrated by reverting the state to a coherent spin state after squeezing it, and the measurement does not require atom number measurement much more precise than the SQL.

The squeezing of ground state is expected to be transferred to the 6s6p$^3P_0$ state, which is the excited state of the clock transition. This would be the first observation of an entangled state between a ground state and an electronic excited state, and the resulting spin squeezed atomic clock would be the first optical transition clock enhanced by spin squeezing.

Thesis Supervisor: Vladan Vuletić
Title: Lester Wolfe Professor of Physics

Acknowledgments

This project had never been completed if it were not for helps by lots of people.

First of all, I would like to express my deepest gratitude to my supervisor, Prof. Vladan Vuletić. Vladan is always optimistic about the progress of the project, which always encourages me to push this complicated project forward. His understanding on experiments is amazing both on physics and engineering. I learned most of the intuitions on strong interaction between atoms and light from Vladan, and the best source of knowledge about electronics is the discussion with Vladan at group meetings.

I also would like to thank Prof. Wolfgang Ketterle and Prof. Scott Hughes for being in my thesis committee. They are always supportive to my project, and their responses to my progress reports are always more positive than I expected.

The experiment is so successful because I have a wonderful labmate: Boris Braverman. His deep understanding on quantum mechanics helps me to understand this cavity QED system that sometimes behaves in a counterintuitive way, and his timely suggestions of upgrade of experimental devices has made the progress of the project smooth. I also am impressed the way he tries to think of all possible explanation of a single phenomenon. In addition, I thank Boris for sharing figures I used in the main text: Figs. 2-4, 3-1, 4-4, 4-6, 4-7, 4-8, 4-9, 4-10, 4-11, 4-12, 4-18, 5-5, 5-9, 5-17, 5-18, 6-9, 6-12, 7-1, 7-3, 7-4, 7-5, 7-8, 7-9, 7-19, 7-20, 7-30, 7-32, 7-34 (a), (b), 7-36, 7-46, 7-48. Most of these are in his thesis [1].

My thanks also goes to other members who worked at the ytterbium clock lab. Visiting scholars, Dr. Daisuke Akamatsu and Prof. Yanhong Xiao, displayed deep understanding on their specialities: atomic clock, and quantum physics. Their expertise told me lots of techniques. Edwin Pedrozo, a new postdoc, gives me inspirations from the world of quantum degenerate gases. Chi Shu, a new graduate student, has been in the lab only for three months, but he already has demonstrated significant contribution to the upgrades of a bunch of devices. Ph.D. students who stayed in the lab for a while, Ozge Ozel, Tailin Wu, and Enrique Mendez, are all talented, and build certain important parts of the experiment. David Levonian, a master student, played

an important role in developing our trapping laser. We had seven MIT undergraduate students (Logan Williams, Sophie Weber, Harry Zhou, Grace Zhang, QinQin Yu, Christopher Sanfillipo, Ileana Rugina, Megan Yamoah) over six years, and all of them had a strength in certain field. We had six visiting students, ranging from Ph.D. students to a high school student (David Ma, Tamara Sumarac, André Heinz, Yasunari Suzuki, Leonardo Salvi, Bojan Zlatković), who also did a great contribution to the experiment.

I also have to mention the contribution by members in other labs in our group. Marko Cetina, who finished his Ph.D. in our group slightly before I join the group, and who was a short term postdoc at the beginning of my life in Vuletić group, told me most part of how to build devices in the lab. I learned how to deal with vacuum chamber components from Thibault Peyronel. Other former and current members (Leon Karpa, Robert McConnell, Ofer Firstenberg, Jeff Thompson, Mahdi Hosseini, Travis Nicholson, Wenlan Chen, Hao Zhang, Alexei Bylinskii, Qiyu Liang, Kristin Beck, Dorian Gangloff, Jiazhong Hu, Ian Counts, Yiheng Duan, Sergio Cantu, Zachary Vendeiro, Yu-Ting Chen, Aditya Venkatramani) are always good colleagues to discuss questions we ourselves do not have good answers. Special thanks go to Ian Counts, Sergio Cantu, and Zachary Vendeiro for proofreading this thesis.

In the end, I would like to show my thanks to people outside the lab. Good friends in the Department of Phyaics (particularly the softball team), and student communities of Japanese and Koreans enriched my life in Cambridge, which made me always fully charged to work at the lab.

Contents

List of Figures

List of Tables

List of acronyms

Acronyms used in the main text are listed in the alphabetical order.

AC	alternating current
AOI	angle of incidence
AOM	acousto-optic modulator
APD	avalanche photodiode
APP	anamorphic prism pair
AR-coating	anti-reflection coating
ASE	amplified stimulated emission
BBR	Blackbody radiation
BEC	Bose-Einstein condensate
CCD	charge coupled device
CMOS	complementary metal-oxide semiconductor
DAQ	Data acquisition
DBR	distributed Bragg reflector
DC	direct current
DFB	distributed feedback
DL	diode laser
DM	discrete mode
ECDL	external cavity diode laser
EMF	electromotive force
EOM	electro-optic modulator
FSR	free spectral range

FWHM	full width half maximum
GT polarizer	Glan-Taylor polarizer
HWP	half waveplate
ID	inner diameter
IR	infrared
KRISS	Korea Research Institute of Standards and Science
LD	laser diode
MOT	magneto-optical trap
NBS	National Bureau of Standards
ND filter	neutral density filter
NI	National Instruments
NIM	National Institute of Metrology
NIST	National Institute of Standards and Technology
NMIJ	National Metrology Institute of Japan
NPL	National Physical Laboratory
OD	outer diameter
OD	optical depth
PBS	polarizing beam splitter
PD	photodiode
piezo	piezoelectric actuator
PM	polarization maintaining
POT	potentiometer
PPLN	periodically poled lithium niobate
PTB	Physikalisch-Technische Bundesanstalt
QED	quantum electrodynamics
QPN	quantum projection noise
QWP	quarter waveplate
RAM	residual amplitude modulation
RF	radiofrequency
ROC	radius of curvature

RWA	rotating wave approximation
SHG	second harmonics generation
SQL	standard quantum limit
TA	tapered amplifier
TCMOT	two-color MOT
TOF	time of flight
TVS	transient-voltage-suppression diode
VCO	voltage controlled oscillator

Chapter 1

Introduction

1.1 Introduction: brief history of precision measurement of time

Humans have measured time since thousands of years ago. For example, we can track back more than 2000 years in historical records in ancient Rome and Greece. During this period, time was mainly measured by the motion of heavenly bodies, mainly the Sun and the Moon. The concept of the year started with the annual motion of the sun, and the month came from the waxing and waning of the Moon. The concept of hour was to divide the time between sunrise and sunset by a certain number in ancient civilization. Later, the hour was redefined as 1/24 of a day.

More precise time measurements were realized when mechanical clocks were invented. Early mechanical clocks that are still used now are pendulum clocks, which were developed by Huygens. These early mechanical clocks enabled the precision of less than 1 minute error per day. In the 20th century, the quartz clock was developed. The first quartz oscillator frequency standard at NBS had a precision of 10^{-5}, and eventually it went up to 2×10^{-8}, which is less than one second error per year. [12]

Later, the atomic clock was invented and it became the most precise clock in the world. After World War II, microwave technology was applied to atomic spectroscopy, and precisely measured atomic resonance started to be used as a frequency standard.

The first atomic clock in NBS was built in 1949 with ammonia's 23.87 GHz inversion transition. [13] This had a precision of 2×10^{-8}, which was equivalent to the best quartz frequency standard at the time.

In 1950's, the atomic clock operating on a microwave transition in the Cs ground state hyperfine structure was developed. In 1951, NBS measured this microwave transition in the ^{133} Cs ground state for the first time as 9192.632 ± 0.002 MHz, and their first Cs atomic clock was estimated to have the precision of 10^{-10}. [14] The first atomic clock as a time standard was built at NPL in 1956. [15] In 1958, the transition frequency was measured with higher precision, and the result was 9192631770 ± 20 Hz. [16] At this moment, the Cs atomic clock was developed by many universities and standard organizations, such as NBS, NPL, PTB, and Bureau de l'Heure. In 1967, the microwave transition in the Cs ground state was selected as the definition of a second. Also, some other atomic frequency standard, such as the Rb microwave transition clock and the H maser, were developed in the 1950's and 1960's.

Since the first advent of the Cs clock, its accuracy improved by orders of magnitude, as Fig. 1-1 shows. Currently, the NIST-F2 fountain clock[1] and other Cs clocks in other metrology agencies have an accuracy on the order of 10^{-16}. [17, 18, 19, 20] A recent long time measurement with Rb microwave transition clocks claims to have stability down to the 10^{-17} level. [21]

Further improvement of clock stability is sought by optical transition clocks, which use visible light as an oscillator, whereas Cs, Rb clocks and H maser use microwaves as an oscillator, because an oscillator of higher frequency is more immune to low frequency drift. The effort on performing spectroscopy of narrow optical transitions started in the 1980's for ions that have a forbidden electric quadrupole or electric octupole transition, or $J = 0 \rightarrow J' = 0$ transition. Examples are the Hg^+ ion [22], Ba^+ ion [23], In^+ ion [24] Sr^+ ion [25], Ca^+ ion [26], Yb^+ ion [27], and Al^+ ion [28]. The first observation of these narrow transitions, which are typically called clock transitions, were performed by the end of the 1990's, and in the 2000's, relative frequency comparisons beyond the accuracy of Cs time standard were performed.

[1] See Section1.2 for the description of a fountain clock.

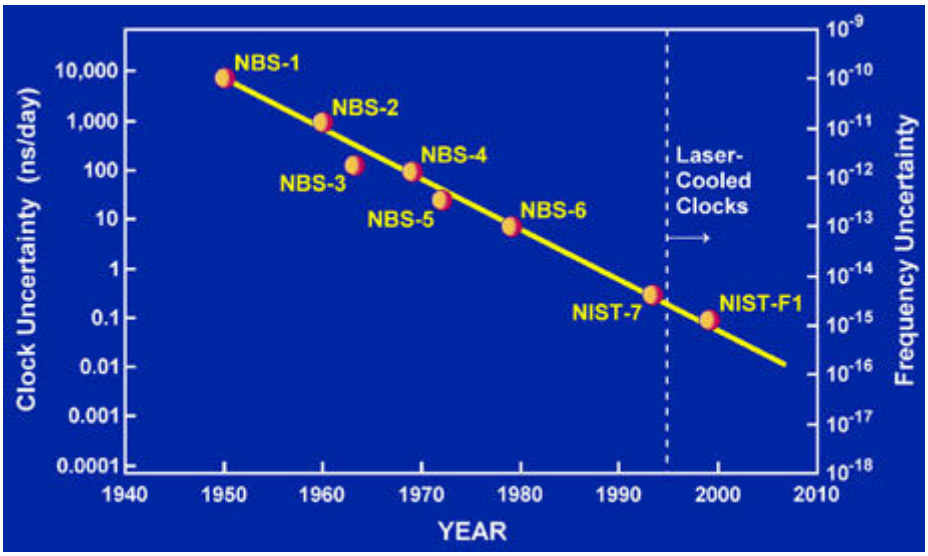

Figure 1-1: Improvement of Cs clock precision [3].

[29] The accuracy of an Al^+ optical clock was narrowed down to the level of 10^{-18} in 2010. [30]. Currently, an $^{171}Yb^+$ ion clock has the smallest systematic uncertainty of 3.2×10^{-18} [31].

The idea of trapping neutral atoms and using them as atomic references existed for a long time, but the problem of the energy shift of clock transitions due to the light field used for trapping had not been solved until the idea of a magic wavelength to cancel the energy shift was proposed in 2003. [32] Once the idea was established, the first optical lattice clock was quickly built for ^{87}Sr atoms, [33] ^{171}Yb atoms, [34] and ^{199}Hg atoms. [35] At first, the accuracy of optical lattice clocks was worse than that of the ion clock, but currently, optical lattice clocks also have accuracy of 10^{-18}, with the best number of 2.1×10^{-18}. [36] Frequency comparisons between different optical lattice clocks were performed with a precision below the Cs time standard. [37, 38]

1.2 Comparison of Cs clocks, ion clocks and optical lattice clocks

The history of clocks described in the previous section is that of finding a precise frequency reference. An atomic clock uses an atomic system as the absolute reference of frequency, and tries to detect it through a local oscillator. Two specific energy levels are chosen in the atomic system whose energy difference constitutes a frequency reference. These two energy levels have to be connected by an electromagnetic transition, and this transition is called clock transition.

The ^{133}Cs clock, which uses a transition between ground state hyperfine levels $|F = 3, m_F = 0\rangle \rightarrow |F = 4, m_F = 0\rangle$ as the clock transition, is still an important clock, because 1 s is currently defined as "the duration of 9 192 631 770 periods of the radiation corresponding to the transition between the two hyperfine levels of the ground state of the caesium 133 atom." The state-of-the-art Cs atomic clock is a fountain clock. Cs atoms are first laser cooled down by a MOT (see Section 6.1 for how MOT works), and shot vertically upward by a push beam. While they are free falling, atom number counting is performed by a probe laser, and they go through a clock sequence by experiencing microwave field. Typically, the stability of Cs clocks, which is described by the Allan deviation [39], scales $\sim 1 \times 10^{-13}\tau^{-1/2}$ [18].[2] The clock is stable enough to be averaged over more than 10^4 s, and this gives a stability and an accuracy below 10^{-15}.

In ion clocks, typically single, sometimes a few ions are trapped in a Paul trap. The ion is laser cooled, and a forbidden narrow optical transition is interrogated by a laser. Although its stability goes down to the order of 10^{-18}, the scaling of Allan deviation is $5 \times 10^{-15}\tau^{-1/2}$ [31], and months of averaging are necessary to get to 10^{-18} level of stability. The poor 1 s stability is due to the fact that there is only single ion to be interrogated, and quantum fluctuations cannot be improved.

[2]Allan deviation $\sigma_y(\tau)$ is defined as $\sigma_y^2(\tau) = \frac{1}{2(M-1)} \sum_{i=1}^{M-1} [\langle y(\tau)\rangle_{i+1} - \langle y(\tau)\rangle_i]^2$, where $\langle y(\tau)\rangle_i$ is the ith measurement of the average fractional frequency difference over averaging time τ, and it is the most common quantity to describe the stability of clocks. More description on the stability of atomic clocks can be found in Section 2.2.

Optical lattice clocks, on the other hand, have thousands of atoms trapped in an optical lattice[3], interrogated by a laser resonant to the clock transition. The stability at 1 s is much better than that of the ion clock, thanks to the larger number of atoms in the lattice. Ref. [36] gives $2.2 \times 10^{-16}/\sqrt{\tau}$, which is an order of magnitude better than ion clocks, and a recent report gives 6×10^{-17} level stability at 1 s [40]. This better stability in a short averaging time is advantageous to quickly estimate systematic effects precisely, and design feedback against long term drifts in an effective way. The superiority of optical lattice clocks over Cs clocks is demonstrated by direct stability comparison. [41] For this reason, optical lattice clocks are regarded as one of the most promising candidates for the next-generation atomic clock, including a new way to define the second, and are researched at various universities and national institutes, such as NIST, NPL, PTB, SYRTE, RIKEN/University of Tokyo, NIMJ, KRISS, and NIM.

One of the challenges to have better atomic clocks is therefore to have better 1 s stability. One obvious method is to use even larger number of atoms as a frequency reference. Another way is to seek better frequency measurement with atoms at a fixed atom number. This is achieved by spin squeezing in rubidium hyperfine clocks [42, 43], and is a promising method to improve the stability of optical lattice clocks. In this thesis, a path towards a spin squeezed optical lattice clock in ^{171}Yb is described.

1.3 Structure of the thesis

Chapter 2 and Chapter 3 serve as an introduction to the main topics. Chapter 2 summarizes the state of the art of optical lattice clocks, and Chapter 3 introduces the idea of spin squeezing. Theory on atom-light interaction in an optical cavity and theoretical aspects of spin squeezing we performed is also summarized in Chapter 3. Chapters 4, and 5 describe the technical details of our apparatus. Chapter 4 sum-

[3]When you send two laser beams of the same frequency counterpropagating to each other, a standing wave of light is formed. When the light generates a trapping potential for atoms, the standing wave becomes a periodic trap for atoms. This is called optical lattice, and it can be made two- or three-dimensional by adding one or two more pairs of counterpropagating beams.

marizes hardware and software in our lab except for lasers, such as vacuum chamber, experimental cavity and optics system around them. Chapter 5 is dedicated to laser systems, including all seven different lasers, and two reference cavities. Chapters 6 and 7 deal with experimental results. Chapter 6 describes details of our atom trapping. This includes a summary on the TCMOT, which is a MOT for low magnetic field gradient we developed, and details of trapping in an optical lattice. Chapter 7 mentions all the experiments using cavity QED tricks, starting from optical pumping to spin squeezing. Chapter 8 mentions a couple of miscellaneous things we did, and the prospects of the experiment in a near future. There are three appendices. List of acronyms is located at the beginning of the thesis. Appendix A is detailed derivations of equations in Chapter 3. Appendix B briefly summarizes the modified current controller we use for the 759 nm and 1157 nm lasers.

Chapter 2

State-of-the-art atomic clock

2.1 Optical lattice clock

An optical lattice clock is an atomic clock where neutral atoms are trapped in an optical lattice, and interrogated by lasers. (Fig. 2-1) The atoms are first laser cooled and trapped in a magneto-optical trap (MOT), and then loaded into an optical lattice. A clock laser, which is used as a local oscillator and locked to an ultrastable reference cavity to reach $\lesssim 1$ Hz linewidth, interrogates a forbidden narrow transition. This interrogation stabilizes the clock laser's frequency to the atomic resonance frequency, and the clock laser works as a stable oscillator for a clock.

In optical lattice clocks, He-like atoms that have two electrons in the outermost shell are used as an atomic reference. ^{87}Sr is the most popular one (e.g. [36, 44, 45, 46, 47, 41, 48]), and ^{171}Yb follows. [4, 49, 50, 38, 51] Clocks with other species, such as ^{199}Hg [35, 37] and ^{24}Mg [52], have been developed. The common feature of these atomic species is the $^1S_0 \rightarrow {}^3P_0$ clock transition, where the $^1S_0$ state is the ground state. Both the ground state and excited state do not have any electronic angular momentum, and thus are immune to the energy shift due to a magnetic field, except for a few hundred Hz/G shift due to the nuclear magnetic sublevels. The clock transition is between the $J = 0$ and $J' = 0$ states, which is completely forbidden unless it has slight mixing with $^3P_1$ state due to the nuclear magnetic moment. This gives an extremely narrow transition, for example 7 mHz for ^{171}Yb [53], which is suitable

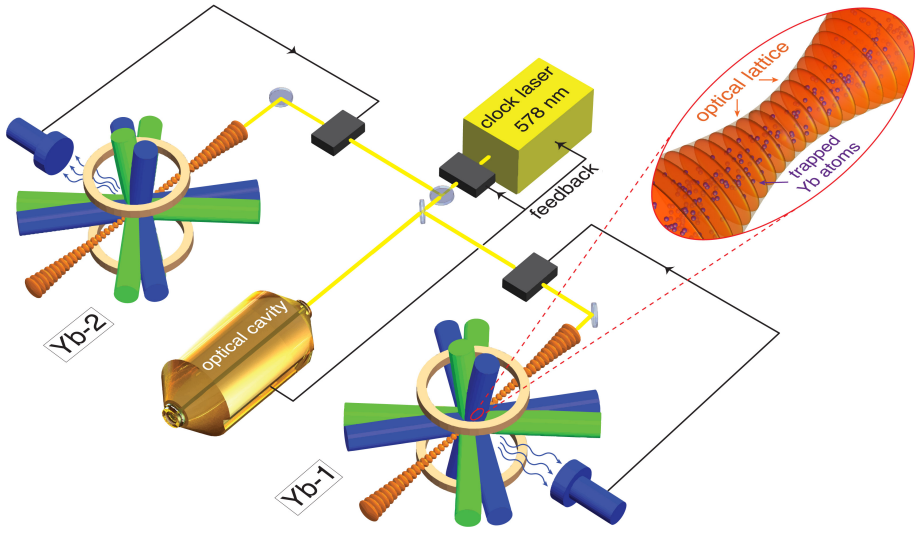

Figure 2-1: Concept of optical lattice clock (Cited from https://phys.org/news/2013-08-nist-ytterbium-atomic-clocks-stability.html, similar figure is also on [4])

for the clock transition.

Still the clock transition cannot avoid the energy shift by the light field, which is used for trapping atoms. The idea of removing this was proposed by Katori *et al.* [32], and the wavelength that gives the same energy shift for the ground and excited states is called the magic wavelength. Theoretical calculation was first made for ^{87}Sr [32], and numbers were soon calculated for ^{171}Yb [54] and ^{199}Hg [55]. The measurements of the actual numbers, which is in some cases a few percents away from the calculation, were performed in various clock systems, and Ref. [56] has a good summary of the numbers for ^{87}Sr and ^{171}Yb.[1] As for ^{199}Hg, the magic wavelength is measured to be 362.53(0.21) nm [57].

With the idea of trapping atoms with a laser of the magic wavelength for the clock transition, the first optical lattice clock was built in 2005 [33], and it has been quickly developing for ten years. At the beginning, its 1 s stability was on the order of 10^{-14} [33, 58], mainly limited by the stability of the clock laser due to the reference cavity[2], and the overall accuracy was on the order of 10^{-16}. There was a significant progress

[1]This reference is a good summary of the state of the art optical lattice clock and ion clock.

[2]Fig. 2 in Ref. [41] nicely shows the stability of optical lattice clocks are limited by the noise of reference cavity

in the evaluation of systematic uncertainties, as the stability of the clock laser was improved by better ultrastable reference cavities [59][3], and now the typical 1 s clock stability is on the order of 10^{-16}, and few hours of averaging gives a precision of 10^{-18}.

With this precision, systematic uncertainties can be investigated with a precision of 10^{-18} or below. Uncertainty budgets are listed in Ref. [36, 44]. In 2015, the major uncertainty was AC Stark shifts[4] by the trapping light and black body radiation. In both Ref. [36] and Ref. [44], a quarter of the contribution comes from the lattice light shift. Ref. [36] has BBR dynamic shift as the major uncertainty, even though they use precise temperature estimates for the atoms based on the temperature stabilization of the whole vacuum chamber and a NIST calibrated thermometer. Ref. [44] puts atoms in a cryogenic thermal shield to reduce the effect of black body radiation. The understanding of the lattice shift, which is a higher-order AC Stark shift, has improved over the past two years, and next generation clocks trap atoms in a three dimensional optical lattice [61] to reduce the effect of atom-atom collisions.

2.2 Standard quantum limit and Ramsey sequence

In the last paragraph, I put emphasis on systematic uncertainties, but statistical uncertainty is also an important factor for clock stability. For simplicity, it is assumed that a single clock sequence is a Ramsey sequence that measures the phase difference of a local oscillator from an atomic system. (see Fig. 2-3 for what exactly the Ramsey sequence is) The statistical uncertainty that limits the stability of a clock is described as

$$\sigma(\tau) = \frac{C}{\omega_0}\frac{1}{\sqrt{NT\tau}}, \tag{2.1}$$

where τ is the duration of overall experiment, which is typically called the averaging time, N is the number of atoms in the system, ω_0 is the clock transition frequency, and T is the interrogation time. C is a constant of $O(1)$, and it is larger than 1. The $C = 1$

[3]This reference has the comparison of their new 40 cm cavity and old 7 cm cavity[60], and new one has one order of magnitude better stability.

[4]AC Stark shift is the energy level shift of an energy level due to an oscillating electric field.

case is called the standard quantum limit. In this limit, what is limiting the precision of the clock is the quantum mechanical fluctuation that appears in the population difference measurement. This is called the quantum projection noise (QPN). QPN is proportional to $N^{-1/2}$, and this is intuitively understood by a phase uncertainty $\Delta\phi$ derived from the uncertainty principle of $\Delta N \cdot \Delta\phi \simeq 1$ with atom number uncertainty following shot noise $\Delta N = 1/\sqrt{N}$. Currently, a QPN limited clock is achieved with a sufficiently stable local oscillator [59, 46].

There are three ways to increase the precision. One is to increase the averaging time. This was already mentioned as a way to get a 10^{-18} stability clock from a 10^{-16} 1 s stability. This method always works, but too long an averaging time is susceptible to long-term drifts. The second one is to increase the interrogation time T. The interrogation time is typically determined by the lifetime of atoms in the optical lattice and by the laser stability, and there is not much room for improvement unless one develops a new method of stabilizing the clock laser. The third method is to improve atom number N. Currently, in an optical lattice clock, a few thousand atoms are interrogated in one sequence. This number is a compromise between the phase resolution in the Ramsey sequence and the energy shift due to the atom-atom collisions; too large an atom number in a one-dimensional lattice increases the probability of collision, which gives an uncertainty in the clock transition frequency. Historically, three-dimensional lattices were once used to avoid the collisional shift [62], but popular consensus returned a one dimensional lattice to avoid higher order AC Stark shift by the trapping light. Some next-generation clocks use three-dimensional lattices again [61], but the uncertainty budget is still to be evaluated.

2.3 Spin squeezed atomic clock beyond the standard quantum limit

Another way to improve the N dependence of the precision is to use entangled states. This changes the N dependence of the shot noise from $N^{-1/2}$ to something closer to

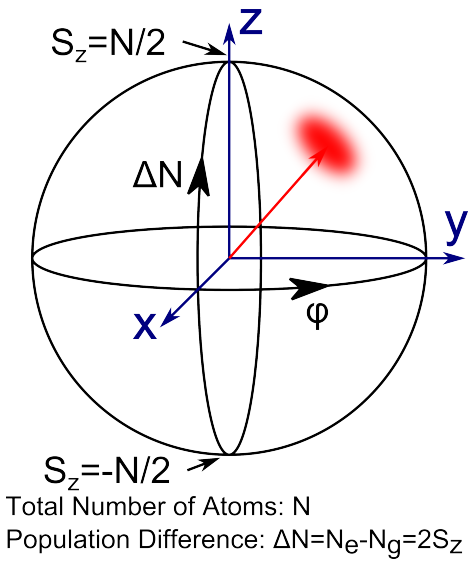

Figure 2-2: Bloch sphere for an atomic ensemble: suppose an atomic ensemble of N two-level system. Because a two-level system is mathematically equivalent to a spin 1/2 system, this is equivalent to a spin S=N/2 system. The state of this atomic ensemble is described on a Bloch sphere. The polar angle direction corresponds to the population difference between the ground and the excited state, and the azimuthal angle corresponds to the relative phase between them. At the south pole, all atoms are in the ground state, and at the north pole, all atoms are excited.

the Heisenberg limit N^{-1}. The simplest entangled state that is useful for improving the phase resolution is a spin squeezed state. The basic idea is to push uncertainty into the population difference direction ΔN on the Bloch sphere (Fig. 2-2) to get smaller uncertainty in the phase direction $\Delta\phi$. Then scaling of $\Delta\phi$ changes from $N^{-1/2}$ to N^{-p} where $-1/2 > p > -1$. For details of spin squeezing and other kinds of entangled states, see the next chapter.

An atomic clock enhanced by spin squeezing has been achieved in Rb microwave transition clocks [42, 43]. In these experiments, spin squeezing was performed before starting the Ramsey sequence (see Fig. 2-3), and factors of a few improvement of the clock precision with the same averaging time were observed. This is a very important demonstration that a clock precision is enhanced by a squeezed state, as well as using squeezed states for real metrology, but the clock used for the experiment is a microwave transition clock, not the state-of-the-art optical clocks. The implementation of spin squeezing in an optical transition clock for enhancing the precision is still to be

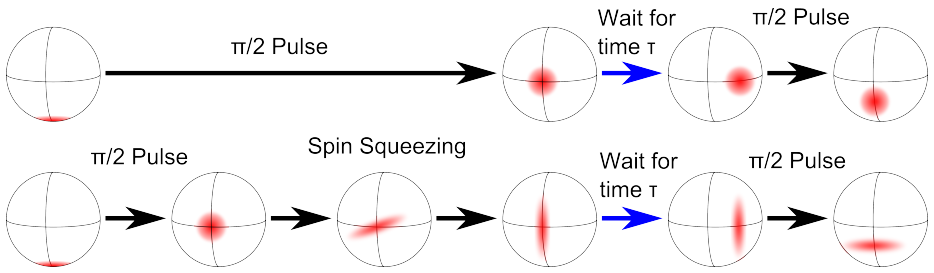

Figure 2-3: Standard Ramsey sequence and Ramsey sequence with spin squeezed state: in the standard Ramsey sequence (top), atoms in the ground state are put into a superposition state between the ground and excited state by a $\pi/2$ pulse. This is the start of the sequence, and then atoms are left over an interrogation time of T. For the measurement of relative phase drift between atoms and a local oscillator, another $\pi/2$ pulse is sent to rotate the phase shift into the shift in population difference. To use a spin squeezed state for the Ramsey sequence, spin squeezing is first performed after bringing a state into a superposition state. In the figure case, spin squeezing is performed by a 1 axis rotation. The squeezed state is rotated to the phase direction, and then the interrogation time of T is inserted. The final read out is performed after a $\pi/2$ pulse.

done. In our project, the primary goal is to implement this spin squeezing technique in an optical clock to demonstrate that spin squeezing can improve the precision of state-of-the-art atomic clocks. It is also notable that all the spin squeezing experiments that have been performed so far are the squeezing of either electron or nuclear spin, whereas the spin squeezing we are targeting is for the pseudo-spin describing the two-level system of the ground state and the electronic excited state of a clock transition. To do this, we chose ^{171}Yb as our atomic species.

2.4 Ytterbium clock

In this section, an optical lattice clock with ytterbium is described. Ytterbium is an element with atomic number 70, which is the second last lanthanoid element, that has a closed 4f shell and two electrons filling the outermost 6s orbital. There are seven stable isotopes whose natural abundance is shown in Table 2.1. Because the atomic number is even, nuclear spin is nonzero only for fermionic isotopes, ^{171}Yb and ^{173}Yb. The low-energy levels of interest are shown in Fig. 2-4. The ground state

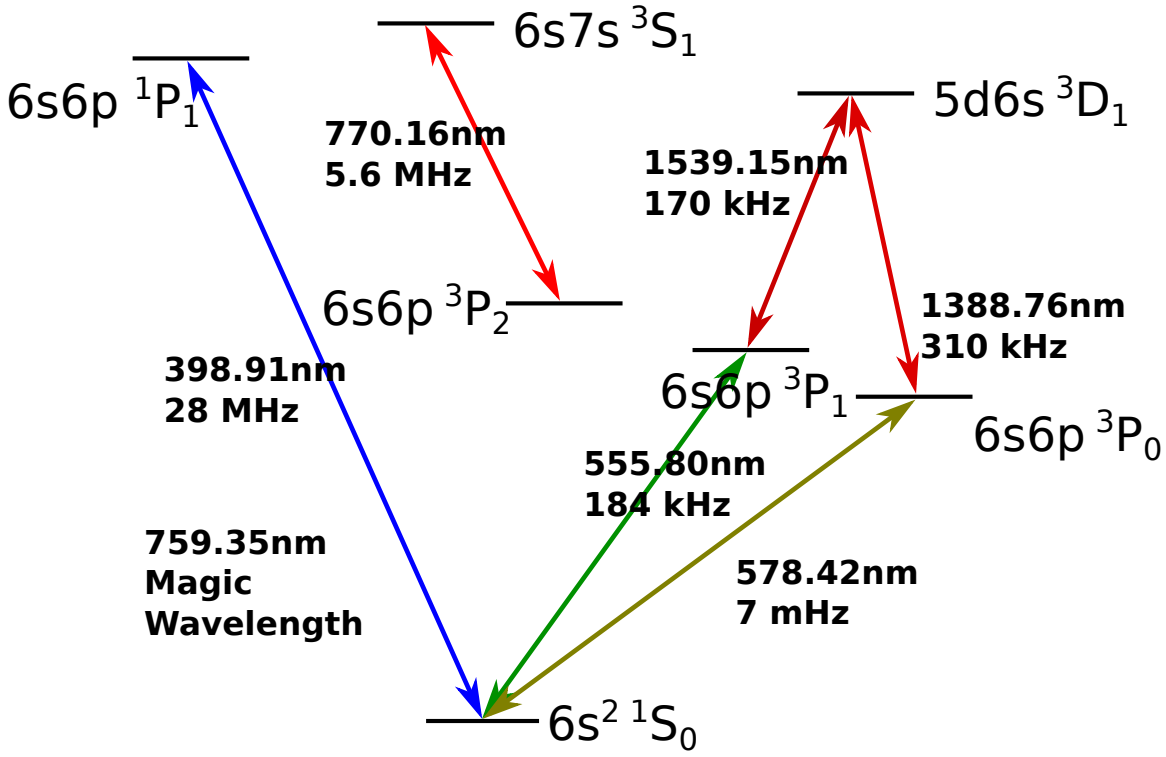

Figure 2-4: Level structure of ytterbium

Table 2.1: Natural abundance of ytterbium isotopes

mass number	nuclear spin	abundance [%]
168	0	0.13
170	0	3.05
171	1/2	14.3
172	0	21.9
173	5/2	16.12
174	0	31.8
176	0	12.7

is the $^1S_0$ state, where all the electronic spin is paired up and therefore there is no spin or orbital angular momentum. The only sublevels for the ground state are the Zeeman sublevels due to the nuclear spin, and the number of sublevels is more than one only for fermionic isotopes.

The broadest transition to an excited state is the $^1S_0 \rightarrow ^1P_1$ transition, whose linewidth is 28 MHz. This is typically used for first-stage cooling and trapping such

as with a Zeeman slower and a MOT. Because there are two outermost electrons, there are some transitions between the ground state and the triplet states that are allowed by LS coupling. The ${}^1S_0 \rightarrow {}^3P_1$ transition is broad enough to use for a MOT, thanks to large atomic number. Transitions from the ground state to two other triplet states for the 6s6p state are forbidden. The ${}^1S_0 \rightarrow {}^3P_2$ transition is forbidden because it is an E2 transition, and the ${}^1S_0 \rightarrow {}^3P_0$ transition is forbidden because it is a $J = 0 \rightarrow J' = 0$ transition. For bosonic isotopes, this transition is completely forbidden, unless some external field mixes this state and the ${}^3P_1$ state, and for fermionic isotopes this transition is slightly allowed due to the mixing with the ${}^3P_1$ state by the nuclear magnetic moment. This narrowness and insensitivity to the magnetic field makes the ${}^1S_0 \rightarrow {}^3P_0$ transition an excellent choice for a clock transition. Other transitions drawn in Fig. 2-4 are repump transitions we decided to use for the two metastable states.[5] Note that some other groups use the $6s6p\,{}^3P_0 \rightarrow 6s7s\,{}^3S_1$ transition (649 nm) for repumping the ${}^3P_0$ state.

The possibility for ytterbium to serve as an optical lattice clock was first suggested in 2004 [54], soon after the first proposal of the idea of magic wavelength. At this moment, ytterbium was already a popular atom for atomic physics experiments, and MOTs with the ${}^1S_0 \rightarrow {}^1P_1$ and ${}^1S_0 \rightarrow {}^3P_1$ transitions were already achieved. (See Section 6.1 for the details of ytterbium MOTs.) Moreover, a Bose-Einstein condensate (BEC) of ytterbium was already achieved [63], and precision measurements regarding atomic parity violation were already performed. [64] Therefore, it did not take very long time to observe the first clock transition, [65] and subsequently the frequency of the clock transition is measured with 1 Hz order precision, first for ^{174}Yb [66], and then for ^{171}Yb [34] at NIST. KRISS [49], NMIJ [51], RIKEN/University of Tokyo [38], INRIM [50] and Chinese Academy of Science [67] also built their own ^{171}Yb clocks. Systematic uncertainties precisely measured by NIST group include the collisional shift [68, 69], the DC Stark shift [70], and the blackbody radiation shift [71, 72]. Cs time standard limited frequency measurements for the clock transition has been performed at various different institutes [56, 49, 50]. The magic wavelength has

[5] The ${}^3P_0$ state has lifetime of 22.6 ± 1.8 s [53], and the ${}^3P_2$ state has lifetime of 14 s.

been measured by different groups, and the current most precise measurement is 394,798,265(9) MHz[6].

The major advantage of using ^{171}Yb for a spin squeezed optical lattice clock over other atomic species, such as ^{87}Sr and ^{199}Hg, is the fact that the nuclear magnetic moment is 1/2. This gives the textbooklike spin 1/2 system in the ground state, and the state preparation and performing of spin squeezing at the ground state becomes much easier than with other atomic species. Also, Yb is a good atom to have a two-color MOT (TCMOT) with a low magnetic field gradient [9] (see also Section 6.2 for TCMOT). Other benefits are the low sensitivity to the BBR shift, access to different transitions by commercially available lasers, and the existence of various different isotopes.

2.5 Application of the atomic clock

With 10^{-18} precision, optical lattice clocks and other atomic clocks have many different applications. First of all, their higher precision and accuracy than the Cs time standard suggests that they can be used for a new definition of time to give better measurement precision. ^{199}Hg, ^{27}Al$^+$, ^{199}Hg$^+$, ^{171}Yb$^+$, ^{171}Yb, ^{40}Ca, ^{88}Sr$^+$, ^{88}Sr, and ^{87}Sr clocks have already become a second description of time [74], and the community is pushing for optical clocks to be the next time standard.

Recently, it was proposed to detect gravitational waves by two satellites having precise atomic clock [75]. The point of the proposal is that the second arm of the large interferometer experiments for gravitational wave detection, such as LIGO, VIRGO and KAGRA, is only for the time reference, and if your clock is precise enough, a second axis is not necessary. The proposed sensitivity is as good as space based light interferometry such as LISA, and with resonant detection mode, satellites with precise atomic clocks have better precision.

Precise atomic clocks can be used for measuring the drift of the fundamental

[6]This is magic only for cancelling energy shift due to the E1 term. Strategies to choose a good intensity and frequency is summarized in [73], and their operational frequency is 394,798,278 MHz, which is closer to [34]

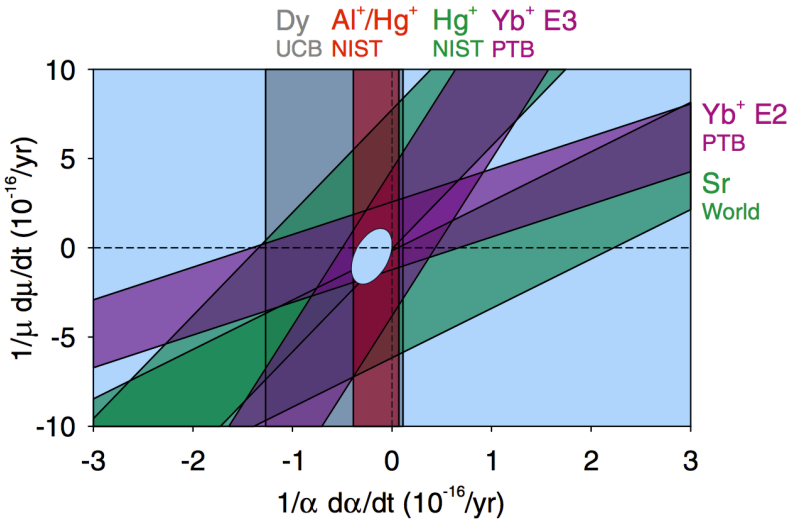

Figure 2-5: Summary of time variation of fundamental constants (Cited from [5])

constants with respect to time. Particularly, any change of the fine structure constant α is of interest, as there are some astronomical observations that claim to show that α changing over time. [76] To measure this with an atomic clock, it is necessary to compare the frequency ratio of two different transitions that have different dependence on α. A good example is the frequency ratio measurement of E2 and E3 transitions in a $^{171}Yb^{+}$ ion clock. [5, 77] The atomic transition in general is also sensitive to the proton electron mass ratio μ, and clock measurement gives the constraints in $\dot{\mu}/\mu - \dot{\alpha}/\alpha$ space. Fig. 2-5 shows a nice summary in [5].

Another proposal is a detection by an array of atomic clocks of a domain wall of topological defect dark matter. [78] The idea is that a certain kind of dark matter generates a delay of time, and therefore as a bulk of this dark matter goes through an array of atomic clocks, certain clocks gets slower in a coincident way.

A classically important application of atomic clocks is the test of special and general relativity. Historically, this was tested by GPS satellites, and an Al^{+} clock with 10^{-18} precision enabled it on the ground. [79] Recently, a more precise measurement was performed with an ^{87}Sr optical lattice clock located $\sim$ 15 km away, and the detected altitude difference was the same as that by independent measurement made by levelling and gravimetry. [80]

There are also attempts to measure some many-body physics phenomena by clock transitions. [81, 82, 4]

For an improvement of these measurements, improvement of atomic clock precision, particularly for a short averaging time, is desired.

Chapter 3

Spin squeezing

In this section, theoretical aspects of spin squeezing and previous experiments are summarized. In typical experiments performed so far, a spin is either an electronic spin of alkali atoms or a nuclear spin in alkali-earth (like) atoms. Spin squeezing is often performed through atom-photon interaction enhanced by an optical cavity. To describe the methods for spin squeezing smoothly, first theories of strong atom-photon interaction are described. Next, the theory of spin squeezing is developed. In the end, the theory of our specific system is mentioned.

3.1 Strong atom-photon interaction through an optical cavity

Strong atom-photon interaction enhanced by an optical cavity is formalized by Janes and Cummings [83]. Their assumption is a two level system, which can be regarded as a spin 1/2 system, that interacts with a light field inside an optical cavity. (Fig. 3-1) The original formalism with a fully quantized field has the Hamiltonian

$$\hat{H}_{JC} = \frac{\hbar\omega_0}{2}\hat{\sigma}_z + \hbar\omega_C\hat{a}^\dagger\hat{a} + i\hbar\left(g\hat{a}^\dagger\hat{\sigma}^- - g^*\hat{a}\hat{\sigma}^+\right) \tag{3.1}$$

A major feature of this system is a splitting of the resonance frequency of cavity transmission when $\omega_C = \omega_0$, which is called vacuum Rabi splitting. This was first

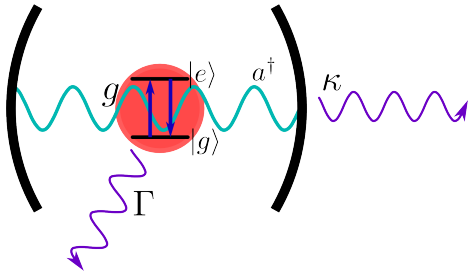

Figure 3-1: A system for the Janes-Cummings model. The resonant frequency for the two level system is ω_0, and the resonant frequency for the light field inside the cavity is ω_C. The coupling constant, decay to the free space, and decay through the cavity are g, Γ, κ, respectively.

calculated with Eq. 3.1 to be $2g\sqrt{N}$. [84, 85] On the experimental side, Jeff Kimble's group has a realization of the vacuum Rabi splitting in a single atom and cavity system [86]. Further developments are summarized in Ref. [87].

This strongly interacting system can also be understood by a fully classical description, as summarized in Ref. [88]. In this formalism, a two level system is described by a Lorentz model that has complex polarizability

$$\alpha = 6\pi\varepsilon_0 c^3 \frac{\Gamma/\omega_0^2}{\omega_0^2 - \omega^2 - i(\omega^3/\omega_0^2)\Gamma}, \tag{3.2}$$

where ω is the frequency of the light field and γ is the decay rate of the oscillator. The light field has an electric field of

$$E(z_0, t) = \frac{\mathcal{E}}{\sqrt{\varepsilon_0 c A}} e^{i(kz_0 - \omega t)}, \tag{3.3}$$

where k is the wave number, z_0 is the position of the atom, and $A = \pi w^2/2$ is the effective mode area. $\mathcal{E}$ is the beam size independent electric field satisfying $P = |\mathcal{E}|^2/2$, where P is the power of a laser beam.

Now, assume the configuration shown in Fig. 3-2. With this configuration, the intracavity electric field satisfies the following equation.

$$\mathcal{E}_\mathrm{c} = r_1 r_2 e^{2ikL} \mathcal{E}_\mathrm{c} + i q_1 \mathcal{E}_\mathrm{in} + 2\mathcal{E}_\mathcal{M} \tag{3.4}$$

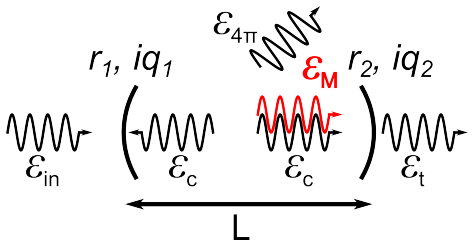

Figure 3-2: Configuration of an atom interacting with a light field in an asymmetric cavity: $\mathcal{E}_{\rm in}$, $\mathcal{E}_{\rm c}$, and $\mathcal{E}_{\rm t}$ are the electric field of the input, intracavity and transmitted light. r_1, r_2 are the reflectivity of two mirrors, and iq_1, iq_2 are the transmission of mirrors. Here, lossless mirrors are assumed, but if loss needs to be implemented, intracavity loss can be modeled by a reduction of $\mathcal{E}$ at each reflection, and transmission loss can be modelled by a beamsplitter in front of a mirror.

Using $\mathcal{E}_{\mathcal{M}} = i\beta\mathcal{E}$, $\beta = \frac{k}{\pi w^2}\frac{\alpha}{\varepsilon_0}$, and RWA, we get the following form for $\mathcal{E}_{\rm c}$.

$$\mathcal{E}_{\rm c} = \frac{2iq_1\mathcal{E}_{\rm in}}{q_1^2+q_2^2}\frac{1}{\left[1+\eta\mathcal{L}_a(\Delta)\right]-\left[\frac{2\delta}{\kappa}+\eta\mathcal{L}_d(\Delta)\right]i}, \tag{3.5}$$

where

$$\mathcal{L}_a(\Delta) = \frac{\Gamma^2}{4\Delta^2+\Gamma^2} \tag{3.6}$$

$$\mathcal{L}_d(\Delta) = \frac{-2\Delta\Gamma}{4\Delta^2+\Gamma^2} \tag{3.7}$$

$$\eta = \frac{24\mathcal{F}}{\pi w^2 k^2} = \frac{4g^2}{\kappa\Gamma} \tag{3.8}$$

are the absorptive Lorentzian, dispersive Lorentzian, and single atom cooperativity, respectively. Δ and δ are defined as $\delta = \omega - \omega_c$, and $\Delta = \omega - \omega_0$. Single atom cooperativity is an important parameter to describe the strength of the interaction between atom and light, and is intuitively understood as the number of interaction between a single atom and a single photon before the photon leaks out of the cavity. If this is more than one, the system is said to be in the strongly coupled regime, where vacuum Rabi splitting manifests for single atom. If it is less than one, the regime is called the dispersive regime. It is often necessary to have $\eta \gg 1$ to generate highly entangled states.

From Eq. 3.5, $\mathcal{E}_t$ is calculated as

$$\mathcal{E}_{\mathrm{t}} = -\frac{2q_1q_2\mathcal{E}_{\mathrm{in}}}{q_1^2+q_2^2}\frac{1}{[1+\eta\mathcal{L}_a(\Delta)]-\left[\frac{2\delta}{\kappa}+\eta\mathcal{L}_d(\Delta)\right]i} \tag{3.9}$$

From Eq. 3.9, transmission power is calculated as

$$\frac{P_{tr}}{P_{in}} = \frac{4q_1^2q_2^2}{(q_1^2+q_2^2)^2}\frac{1}{[1+\eta\mathcal{L}_a(\Delta)]^2+\left[\frac{2\delta}{\kappa}+\eta\mathcal{L}_d(\Delta)\right]^2} \tag{3.10}$$

The ratio of free space scattering and input power is

$$\frac{P_{4\pi}}{P_{in}} = \frac{2q_1^2}{q_1^2+q_2^2}\frac{2\eta\mathcal{L}_a(\Delta)}{[1+\eta\mathcal{L}_a(\Delta)]^2+\left[\frac{2\delta}{\kappa}+\eta\mathcal{L}_d(\Delta)\right]^2} \tag{3.11}$$

In the strongly coupled regime $\eta \gg 1$, this has two peaks separated by

$$2f = \sqrt{\eta\Gamma\kappa} \tag{3.12}$$

This matches the amount of vacuum Rabi splitting calculated by the fully quantized description. When the cavity resonance is far detuned $\Delta \gg \Gamma$ from atomic resonance, $\eta\mathcal{L}_a \ll 1$ holds, and the transmission peak is at

$$\delta = -\frac{\kappa\eta}{2}\eta\mathcal{L}_d \approx \eta\frac{\Gamma\kappa}{4\Delta} \tag{3.13}$$

This means that the cavity resonant frequency shifts by the amount $\delta\omega_c = \eta\Gamma\kappa/4\Delta$. When there are more than one atoms in the cavity mode, coherent scattering from atoms simply becomes N times larger, assuming that there are no effects of saturation. This results in all η substituted by $N\eta$, and the vacuum Rabi splitting and cavity resonance shift by an atomic ensemble in a cavity becomes

$$2f = \sqrt{N\eta\Gamma\kappa} \tag{3.14}$$

$$\delta\omega_{\mathrm{c}} = N\eta\frac{\kappa\Gamma}{4\delta} \tag{3.15}$$

$N\eta$ in the formula does not reflect the actual number of atoms trapped in the

cavity mode, because each atom has a different coupling constant to the cavity mode depending on their position relative to the cavity mode. In the case of a Gaussian beam inside a standing wave Fabry-Perot cavity, the effective cooperativity is $\eta_{\rm eff} = \frac{2}{3}\eta$, where η is the cooperativity at the center of the Gaussian beam. [89]

The phase shift due to the atoms in the cavity is calculated as the phase of $\mathcal{E}_{\rm c}/\mathcal{E}_{\rm in}$. From Eq. 3.9, the phase shift $\phi_{\rm ph}$ is

$$\phi_{\rm ph} = \tan^{-1} \frac{\frac{2\delta}{\kappa} + \eta\mathcal{L}_d(\Delta)}{1 + \eta\mathcal{L}_a(\Delta)} \tag{3.16}$$

This phase measurement is performed with a homodyne measurement with some reference light.

3.2 Bloch sphere and coherent spin state

To explain what a squeezed spin state is, it is useful first to mention a few basic concepts to describe a spin state. For simplicity, it is assumed that the spin state we deal with is an ensemble of $N = 2S$ particles of spin 1/2. For a single spin state, the Bloch sphere is useful to describe the orientation of the spin, which quantum mechanically is the amount of the relative phase of the $|\downarrow\rangle$ state and the $|\uparrow\rangle$ state. The notion of a coherent spin state (CSS) was first developed by Ref. [2] for solid state physics as a spin equivalent of an optical coherent state in the sense that the uncertainty in two quadratures is minimized by same amount. Intuitively this is the situation where N spins are pointing in the same direction, and mathematically formalized as follows for atomic physics, where it is easy to flip all the spins. [90]

$$|\theta,\phi\rangle = \frac{1}{\sqrt{N!}}\left[\sin\frac{\theta}{2}\mathrm{e}^{-i\phi/2}\hat{a}^\dagger + \cos\frac{\theta}{2}\mathrm{e}^{i\phi/2}\hat{b}^\dagger\right]^N |\mathrm{vac}\rangle \tag{3.17}$$

$$= \sum_{m=-S}^{S}\binom{2S}{S+m}^{1/2}\cos^{S-m}\frac{\theta}{2}\sin^{S+m}\frac{\theta}{2}\mathrm{e}^{-i(S+m)\phi}|S,m\rangle \tag{3.18}$$

$$\hat{S}_+ = \hat{b}^\dagger\hat{a},\ \hat{S}_- = \hat{a}^\dagger\hat{b},\ \hat{S}_z = \hat{b}^\dagger\hat{b} - \hat{a}^\dagger\hat{a} \tag{3.19}$$

Here, $\hat{a}^\dagger$ and $\hat{b}^\dagger$ are creation operators for the $|\downarrow\rangle$ state and the $|\uparrow\rangle$ state. The state is on a sphere whose point is specified by the polar coordinate (θ, ϕ) and whose radius is S. This is the Bloch sphere for a spin ensemble, and it describes the coherent spin state in the way same as a Bloch sphere for a single spin; the θ direction corresponds to the population difference between the $|\downarrow\rangle$ state and the $|\uparrow\rangle$ state, and the ϕ direction corresponds to the relative phase between them.

The coherent spin state has the same amount of uncertainty in both orthogonal directions. Particularly when the state is on the equator of Bloch sphere, the uncertainty becomes $\Delta S = S\Delta\phi$. With the knowledge of uncertainty relation for the spin $\langle\Delta S_i^2\rangle\langle\Delta S_j^2\rangle \geq \frac{1}{4}|\langle\Delta S_j^\rangle|^2$, this becomes

$$(\Delta\phi)^2 = \frac{1}{2S} = \frac{1}{4N} \sim \frac{1}{N} \tag{3.20}$$

This N^{-1} scaling is called the standard quantum limit (SQL) of the phase resolution.

3.3 Spin squeezed state

The idea of a squeezed spin state was first proposed in 1993 [91]. A spin state is regarded as squeezed if the uncertainty of one of the two direction that is orthogonal to the mean spin vector is smaller than the SQL. This kind of squeezed spin state is possible if spins are correlated in an appropriate way. To generate a spin squeezed state, a special procedure described in Section 3.4 is necessary.

The amount of the spin squeezing described here is quantified by the following parameter:

$$\xi_{UK}^2 = \frac{2}{S}\Delta S_{\min}^2 \tag{3.21}$$

If $\xi_{UK}^2 < 1$, a spin state is squeezed. This criterion is called the Kitagawa-Ueda criterion. To the extent that the radius of a Bloch sphere is fixed, this is a good enough criterion to use, but practically, the preparation of a state shortens the spin length, and this effect should be taken into account to have a criterion for usefulness of spin squeezing. This practically useful criterion is called the Wineland criterion,

described in the following equation [92]:

$$\xi_W^2 = 2S\frac{\Delta S_{\min}^2}{\langle \hat{S} \rangle^2} \tag{3.22}$$

If this parameter is less than 1, a spin state is squeezed. Here, the picture is you start from a spin S, and during the process of squeezing, your spin length shrinks to $\langle \hat{S} \rangle$, which is the effective mean spin length. The contrast C is defined as

$$\langle \hat{S} \rangle = CS. \tag{3.23}$$

With this and $N = 2S$, Eq. 3.22 becomes

$$\xi_W^2 = \frac{1}{C^2}\frac{4\left(\Delta S_{\min}\right)^2}{N} \tag{3.24}$$

Typically, the amount of squeezing is described by the inverse of ξ_W^2 in units of dB. This quantity is called metrological gain.

In Section 3.2, the uncertainty of the SQL was mentioned to be $\left(\Delta\phi_{\mathrm{SQL}}\right)^2 \sim 1/N$. The squeezed state makes this resolution better, but there is an absolute limit you can get from a maximally entangled state: the Heisenberg limit. The uncertainty of Heisenberg limit scales as $\left(\Delta\phi_{\mathrm{HL}}\right)^2 \sim 1/N^2$, and spin squeezing enhances the phase resolution from the SQL to somewhere between the SQL and the Heisenberg limit.

3.4 General strategy to generate spin squeezed state

To generate the squeezing, we need some kind of nonlinear process that correlates spins. In this section, a few examples of such nonlinear processes are discussed.

3.4.1 Measurement-based squeezing

One method is to use a measurement. In quantum mechanics, measurement collapses a quantum state into certain eigenstates. Suppose a coherent spin state undergoes a measurement. The measurement we can perform is always a population measurement,

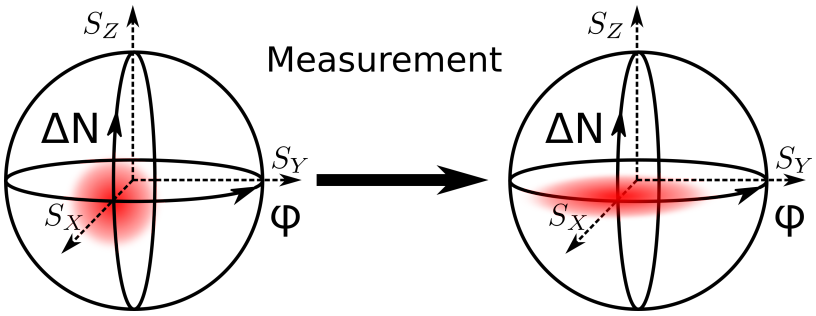

Figure 3-3: Concept of measurement-based squeezing

not a phase measurement, so the S_z component is measured. If this measurement

(i) is weak enough not to collapse the state into a certain S_z eigenvalue,

(ii) is strong enough to resolve S_z better than the SQL,

(iii) does not resolve each spin,

the coherent spin state after a measurement is squeezed, as shown in Fig. 3-3. (i) is important to maintain the phase coherence. If a state collapses to a specific S_z state, the uncertainty in the S_z direction is zero, but the usefulness of this spin state is zero, because the state wraps all around the sphere, and there remains no phase resolution. (ii) sets a technical requirement on how strong the measurement is. A squeezed spin state is generated only when the resolution of the measurement is larger than SQL. (iii) means that we should keep the contrast of the state through the measurement. In a typical situation of measuring the atom state with photons, the scattering of a photon into free space, which is not captured by a photon detector, cannot be avoided. This free space scattering picks a certain spin out of the coherent spin state, and the loss of contrast incorporated in Wineland criterion occurs.

In typical experiments so far, a spin is either an electronic spin of alkali atoms or a nuclear spin in alkali-earth (like) atoms, and measurement is made through an interaction between atoms and photons. Often, to enhance the interaction, atoms are trapped in an eigenmode of an optical cavity, and photons interact with atoms in the cavity. The measurement can be performed through vacuum Rabi splitting or a dispersive cavity resonance shift. The measurement can be done through the power or phase of transmission or reflection. In previous reports, most of the experiments

use the dispersive cavity resonance shift to measure the atom number. Ref. [43, 93] use the phase shift of reflected light. As for transmission, Ref. [94] uses power, and Ref. [95] uses phase. Ref. [96] uses the power of reflected light to detect the amount of vacuum Rabi splitting. A popular measurement without a cavity resonance shift is through Faraday rotation of linearly polarized light. [97, 98, 99]

The advantage of measurement-based squeezing is that it is conceptually simple, and information obtained by the measurement can be used for the following process. If a spin squeezed atomic clock is operated with measurement-based squeezing, each time the initial atomic phase is slightly different due to the quantum mechanical fluctuation of the coherent spin state, but this fluctuation can be compensated by the measured value of the phase. On the other hand, maximum squeezing depends on the measurement efficiency. In particular, it is very difficult to collect all the scattered light, part of which is into free space, and this would put additional constraints on the achievable squeezing.

3.4.2 Unitary squeezing

Unitary squeezing uses as the source of squeezing the unitary evolution of a state by a nonlinear Hamiltonian. In the original proposal of spin squeezing [91], one-axis squeezing and two-axis squeezing are described. These are implemented by the lowest order nonlinear Hamiltonian regarding spin operators S_x S_y and S_z, and higher order nonlinear Hamiltonian gives different kind of quantum states. Here, the discussion will be concentrated on the lowest order nonlinear Hamiltonian.

Generally, unitary transformation $\hat{U}(t) = \exp[-itF(\hat{S}_z)]$ generated by the Hamiltonian $H = \hbar F(\hat{S}_z)$ transforms the ladder operator $\hat{S}_+$ as

$$\hat{S}_+(t) = \hat{U}^\dagger \hat{S}_+ \hat{U} = \hat{S}_+(0) \exp\left[itf(\hat{S}_z)\right] \tag{3.25}$$

$$f(\hat{S}_z) = F(\hat{S}_z + 1) - F(\hat{S}_z) \tag{3.26}$$

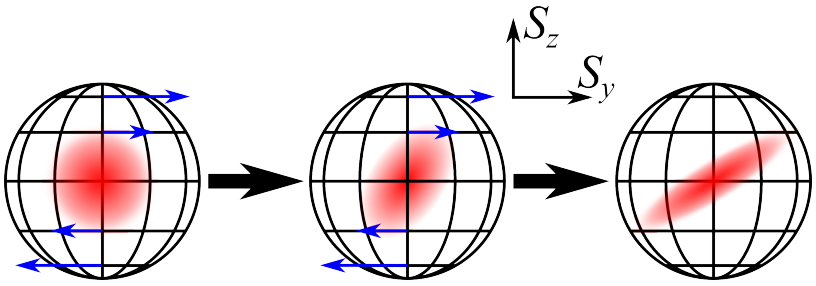

Figure 3-4: One axis squeezing

When the Hamiltonian is the lowest order nonlinear Hamiltonian

$$\hat{H} = \hbar\chi\hat{S}_z^2 \tag{3.27}$$

$f(\hat{S}_z) = 2\chi(\hat{S}_z + 1/2)$. This gives a shearing of the state as shown in Fig. 3-4. For $S \gg 1$ and $|\mu| = |2\chi t| \ll 1$, the reduced variance takes the minimum value of

$$V_{\min} \approx \frac{1}{2}\left(\frac{S}{3}\right)^{1/3} \sim S^{1/3} \tag{3.28}$$

at $|\mu| = 24^{1/6}S^{-2/3}$. This means that with one axis squeezing, the number scaling of phase uncertainty is reduced from $V \sim S$ to $V \sim S^{1/3}$ by a factor of $S^{2/3}$. For example, if $S = 1000$, the reduction of uncertainty is a factor of 100, which means that 20 dB of squeezing is possible, except for a numerical factor of $O(1)$.

Intuitively, the rigorous calculation above is understood as follows. When a time evolution happens for a linear Hamiltonian $\hat{H} = \hbar A\hat{S}_z$, what happens on the Bloch sphere is a precession of the state $e^{-iAmt}|S, m\rangle$. When the Hamiltonian is given by Eq. 3.27, the precession is $e^{-iAm(Amt)}|S, m\rangle$, which means the velocity of precession is proportional to S_z. This is simplified on a flat plane as shown in Fig. 3-5. The transformation is a slide in the x direction proportional to the value of y. The resulting state has a narrower distribution along the direction perpendicular to the line $y = x/\mu$. The distance between the two lines $y = (x \pm 1)/\mu$ shows the width of the distribution, which is $2/\sqrt{1+\mu^2}$. The ratio to the original width is $1/\sqrt{1+\mu^2}$, which is smaller than 1. Here, the width decreases monotonically against μ, but on the Bloch sphere,

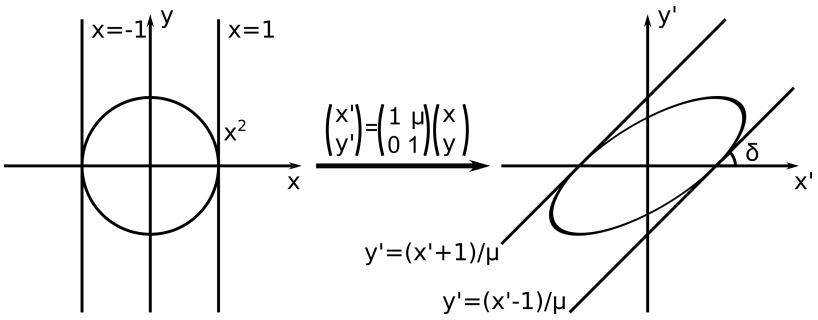

Figure 3-5: Simplified picture of one axis squeezing: a circle of radius 1 symbolizing SQL is transformed by a translation proportional to its y value.

the cross section with a larger $|S_z|$ has a smaller radius, and the transformation has a quadratic term due to the geometry. Consequently, the sheared state gets distorted to an S shape, which gives a minimum for the reduced variance. It has to be noted that in the real system, sending photons means that a certain number of photons interact with atoms, and this generates measurement-based squeezing in the y direction. This effect, which is quantified by the Fisher information, is not included in this intuitive explanation.

To implement one axis squeezing, atom collision is first used to get a nonlinear Hamiltonian. It was first proposed in Ref. [100], and achieved by a bunch of different groups. [101, 102, 103, 104, 105, 106, 107, 108, 109, 110] Another method is cavity feedback squeezing, which is described in the next section.

Another proposal for unitary squeezing is two axis squeezing. In this case, the Hamiltonian is

$$\hat{H} = \frac{\hbar\chi}{2i}\left(\hat{S}_+^2 - \hat{S}_-^2\right), \tag{3.29}$$

and rotation is along the axis of $S_y = \pm S_x$. Because the rotation along two axes happens at the same time, the shearing in the one axis squeezing case becomes an elongation as shown in Fig. 3-6, when the initial state is the $S_z = S$ state. The reduced variance minimum can reach $1/2$. Generally, two axis squeezing is more difficult to implement, and there are only a few reports. Ref. [111] proposed a way to perform effective two axis squeezing by composite Rabi pulses. Ref. [112] is another proposal for changing one axis squeezing into effective two axis squeezing. Ref. [113]

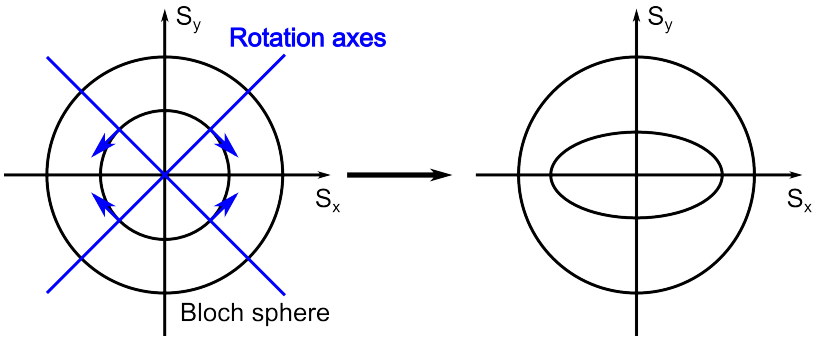

Figure 3-6: Two axis squeezing: the Bloch sphere is observed from north pole.

shows a scheme to perform two axis squeezing with a BEC in an optical cavity. Ref. [114] is an experimental realization of two axis squeezing, though the amount of squeezing is not very high.

3.5 Cavity feedback squeezing-implementation of unitary squeezing

One way to implement unitary squeezing is cavity feedback squeezing [6]. The system is described in Fig. 3-7. A two level system $|\downarrow\rangle$ and $|\uparrow\rangle$ interacts with the light field in a cavity that is on resonant to an excited state $|e\rangle$ and to the average energy of the two level system. Due to the energy difference of the $|\downarrow\rangle$ and $|\uparrow\rangle$ states, the cavity resonance is far off resonant from these two states. The light sent into the cavity has a frequency that is on a slope of the cavity resonance. In this situation, the effective Hamiltonian becomes

$$\hat{H}_{\text{eff}} = \hbar\omega_c \hat{c}^\dagger \hat{c} + \hbar\Omega \hat{c}^\dagger \hat{c} \hat{S}_z + \hbar\omega_0 \hat{S}_z, \tag{3.30}$$

where $\hat{c}$ is the annihilation operator of the cavity field. $\Omega = 2g^2/|\Delta|$ is satisfied, with the definition that g is the coupling constant for atom light interaction, and Δ is the detuning from $|\downarrow\rangle$ and $|\uparrow\rangle$ and the cavity resonance.[1] The first term in Eq. 3.30 is

[1]Thus, $\Delta = \omega_a/2$ from Fig. 3-7.

the energy of the light field, the third term is that of atomic system, and the middle term is the interaction term. This term gives the following time evolution for $\hat{S}_+$ and $\hat{c}$:

$$\frac{d\hat{S}_+^n}{dt} = in\Omega\hat{c}^\dagger\hat{S}_+^n\hat{c} \tag{3.31}$$

$$\frac{d\hat{c}}{dt} = \left(-\frac{\kappa}{2} - i\omega_c - i\Omega\hat{S}_z\right)\hat{c} + \sqrt{\frac{\kappa}{2}}\left(\hat{b}_1 + \hat{b}_2\right) \tag{3.32}$$

where n is a positive integer and $b_{1,2}$ are the annihilation operators for the input fields from the two sides of the cavity. Using the steady state solution of Eq. 3.32 for the coherent state inside the cavity, the following expression is obtained for $\hat{S}_+^n$:

$$\frac{d}{dt}\langle\hat{S}_+^n\rangle_\beta = if_n(\hat{S}_z)\langle\hat{S}_+^n\rangle_\beta \tag{3.33}$$

$$f_n(\hat{S}_z) = n\Omega|\beta|^2\left(1 + n(i-1)\frac{\Omega}{\kappa} + 2\frac{\Omega}{\kappa}\hat{S}_z\right), \tag{3.34}$$

where the subscript β indicates the tracing over the light field states. Eq. 3.33 gives an expression for $\langle\hat{S}_+^n\rangle_\beta$ equivalent to Eq. 3.25, with $f_n(\hat{S}_z)$ linear to $f_n(\hat{S}_z)$. This is the same form as what is discussed in the previous section, and therefore this gives squeezing. The resulting normalized variance $\Delta S_{SSS}^2/\Delta S_{CSS}^2$ is plotted against the shearing strength $Q = Sp_0(2\Omega/\kappa)^2$ in Fig. 3-8, where p_0 is the number of transmitted photons through the cavity.

Fig. 3-8 tells a few things. For cavity feedback squeezing, it is important to have collective cooperativity $N\eta$ to be much larger than 1, but single atom cooperativity η can be smaller than 1. When shearing gets large, the curvature limits the amount of squeezing, as discussed in the previous section.

Intuitively, it uses light atom interaction as a way to generate the $\hat{S}_z^2$ Hamiltonian. This $\hat{S}_z^2$ Hamiltonian is explained as a result of the AC Stark shift. If you have n atoms in a single state that is off resonant from a transition, each atom has an index of refraction. This changes the effective path length inside the cavity, and thus shifts its resonant frequency. In the situation described in Fig. 3-7, one state is red detuned, and the other is blue detuned, so $n \propto N_\uparrow - N_\downarrow = S_z$. This resonant frequency shift

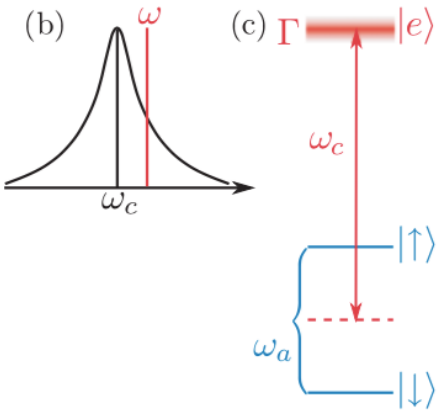

Figure 3-7: System for cavity feedback squeezing (Cited from [6])

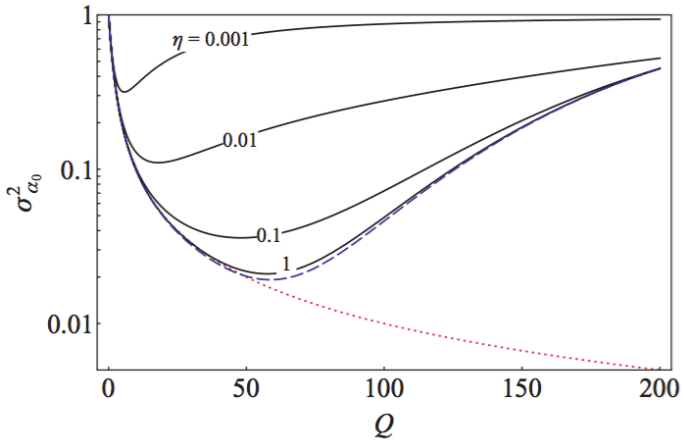

Figure 3-8: Minimum normalized variance (i.e. maximum amount of squeezing) due to cavity feedback squeezing as a function of shearing strength (Cited from [6]): it is assumed that $S = 10^4$. The blue dashed line is the limit due to the curvature of the Bloch sphere, when decoherence due to free space scattering is ignored, and the red dotted line is when both curvature and free space scattering are ignored.

changes the amount of light that is stored in a cavity mode, and thus changes the AC Stark shift of the state. As the lowest order is linear for all the process, the AC Stark shift is proportional to n. The overall energy shift is the number of atoms n times the energy shift, which is proportional to n, and therefore $H \propto S_z^2$. This picture holds as long as one of the two state interacts with light dispersively. For example, if the $|\uparrow\rangle$ state is far detuned and does not have any AC Stark shift due to the cavity light,

$n \propto -N_\downarrow = (S_z - N_{tot})/2$, and the proportionality of n to S_z remains.

The advantage of cavity feedback squeezing, or unitary squeezing in general, is that it does not require any detection, and we don't have to worry about the detection efficiency. The downside is that there is a slight difference between the angle of the squeezed direction and the S_y axis. This means that this angle needs to be measured precisely, and the $\pi/2 - \delta$ pulse has to be applied precisely. Otherwise the squeezed direction has a tilt and the benefit of squeezing goes away.

Cavity feedback squeezing is demonstrated by Ref. [115], and Ref. [116] uses this idea to perform an enhanced measurement of the quantum state.

3.6 Previous works and applications of squeezing

The previous works of spin squeezing are well summarized in Ref. [7]. What is important is how much the variance is reduced compared to the SQL, and how much it is useful for actual applications. This information is nicely summarized in Fig. 3-9 cited from Ref. [7]. The two largest metrological gains were reported from [43, 93] (27 and 28 in Fig. 3-9) These experiments took advantage of the fact that large atom number has larger maximum squeezing, and they are far from the Heisenberg limit. When it comes to a few trapped ions, squeezing down to the Heisenberg limit is achieved. Most of the experiments with cold thermal gas were performed with rubidium atoms. Ref. [99] used ytterbium without an optical cavity.

Spin squeezing has applications to measurements that involve phase measurement. One example is an atomic clock, as discussed in Section 2.3. Ref. [117, 114] also did an atomic clock experiment with squeezed states, though they don't show an Allan deviation graph. Another application is a magnetometer, as the precision of the measurement of precession of spin is enhanced by spin squeezing. Ref. [109, 107] achieved enhanced magnetometry with spin squeezing. Atom interferometry is also a precision measurement that is benefited by spin squeezing. Ref. [118] put emphasis on the application to atom interferometry to describe the significance of their result. EDM measurements, both electron EDM and nuclear EDM, also should be benefitted

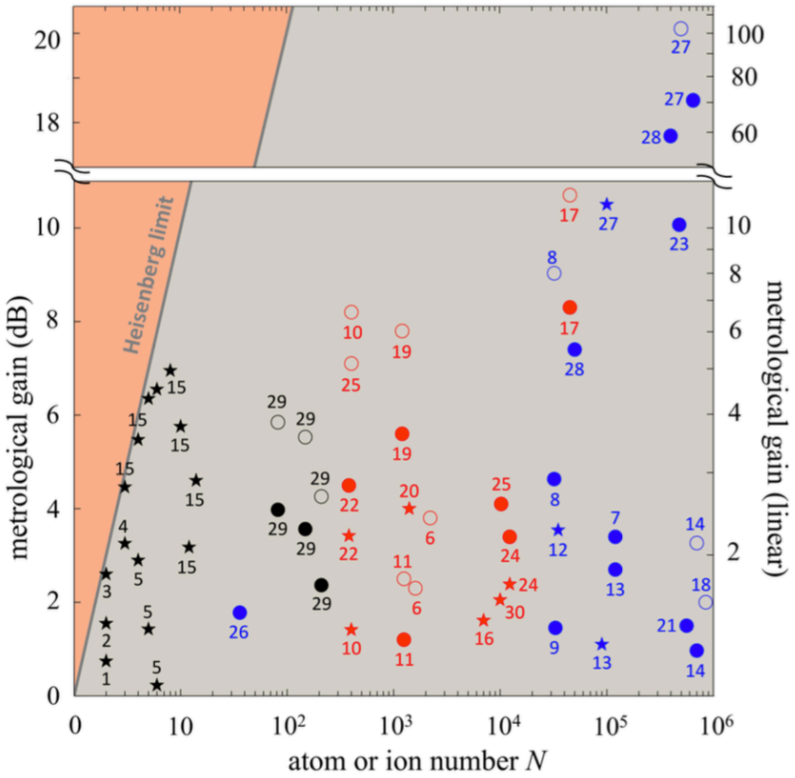

Figure 3-9: Previous results of spin squeezing (Cited from [7]): metrological gain is plotted against atom number. Black, blue, and red points are measurements with trapped ion, BEC and cold thermal gas, respectively. Filled (open) circles are the Wineland squeezing parameter ξ_W^2 obtained without (with) subtraction of technical and/or imaging noise. Stars are the direct measurement of the sensitivity in phase measurement. Numbers show different reports. For the citation, please refer to Ref. [7].

by the spin squeezing, as they also measure the precession of spins.

3.7 Beyond spin squeezed state: non-Gaussian states and their applications

A spin squeezed state is a simple step to get phase sensitivity beyond the SQL, and reports on squeezing so far do not go beyond the Gaussian state, which is defined as a quantum state whose distribution is Gaussian no matter onto which axis you project a state. One-axis squeezing described in Section 3.4.2 has the assumption of $|\mu| \ll 1$.

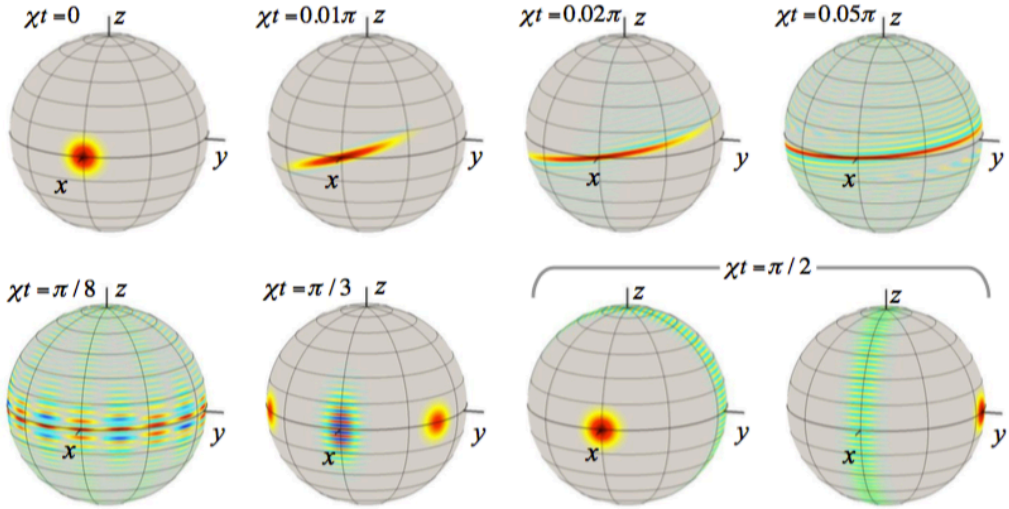

Figure 3-10: State evolution by one axis squeezing from coherent spin state (Cited from [7]): two $\chi t = \pi/2$ case shows $N = 100$ (left) and $N = 101$ (right).

When this limit is removed, and a state has extensive shearing, eventually the two ends of the state wrap up the Bloch sphere and start to interfere with themselves. Generation of Schrödinger's cat state (or NOON state, in this context) in this way is first proposed by Ref. [119], and Fig. 3-10 cited from [7] has a good visualization of the state evolution for different $\mu = 2\chi t$. As shown in the figure, the cat state has an interference fringe between two blobs. This fringe becomes a source of better phase sensitivity. As this is the maximally entangled state, the cat state has a Heisenberg limit sensitivity.

Even if a state is not as entangled as a cat state, typically if it has separate blobs like a kitten state, there can appear an interference fringe between them. This still gives a better phase sensitivity, and therefore a non-Gaussian state in general is a good way to enhance phase sensitivity in metrology.

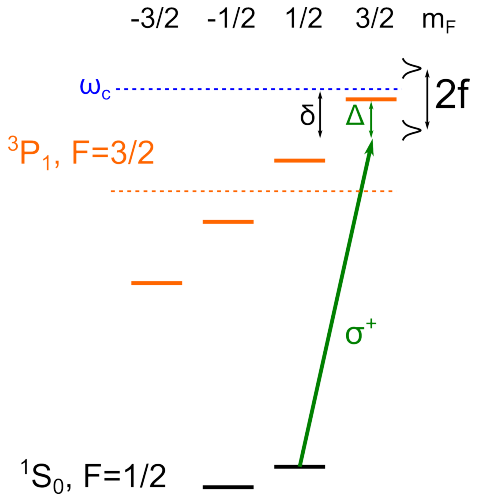

Figure 3-11: The level structure we used for spin squeezing: the ground state has Zeeman splitting of 750 Hz/G, where as the excited state's Zeeman splitting is 1.4 MHz/G. Thus, there is negligible amount of interaction between $m = -1/2$ state of the ground state and the excited state.

3.8 Amount of measurement-based squeezing in our system

In this section and the next section, the theoretical prediction of the maximum squeezing achievable in our system is described. We perform spin squeezing on the nuclear spin 1/2 system of the ^{171}Yb ground state through the interaction between the $m_F = 1/2$ state (i.e. the $|\uparrow\rangle$ state) and the $F = 3/2$, $m_F = 3/2$ state of the $^3P_1$ excited state via 556 nm light. (Fig. 3-11). Because the total atom number N is conserved, measuring only the $|\uparrow\rangle$ state gives information about S_z. We define the atomic resonance between the $m_F = 1/2$ state of the $^1S_0$ ground state and the $F = 3/2$, $m_F = 3/2$ excited state as ω_0, the cavity resonance frequency as ω_c and the laser frequency as ω. Detunings normalized by the cavity linewidth κ and the atomic linewidth Γ are defined as $x = 2\delta/\kappa$ and $y = 2\Delta/\Gamma$. The number of atoms in the $|\uparrow\rangle$ state and the $|\downarrow\rangle$ state are defined as N_1 and N_2.

First, we think of an atom number measurement by transmission power of the vacuum Rabi splitting. The setup is described in Fig. 7-2. The transmission photon is detected by a single photon counter of quantum efficiency of c, including all the

coupling efficiency. The maximum squeezing possible described by the Wineland parameter is

$$\xi^2_{W,\mathrm{tr}} = \frac{32}{N_1\eta}\frac{0.8978}{c}\frac{\gamma_{\mathrm{av}}}{\gamma_{\mathrm{g}}}\frac{\Gamma}{\kappa}, \tag{3.35}$$

where $\gamma_{\mathrm{av}} = (\kappa + \Gamma)/2$ and $\gamma_{\mathrm{g}} = \sqrt{\kappa\Gamma}$. With values of $N_1\eta = 450$, $c = 0.12$, $\kappa = 400$ kHz, and $\Gamma = 184$ kHz, we get

$$\xi^2_{W,\mathrm{tr}} = 1.343 \tag{3.36}$$

Next,the amount of squeezing by phase measurement is given by the following equation:

$$\xi^2_{W,\mathrm{ph}} = \frac{8}{N_1\eta}\frac{0.8978}{c}\frac{\gamma_{\mathrm{av}}}{\gamma_{\mathrm{g}}}\frac{\Gamma}{\kappa} \tag{3.37}$$

This is a factor of four better than that of the transmission power measurement. When values to get Eq. 3.36 are substituted,

$$\xi^2_{W,\mathrm{ph}} = 0.3357 \tag{3.38}$$

This assumes that the probe frequency is parked on a peak of the vacuum Rabi splitting. An easier situation is when the probe frequency is scanned over a peak. In this case, the efficiency is 3/8 of Eq. 3.37, and the Wineland parameter is

$$\xi^2_{W,\mathrm{ph}} = \frac{64}{3N_1\eta}\frac{0.8978}{c}\frac{\gamma_{\mathrm{av}}}{\gamma_{\mathrm{g}}}\frac{\Gamma}{\kappa}, \tag{3.39}$$

and the numerical value of Eq. 3.38 becomes

$$\xi^2_{W,\mathrm{ph}} = 0.8952 \tag{3.40}$$

3.9 Amount of cavity feedback squeezing in our system

The system for cavity feedback squeezing is also the same as that for measurement-based squeezing. The difference is that the probe laser frequency is off resonance,

i.e. off from both the bare atomic resonance and the resonance of the vacuum Rabi splitting. The cavity feedback squeezing is performed through the atomic phase shift due to the light, and therefore the first step is to calculate the atomic phase shift due to the light in the cavity. To estimate it, the starting point is the following relation between the atomic phase per transmission photon and the light phase.

$$\varphi_{\mathrm{at,t}} = \frac{d\phi_{\mathrm{ph,t}}}{dS_z} = \frac{d\phi_{\mathrm{ph,t}}}{dN_1} \tag{3.41}$$

Summing up $\phi_{\mathrm{ph,t}}$, $\phi_{\mathrm{ph,s}}$, and $\phi_{\mathrm{ph,r}}$ we obtain the following total atomic phase shift per incoming photon.

$$\varphi_{\mathrm{at,tot}} = -\eta \frac{y}{1+y^2} \frac{1+q^2}{2} T, \tag{3.42}$$

where $q = q_1/q_2$ and $\varepsilon = 2q^2/(1+q^2)$.

The shearing per incoming photon is calculated as

$$Q_1 = S \frac{d\varphi_{\mathrm{at,tot}}}{dS_z} \tag{3.43}$$

From Eq. 3.42, we obtain

$$Q = -\eta p_{\mathrm{sc}} \frac{y(xy - N_1\eta - 1)}{1+y^2} T \tag{3.44}$$

Whenever photons interact with atoms, we can obtain the information on atom number, and this information always collapse the state partially into certain population difference state on the Bloch sphere. Situation is we send fixed number of probe beam, and certain number of photons are detected, so we know the detected photon number, and from this we can estimate the atom number. This broadens the state in phase direction, and the amount of broadening is governed by the Fisher information. To estimate the amount of squeezing, the antisqueezing due to this Fisher information needs to be calculated. The total Fisher information due to the squeezing light is

$$F_{\mathrm{tot}} = 2\eta p_{\mathrm{sc}} \frac{1+y^2+N_1\eta}{1+y^2} T \tag{3.45}$$

Overall squeezing is

$$\xi_W^2 = \frac{1+F}{Q^2} = \left(\frac{2}{1+q^2}\right)^2 \frac{(1+y^2)^2 + 2\eta p_{\rm sc}(1+y^2+N_1\eta)(1+y^2)T}{\eta^2 p_{\rm sc}^2 y^2 (xy - N_1\eta - 1)^2 T^2} \tag{3.46}$$

When these are converted into the function of transmitted photon number $p_{\rm tr}$,

$$\begin{aligned} Q &= -2N_1\eta^2 p_{\rm tr}\frac{1+q^2}{2}\frac{y(xy-N_1\eta-1)}{(1+y^2)^2}T & (3.47)\\ F_{\rm tot} &= 4N_1\eta^2 p_{\rm tr}\frac{1+q^2}{2}\frac{1+y^2+N_1\eta}{(1+y^2)^2}T & (3.48)\\ \xi_W^2 &= \frac{1+F}{Q^2} \\ &= \left(\frac{2}{1+q^2}\right)^2 \frac{(1+y^2)^4 + 4N_1\eta^2 p_{\rm tr}(1+y^2+N_1\eta)(1+y^2)^2\frac{1+q^2}{2}T}{4N_1^2\eta^4 p_{\rm tr}^2 y^2 (xy-N_1\eta-1)^2 T^2} & (3.49) \end{aligned}$$

Chapter 4

Apparatus

The apparatus mainly consists of a vacuum chamber that contains atoms and an optical cavity, lasers whose lights are sent to atoms, detectors of photons, and the hardware and software for controlling the system and acquiring the data. In this chapter, these apparatus except for the lasers are described. Lasers are described in Chapter 5.

4.1 Laboratory structure

An atomic physics lab has certain requirements. First of all, a certain amount of space is necessary to have a vacuum chamber where cold atoms are trapped and manipulated. This space is typically large optics tables, because laser beams are sent into vacuum chamber to manipulate atoms. In addition to these most basic features, the following features are useful.

- shelves above optics tables to put electronics that control lasers and other devices
- outlets for control devices
- a workbench to do soldering and other electronics manufacturing
- a workbench to assemble optics components

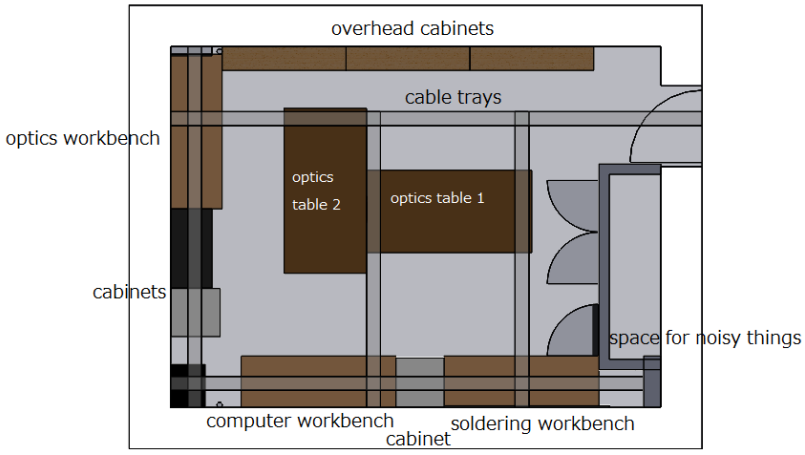

Figure 4-1: Structure of the laboratory

- computers and a control system for experiments
- paths for cables between different control devices
- a cabinet to put noisy things.
- air conditioning system for room temperature stabilization
- chilled water circulation system, so that heat from components consuming high power can be dumped into water
- storage space for various components

Based on these requirements and fire safety, our lab is designed as shown in Fig. 4-1. The room has 5.3 m x 7.2 m rectangular shape, and two optics tables, three working benches, three main cabinets, and a bunch of other storage space are installed. Above the optics tables is two layer canopy for putting electronics boxes and other equipments to control the system. Three work benches are used for soldering, computer controls, and optics building, as shown in the figure.

The optics tables are from TMC (783 Series), and are 4' x 8' in size. They have a pneumatic floating feature for passive vibrational isolation, compressed air for which is supplied from the building. Closing a valve from the building disables the floating without damaging the legs. Also, we have valves that can disable the floating of each

table independently. One of the two optics table is custom ordered, and has a 7" square hole in the middle, for the purpose of holding the main vacuum chamber. It also has some tapped holes for 1/4-20 screws on the bottom surface, so that an optics breadboard can be hung from the bottom surface of the table.

Inside the space for noisy things, a water chiller (Thermo Neslab System I) and high current power supply (Agilent 6031A and Lambda GEN 15-220) are located. The water chiller is for separating water circuit from the building, and dumps heat to the building cold water supply. water hoses are put along cable trays, and water goes to a splitting station below optics table 2. The splitting station is made of Swagelok components, and sends cold water (temperature regulated at 20°C) to the MOT coils and to cold plates for FETs controlling coil current and AOM drivers. Electrical cables and coaxial cables for transmitting signals are also put along the cable trays.

4.2 Vacuum chamber design

The vacuum chamber is the place where cold atoms are trapped and interrogated by lasers. For different purposes, following features are required, or desired.

- large enough number of AR coated viewports that are at different angles from each other, for optical access of different kind of lights with 0 degree AOI to prevent unwanted reflection and polarization change.

- low vacuum pressure: 10^{-9} Torr or less depending on background gas collision limited lifetime required in experiments

- non-mechanical pumping system to keep the vacuum pressure low without generating mechanical vibration.

- at least one viewport that covers large numerical aperture from atoms for imaging

- oven or other source of atoms

- differential pumping system for the oven: as the oven gets hot, typically vacuum pressure is worse than the main part of the chamber, and independent pumping is desired.
- coils surrounding the chamber for MOT and cancelling background magnetic field
- ability of baking
- tight holding from the optics table

In addition to these general requirements, for cavity QED experiments, following factors are also important.

- large enough space for the cavity structure
- mechanical stability of the cavity inside the vacuum chamber
- good coupling to the cavity mode from the outside of the chamber
- electrical feedthrough for sending signals to control the cavity

Based on these requirement, our vacuum chamber is designed and built as shown in Fig. 4-2. The main part consists of a 4.5" long nipple for 6.75" flange. On each 6.75" flange, a viewport is attached, and these work as the main windows for sending light in and imaging the atoms. On the side of the cylinder, 10 different half nipples are welded. Two 4.5" flange nipples are oriented in the vertical direction. The top flange has a custom reduced flange from 4.5" to 2.75" onto it. The reducing flange has six 6-32 screw for mounting the cavity structure (for the details of the cavity structure, see Chapter 4.3). On the top, a Tee is mounted for sending electrical signal to the cavity system. The bottom 4.5" flange is connected to another reducing flange from 4.5" to 6.75". Four 2.75" flanges are angled 50° from the vertical axis, and are used for sending the MOT beams in. Four 1.33" flanges are angled 10° from the horizontal. The right bottom one in Fig. 4-2 is used for the oven. The tube sticks out from the main part of the chamber by 0.535", and its end is closed except for a

3 mm diameter hole for collimation. The oven is in the tube, with a Tee holding a 2 l/s ion pump (Agilent 919520) for differential pumping. (for the detailed description of the oven, see Section 4.4.) Three other 1.33" flanges have conical reducers that expand the flange size to 2.75". Two flanges simply have 2.75" viewports on their ends. For these flanges, the reason for expanding the size is that 1.33" viewports have thickness variations on the glass part large enough to have some lensing effects, and they should be avoided for use as a window. The last 1.33" flange, which is on the opposite side of the oven has heated window inside a Tee on the reducing conical nipple, and then has 2.75" flange (for the heated window, see Section 4.4). This path is used for sending the longitudinal cooling beam.

A unique feature of this chamber is that it is held in the middle of an optics table, and goes through a hole in a optics table. Pumps are below the optics table. The connection to the bottom part of the chamber is done by 13.68" long 6.75" flange nipple, which is connected to the bottom 4.5" flange of the main part through a reducing flange. The bottom surface of the top 6.75" flange of the tube is clamped by a clamp onto the optics table. The tube is so large to increase the flow rate. At the bottom, the 6.75" flange has a 4.5" 6-way cross connected via another reducing flange. The 6-way cross has a 40 l/s ion pump (Agilent VacIon Plus 40 Starcell Ion pump), a 4.5" tube for titanium sublimation pump (Thremionics PS-500), an 1-1/2" angled all metal valve (MDC 314003), a blind flange, and a 4.5" viewport. The viewport is at the bottom flange of the 6-way cross, and serves as input for light going into the cavity. For the purpose of baking, the 6.75" tube that is in the hole of the optics table has heating tape and aluminum foil permanently wrapped onto it.[1] The valve is connected to a pumping system consisting of a turbo pump and a rotary pump when the initial pumping happens, but once pressure goes below safe operation pressure of the ion pump (typically 10^{-4} Torr), the valve is closed and the roughing pumps are disconnected.

[1]Although it is very good for this structure to have tight fixture onto the optics table and to save the space on the table, baking is a bit tricky. Because the maximum temperature for the optics table is 70 °C, the chamber has to be lifted during a baking, when the temperature of the chamber goes up to 150 °C, and a fan has to be continuously run to have cold air flowing around the table.

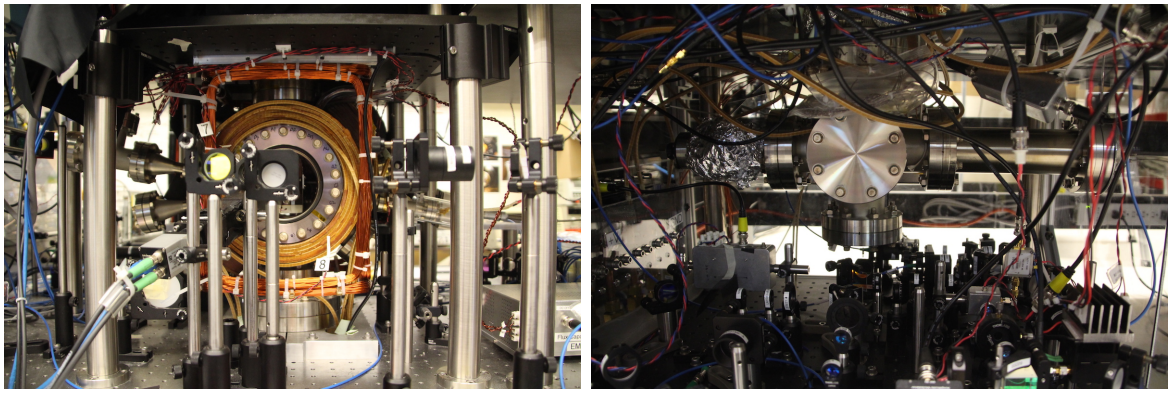

(a) top part (b) bottom part

Figure 4-2: Vacuum chamber

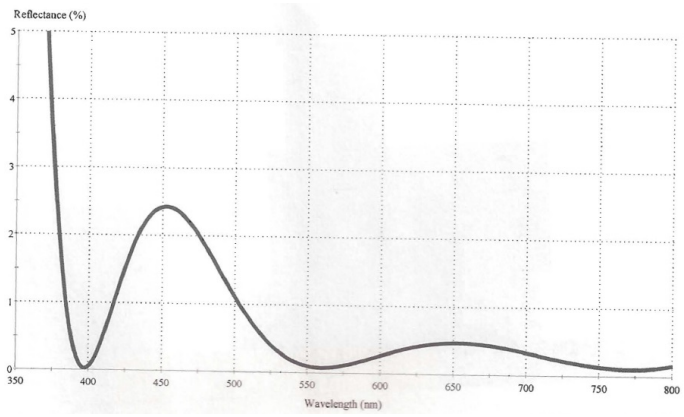

Figure 4-3: Reflectivity of the AR coating on the viewport for different wavelength (This is a scan of a specification from the coating company.)

All the viewports on the vacuum chamber are AR-coated for 399 nm, 556 nm, 578 nm and 759 nm light. The estimated reflectivity by the coating company is shown in Fig. 4-3.

4.3 Optical cavity

4.3.1 Designing the cavity configuration

The optical cavity in the main vacuum chamber is the heart of our experiment for cavity QED interrogation. This cavity in the main chamber that interacts with atoms

is called the experimental cavity to distinguish it from the other optical cavities in the lab. In this section, the design of this experimental cavity is described. For the detailed procedure of assembly and wiring, refer to Boris Braverman's thesis [1].

As described in Section 3.1, the most important parameter for spin squeezing and cavity QED in general is the single atom cooperativity η (see Eq. 3.8 for definition). High η is better for generating quantum mechanically interesting states, and a tight waist w is desired for it, because η is purely geometric if you specify a wavelength and mirror properties. Fig. 4-4 shows η for different mirror configurations. A pair of mirrors of the same size (red curve) are typically used, and in this case, there are two regions of high η. One is to put two mirrors very close, such as 10 μm apart. This is what Jeff Kimble has achieved [87], but only a few atoms were loaded at a time, which does not work for an optical lattice clock experiment, where we need thousands of atoms in the cavity. The other choice is to put the cavity near confocal configuration. This has large enough distance between the two mirrors to load thousands of atoms into the cavity mode, but the structure is mechanically unstable. When two different size mirrors are used, the situation changes. As one of the two mirrors has smaller radius of curvature, the stability region gets split. Also, the most mechanically stable part has higher cooperativity than that of the symmetric structure.

In our case, we have a technique to have a micromirror [120], which is suitable for the small radius of curvature mirror: a mirror with both diameter and radius of curvature of a few hundreds of μm. The is made by shooting a CO_2 laser pulse onto a flat substrate, and then coating substrates in the same way as ordinary commercial superpolished mirrors. The quality of micromirrors is not well controlled, and therefore a typical way of making a good micromirror is to have many mirrors, test all of them, and then choose the best one.

Based on these considerations, the cavity structure is chosen to be an asymmetric cavity; one mirror is a commercial 2.5 cm radius of curvature one, and the other one is a micromirror. The designed cavity is in the stability region of two mirrors far

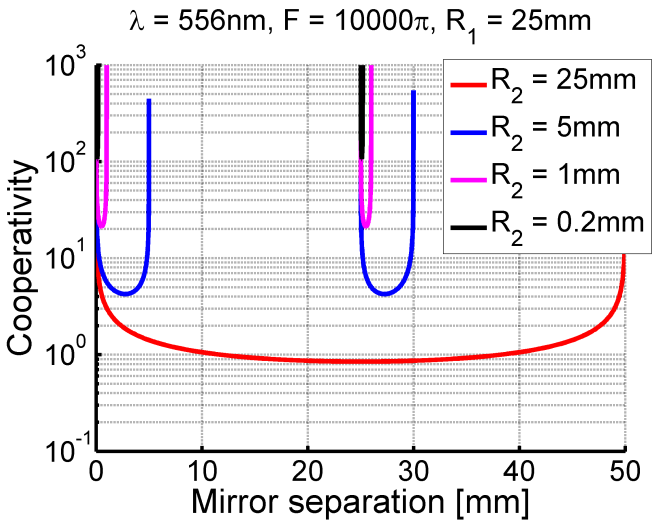

Figure 4-4: Cooperativity for different mirror configuration: red curve is for two mirrors of 25 mm radius of curvature. Blue, pink, and black curves show the situation where one 25 mm radius of curvature mirror and another smaller radius of curvature mirror is used.

apart, satisfying the following equation.

$$R_1 < d < R_1 + R_2, \tag{4.1}$$

where R_1 and R_2 are the radius of curvature of the two mirrors ($R_1 \gg R_2$) and d is the distance of two mirrors. This satisfies both high η and large distance between the two mirrors for directly loading many atoms into the cavity mode, maintaining the mechanical stability.

4.3.2 Design of structure holding mirror

The next thing that should be determined after deciding on the choice of mirror shape and distance is the structure to hold them. Followings are some important factors to be considered.

- Overall structure has to be stiff to prevent mirrors from moving with respect to each other.

- The holding structure has large enough optical access for various lights, such as

MOT beam and path for imaging atoms.

- The distance between the mirrors must be tunable to stabilize the cavity length inside the vacuum chamber. This is typically done by piezo.
- The vibration due to the piezo's motion should not be transmitted to the whole structure, and the mirror should be fully moved by the motion of the piezo. This means the piezo should be on a counter weight, and there should be a damping material between the piezo and the whole structure.
- It is necessary to have fine tunability of axial relative position of two mirrors before they are fixed.
- The temperature of the cavity should be stabilized for a better stability of the mirror distance.
- The structure holding the two mirrors together should be well isolated from the environment to avoid vibrations and temperature fluctuations.
- The cavity should be fixed relative to the optics outside the vacuum chamber.[2]
- There should be some focusing optics near the cavity structure, as the high cooperativity cavity mode diverges quickly.
- The structure should have insulating material to prevent eddy currents over whole structure.
- Metallic components should be nonmagnetic to prevent any unwanted magnetic field.

Based on these criteria, our cavity is designed as shown in Fig. 4-5. Basic structure is two baseplates connected by four rods (2.324" long). Bottom baseplate is made of macor, and top baseplate and the rods are made of 316 stainless steel, which is nonmagnetic. On the bottom baseplate, a VESPEL ring (0.29" ID, 0.7" OD, and 0.05" thick), counter weight ring (316 stainless steel, 0.29" ID, 0.7" OD, and 0.1"

[2]This is contradictory to the previous point. We should find a compromise.

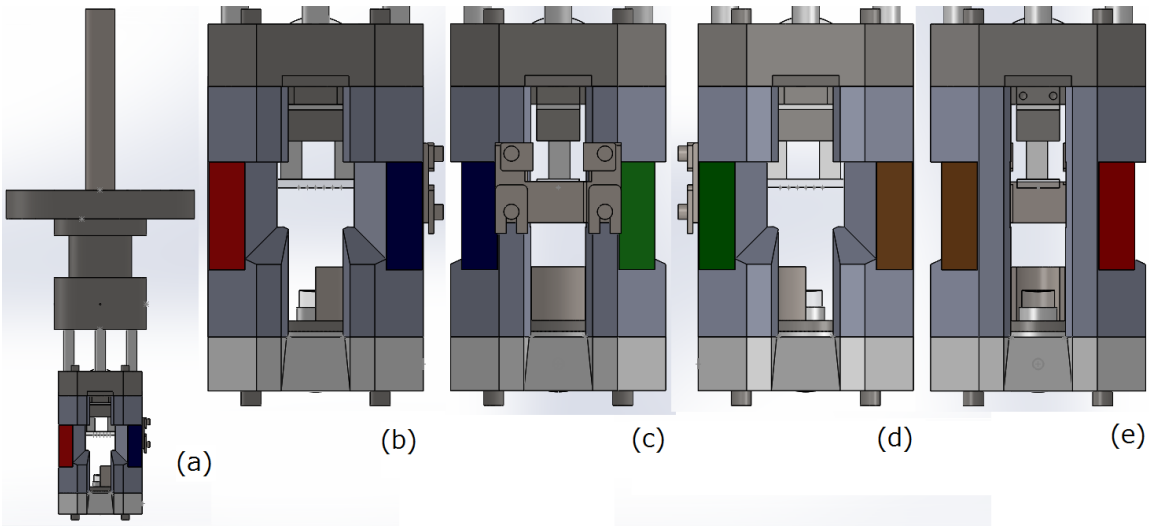

Figure 4-5: The design of experimental cavity: (a) whole picture, (b) side facing computer table, (c) side facing oven, (d) side facing white board, (e) side facing heated window. The heater is colored in different way to easily specify the number of heater: red: 1, blue: 2, green: 3, brown: 4. Width of top and bottom baseplates is 2".

thick), piezo, and commercial 25mm ROC mirror are glued in this order. (The glue is Epotek, H77). The counter weight has an atomic beam shield, whose shape is the half of a hollow cylinder (0.20" ID, 0.25" OD, 0.5" tall), for the mirror. The dimension of the piezo is 0.29" ID, 0.35" OD and 0.125" long, and it is a single layer actuator that has electrodes on the inner and outer sides. (material: C5700 manufactured by Channel Industries) For convenience, this piezo is called short piezo. Its tuning rate is 0.725 nm/V. The counter weight, the VESPEL ring and the bottom baseplate have a hole that has the same inner diameter as the piezo. On the bottom end of the baseplate, a 38.1 mm focal length 1/2" diameter lens is mounted at the distance of 16.4 mm from the back side of the 25 mm ROC mirror. This lens is AR coated for 399, 556, and 759 nm light. The baseplate has a hole to send an electrical wire for the inner electrode.

On the top baseplate, the mirror structure is screwed down. The mirror is 25 mm x 10 mm x 2 mm rectangular substrate, on the center of which the micromirror is located (for more detailed description of micro mirror, see Subsection 4.3.3). The micromirror substrate is held by two rectangular piezos (P-885.11 manufactured by

PI). They are multistack piezos of 9 mm x 5 mm x 5 mm size, and tuning rate is 65 nm/V. These are called long piezos, and are operated with the same voltage. The back of the micromirror substrate except for the micromirror part and the piezos are gold plated to ground to prevent electric field from the piezos from leaking into where the atoms are. The piezos sit onto a counter weight (0.4" D $\times$ 0.29" H $\times$ 1" W) made of 316 stainless steel. The counter weight is on a VESPEL layer (0.05" thick, same area as counter weight), which is on a cross (0.165" thick) that is screwed down to the top base plate. On the back side, a 38.1 mm focal length 1/2" diameter lens is mounted at the distance of 35.15 mm from the micromirror substrate. All the connections up to the cross are fixed by gluing. On the side, we have a thermistor for temperature stabilization. (Epcos, B57550G0103+)

The four rods connecting the two baseplates have a bunch of cutoffs from a basic pentagonal cross section. On the top and bottom of it, there are tapped screw holes to screw the top and bottom baseplates down. On the side, each rod has a heater (Birk Manufacturing 3503-57.5-200-00, 57.5 Ω resistance, glued by Epotek, 353ND) for temperature stabilization and length tuning due to the thermal expansion. It has some screw holes on the side for future upgrade and fixing electrical wires down. On the side of the oven, an atomic beam shield for the micromirror substrate is located.

This part has relatively rigid structure, and a finite element method simulation by SOLIDWORKS shows that the lowest mechanical resonance for the structure up to the top base plate is 2.7 kHz, and the mirror holding structure has the lowest resonance frequency of 7.5 kHz (top) and 14.4 kHz (bottom). This ensures a few kHz locking bandwidth of the cavity length by putting feedback onto the piezo length.

The structure is held by four 0.25" OD x 1.1" long VESPEL hollow cylinders inside of which 4-40 screws press the structure onto the top structure. Top joint is a huge stainless steel cylinder that is screwed down to the reducing flange from 4.5" to 2.75" on the top of the main part of the chamber. It has some holes through which electrical wires go from a micro D-sub feedthrough (MDC 9162003) on the top Tee to the cavity structure. On the top side of the top joint, a 0.7" OD $\times$ 0.6" ID $\times$ 5.5" long hollow cylinder is screwed down for the purpose of preventing electrical wires

from blocking the optical path to the cavity.

4.3.3 Optical design and its properties

High reflectivity coating

We have a few requirements for the high reflectivity coating. First of all, we have to have a high finesse for 556 nm at the 0 degree AOI, which is resonant to ${}^1S_0 \rightarrow {}^3P_1$ transition. Secondly, we want to have reasonably high finesse at 0 degree AOI to enhance the power of 759 nm laser for an optical lattice. In addition, it should be reflective for 399 nm and 556 nm light at $\sim 45^\circ$ AOI, because the micromirror substrate is used for the mirror MOT. This is doable at AT Films. Basically, the high reflectivity coating for 556 nm at 0 degree AOI comes at the top layer (farthest from the substrate, closest to the air), and below this, there are layers of reflective coating for 759 nm. The high reflectivity coating at 0° AOI works at 45 deg AOI to some extent. The coating is a dielectric stack made of alternating layers of Ta_2O_5 and SiO_2. As the Ta_2O_5 at the top results in degradation of the mirror reflectivity [121], it is specified to have a top layer of SiO_2.

At the beginning, the typical transmission to loss ratio of the micromirrors was 1:3, and this being less than 1 is not good for extracting information from the cavity. To increase transmission, we etched 4.5 pairs of dielectric layers. The etching is performed with hydrofluoric acid for SiO_2 layers, and plasma etching for Ta_2O_5 layers, following the original idea by Dan Stamper-Kurn's group. [122] Because plasma etching does not have any deterministic stopping point, the top layer is Ta_2O_5 layer after etching to have smooth surface. To prevent the degradation, we add 10 nm layer of SiO_2.[3]

For a more detailed discussion, see Boris Braverman's thesis [1].

[3] All of the etching was practiced on the damaged substrates. There were some damaged substrates due to poor packing when they were sent to the coating company. We asked them to coat it as well, because they still had some space in the coating machine.

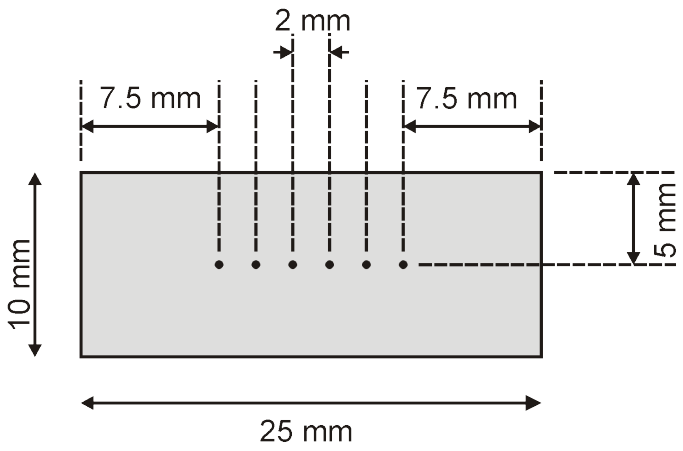

Figure 4-6: The design of micromirror substrate

Micromirror

The micromirror substrate is a 25 mm x 10 mm x 2 mm fused silica glass substrate. In the middle of substrate, we made six micromirrors, as shown in Fig. 4-6. 16 substrates are made, targeting different radii of curvature by changing the focusing of a CO_2 laser.(Table 4.1) An intuitive understanding of why we can get a spherical mirror simply by shooting a CO_2 laser is that the laser locally heats the substrate up and evaporates the material, and the amount of evaporation is proportional to the intensity, which has gaussian profile that is approximately spherical in the center. The coating was performed together with the commercial mirror substrates at ATFilms.[4]

All of the micromirrors[5] are tested. The tests are microscopic measurements of radius of curvature of two axes, transmission, and finesse; since the micromirror is slightly elliptical, long and short axes have slightly different curvature. Fig. 4-7 shows a microscope photo of a micromirror, and Fig. 4-8 shows a cross section of a micromirror. Transmission and finesse measurements are performed with the 556 nm laser. The transmission measurement is performed simply with a photodiode and the laser. The finesse is measured by making a cavity with 25 mm ROC mirror and

[4]They do not like to guarantee any kind of spec regarding coating on micromirrors, but we can just ask put the substrates into the same run as the commercial ones. Another tip on coating is what is expensive is a coating run, not the substrate. Thus, typical strategy is to add some extra mirrors for the future.

[5]In total, we have 96 mirrors.

Table 4.1: The micromirror target ROC and actual ROC: actual ROC is an average over two axes of six mirrors. Uncertainty is standard deviation.

substrate No.	target ROC [μm]	actual ROC [μm]
1	700	753.2 ± 178.6
2	700?	361.6 ± 81.4
3	300	225.0 ± 32.0
4	100	106.8 ± 32.0
5		
6	500	562.8 ± 82.0
7	100	127.5 ± 33.6
8	700	692.6 ± 177.6
9	100	107.6 ± 28.2
10	500	596.4 ± 63.9
11	500	412.1 ± 98.0
12	300	209.8 ± 30.6
13	300	166.1 ± 32.7
14	100	122.5 ± 51.2
15	100	151.4 ± 58.1
16	300	206.6 ± 28.1

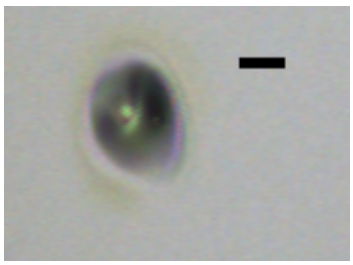

Figure 4-7: Photos of micromirror: the bar shows 100 μm

performing a ringdown measurement. Based on the finesse and transmission, amount of the loss is extracted, and the information of the curvature gives the maximum cooperativity η at the waist. Fig. 4-9 shows the summary of the properties of different micromirrors. This shows the estimated cooperativity against the micromirror's radius of curvature. Among these substrates, we chose the highest cooperativity one, and etched the surface, as described in Section 4.3.3.

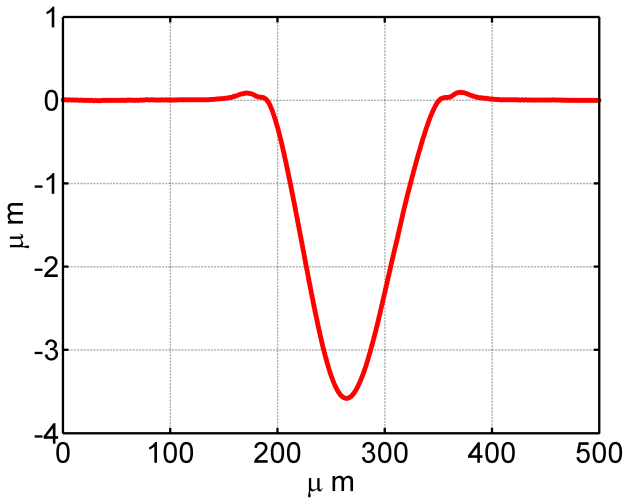

Figure 4-8: Cross section scanning of a micromirror: this is the same mirror as the one in Fig. 4-7.

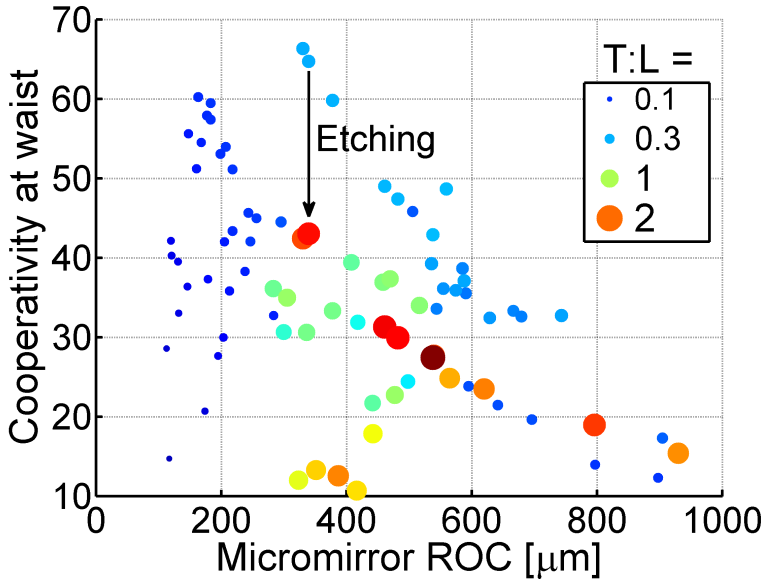

Figure 4-9: Properties of micromirrors: the expected cooperativity is plotted against the radius of curvature.

Properties of the completed cavity

In this section, the property of the experimental cavity is summarized. The cavity consists of a 25 mm ROC commercial mirror and a micromirror. The micromirror has ROC of 387 μm (long axis) and 298 μm (short axis). Fig. 4-10 shows the

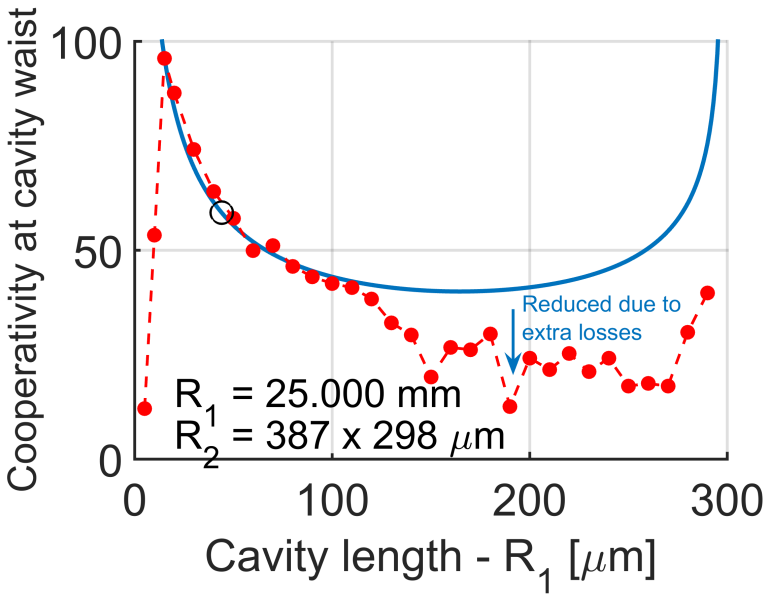

Figure 4-10: Estimated cooperativity for the experimental cavity with different mirror distance

cooperativity dependence on cavity length. Red dots being on blue curve shows that our theoretical prediction was correct, and smaller measured cooperativity compared to the theoretical calculation presumably is due to the fact that beam size on the micromirror is larger than the spherical part of the micromirror for long cavity lengths.

We fix a distance at 25.1225(25) mm, which corresponds to a free spectral range of 5.9666(6) GHz. This gives an estimated waist size of 4.7 μm x 4.3 μm, and a maximum cooperativity of 44.3. Fig. 4-11 shows cooperativity against atom distance from the micromirror substrate. Note that the cavity has also high finesse for 578 nm light. The maximum cooperativity is estimated to be 27.3. Other cavity QED parameters are summarized in Table 4.2, and Fig. 4-12 shows transmission and loss at each cavity mirror. The finesse for 759 nm light is 3000.

The temperature of the cavity is stabilized at 30°C, and its stability is $\pm$50 mK. Only two of the four rods are heated, and one has a current fedback by a four point temperature controller, and the other is driven by a constant current. It is crucial to have correct rods heated to have a good coupling into cavity mode. The length tunability is 640 nm/K by heating, and -65 nm/V by the long piezo. The tunability

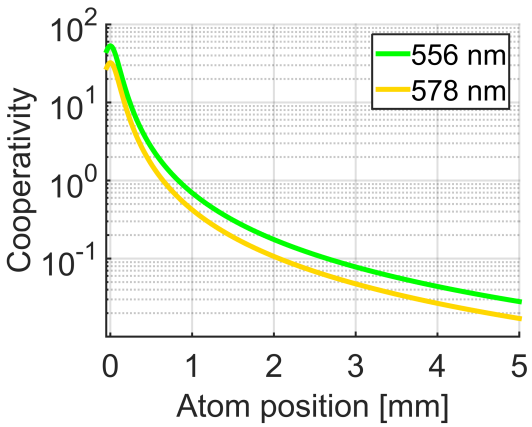

Figure 4-11: Estimated cooperativity for the experimental cavity with different mirror distances

Table 4.2: Cavity QED parameters of the experimental cavity for 556 nm and 578 nm light

wavelength	556 nm	578 nm
finesse	15 k	9.3k
Γ	184(1) kHz	7.0(2) mHz
κ	400 (2) kHz	640 (4) kHz
$g_{\max}$	902(5) kHz	175 (1) Hz
$\eta_{\max}$	44.3	27.3

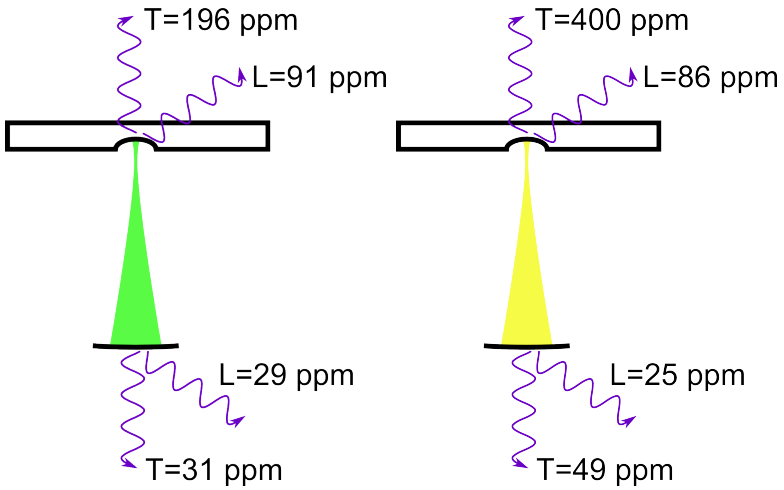

(a) 556 nm (b) 578 nm

Figure 4-12: Summary of transmission and loss on each mirror

by the short piezo is 11.4 MHz/V for 759 nm, which corresponds to 0.725 nm/V.

The coupling efficiency of the light into the cavity is 70 % for 556 nm, and 60 % for 759 nm. The 759 nm light has higher divergence, and output cavity mode has some interference fringes due to a cropping by a part of the structure. After all coupling efficiencies and quantum efficiency are combined, the overall coupling efficiency of intracavity light to a single photon counter is 12 %.

Construction of the cavity

Since the alignment involves putting the focal point of a 25 mm ROC mirror into a cone of 300 μm diameter and 300 μm height, how to align two mirrors and put it onto the holding structure is not trivial.[6] Detailed procedure of the construction of the cavity and electrical connection should be referred to Boris Braverman's thesis [1]. Here, the basic idea is briefly described.

Before starting all the alignment, the mirrors are glued onto the baseplate and the holding structure is constructed. The first step is to carefully calculate the coupling into the cavity mode, and make an optics setup accordingly. 556 nm light coupled into the cavity mode is sent from the micromirror side, which is the top of the structure. Next, we put a 25 mm ROC mirror, and retroreflect the light back to the incoming path. This fixes the position of the 25 mm ROC mirror against the laser beam. The bottom baseplate is screwed down to the structure. The micromirror substrate is inserted to the path. To determine the position of the mirror, we first fix the distance between the micromirror substrate and the 25 mm ROC mirror. The method is to make a 25 mm ROC and flat mirror cavity mode, using the flat part of the micromirror substrate. When the distance is more than 25 mm, the cavity mode disappears, and this sets the distance at 25 mm. Once we find the position for the 25 mm distance, we set the distance slightly larger than 25 mm, and slide the micromirror into the laser beam path. Strongly scattered light from the micromirror is the sign of correct positioning. At this point, sliding micromirrors around horizontally gives some kind of cavity output. Usually, this has two spots, and this corresponds to a V shaped

[6] Actually, it was so nontrivial that we first had to make a prototype and practice the alignment.

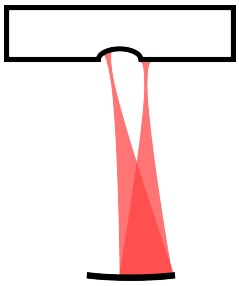

Figure 4-13: V shaped cavity mode that appears when the alignment of micromirror and 25 mm ROC mirror is not perfect.

cavity mode shown in Fig. 4-13. The goal is to make these two spots into one, and then alignment is done.

During the alignment, fine tuning of the mirror distance, including compensation of the effect of the thickness of the glue layer and machining precision, was done by inserting shims in between the rods and bottom baseplates to increase the mirror distance, and between the cross and the top baseplate to decrease the cavity length. Final adjustment of the relative position is done by moving the 25 mm ROC mirror.[7]

After the alignment, wiring electrical wires from a feedthrough is done. The cavity structure is inserted into the main vacuum chamber by putting the reducing flange onto the top 4.5" flange of the main cavity.

4.3.4 Optics around the cavity

Optics are needed for coupling the light into the cavity mode, and out of the cavity mode. In this section, these optics are summarized. Input optics are on a optical breadboard below the optics table, which we call the bottom layer breadboard. The bottom layer breadboard (Thorlabs, PBG11105) is hung from the bottom surface of the optics table by 14.5" long 1.5" thick pillar. The output optics are above the vacuum chamber. To have optics there, we first have 14.5" tall 1.5" thick pillars to support an aluminum breadboard (Thorlabs, MB18). This layer is called the middle

[7]The adjustment involves estimating the motion due to the screwing, and compensating it, and interestingly, after trying all the sophisticated translational stage, most effective way of moving the baseplate into correct position was by fingers.

layer breadboard, and it has a cutoff to prevent eddy currents. On top of this we have 4" tall 1.5" thick pillars, and another layer of optical breadboard (Thorlabs, MB18). In addition, we have a 2' x 2' 2.2" thick breadboard (Thorlabs, B2424F) next to the structure right above the chamber. This whole structure for the output optics is called the top layer breadboard.

A diagram of the input optics is shown in Fig. 4-14. the idea is first to shape the beams of different color independently, and then combine them with dichroic mirrors, because chromatic aberration and the difference in the size of cavity mode between different color are significant. 556 nm laser has two sub parts. One is for the pump beam, and the other is for the probe beam. The pump beam is used for optical pumping through the cavity, and the probe beam is used for probing through the cavity. Since both of them require a specific polarization, the polarization is cleaned with a PBS and HWP right after a fiber outcoupler (Thorlabs, C230TMD-A). After that, each path has a QWP to make a circular polarization, and two beams are combined by a non-polarizing 50:50 beam splitter. Because both beams do not require so many photons, OD=3.0 ND filter is located after the non polarizing beam splitter. The probe path has an additional OD=1.0 ND filter before the beam splitter, as the pump requires more power than the probe (see Section 6.5 for the details of optical pumping). The beam changes its direction by 180 degrees by two mirrors, which work as a pair of mirrors to independently align the green path into the cavity, and goes through a $\times 1.25$ telescope. Right before the dichroic mirror reflecting 556 nm and transmitting 759 nm and 578 nm (Semrock FF562-DI03), there is a 119.23° waveplate (custom order from CASIX), which compensates the phase shift between S and P polarizations at the dichroic mirror.

The 759 nm path has features for locking the experimental cavity to the 759 laser, and an intensity feedback for the cavity light. The output from a fiber coupler (Thorlabs, C230TMD-B) first go through a PBS and then 20 MHz free space EOM (Qubig, EO-F20L3-NIR). Light is next reflected by a R:T=90:10 non-polarizing beam splitter (Thorlabs, BS025). The light next goes into another free space EOM (Thorlabs, EO-AM-NR-C1). This is located between the QWP and PBS, and modulated based on

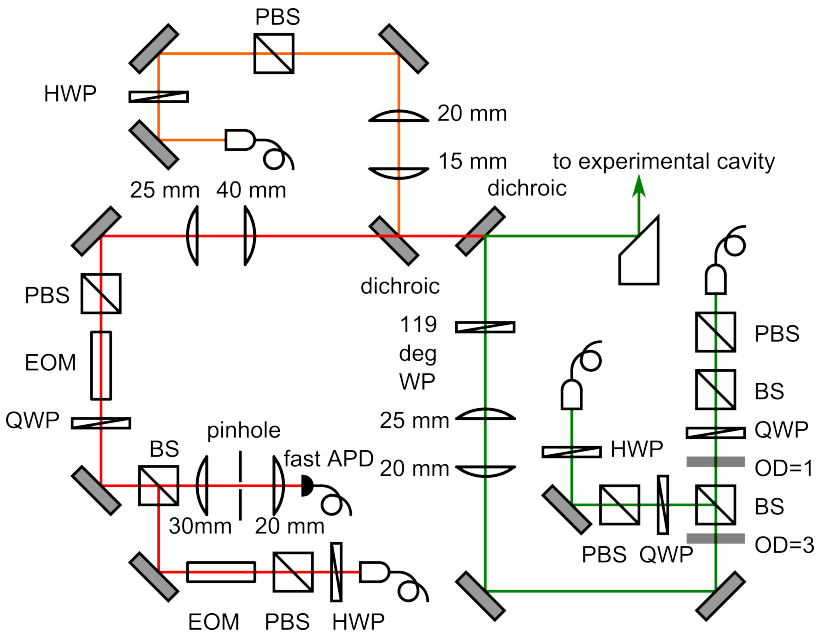

Figure 4-14: Optics schematics for bottom layer breadboard: These optics are used to combine light of different wavelengths and send them into the cavity mode of the experimental cavity.

the intensity stabilization feedback signal. This intensity stabilization components are between two mirrors, and these mirrors works as a pair of mirrors to independently align the 759 nm path. After the mirror, the light goes through a $\times 1.6$ telescope, and then goes through two dichroic mirrors, both of which transmit 759 nm light. Light reflected by the experimental cavity goes back along the path, and part of the light is transmitted by the 90:10 non-polarizing beam splitter. the light goes through a 25 μm pinhole (Thorlabs, P25S) that is located at the focus of a 30 mm focal length lens to block the reflection due to the higher order transverse modes of the experimental cavity. The light is focused down to an AC coupled APD by a 20 mm focal length lens.

The 578 nm laser path is also implemented. The light coming out from the fiber outcoupler (Thorlabs, C111TME-A) first goes through a polarization cleaning system with a HWP and PBS. It then goes through a $\times 0.75$ telexcope, and then a bandpass filter (Semrock, FF01-578/21-25) to protect from 556 and 759 nm reflection. At the end, the light goes into the dichroic mirror (Semrock, FF649-DI01) to combine it with

the 759 nm light.

The top layer splits 556 nm, 578 nm and 759 nm light into a separate paths, using the same dichroic mirrors as the bottom side. Fig. 4-15 shows the schematic. 556 nm light goes to single photon counters, a DC coupled APD, and a camera. The light first goes through a 119.23° waveplate. After the beam size is shrunk by a $\times 0.33$ telescope, it goes through a QWP that changes circularly polarized light into linearly polarized light so that a PBS downstream can send σ^+ and σ^- light for the atoms to different single photon counters. There is also a mechanical shutter [123] for protecting single photon counter when high power light is sent to cavity. Next, a pellicle beam splitter (BP108) splits a small amount of light (0.27% for H polarization light, 2% for V polarization light) into a path to a DC coupled APD and a camera. The camera gets 8% of this light reflected by a beam sampler (BSF10-A). Rest of the light goes into a PBS, and on both the reflection side and the transmission side, the light is fiber coupled. Right infront of each fiber coupler, a bandpass filter (Semrock, FF01-554/23) and an iris are placed for reducing background light and blocking light if necessary. The fiber coupling efficiency here is around 65%, and the light is sent to single photon counters (Hamamatsu Photonics, C13001-01(x)). This single photon counter is an APD operated in a Geiger mode, and the quantum efficiency at 556 nm is 45%, including outcoupling efficiency from the fiber to the active area of the detector. Note that the 759 nm light is sufficiently suppressed by not only a dichroic mirror and a bandpass filter but also a bunch of mirrors coated only for 556 nm light.

759 nm path sends the cavity output to a camera and two APDs. After the dichroic mirrors, the light goes through a mirror for 556 nm light to filter the 556 and 578 nm light. The beam is next shaped by a $\times 0.5$ telescope, and then split by a HWP and a PBS. One path has a camera and a DC coupled APD for monitoring purposes. Only a small amount of the light comes to this path, and 8% of it goes into the camera by a beam sampler (Thorlabs, BSF10-B), and the rest goes into the DC coupled APD. Most of the light goes into another AC coupled APD that generates an error signal for an intensity feedback. A diagram of the circuit that generates the

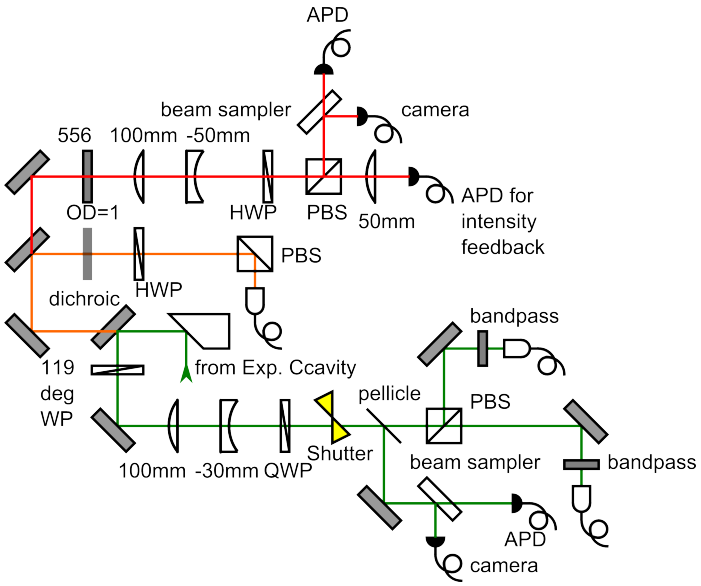

Figure 4-15: Optics schematics for the top layer breadboard: these optics ar used to split different wavelengths of light and send it into different detectors. Two fibers at the end of 556 nm light path are connected to single photon counters.

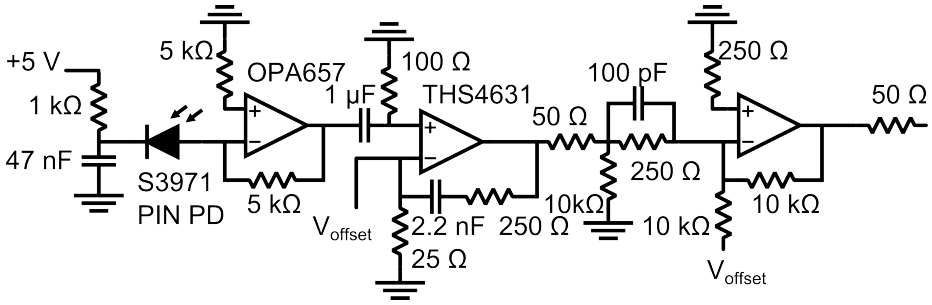

Figure 4-16: Circuit to generate the error signal for the intensity feedback of the 759 nm laser

error signal is shown in Fig. 4-16 The basic idea is to AC couple the signal at 1.6 kHz, and have 40 dB of amplification, so that a small fluctuation in power can generate large enough modulation voltage for the non-resonant EOM.

Locking of the experimental cavity

To perform a stable probing by 556 nm light, the resonant frequency of the experimental cavity has to be tightly fixed. To do this, we lock the experimental cavity to the 759 nm laser for the optical lattice, which is locked to a reference cavity (for

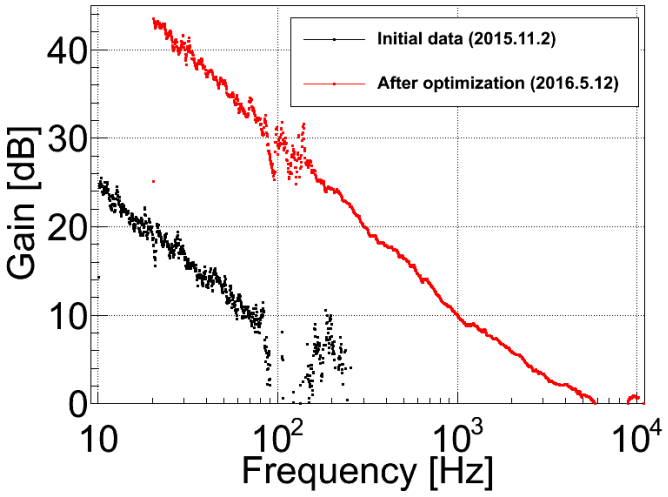

Figure 4-17: Gain curve of the feedback system for experimental cavity locking: red curve is after the optimization of PI gain parameters to maximize the gain of the feedback.

the locking of the 759 nm laser, see Section 5.4). The locking is a standard PDH technique. The RF modulation frequency is 20 MHz, which is the resonant frequency for the Qubig EOM. The retroreflected light is detected by an AC coupled APD. The error signal is processed with our standard lockbox, and fed back to the voltage on the short piezo. As the short piezo's tuning range is as small as 150 MHz, long term stability is maintained by generating an error signal from the short piezo voltage, and sending a feedback to the long piezos' voltage so that the short piezo's voltage stays at a constant value. The bandwidth of the feedback to the short piezo is 6 kHz, as shown in the gain curve shown in Fig. 4-17. This is limited by the lowest mechanical resonance at 7.5 kHz.[8] Few high frequency resonances, which are 7.5 kHz and 67 kHz for short piezo and 4.5 kHz, 7.5 kHz, and 22.4 kHz for the long piezo, are suppressed by a notch filter.[9]

Even when we lock the experimental cavity to the 759 nm laser, there still remains

[8] 2.7 kHz resonance mentioned in Section 4.3.2 is swinging sideways, and it does not seem to affect the cavity resonance frequency.

[9] Basically, this is good enough for having a stable enough 556 nm probe. Sometimes, a $\sim$ 100 Hz oscillation is visible in the error signal of the experimental cavity locking. This is from the whole cavity holding structure swinging due to the thin VESPEL rod structure. This 100 Hz noise is suppressed reasonably well when the gain of the locking is high enough, and removed by floating the optics table.

a decent amount of intensity noise of the trap light in the cavity. Since the intensity noise of a trapping light results in parametric heating of atoms in the trap [124], this intensity noise should be suppressed, ideally to the level that the atom lifetime in the lattice is not limited by the intensity noise. With an optical cavity of finesse ~ 3000, both intensity noise of the laser and frequency noise of the laser lead to intensity noise of the intracavity light, as the cavity's sharp resonance peak converts frequency noise to intensity noise. At the beginning, we had only a $\lesssim 200$ ms lifetime in the lattice, and had to reduce the intensity noise. At first, we implemented fast frequency feedback by getting the error signal from a PDH signal from the experimental cavity and putting feedback onto an AOM which shifts the frequency of 759 nm slave laser. This did reduce the frequency noise around 100 kHz by 10 dB, but we did not observe any improvement of the intensity noise. Therefore, we decided to simply measure the power of the laser after the cavity, and put feedback based on it to the power of input light.

The circuit for the intensity feedback is shown in Fig. 4-16. The error signal is sent to the non-resonant EOM in the 759 nm light path on the bottom breadboard, with the shortest cable length that is geometrically allowed, to ensure a large bandwidth. The gain curve and phase is shown in Fig. 4-18, and the resulting enhancement of the expected lifetime in the lattice calculated by Eq. 6.3 is shown in Fig. 4-19. The enhancement is a factor of ~ 10 in the region of our interest, which is around the 100 kHz trapping frequency, and this intensity feedback enables a >1 s atom lifetime in the lattice.

4.4 Oven, atomic beam, and heated window

Ytterbium has a melting point of 1097 K, and boiling point of 1469 K, and therefore we need an oven that can heat up to few hundred degrees Celcius. To design an oven, there are few things to consider.

- Amount of material; if it is a large amount, you do not have to replace it frequently, but the structure gets larger.

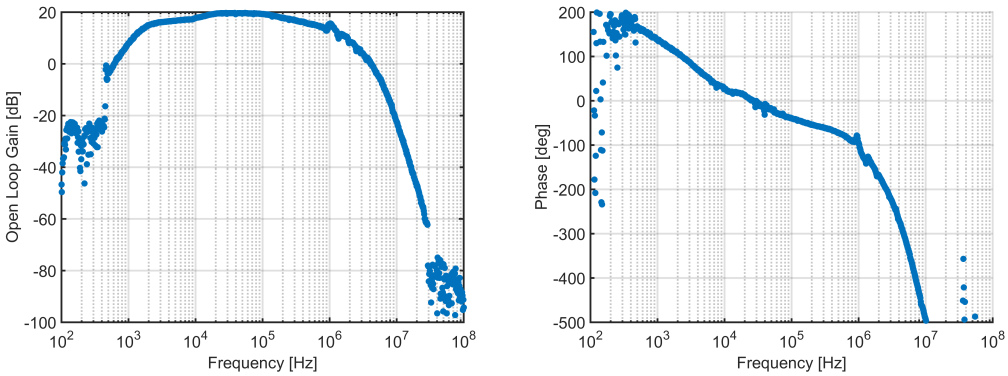

(a) Open loop gain (b) Phase

Figure 4-18: Property of the intensity feedback circuit of the trap laser

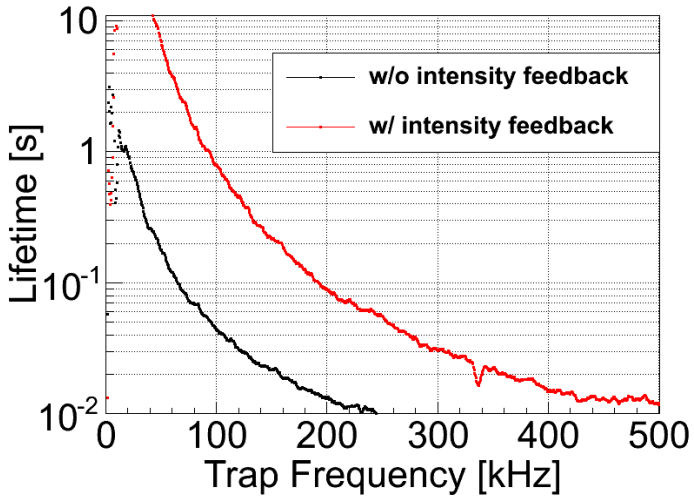

Figure 4-19: Enhancement of the atom lifetime by intensity feedback

- Flux of atomic beam you want to have

- Distance between an oven and the region where you actually trap atoms; if the distance is small, the flux gets larger because of the larger solid angle. However, when a hot object gets close to trapped atoms, there are potentially bad effects due to outgassing from the oven that increase the vacuum pressure, and blackbody radiation from the oven.

- Management of heat: how to heat the oven efficiently, and if the surrounding part gets warm, how to dissipate that heat in a good way.

- How to collimate the atomic beam; a couple of holes, or honeycomb structure is commonly used. However, if the collimating structure is cold enough for the atomic species to condense, there is a danger of clogging it.

Based on these criterion, we chose a relatively compact setup that is close to the MOT region. To get a reasonable atomic flux, we put the oven 2" away from the MOT region. The system does not have any Zeeman slower, and therefore the solid angle over which we can gather atoms is larger than that for a system with a Zeeman slower. Still we send a counter propagating cooling beam to enhance the atom number in a MOT. (regarding the counter propagating beam, see Section 6.2.)

The oven is made by wrapping 2 g of ytterbium bulk by 0.0005" thick tantalum foil. The shape of the foil and how to wrap the ytterbium bulk and connect it to a conductor rod is shown in Fig. 4-20. Fixing open ends is done by spot welding. The tantalum bag is spot welded to a conductor rod. The rod is made of 0.032" diameter 1.7" long steel that is welded on 0.032" diameter 6.2" long copper rod. The length of the copper includes the commercial electrical feedthrough (Lesker, EFT0023032), and there are 0.2" overlap between the copper and the steel part. The overall length is determined by the length of the vacuum chamber, including a Tee splitting the tube to a 2 l/s ion pump for differential pumping. The steel part prevents the heat of the oven from being dissipated through the conductor rod, and copper part ensures the conductor itself has low resistance. [10] The rods are supported by two macor rings so that the whole structure does not touch the chamber wall due to gravity. The air side of the electrical feedthrough is connected to a power supply by 16 AWG wire. The tantalum bag has a hole of 1 mm diameter, so that ytterbium vapor can come out. The bag is located at the end of the oven tube. The distance of the oven bag and the closed end with the 3 mm hole is estimated to be a couple of millimeters.

To get 10^{10} s^{-1} overall atom flux, we typically run 5.4 A to the oven. This requires a voltage of 2.0 V, including all the resistances of wires and conductors, and thus the overall heat dissipation at the oven is 10.8 W.[11] Most of the resistance is due to the

[10]The first generation oven had an all steel structure. The conductor part was too resistive and so only a third of the overall resistance was attributed to the tantalum bag.

[11]The previous all steel design required 10.4 A and 3.1V, which gives more than 30W.

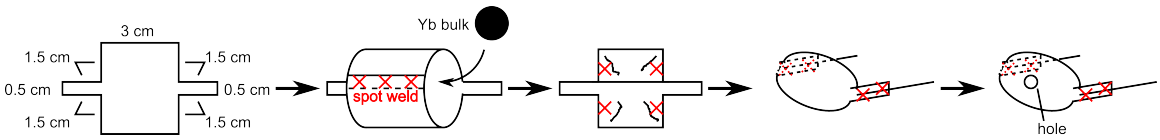

Figure 4-20: How we wrapped ytterbium oven: the number in the left most picture is the length scale in cm.

wires connecting a power supply and the feed through, and the resistance inside the vacuum is only 78 mΩ, 75 mΩ of which is due to the steel and the foil part. This does not give any heat onto the chamber surrounding the tantalum bag part.

Because ytterbium has high boiling point, and low vapor pressure at room temperature, once it sticks onto a cold surface, it never goes off. This is the same for the vacuum viewport at the opposite end of the oven through which a counter propagating beam is sent. To prevent ytterbium from coating it, which reduces the transmission of the viewport, we implemented a heated window inside of a Tee on the counter propagating beam path. The structure of the heated window is shown in Fig. 4-21. The main part is an AR-coated Sapphire window that is clamped by two copper parts. The main copper plate has a heater (Watlow, Ultramic 600 Heaters WS-CER-1-01-00098) screwed onto it, and the heat flows to the window through copper. This structure sits onto a macor mount, which is held in a 2.75" flange Tee by gravity. Because of the small thermal conductivity of macor and small amount of mechanical contact between the window and the macor mount, and between the macor mount and the Tee, we need only 7.7 W (33.3 V and 0.23 A) to heat the window up to 300 °C. The AR-coating for the sapphire window is performed with the same run as the one for the viewport (See Fig. 4-3, however, due to the difference in material (sapphire and 7056 glass), actual reflectivity should be different) The power for the heater is supplied from an electrical feedthrough (MDC 9132006) on the top of the Tee. A thermocouple on the heater is also wired through this feedthrough, and this allows us to estimate the temperature of the window.

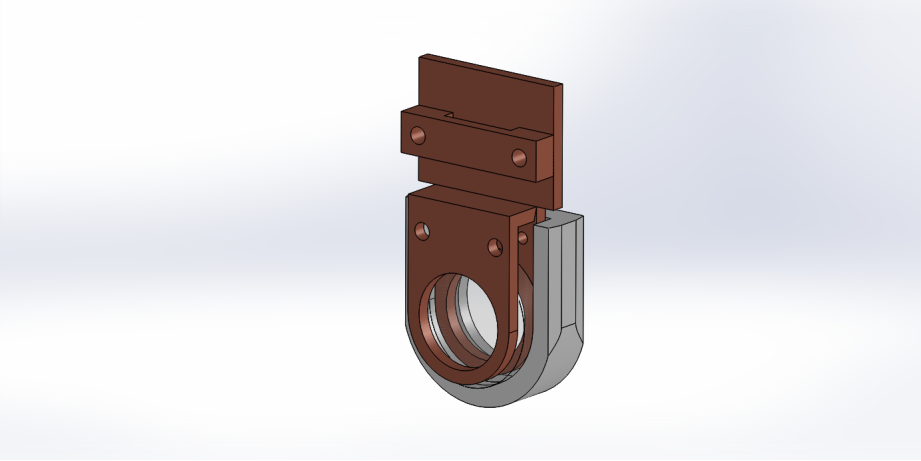

Figure 4-21: The structure of the heated window

4.5 Coils and optics for MOT

In order to have a MOT and apply the proper magnetic field during interrogation through the experimental cavity, it is necessary to have a proper coil to generate the magnetic field. For historical reasons, we have two pairs of MOT coils. One is on the 6.75" flanges, which is large enough to generate a 50 G/cm field gradient for a MOT with the ${}^1S_0 \rightarrow {}^1P_1$ transition. This only worked when we did not have the cavity structure inside the chamber, due to the relation of the polarization and the sign of the field gradient in the mirror MOT. As we use a mirror MOT with the cavity structure, the MOT coil axis has to be along the MOT beam axis that is reflected by the mirror. To satisfy this, we put relatively small MOT coils on the 2.75" flanges. To have compensation of the background field, to shift the MOT position, and to apply the proper magnetic field for the interrogation of atoms in the cavity, we have bias field coils for the x, y, and z directions, where th+z, +x, and +y direction are defined as vertically upward, horizontal direction from heated window to oven direction, and axis of 6.75" viewport that makes the right hand system.

Large MOT coils are made of a hollow copper wire whose cross section is 0.1875" square and the tube inside is 1/16" diameter circle. (S & W Wire Company, .1875SQ SPEC#MW46C) The cross section of the coil is shown in Fig. 4-22. Total number of windings is 54, making a 6 x 9 rectangle. Two coils of identical shape are made. Each

Figure 4-22: Cross section of the large MOT coil (left) and the small MOT coil (right): this shows the number of windings. The arrow shows how we wound the coil, which corresponds to the order of water flow.

end of the wire for both coils are left straight for $\sim$ 2 m. This part is used for the connection to the chilled water system and cables to the high current power supply. To wind the MOT coils, we use a lathe. After fixing one end onto a 6.75" diameter tube working as a core, we rotate the lathe slowly, such as few rpm, applying decent amount of tension onto the wire and pasting an epoxy glue, and the wire is tightly wound. The OD of the core matches the OD of the flange, so that the ID of the coil matches the OD of the flange.[12]

The small MOT coils are made of the same hollow copper wire as the large MOT coil. The cross section is shown in Fig. 4-22. This is also made by the same method, and each end has $\sim$ 2 m of free wire for the connection to the chilled water system and cables to the high current power supply. Both the large and small MOT coils are mounted onto the flange by the friction generated by inserting thin stainless steel sheets in a small gap between the coil and the flange.

Bias field coils are made of 16 AWG single stranded insulated wire. The coils are a 11" (vertical)$\times$8" (horizontal) rectangle for the x and y directions, and an 8" square for the z direction. The coil has 60 windings for each direction. To make the coil of X"$\times Y$", we first put four Thorlabs optics posts at the corners of a $(X-1)$"$\times(Y-1)$" rectangle, and then wind the wire onto the rectangle made by the posts. Each end of a coil has $\sim$ 2 m of free wire for the connection to the power supply and driving system. Bias field coils are fixed to the middle layer breadboard by cable ties.[13] The

[12]You should carefully think of how to remove the core after winding. As the wire is tightly wound onto the core, quite large amount of force is necessary to remove the core from the coil.

[13]For the z direction of the bottom coil, we cannot insert the coil after we built the chamber.

Table 4.3: Summary of the magnetic field generated by different coils

Coil	Field (gradient)
Large MOT	0.42 G/cm/A
Small MOT	0.08 G/cm/A
Bias X	2.5 G/A
Bias Y	2.5 G/A
Bias Z	1.6 G/A

calibrated magnetic field is summarized in Table 4.3. The calibration is performed by sending a few amperes of current, and the magnetic field is measured by a Hall probe that is held above the center of the coil.

The coils are connected to control circuits. We have two kinds of control circuits: unipolar and bipolar. Simplified diagram of these control circuits is shown in Fig. 4-23. The idea is to regulate the current flowing on the coil with a FET connected downstream for the unipolar controller and upsteam for the bipolar controller. To have the exact same current through the two coils, a pair of bias field coils of each direction and MOT coils are connected in series, respectively. The set point of the current is controlled by a LabVIEW signal that goes into the External Signal input of the controller box. In order for the circuit to work against large emf due to the inductance of the coil, the DC voltage applied to the bias field coil is made as large as possible, which is limited by the maximum output voltage of the power supply for the coil. Currently, the bias field coils have 30 V DC voltage, and the MOT coils have 7.5 V DC voltage. Thanks to the TVS bridging two ends of a single coil, the MOT coil has a decay time of 1 ms when the coil is suddenly switched off. The bias coils have a bandwidth of 2 kHz, 4 kHz, and 2 kHz for the x, y, and z directions, respectively. The maximum current is set to be 120 A, 5 A, 5 A, and 10 A for the MOT coil, X, Y, and Z direction bias coils, respectively.

It is no problem to connect the bias coil to the control system by standard 16 AWG wire, ring connector, and Eurostrip. On the other hand, the connection for the MOT coil needs special care due to the high current. First of all, the hollow wire

Thus, we wound the coil on site with high temperature resistant cable ties.

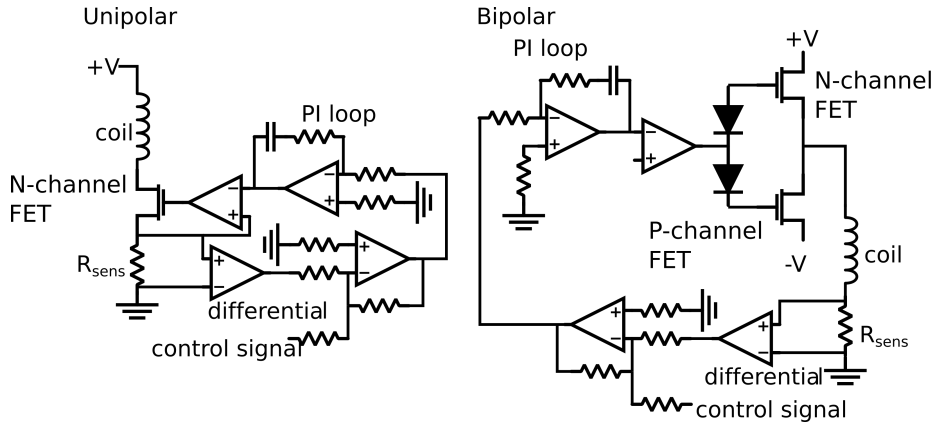

Figure 4-23: Simplified diagram of the unipolar and bipolar current controlling systems: we use IXFN520N075T2 for the N-channel FET, and IXTN170P10P for the P-channel FET, both of which are manufactured by IXYS.

for the MOT coil needs to be connected to the chilled water system. To do this, we remove the insulation of the hollow wire, wind woven copper for solder removal onto the naked copper part of the wire to make the wire outer diameter thicker, and solder it onto a 3/8" OD copper tube. Since the copper has a high heat conductivity and the part that needs to be heated is large, a blow torch is used for the soldering. The water is connected to the chilled water system by Swagelok through the 3/8" OD copper tube. The copper tube is clamped by a custom made clamp , and the ring connector is screwed down to the copper clamp. To convey 180 A current without overheating, 2 AWG wire is used for the wires for MOT coils.[14] Parts that dissipate lots of heat, such as current sensing resistors and FETs, are screwed down to an aluminum board that is water cooled by the chilled water system for the purpose of effective heat dissipation to prevent overheating.

AC coil for Rabi pulse

As described in Section 7.3, the Rabi frequency we can get by applying an AC magnetic field with the x direction bias coil is as small as < 40 Hz. Two main limiting factors are the low power supply voltage which struggles to overcome the back emf,

[14] 2 AWG is a bit too thin for 180 A. The gauge was chosen to handle the 120 A specified in the original design. Still the cable does not heat up too much, and we even send 220 A for ~ 100 ms.

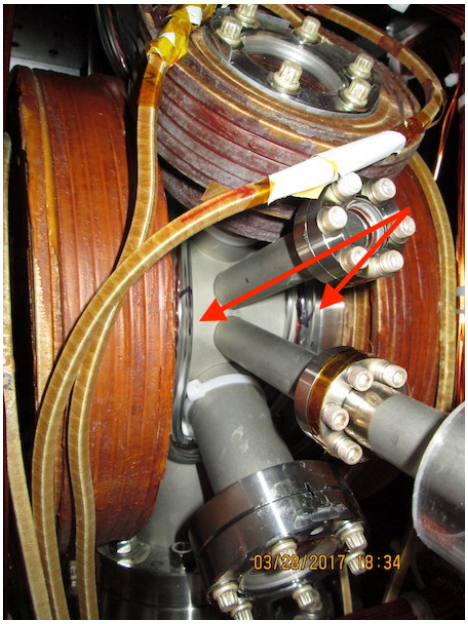

Figure 4-24: The position of the AC coil: the tube indicated with arrows has coils inside.

and the eddy current that is generated over whole chamber which cancels the AC field generated by the coil. To solve these problems, a single winding coil with smaller cross section driven by huge current was made. To generate current higher than the power supply can give, we used a 100 mF capacitor and a 680 mF capacitor in parallel. The coil current is regulated by a FET that is controlled by a feedback circuit similar to coil current controller that is tuned by the LabVIEW analog output voltage. When the coil is driven, we add a DC offset voltage and an AC current at the same time. If it were for single coil, this gives a DC magnetic field, in addition to the AC field. To cancel this DC field, we put another coil that has the opposite winding direction. We drive the opposite winding coil with the same DC current as the standard coil, and AC current with flipped sign. In this way, we generate a pure AC field. The coil is mounted on the oven side of the chamber, as shown in Fig. 4-24.

The maximum amplitude of the AC current achieved is 200 A, and this improved the Rabi frequency by a factor of 10. Currently, the AC coil is operated with 50 V voltage. For more details, refer to Boris Braverman's thesis. [1]

4.5.1 High current operation for MOT coil

In the standard operation of the MOT, we chose 115 A for the current on the MOT coil, which gives 9.2 G/cm magnetic field, but in the cavity feedback squeezing experiment (Section 7.10), we increased the current to 180 A to increase the atom number trapped in an optical lattice. To do this we used 220 A power supply (Lambda, GEN 15-220) instead of 120 A one (Agilent, 6031A). With a current of $\sim$ 200 A, heat dissipation at the FET (IXYS, IXFN520N075T2) becomes an issue, and we cannot have a fixed output voltage of the power supply. To minimize the heat dissipation at the FET, we tune the output voltage of the power supply in addition to the current regulation with the FET. The control of two parameters at the same time is done by splitting the control signal by a Tee, and setting the voltage to correct ratio by a voltage divider. With this feature, we confirmed a safe operation up to 180 A constant current, and 220 A for a short amount of time ($\sim$ 100 ms in 5 s sequence).

4.6 Imaging system

To monitor the MOT and perform absorption and fluorescence imaging, we have a few imaging systems. Two of them use Baumer cameras (Baumer, VLG-02M), and one of them uses an Andor camera (Andor Zyla-5.5-USB3). The two Baumer camera have different optics: one with 1:2.2 magnification, and the other with 1:1 magnification. Here, for simplicity, the camera with 1:2.2 magnification optics is called the wide-view camera, and the camera with 1:1 magnification optics is called the narrow-view camera.

The Baumer camera has 656 (horizontal) $\times$490 (vertical) pixels, where the size of single pixel is 5.6 μm $\times$5.6 μm. The overall CCD area is 4.46 mm $\times$3.80 mm. The quantum efficiency for 399 nm and 556 nm light including the loss due to the insensitive area is 56 % and 74 %, respectively. Its dynamic range is 8 bits. The camera is connected to the DAQ computer through ethernet cable, and the data transfer is fast enough for a 10 Hz frame rate. It has 18 e^- read noise.

The Andor camera is a CMOS camera that has quantum efficiency of 31 % for 399

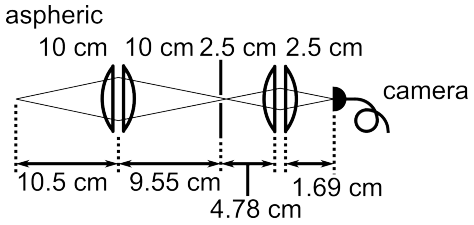

Figure 4-25: Optics for wide-view camera

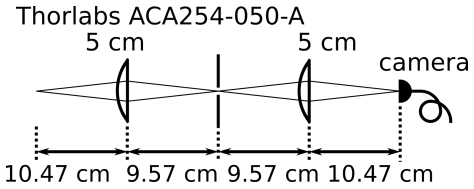

Figure 4-26: Optics for narrow-view camera

nm light and 58 % for 556 nm light. The pixel size is 6.5 μm (horizontal) $\times$6.5 μm (vertical), and it has 2560 (horizontal) $\times$2160 (vertical) pixels. The overall CMOS detector size is 16.6 mm (horizontal) x 14 mm (vertical). Its dynamic range is 33000:1. Connection to a computer is done by USB3 cable to the analysis computer. The ata transfer is fast enough to have a 40 Hz frame rate for the full size image.

The optics for the wide-view camera are shown is Fig. 4-25. The idea is to once focus down the light with an iris on the focal point. This and black aluminum foil surrounding the optics system reduces the amount of stray light. Currently, we put a bandpass filter (Semrock, FF01-554/23-25) to use this camera exclusively for detecting the 556 nm fluorescence from the atoms. As the first lens is 1" in diameter and it is 4" away from the atoms, it covers 3.9×10^{-3} sr out of 4π overall solid angle.

The narrow-view camera has the optics shown in Fig. 4-26. The concept of the structure is the same as the wide-view camera, and currently it is used without any filter. As it also has the 1" lens at the beginning, the solid angle coverage is 3.9×10^{-3} sr.

The optics for the Andor camera start with a 2" achromatic doublet lens (Thorlabs, AC-508-075-ML). This ensures 4 times larger solid angle coverage compared to

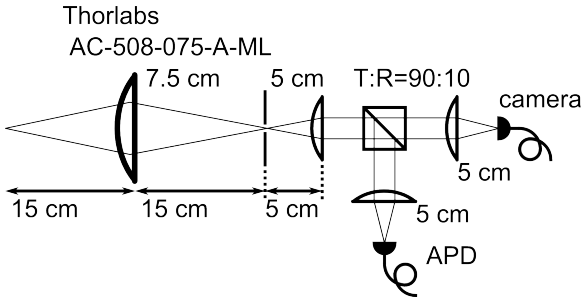

Figure 4-27: Optics for Andor camera

1" optics, though it is actually put at least 6" away from the atoms and therefore the actual solid angle enhancement is a factor of 2.67. The following optics are shown in Fig. 4-27. In addition to the focusing and iris feature, the optics split the light into two paths using a 90:10 non-polarizing beam splitter. 90 % of the light goes into the Andor camera, and the remaining 10 % is sent to the second path, which can be used for monitoring by APD or other fast devices.

Currently, monitoring of the atoms is done by the narrow-view camera and the wide-view camera. The narrow-view camera mainly works for the TCMOT, and the wide-view camera is used for monitoring the green MOT. To use the Andor camera, the MOT beam needs to be sent diagonally, so that the optics axis of the 2" lens is perpendicular to the 6.75" viewport.

4.7 Optics for MOT

The optics of the MOT beam are depicted in Fig. 4-28. The idea is to superpose the 399 nm and 556 nm beams to send them together into the vacuum chamber. First, they are independently outcoupled from optical fibers, go thgough a PBS to clean the polarization, and are expanded to 1.8 cm diameter by telescopes. The light is combined by a dichroic mirror (Thorlabs, DMLP505R), and then sent into the main paths. The extra U shaped path for the 556 nm light is used for the relative alignment of the two beams. After combining the beams, all the optics, including the waveplates, work for both 399 nm and 556 nm light in the same way.

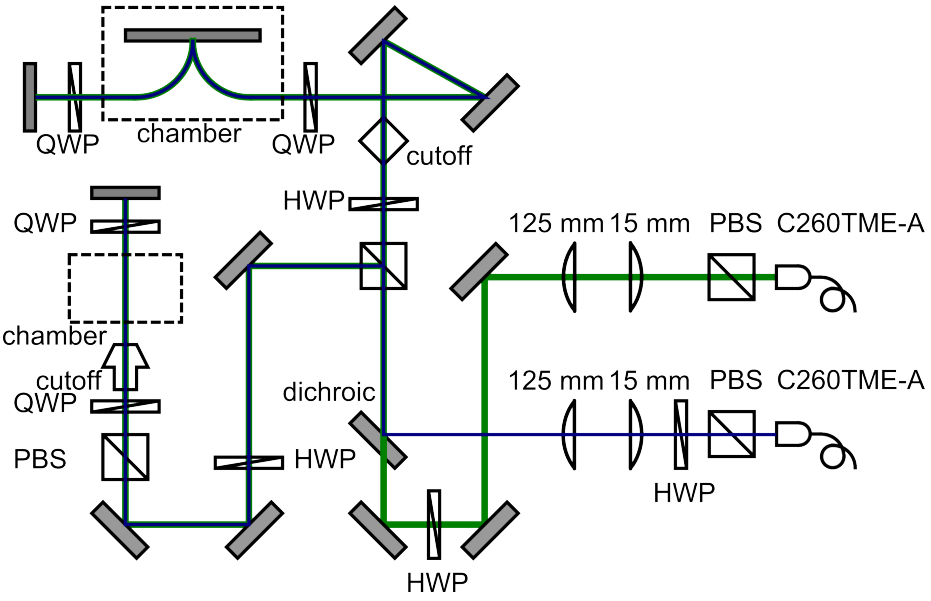

Figure 4-28: Optics for the MOT

The horizontal beam is lifted up by a periscope to the optics breadboard 6.375" above the optics table, and sent to the vacuum chamber. It is simply retroreflected by a flat mirror and QWP, in the same way as standard MOT optics.

The diagonal beam first goes through a HWP to rotate the linear polarization to an optimal polarization for reflecting it diagonally upward. The QWP used to generate circularly polarized light is located right in front of the viewport to prevent unwanted polarization mixing due to reflections by mirrors outside of the vacuum chamber. After being reflected by the flat part of the micromirror substrate, it comes out of the vacuum chamber and is retroreflected. Here, the QWP is mounted onto a rotational mount, so that we can optimize the angle of the QWP. This adjustment is necessary, because the incoming circularly polarized light changes to elliptically polarized light after the reflection at the micromirror substrate, and a specific ellipticity is better than others for the retroreflected light to keep the light force balanced to the input light. The change of polarization at the micromirror happens due to the phase shift between S and P polarized light. The phase shift strongly depends on AOI, as shown in Fig. 4-29. Currently, the AOI is around 45.95°.

To avoid extra scattered light from the cavity structure, both horizontal and

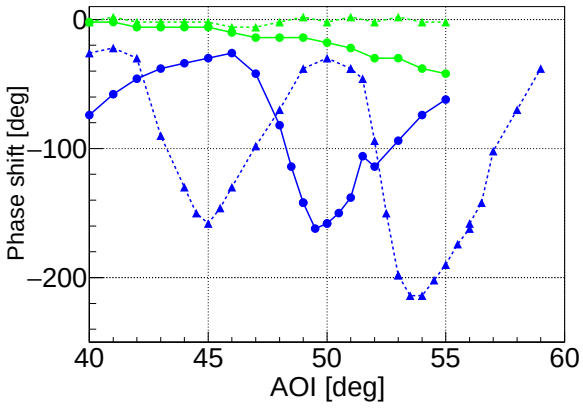

Figure 4-29: The phase shift of S and P polarizations after the reflection on micromirror substrate: green and blue points are for 556 and 399 nm respectively. The dotted line with triangular points and the solid line with circular points are for without and with etching, respectively.

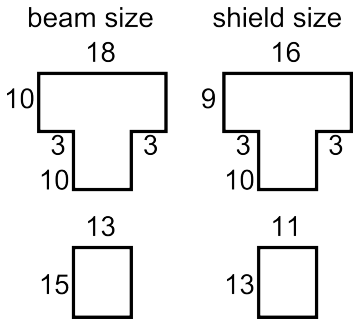

Figure 4-30: The shape of the cutout for the MOT beam; top: horizontal beam, bottom: diagonal beam: the numbers are dimensions in mm.

diagonal beams go through cutouts to remove the unnecessary part of the beams. The shape of the cutoff is shown in Fig. 4-30.

We sent a longitudinal cooling beam counter propagating to the MOT. This is a 399 nm light, and detuned by −110 MHz from the frequency of the MOT beam. It is circularly polarized by a pair of PBS and QWP so that it has a slight amount of Zeeman slowing due to the quadrupole field from the MOT coils, and sent from a viewport that is on the opposite side of the oven. The beam is focused down with an effectively 65 cm focal length lens from a 1.3 cm initial diameter and is focused to 13 μm at the waist.

4.8 Control system

To control the system and analyze the data, we have three computers. One is for general purpose, and is not covered here. Another one is specifically for running sequences and controlling systems. This computer has LabVIEW software and hardware installed, with a custom made 10 PCI slot. The third computer is for getting data from the control computer and analyzing the data.

The control of the experiment system is done by a LabVIEW program on the DAQ computer that generates analog and digital outputs. Digital outputs switches things on and off by TTL signal, such as AOM modulation, shutter, and RF modulation for the EOM for probe light. Analog outputs control values that require a control by continuous numbers, such as the quadrupole and bias magnetic fields, and the power of lasers. The camera shutter, which is operated with an 8 V input is also controlled by an analog output.[15] Each analog output is controlled by the value of an output voltage. The analog output has two types: constant and ramp. As explained in details in the next paragraph, we specify values for the outputs at few times; for example, V_0 at t_0, and V_1 at t_1. The constant analog output gives V_0 for all the time between $t = t_0$ and $t = t_1$. The ramp analog output gives the interpolation of V_0 and V_1 for t that satisfies $t_0 \leq t < t_1$.

To have a good timing between different outputs of NI boards, one specific digital output is set to generate a 1 MHz clock signal that is sent to the other NI boards for triggering signal. All the outputs are slaved to this triggering signal, and we don't observe any significant delay of the output signals. To have the correct output value, NI boards need to know what specific voltage they have to give out at every clock signal. To inform the boards of this, we specify the output voltages by a table of times $t = 0, t_1, ..., t_n$ and corresponding voltages $V_i(0), V_i(t_1), ..., V_i(t_n)$, where the subscript i indicates the output voltage for ith output channel. In the LabVIEW code, using a MATLAB script, we processs this table into the table of times $t = 0, \Delta t, 2\Delta t, ..., N\Delta t$, where $N = t_n/\Delta t$, and output voltages $V_i(0), V_i(\Delta t), V_i(2\Delta t), ..., V_i(N\Delta t)$. Currently,

[15] The spec sheet says the low threshold is 4.5 V and high threshold is 11 V, but 8V is high enough to activate the shutter.

$\Delta t = 10$ μs. As for the ramp analog output controlling the bias coil current, we have a special feature to implement the AC field for a Rabi pulse of a few kHz. The MATLAB script has a feature to generate a sinusoidal wave by specifying the frequency, amplitude and starting phase. Note that these feature gives a continuous voltage change for the ramp analog output as far as the discretization due to the resolution of the output channel.

Outputs are sent to different controlling components. Analog outputs controlling coil currents are sent into external signal inputs of coil current controllers. Laser power controllers are sent to I port of mixers to tune the RF power for the AOM with a DC signal. The RF power for EOM modulation is tuned by an analog output by the same way with a mixer as the laser power control. Digital signals for switching RF signals are sent to an RF switch (MiniCircuits, ZASWA2-50DR+). As for lasers that require precise timing control and completely turning off the light, we use a combination of an AOM and a shutter. We keep the AOM on to load constant heat dissipation to keep the diffraction angle constant[16], and turn it off only when the shutter is moving. The digital output signal for this kind of purpose is Tee'ed out to the shutter driver and a FPGA box that generates a short Off signal for the AOM that works both on the rising and falling edge of the TTL signal. This turns off the AOM for 4.5 ms starting 0.5 ms after the TTL signal, and the shutter moves while the AOM is off due to the 1-2 ms delay of the mechanical motion.

The connection from NI boards to actual hardware that outputs LabVIEW signals is done by BNC panels mounted on the top of the canopy. Specifically, we use PCI-6284 for digital outputs, PCI-6713 for constant analog outputs, and PCI-6713 for ramp analog outputs. These boards are connected to connection box of SCB-68A, BNC-2110, and BNC-2110, respectively, and each output is wired to a BNC connector on the panels. The BNC panel has some additional connections, such as to the AOM driver switch and coil controlling signal. These connections are also done by BNC cables.

[16]The change in AOM temperature results in the change of diffraction angle due to the thermal expansion of the crystal. This is particularly strong in Isomet AOM (1205C-1)

4.9 Data acquisition system

Data acquisition is done by analog inputs of an NI board, cameras, and single photon counters collecting the transmission through the experimental cavity. Analog inputs are controlled by the LabVIEW sequence.[17] Camera data acquisition is also done by the LabVIEW sequence. For now, those for the Baumer cameras are implemented, and every time the camera shutter is triggered, the camera image is captured and sent to the DAQ computer.

Single photon counter data is captured by a counting board (FastComtec, P7888). The single photon counter is purchased from HAMAMATSU (C13001-01(x)). This is a fiber coupled module, and its quantum efficiency including the fiber outcoupling efficiency to the detector is 45 % at 556 nm. Up to 2 MHz, we did not observe any saturation effect. It is an APD operated in Geiger mode, and its dark count rate is 7 Hz. The output of the photon counter is a 15 ns long TTL signal. The TTL signal goes into the counting board. Currently, the counting board is operated in a 4 channel mode, that has a time resolution of 2 ns. Channels one and two get TTL signals from the two single photon counters, and the third channel receives a trigger signal from a function generator for a phase reference of the chirp measurement (see section 7.1.3 for the details of the chirp measurement). The data is saved in a form of binary data, and analysis is performed by a MATLAB code.

[17] Currently, it is set up, but is not used.

Chapter 5

Lasers

As Fig. 2-4 shows, there are six different transitions of our interest, and our trapping laser frequency has to be a specific value. Thus, we need seven different lasers. In this chapter, the configuration of each laser is described.

5.1 399 nm laser

The 399 nm laser is for driving the ${}^1S_0 \rightarrow {}^1P_1$ transition. The laser consists of a homemade master ECDL and a slave DL. The schematic for the optical system is shown in Fig. 5-1.

The master laser is an ECDL with an AR-coated LD (Nichia NDV4411T, currently available equivalent product is NDUA116T). The nominal threshold is 43.7 mA, central wavelength is 401 nm, and its maximum output power is 45 mW. The light from the LD chip diverges 9.3 degrees horizontally, and 19.8 degrees vertically. It is collimated by an aspheric lens (Thorlabs, C671TME-A). A part of the light is sent back to the LD by a grating (Newport, 33025BF01-530H, 3600 gratings/mm). The structure of the LD and the grating mount is shown in Fig. 5-2. The grating is mounted in a way we can manually tune both horizontal and vertical angles of the reflection. In addition, a piezo in the grating mount controls the external cavity length. The incident angle of the grating is optimized to set the output wavelength at 398.911 nm, and due to this being off the center wavelength, a typical threshold

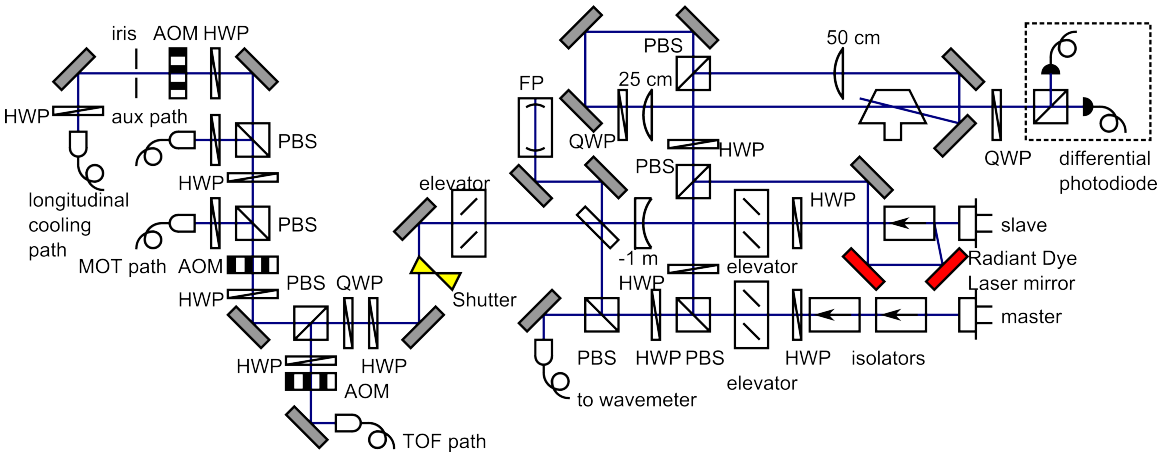

Figure 5-1: Optics arrangement for the 399 nm laser system

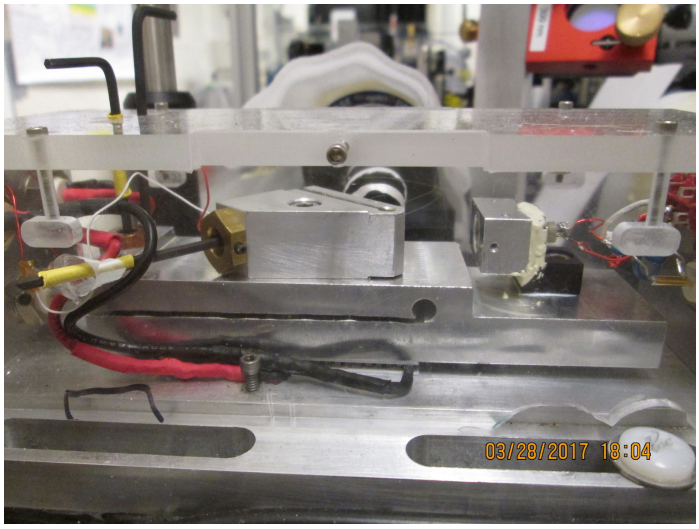

Figure 5-2: Structure of 399 nm master laser: grating is on the back side of aluminum block in the center of the photo.

current is 40.4 mA. The whole mount is temperature stabilized by a TEC at 18 °C. Due to the large size of the baseplate, the time constant for the temperature stabilisation is $\sim$ 20 s. We typically operate this laser at a current of 53 mA, and get 11 mW power before isolators.

After going through two 30 dB isolators (Conoptics, 711C-2), whose isolation and transmission are measured to be 40.6 dB and 81 %, respectively, the light is split by a PBS and a HWP. One goes into a wavemeter (Bristol, 521-VIS) through

a PM fiber. Typically 100 μW is necessary for the wavemeter to operate correctly. The wavemeter had a slight inaccuracy, and when the error signal for the locking is observed, the number on the wavemeter is 398.909 nm. In front of the fiber coupler to the wavemeter is another PBS, which sends a part of the light into a Thorlabs Fabry-Perot cavity (Thorlabs, SA200-3B) to monitor if the master laser is single mode.

The reflection side of the first PBS is split into two paths: an injection locking path and a DAVLL locking path. Injection locking path sends the master laser light into a slave laser. A typical power sent into the slave laser is 2.8 mW. The injection locking is subjected to the daily realignment. The alignment is done by two Radiant-Dye Laser mirrors (MDI-2-3030z-M6).[1]

The master laser is stabilized by locking to the $^1S_0 \rightarrow ^1P_1$ transition. Because ytterbium has a high boiling point, a vapor cell is not available, and instead we use a hollow cathode lamp (Hamamatsu Photonics, L2783-70NE-YB). Typically the hollow cathode lamp is operated at 165 V, and the current due to this voltage is 1.14 mA[2]. Around the hollow cathode lamp, two permanent magnets are mounted to generate Zeeman shifts for the dichroic atomic vapor laser lock (DAVLL) [125, 126] Based on the shape of the error signal, the magnetic field is estimated to be 700 G. Typically 120 μW of linearly polarized light is sent into a differential photodiode through the hollow cathode lamp. The differential photodiode subtracts the σ^- component from the σ^+ component. The resulting error signal typically has 140 MHz/V slope. In addition to the Doppler broadened DAVLL signal, we have a counterpropagating beam to generate a Doppler free feature. When we send 0.15 mW power in the pump path, this generates a small dispersive feature corresponding to each isotope as shown

[1]Radiant-Dye Laser mirror mounts are believed to be stabler than Thorlabs KM100 mount, but no quantitative measurement has been done.

[2]This current is decreasing over time, for the previous hollowed cathode lamp, which we replaced about two months ago, presumably due to the degradation of the hollow cathode lamp. At the beginning, it was 180 V and 1.51 mA, we have observed 1.29 mA at 180 V, and the speed of decrease is increasing. After we observed some extra instability, we operated at the voltage of 265 V with a current of 0.75 mA. The spec sheet from Hamamatsu only guarantees the operation of 8000 Ah, and the degradation might mean that it is approaching to the end of its life. and changed the current and the voltage to 0.75 A and 265 V.

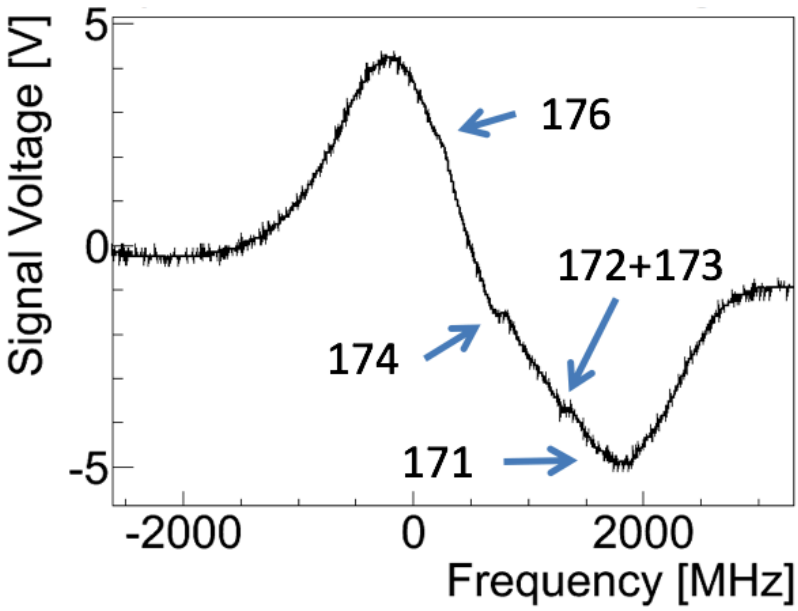

Figure 5-3: Doppler free DAVLL signal

in Fig. 5-3. The error signal generated by the differential phododiode is sent into our standard lockbox, and fed back to the current and the piezo of the master laser. The linewidth of the laser is estimated by the fluctuations of the error signal as 5 MHz.

The slave laser is a DL (Nichia NDV4313, non AR-coated). The laser does not have any external optical feedback, and at the free running, a chip mode is the only mode that selects the wavelength. The divergence angle is 10.9° vertically and 18.9° horizontally, and the beam is collimated by an aspheric lens. Frequency selection is done by an injection locking from the master laser. The laser chip is temperature stabilized with a TEC at 16°C. An approximate thermal time constant is 5 s. Typically, 2.8 mW of master laser light is injected, and 115 mW of the output power before isolator is extracted by a current of 96 mA.

The slave light is sent into a splitting system. First, the light goes through a $f = -100$ cm cylindrical concave lens to compensate the different amount of divergence between horizontal and vertical direction. Then a beam sampler sends a part of the light into a Thorlabs Fabry-Perot cavity (SA200-3B) for a monitoring purpose. This monitoring is important for checking the quality of injection locking. After going

through a pair of mirrors to compensate alignment drifts[3], the light is split into four paths. The first one is a TOF path. This has a 110 MHz AOM for fast switching, and 1st order diffraction is sent into an optical fiber. The light is then split into three paths after going through an 80 MHz AOM. The 1st order diffraction is coupled into optical fibers. The first path is used for MOT beams, the second path is an auxiliary path for alignment or other purpose, and the third path is for a longitudinal cooling beam. This beam is -110 MHz detuned by another AOM. The diffraction efficiency for each AOM is 80 %, and the fiber coupling efficiency is 50 %, which gives an overall coupling efficiency into a PM optical fiber of 40 %. The standard fiber for 399 nm laser is from OZ Optics (QPMJ-3AF,3AF-350-2/125-3-3-1), which only has a maximum rated power of 10 mW. To avoid damage in the fiber, which typically happens on the tip, we use a fiber from Shafter-Kirchhoff (PMC-E-400Si-3.1-NA010-3-APC.EC-300-P) for the MOT beam, which typically carries 18 mW. This fiber has a layer of glass that has smaller index of refraction on the tip as a safety feature.

5.2 556 nm laser

A 556 nm laser is used to address the ${}^1S_0 \rightarrow {}^3P_1$ transition, and it is the most important laser in our experiment. First of all, this transition is used for the second stage MOT. Secondly, this transition is used for performing spin squeezing and other cavity QED probing. The laser is a commercial fiber laser that generates 556 nm light by frequency doubling. Overall diagram is in Fig. 5-4.

The laser is manufactured by Menlo Systems (Orange one-SHG). It consists of three components: seed, pre-amp, and power-amp. The seed laser is an ytterbium doped fiber laser manufactured by NKT Photonics (Koheras BASIK), which gives 10 mW of 1112 nm light. The seed laser has two ways to tune the frequency. One is temperature tuning of the fiber, and the other is tuning piezo length that changes the length of the fiber. Temperature tuning gives a tuning coefficient of 6.5 GHz/K, and

[3]This drift happens daily basis, and it is attributed to the soft rubber between the laser mount and breadboard.

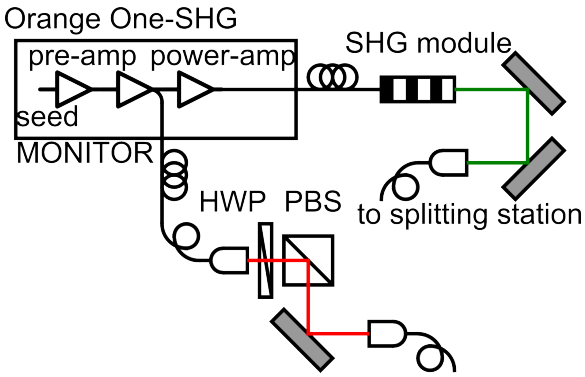

Figure 5-4: Optics arrangement for the 556 nm laser system: 556 nm output goes to the splitting station (Fig. 5-6. IR output goes to te ultrastable cavity after polarization cleaning system.

piezo gives 21.8 MHz/V. The overall frequency tuning range by the piezo is about 3 GHz, and this is good enough to cover the long term drift of the laser, and isotope shift of the ${}^1S_0 \rightarrow {}^3P_1$ transition for most isotopes of ytterbium. Nominal linewidth of the free running laser is 35 kHz.

The seed light then goes into pre-amp, which gives 100 mW of 1112 nm light. About 890 μW of the light is split into a monitor port. The rest of the light goes into the power-amp. The power-amp can give at most 0.69 W of 1112 nm light. The IR light is next sent into a frequency doubler. This is a waveguide PPLN, manufactured by NTT Electronics. Conversion efficiency is 70 %/W^2, and at the maximum power, we can get 335 mW of 556 nm light. Typically we don't need this much light, and only use 25 % of the full power of the power-amp, which gives 18 mW of 556 nm light. Up to the frequency doubler is all fiber coupled, and all parts described so far except for the doubler are in a 19 inch rack. The free-space output of the frequency doubler is coupled in to an optical fiber, whose coupling efficiency is 60 %,[4] and whole setup is on top of the canopy. The frequency doubler needs temperature stabilization so that the length of the SHG crystal matches precisely the wavelength of the light. The stabilization is done by a comercial temperature controller (Thorlabs, TED200C), and it is stabilized to 39.4 °C. Fig. 5-5 shows the relation between the temperature

[4]Initially, this was 80 %.

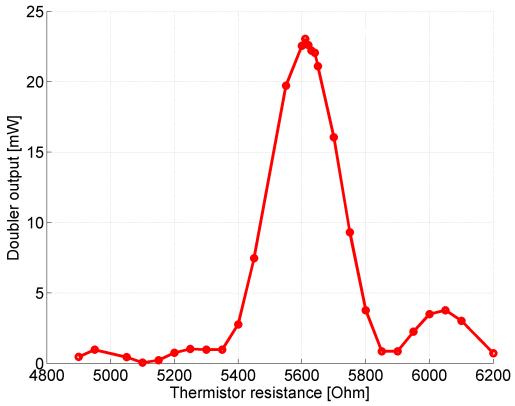

Figure 5-5: Relation between the temperature and the output power of SHG module: the data was taken at 100 mW input (seed and pre-amp being on) at 1111.603 nm.

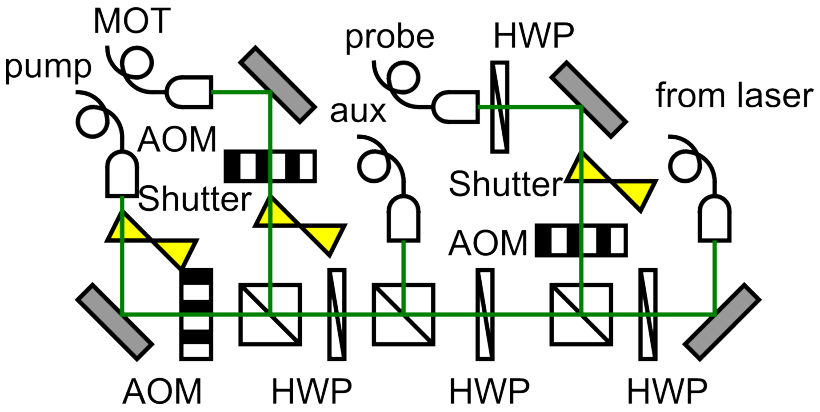

Figure 5-6: Optics arrangement for the 556 nm splitting station

and the output power by a constant input.[5]

Fiber coupled 556 nm light is first sent to a double pass AOM, and then sent into a splitting station (Fig. 5-6). The light is split into four paths. The first path is for a probe beam for the experimental cavity. This path has a shutter and an 80 MHz AOM for switching. The diffraction order of the AOM is positive first order. The second path is an auxiliary path. The third path is for MOT beams, whose frequency is shifted by the negative first order diffraction, and a shutter is also implemented. The fourth path is for a pumping beam. This path also has a shutter and an AOM, whose diffraction order is the negative first order.

[5]This data is taken in 2012. The optimal number drifted since then.

Frequency stabilization of the laser is done by locking to an ultrastable cavity. (For detailed description of the ultrastable cavity, see Section 5.8) The unstable path of the cavity is used for the 556 nm laser. The cavity has a finesse of 330,000 for 1112 nm light, and a free spectral range of 3.157 GHz. This corresponds to a linewidth of 9.5 kHz. The light from the monitor port is sent to this cavity. The light first experiences polarization cleaning by a PBS, and then goes into a fiber coupled EOM (EOSPACE, PM-0K5-10-PFA-PFA-1112). Since the polarization of the monitor output is not maintained, occasional rotation of a HWP in front of the PBS is necessary to maintain the large enough power going into the reference cavity. The power sent into the reference cavity is 750 μW. An error signal for the feedback is generated by the PDH technique [127]. The feedback is performed by two paths: a slow path and a fast path. The slow feedback drives the piezo that tunes the frequency of the seed laser. The bandwidth of this feedback is ~ 1 kHz, and it mainly compensates the long term drift of the laser. As the laser has high frequency fluctuation, this slow lock does not narrow its linewidth.

The fast feedback is sent through an RF signal. First of all, since the resonance frequency for the reference cavity $\omega_{\rm cav}$ and the resonance frequency for the ${}^1S_0 \to {}^3P_1$ transition $\omega_{\rm atom}$ is different in general, we need to bridge these two frequencies. The frequency difference is $\omega_{\rm bridge} = \omega_{\rm atom} - \omega_{\rm cav}$. To do this, we send an RF signal of $\omega_{\rm DDS} + \omega_{\rm VCO}$ to the EOM in addition to the PDH modulation frequency $\omega_{\rm PDH}$. $\omega_{\rm VCO}$ receives fast feedback, so that $\omega_{\rm cav} = \omega_{\rm L} + (\omega_{\rm DDS} + \omega_{\rm VCO})$ is free from the frequency fluctuation due to the laser.[6] The frequency fluctuation of the 556 nm light is twice as large as that of the 1112 nm light. The double pass AOM is used for both the frequency feedback and the frequency tuning. To do this, we mix $\omega_{\rm VCO} \simeq 40$ MHz and another ~ 50 MHz signal from a synthesizer (PTS3200) for frequency tuning, and an ~ 90 MHz RF signal is sent to the double pass AOM. The light that is sent to the atoms is shifted by another 80 MHz AOM (MOT and pump beams, -1st order) or a combination of 80 MHz AOM (+1st order) and -160 MHz sideband of an EOM (probe beam). This system stabilizes the frequency for 556 nm light interacting with

[6]Here, what is fluctuating is the bare laser, $\omega_{\rm L}$.

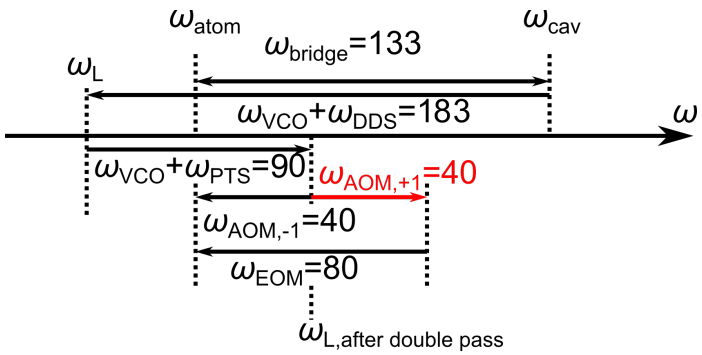

Figure 5-7: Frequency relations regarding 556 nm laser locking. Note that all the numbers here are those for 1112 nm light, and frequencies for 556 nm light are twice as large.

atoms, and estimated linewidth for the sideband is 5 kHz. Overall frequency relations of various RF signals are summarized in Fig. 5-7. For ^{171}Yb, we have

$$\omega_{\mathrm{PTS}} = 50\mathrm{MHz} \tag{5.1}$$

$$\omega_{\mathrm{VCO}} = 143\mathrm{MHz} \tag{5.2}$$

$$\omega_{\mathrm{PDH}} = 15\mathrm{MHz} \tag{5.3}$$

5.3 578 nm laser

A 578 nm laser is for interrogating the $^1S_0 \rightarrow {}^3P_0$ transition, the clock transition. In order to have interactions with the 7 mHz narrow transition, the laser has to have as narrow linewidth as possible, ideally 1 Hz or less. Here, only a brief summary of the laser is described, and further technical details should be referred to Boris Braverman's thesis [1].

578.4 nm light is generated by frequency doubling of 1157 nm light, and therefore lasers consists of 1157 nm lasers. It is a master-slave laser system, where the slave light goes into a frequency doubler. The master laser is a free space DFB laser (Nanoplus, DFB110130). Typically we get 16 mW from a current of 80 mA. The chip has an integrated TEC and thermistor, and the temperature is stabilized to 30

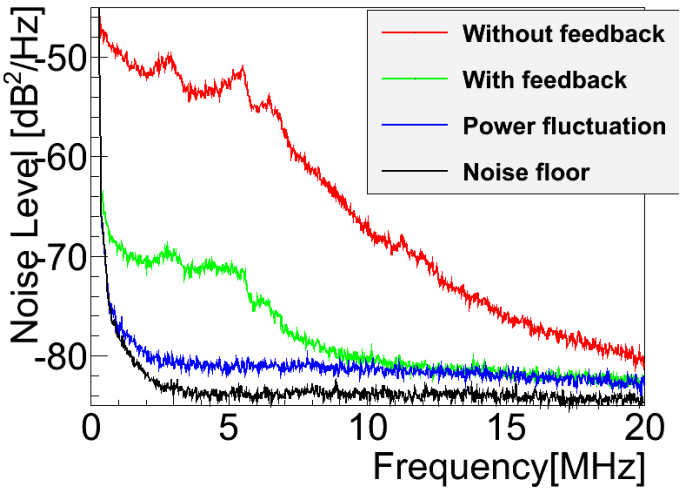

Figure 5-8: Noise spectral density of 1157 nm master laser

°C. The master laser has a long-path optical feedback feature [128] to prenarrow the linewidth. The effective path length of the cavity is $\sim$ 1.7 m with a 1 m optical fiber, and this gives about 10 kHz linewidth out of 1 MHz linewidth laser, as Fig. 5-8 shows. Most of the master laser light goes into an injection locking path for a slave laser. The slave laser is a quantum dot DL (Innolume, GC-1156-TO-200), and its AR-coated feature results in a good injection locking no matter what the input and output powers are. The chip has an integrated TEC and thermistor, and the temperature is stabilized to 18 °C. It gives at most 100 mW output. The slave laser light goes into a waveguide PPLN SHG module (NEL America, WH-0578-000-A-B-C). The conversion efficiency of this SHG module is 1269%/W^2, and it can output 20 mW from the slave light outputting 100 mW.

Frequency of the 1157 nm laser is stabilized by locking to the stable axis of the ultrastable cavity. For the stable axis, free spectral range is 3.14 GHz, and finesse is 330000 for 1157 nm light, which gives the linewidth of 9 kHz. We use the PDH technique to generate an error signal, and the error signal is fed back to the current of the master laser and the length of the long external cavity. The slow signal up to 30 kHz bandwidth is processed in a lockbox with proportional and integral gains. This signal is fed into a piezo that modulates the length of the long external cavity, whose bandwidth is 100 Hz. The feedback to the current is high-pass filtered at 3 Hz

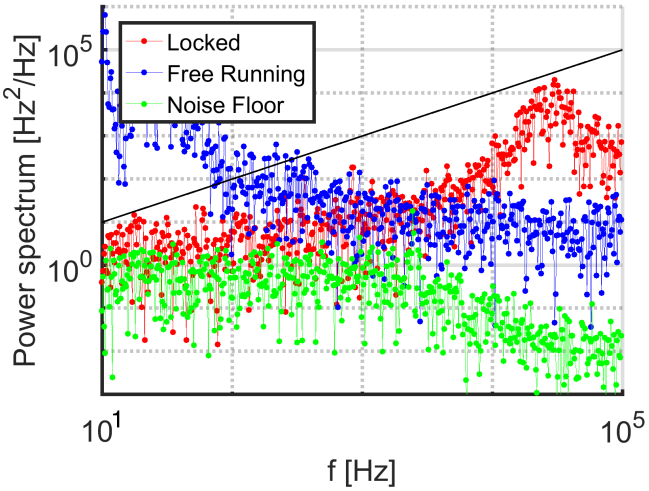

Figure 5-9: Noise spectral density of 1157 nm laser when it is locked

to avoid putting unnecessary slow feedback onto the current by a thermal drift of the path length of the long optical feedback path. Faster signal from 3 kHz to $\sim$ 3 MHz is directly fed back to the current of the master laser through a lead-lag filter. Here, the lead-lag filter is for compensating the sign change of the current-frequency relation at high frequency (200 kHz). The overall feedback system gives the noise spectral density shown in Fig. 5-9, which suggests the linewidth of 10 Hz. The bridging of the frequency difference between the ultrastable cavity resonance ω_{cav} and atomic resonance ω_{atom} is done by the same way as 556 nm laser, which is to send RF signal of $\omega_{\mathrm{bridge}} = \omega_{\mathrm{atom}} - \omega_{\mathrm{cav}}$ into the EOM and lock the ω_{bridge} sideband to the cavity. Currently ω_{bridge} is estimated to be 1508.37 MHz for ^{171}Yb.[7]

5.4 759 nm laser

5.4.1 Photodigm master setup

A 759 nm laser is used as a trapping laser. This wavelength is the magic wavelength, which cancels the AC Stark shift for the clock transition. As the AC Stark shift for

[7]This measurement was performed before we tune the temperature of ultrastable cavity from 32.5 °C to 3 °C. Therefore, temperature change should be compensated.

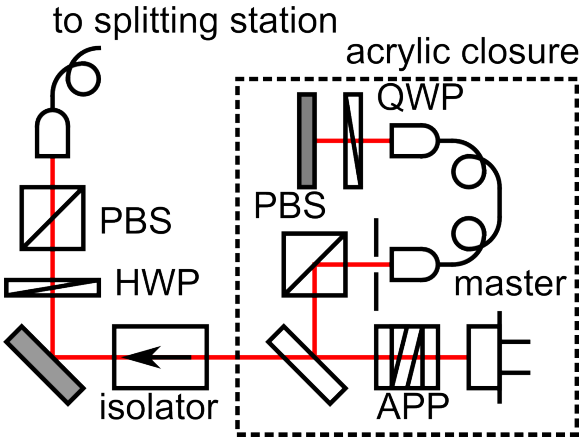

Figure 5-10: Optics system for 759 nm master laser

the ground state is 0.7 MHz for 100 kW/cm^2 light[8], it is necessary to have around 1 W laser power to have an order of 10 μK trap depth with a few tens of μm waist size one dimensional lattice. However, since our optical lattice is along an optical cavity that has $\mathcal{F} \sim 3000$ finesse for the 759 nm light (see Chapter 4.3 for more details), only 7 mW of input laser power is required for a one dimensional lattice deep enough to trap atoms. For future installation of two dimensional lattice for a clock experiment, where we send the clock laser from the side and need to Lamb-Dicke regime trapping in the radial direction for the experimental cavity axis, a TA is implemented, but the main part of the laser is a DBR laser and an AR-coated DL as a slave laser.

The master laser is a DBR laser from Photodigm (PH760DBR020T8).[9] The chip is mounted onto its laser mount (Photodigm, T08-1000-A). Nominal divergence of the beam is 28 degrees in the horizontal direction and 6 degrees in the vertical direction. Collimation is done by an aspheric lens (Thorlabs, C230TME-B) and an anamorphic prism pair (Thorlabs, PS881).[10] This is operated at 110 mA current, and we get $\sim$ 15 mW power. The temperature of the laser is stabilized to 17 °C with a built-in TEC and thermistor driven by our standard temperature controller. This laser also has a long-path optical feedback [128], and therefore part of the light is picked

[8]This is calculated from the lattice depth in [129].

[9]Now, the LD chip for the master laser of this system is dead and this setup is not used right now. However, we have another alive chip, and replacing the chip should revive the system. Thus, the description is kept here.

[10]Therefore there is certain amount of light not well coupled into fibers.

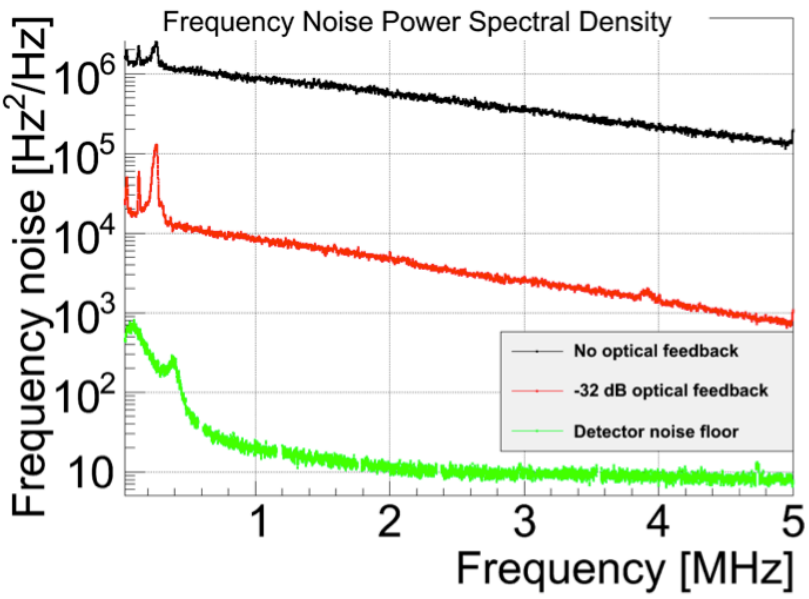

Figure 5-11: Effect of long path optical feedback on 759 nm master laser

up into a 1 m long PM fiber (OZ Optics, PMJ-3AF,3AF-780-5/125-3-1-1) before an isolator. The light going into the optical fiber is retroreflected at the output side, and sent back into the laser. The retroreflecting mirror is mounted onto a piezo (Thorlabs, AE0203D08F) for the purpose of feedback path length stabilization. The amount of optical feedback is around -32 dB, and this gives around a factor of 100 reduction of high frequency noise, as Fig. 5-11 shows. The laser light goes to a 60 dB isolator (Isowave, I-80U-4L), and then sent into a splitting station by a PM fiber. The coupling efficiency to the output optical fiber is 60 %.

The splitting station splits the light from the master laser into three. The first path sends the light to the slave laser for injection locking. The second path sends the light first into a fiber-coupled EOM (EOSpace, PM-05K-10-PFA-PFA-760), and then send it to a reference cavity. The third path is an auxiliary path, which is usually connected to a wavemeter (Advantest, Q8326). All the input and outputs are fiber-coupled, and each path has a power-tuning feature by a combination of a HWP and a PBS.

The slave laser is an AR-coated DL (Eagleyard, EYP-RWE-0780-02000-1300). The chip is mounted onto a laser diode mount (Thorlabs, LM9F), and the output

beam is collimated by an aspheric lens. To have a lasing output, there has to be an injection locking light, and otherwise it only gives out 3 mW of ASE at a current of 90 mA. Typically the laser gets 2 mW of seed light for injection locking, and it outputs 31 mW with the current of 140 mA after a 30 dB isolator. The laser is temperature stabilized by a TEC onto which the laser mount is fixed, and the temperature is set to 20 °C. The output is split into two paths, after being shaped by an anamorphic prism pair (Thorlabs, PS875). The first path is an auxiliary output, and the second path is sent into the experimental cavity setup. Both outputs have an AOM (Isomet, 1205C-2) for frequency shifting, and coupled into PM fibers. The AOM is essential to prevent an unnecessary feedback from the retroreflected light from the experimental cavity. The diffraction efficiency for Isomet AOM in the main path is 72 %, and the coupling efficiency to the optical fiber is 54 %.[11]

Frequency stabilization of the master laser is done by locking to a reference cavity. The 759 nm axis of the reference cavity has the finesse of 1250, which corresponds to a linewidth of 1.2 MHz. Error signal for the locking is generated by the PDH technique [127]. The RF frequency for the PDH technique ω_{PDH} is 41 MHz. The RF signal of $\omega_{\mathrm{bridge}} \sim 530$ MHz is also sent to the fiber-coupled EOM to shift the 759 nm laser frequency from the reference cavity resonance. The magnitude of the PDH signal is around 200 mV peak to peak. The feedback is applied by three paths. The first path is a slow feedback onto the laser current. An error signal is processed by a lockbox with a gain curve shown in the Fig. 5-12. The output of the lockbox is sent into the $\mathrm{MOD}_{\mathrm{in}}$ input of the current controller. The current controller for 759 nm master laser is a modified current controller from the standard Libbrecht-Hall laser diode current controller [130] in our group to AC couple the feedback onto the current. (see Appendix B for the detailed description of the modified current controller) The cutoff frequency for the high-pass filter is 0.7 Hz. The second path is that to the piezo of the optical feedback path. This is through the current controller, with a bandwidth of 100 Hz, due to the capacitance of the piezo and high output impedance of the piezo driver. The third path is the direct feedback onto the current of the LD. The

[11] These numbers were larger at the beginning.

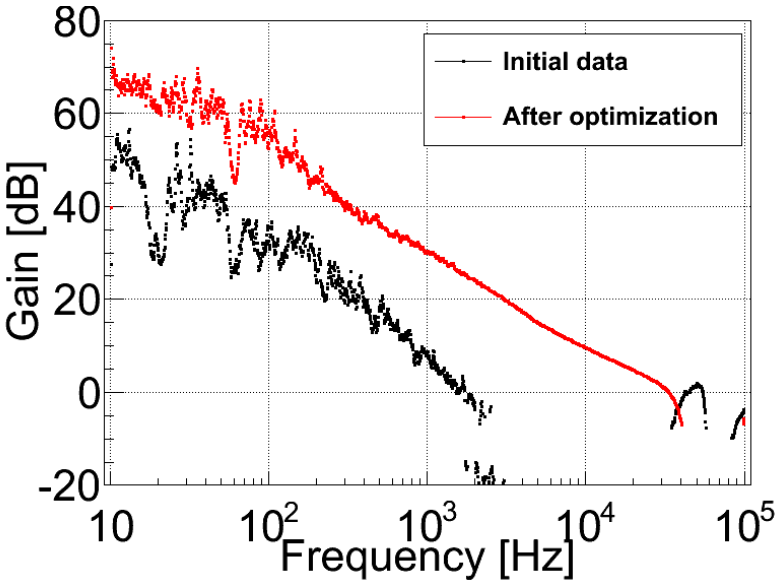

Figure 5-12: The gain of the lockbox for the 759 nm master laser lock

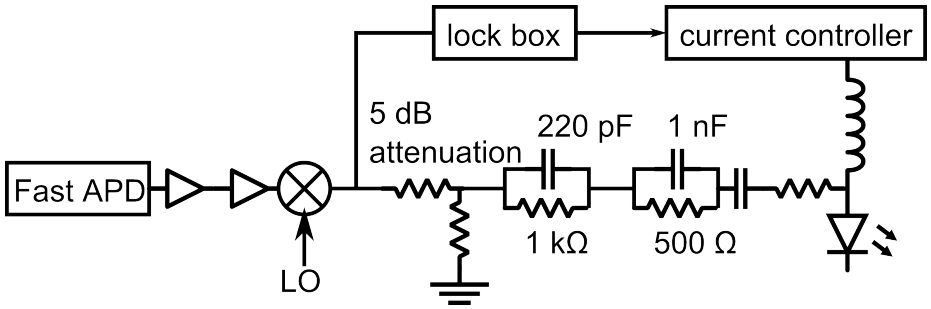

Figure 5-13: The circuit diagram for the fast feedback of 759 nm master laser: the path that does not go through lockbox is called fast feedback.

PDH error signal is tee'ed out into a fast feedback path, and directly connected to the diode chip. The signal is processed through a 5 dB attenuator, a lead-lag filter, and an AC coupling feature as shown in Fig. 5-13. The bandwidth of the fast feedback is around 3 MHz, and frequency noise is suppressed by about 9 dB around 100 kHz, as shown in Fig. 5-14.

5.4.2 Eblana master setup

A problem of the long path optical feedback is that this feedback path is sensitive to the vibration, and it easily falls out of lock if any strong vibration happens on the

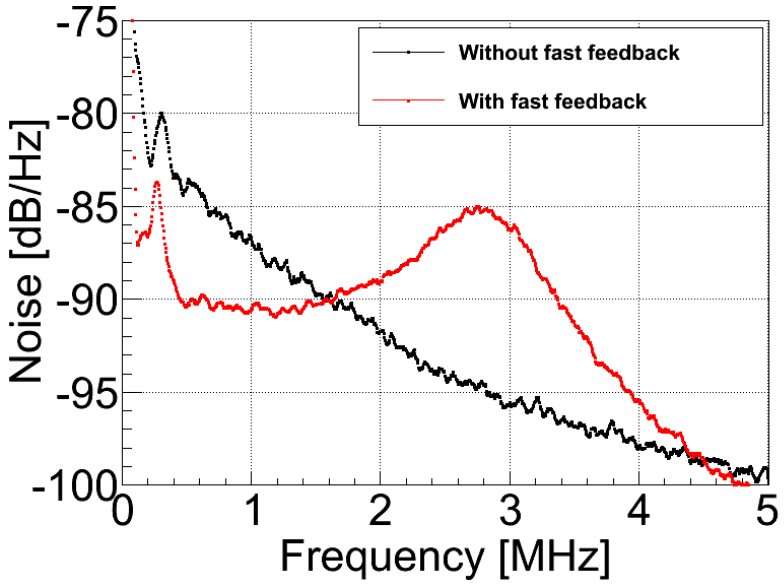

Figure 5-14: The effect of fast feedback on the frequency noise of 759 nm master laser

optics table. To have better locking, we developed an EOM feedback system in the optical feedback path.

The new system uses a DM laser from Eblana Photonics (EP759-0-DM-7P39-01). The chip is mounted on a cubic mount from Nanoplus (OPT-HEAT-T05) with a 22.5 degrees tilt to house the chip with 6 pins in a correct way with the output of H linear polarization. The chip has an integrated temperature controlling system, and the temperature of the chip is stabilized to 20 °C with our standard temperature controller. The threshold current at 20 °C is 80 mA, and we typically operate it at 110 mA, which gives 12 mW output. The light that is collimated by an aspheric lens and an anamorphic prism pair (Thorlabs, PS879-B) first goes through an isolator (OFR, 10-3C-780-HP-Z). then a part of the light is picked up by a beam sampler, and sent into a fiber-coupled EOM (PM-0S5-10-PFA-PFA-770) by a mirror on a piezo. The output of the EOM is sent back to the return port of the isolator, and fed back to the LD chip. The amount of optical feedback is controlled by ND filters and a HWP before and after the fiber coupled EOM. This itself gives certain amount of high frequency noise reduction, and narrows the laser linewidth down to $\sim$ 100 kHz.

The stabilization of the laser is done by the PDH locking to a reference cavity.

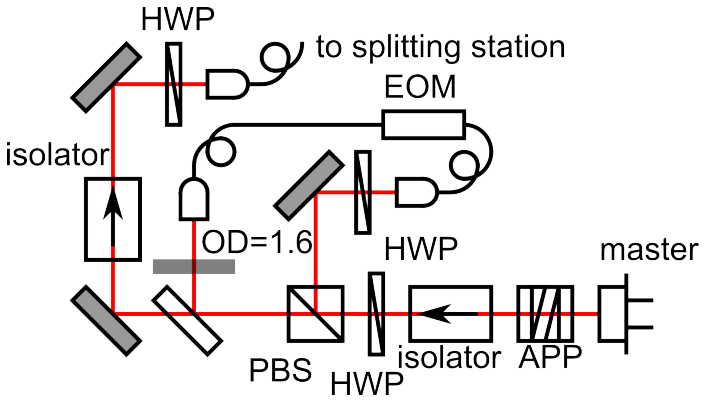

Figure 5-15: Optics system for 759 nm Eblana master laser

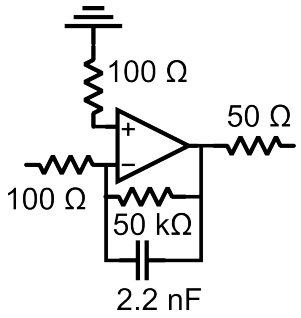

Figure 5-16: Amplifier for the feedback to EOM

The basic idea of how to generate a signal is the same as the previous subsection. Difference is how to put the feedback. This has two feedback paths.[12] First one is a slow feedback to the piezo that can change the path length of the optical feedback. The bandwidth is around 100 Hz, and the signal is sent to a piezo driver after our standard lockbox. The second path is the path to the EOM. This path has an amplifier to put a large enough phase shift onto the optical feedback, as shown in Fig. 5-16. This has gain and phase behavior as shown in Fig. 5-17, and when we change the overall gain by putting different attenuators into this path, we can reduce the noise around 100 kHz by two orders of magnitude compared to simple optical feedback, as shown in Fig. 5-18.

Note that the output of this laser is simply sent to the splitting system described in the previous subsection, so that we can easily change between two systems.

[12]We also have a current feedback feature through a lockbox, but it is not currently used.

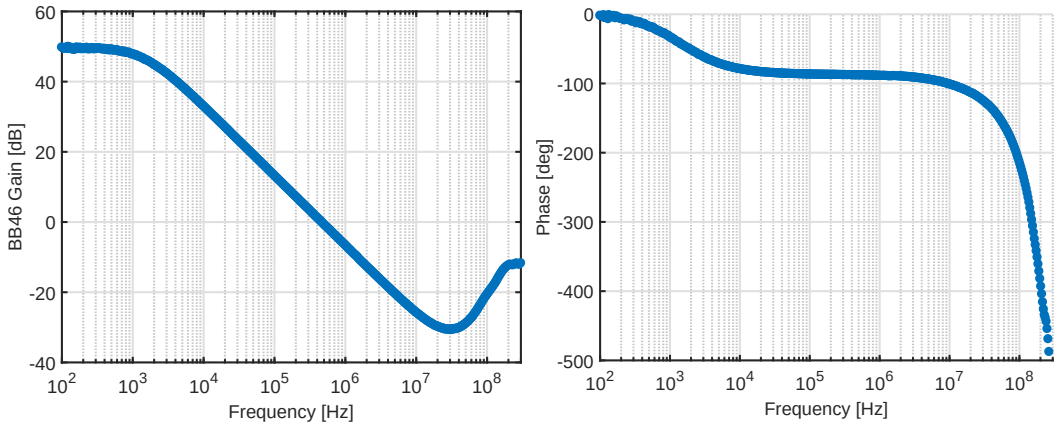

(a) Gain (b) Phase

Figure 5-17: Gain curve of the EOM feedback amplifier

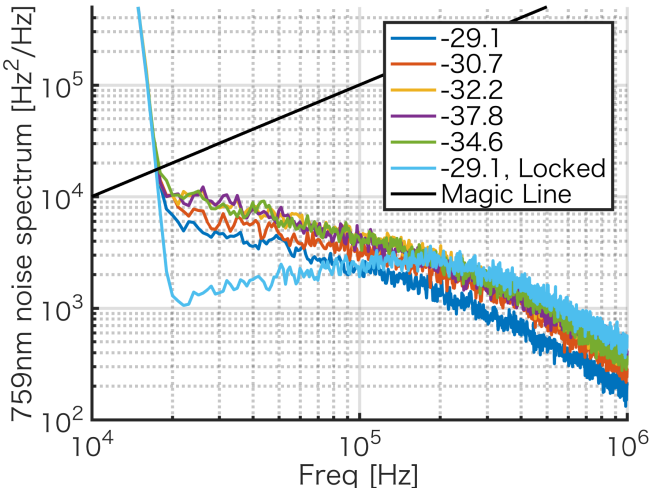

Figure 5-18: Reduction of frequency noise by EOM feedback: free running is without the EOM feedback, which means the effect is only by the optical feedback. The magic line is the line the cross section of the spectral noise density with which gives the linewidth of the laser.

5.5 770 nm laser

A 770 nm laser is used for coupling to the $6s6p\,^3P_2 \rightarrow 6s7s\,^3S_1$ transition. This is a repump transition for the $^3P_2$ metastable state. The laser is a commercial ECDL from TOPTICA (DL100L). The output wavelength is tuned at 770.2 nm, and the laser has 27 GHz of modehop-free tuning range. Output light is separated into three paths: the main output, a frequency lock path, and an auxiliary path, which is usually used

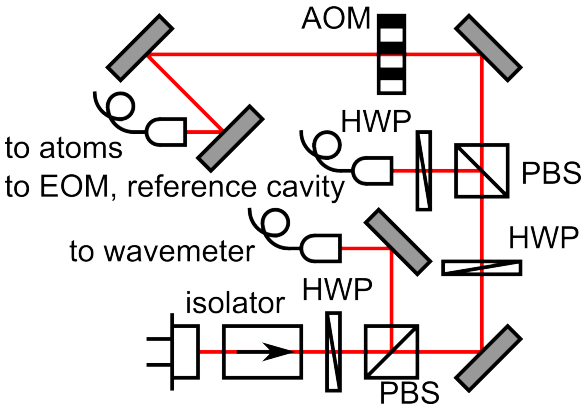

Figure 5-19: Optics system for 770 nm laser

for wavelength measurement by a wavemeter. The main path has an 80 MHz AOM (ISOMET 1205C-2) for a switching purpose. In the frequency lock path, the light is first sent into a fiber coupled EOM (EOSpace, PM-05S-10-PFA-PFA-770), and then is transferred to the reference cavity. All outputs are fiber coupled.

Frequency locking of the 770 nm laser is done by the PDH locking to the reference cavity. The 770 nm axis of the reference cavity has finesse of 682, which gives 2.2 MHz linewidth. The free spectral range of the cavity is 1.474 GHz. Feedback has fast and slow paths. The slow path goes to the mod inp. input for the current and the trigger input for the piezo on the comercial controller from TOPTICA, which tunes both piezo and current of the DL. Corner frequency of a low pass filter on this path is 7 kHz. The path to the piezo has additional low-pass filter of a couple of hundred Hz to avoid mechanical resonances around 1-2 kHz. The fast path is directly sent to the current of DL. The bandwidth of the path istelf is 20 MHz, and the bandwidth of the feedback is 1.5 MHz. With this feedback, the linewidth of the laser is narrowed down from 25 kHz to 5 kHz. The way to bridge the reference cavity resonance and atomic resonance with a sideband of ω_{bridge} is the same as 556 nm laser. ω_{bridge} is -175 MHz and 393 MHz for ^{171}Yb and ^{174}Yb, with a wavemeter reading of 389.25689 THz and 369.26074 THz, respectively.

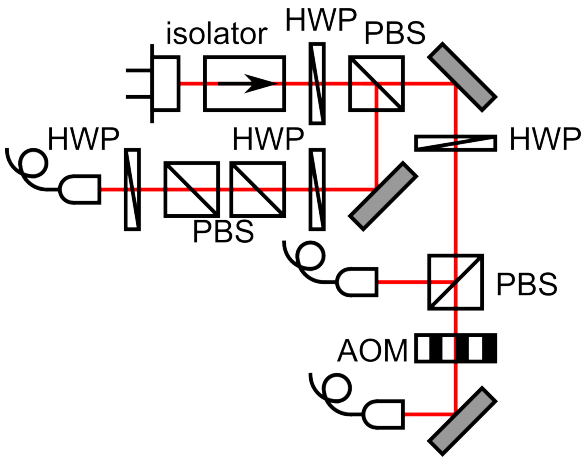

Figure 5-20: Optics system for 1389 nm laser

5.6 1389 nm laser

1389 nm laser is to be resonant with the $6s6p^3P_0 \rightarrow 5d6s^3D_1$ transition, which works as a repump transition for the $^3P_0$ metastable state. The laser is a fiber coupled DFB laser from NEL-America Inc.(NLK1E5GAAA). The LD is enclosed in a 14 pin butterfly can, and mounted on a butterfly mount (Arroyo, 203 Butterfly laser Mount). Typically the laser gives 12 mW output with 50 mA current. The laser diode chip has an integrated TEC and thermistor, and the chip is temperature stabilized to 19 °C by our standard temperature controller. The laser has a built-in 30 dB isolator.

The laser is outcoupled from the fiber, goes through a 35 dB isolator (Thorlabs IO-4-1390-VLP), and then split into three: the main output, an auxiliary output, and a locking output. The main output has a 80 MHz AOM (Intraaction, ACM-802AA1) for a switching purpose. The auxiliary output is for a wavelength measurement by a wavemeter. The locking output sends the light to the reference cavity through a fiber coupled EOM (EOSpace, PM-0S5-10-PFA-PFA-1390). All the outputs are coupled into PM fibers.

Frequency stabilization of the 1389 nm laser is done by locking to the reference cavity. The 1389 nm axis has a finesse of 213, which corresponds to a linewidth of 7.0 MHz. Locking is done with the standard PDH technique to a ω_{bridge} sideband to shift the carrier frequency to the atomic resonance from the reference cavity resonance.

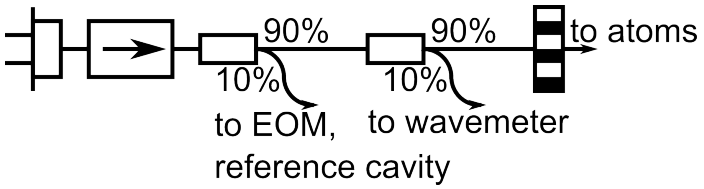

Figure 5-21: Optics system for 1539 nm laser

The value for ω_{bridge} has not been measured, but the transition has been observed at 215.87221 THz through a wavemeter reading for ^{171}Yb. The feedback is put to the LD current through our standard lockbox. The lock is only for long term stability and there is no frequency narrowing by the locking for now.

5.7 1539 nm laser

1539 nm is the wavelength for the 6s6p$^3P_1 \rightarrow$ 5d6s$^3D_1$ transition, and this transition is used to send the population from the ground state to the excited state of the clock transition without using the clock transition. The laser is a fiber-coupled DFB laser (Eblana Photonics, EP1539-1-DM-B01-FM). The chip has a 30 dB integrated optical isolator, and a thermistor and a TEC for temperature stabilization. A typical output power from the fiber is 6 mW with a current of 80 mA. The temperature is stabilized to 18 °C by our standard temperature controller. The laser system is all fiber coupled, and the output is split into three paths by two fiber coupled beam splitters (Thorlabs, PMC-1550-90B-APC). 81 % of the light goes to the main output path, 9 % goes to an auxiliary output, and 10 % goes to a locking path. The main output has a 80 MHz fiber coupled AOM (Intraaction FCM-801-E38AP)for a switching purpose, and the locking path goes through a fiber-coupled EOM (EOSpace, PM-0S5-10-PFA-PFA-1539).

The locking of the 1539 nm laser is performed by a PDH locking to a reference cavity. The 1539 nm axis of the reference cavity has a finesse of 1522, which gives a linewidth of 0.99 MHz. The locking technique is the PDH technique with an ω_{bridge} sideband to shift the carrier frequency to the atomic resonance from the reference

cavity resonance. The feedback is sent to the current of the LD through our standard lockbox. The locking only suppresses the long term drift of the laser, and linewidth narrowing due to the locking is not observed. For ^{171}Yb, ω_{bridge} is measured to be 102 MHz, with wavemeter reading of 194.77757 THz.

5.8 Ultrastable cavity

Six of seven lasers are locked to reference cavities, because it is difficult to couple to atomic transitions due to narrow linewidths or the fact that transitions are between excited states. To lock these lasers, we have two reference cavities: an ultrastable cavity and a reference cavity. The ultrastable cavity is a commercial reference cavity that is designed to have a narrow linewidth laser down to 1 Hz level. The reference cavity is our home made cavity that is inspired by this commercial cavity. Here in this thesis, when the cavity is mentioned as the reference cavity, it means this homemade reference cavity, and the commercial reference cavity is referred as the ultrastable cavity.

The ultrastable cavity is a commercial reference cavity from AT Films (spacer and mirror, ATF-6302) and Stable Laser Systems (housing structure, VH-6300). The design is based on a spherical cavity from Bergquist group [131]. A spacer is made out of ULE, which has a zero crossing of the thermal expansion coefficient. The holding structure of a sphere is at a special angle between the cavity axis that cancels contraction of the cavity mirror distance due to holding force and expansion of it in the perpendicular direction governed by a Poisson ratio. This results in a very low acceleration sensitivity of $10^{-10}g$ or below. Our spacer is custom made to have another axis that is perpendicular to the original cavity axis. We call this original cavity axis a stable axis, and the additional one an unstable axis. The spacer is held by a fork as Fig. 5-22 shows, and the whole structure is sitting inside a vacuum chamber that is pumped by a 2 l/s ion pump (Agilent, 9190520). The spacer and the gold plated thermal shield is temperature stabilized by a TEC and thermistors mounted on the bottom plate of the thermal shield. The temperature is set to 2.500

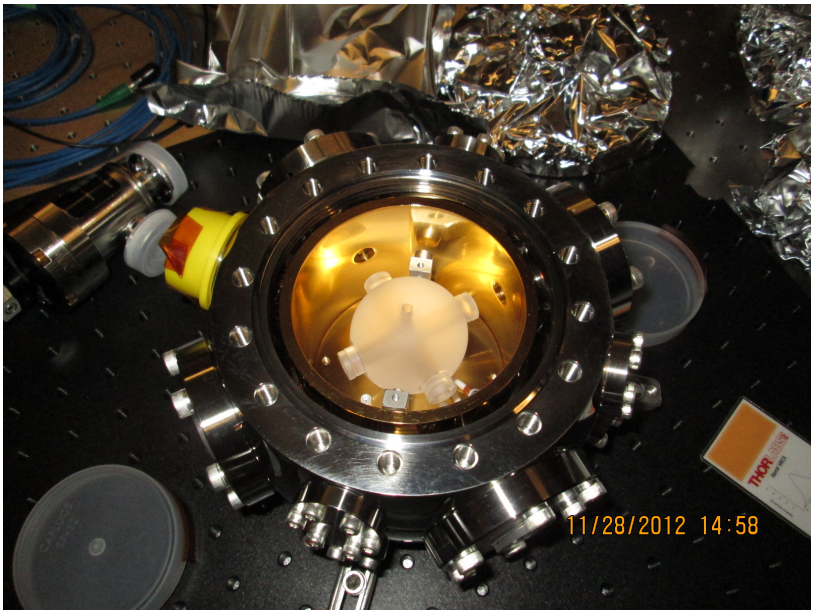

Figure 5-22: Photo of the inside of ultrastable cavity

°C,[13] which is the zero crossing point we measured, by a commercial temperature controller (Wavelength Electronics, LFI-3751). [14]

The stable axis is used for 578 nm laser locking, and unstable axis is used for 556 nm laser locking. The vacuum chamber and surrounding optics are put onto a 1.5' x 1.5' optical breadboard (Thorlabs, MB18), and the whole structure is put onto a vibrational isolation stage (Minus-K Technology, 100BM-8). The overall structure is put inside an acrylic box for a passive suppression of the temperature fluctuation and acoustic noise. To cool the cavity down to 2.5 °C, the TEC has to dissipate heat into the environment. To make this efficient, we send air to the vacuum chamber by a fan mounted on the acrylic closure, and the top lid has a hole for good air circulation.

Cavity mirrors have high reflectivity coating for both 1112 nm and 1157 nm lights. Measured finesse is 330000 for both 1112 nm and 1157 nm, which correspond to linewidths of 9 kHz. Free spectral range is 3.1565 GHz for 1112 nm light in the

[13]Currently, it is at 3.000°C, but it should be tuned to 2.500 °C.

[14]The manufacturer originally reported the zero crossing temperature as 32.5 °C, with a note of the actual zero crossing point including the mirror would be 6 °C lower, but measured value was far off. It turned out that their method of using sound wave velocity in the spacer did not work well for this spherical cavity.

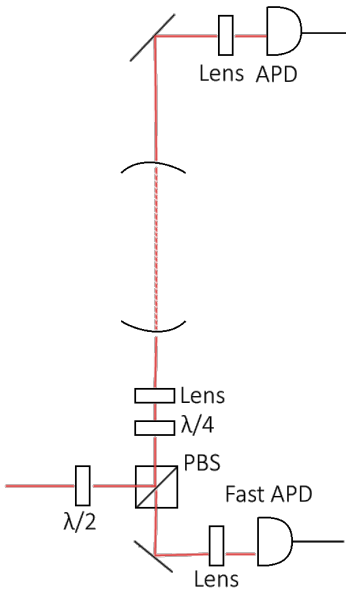

Figure 5-23: Optics components around ultrastable and reference cavity (Cited from [8]): each axis has these optics components for PDH locking and transmission detection.

unstable axis, and 3155.8282(4) MHz for 1157 nm light in the stable axis. A pair of mirrors consists of a flat mirror and 50 cm radius of curvature mirror, which gives 323 MHz separation from adjacent higher order modes. Surrounding optics are for near IR. Particularly, INGaAs APDs (Hamamatsu Photonics, G8931-20) are used for the transmission peak detection and the detection for the reflected light, though a silicon photo detector still can detect 1157 nm light, as proven by a security camera detecting transmitted light.

Each axis has optics described in Fig. 5-23. The idea is to detect the transmission through the cavity by DC coupled APDs, and the reflected light is detected by fast APDs.

5.9 Reference cavity

The reference cavity[15] is for locking the 759, 770, 1389, and 1539 nm lasers. The design is inspired by comercial reference cavities. A spacer is made of ULE, and it is held in the middle. Cavity axes are along vertical direction. To have four lasers locked to the cavity, four different holes are drilled onto the spacer, and each axis has mirrors for different wavelength. The spacer has a heater glued onto it for the temperature stabilization. The spacer is surrounded by a gold plated copper thermal shield, which has some heaters for the temperature stabilization. These structures sit on a teflon baseplate, and whole structure is inside a vacuum chamber that is pumped by a 2 l/s ion pump (Agilent, 9190520). (see Fig. 5-24) The vacuum chamber is wrapped by a three layer passive thermal shield (fabric, Mylar, fabric), and the chamber is temperature stabilized to 25 °C by a heater, thermistors, and a four point measurement temperature controller. The chamber and surrounding optics are on 2' x 2' optical breadboard (Thorlabs B2424F), as shown in Fig. 5-25. The incoming light is sent horizontally into the chamber, and reflected upward by a 45 degree mirror in the vacuum chamber. The output light is detected by optics on an upper layer breadboard.

Length of the spacer is 10 cm, and therefore the free spectral range of each axis is 1.5 GHz. Properties of the mirrors on each axis are summarized in Table 5.9. Optics components around the reference cavity is shown in Fig. 5-23. The input side is on the bottom layer, which also works for reflected light detection for the PDH technique, and transmission light is detected at DC coupled APDs on the top layer.

[15] André Heinz's thesis [8] has some technical details on this cavity.

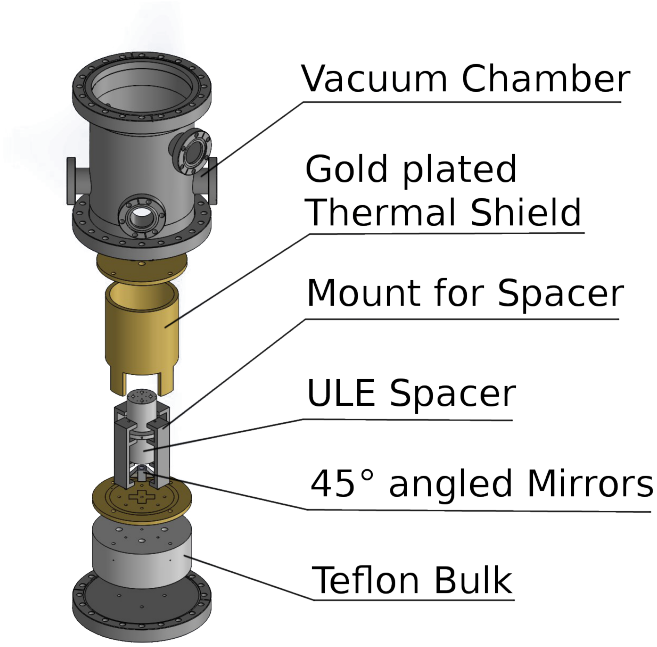

Figure 5-24: Structure of reference cavity (Cited from [8])

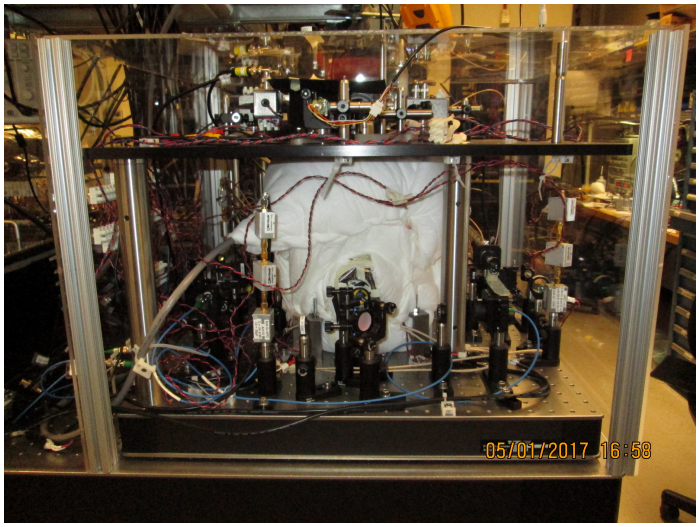

Figure 5-25: Photo of optics around the reference cavity

wavelength	mirror 1		mirror 2		finesse	linewidth
	ROC	transmission	ROC	transmission		
759 nm	∞	0.13 %	50 cm	221 ppm	1250	1.2 MHz
770 nm	∞	0.10 %	50 cm	126 ppm	682	2.2 MHz
1389 nm	∞	0.14 %	50 cm	323 ppm	213	7.0 MHz
1539 nm	∞	978 ppm	50 cm	1084 ppm	1522	0.99 MHz

Table 5.1: Summary of the properties of reference cavity axes

Chapter 6

Atom Trapping

In this chapter, the way we trap atoms into an optical lattice is described. Because we have a waist of a cavity mode close to the micromirror, we use a mirror MOT. [132] In our setup, mirror MOT geometry limits the maximum quadrupole magnetic field gradient, and this constraint motivated us to develop a MOT TCMOT that works at smaller magnetic field gradient than standard MOT. This leaded to TCMOT, where we send 399 nm laser and 556 nm laser at the same time to form a MOT. In the experimental sequence for cavity QED experiments, we first make TCMOT with 399 nm and 556 nm laser, turn off 399 nm light to have green MOT, and then turn off 556 nm laser to load atoms into an optical lattice made by 759 nm laser. The trap laser is always on during the MOT stage. In the following sections, each part of these techniques and sequences are described.

6.1 MOT for ytterbium

MOT [133] is the starting point of trapping atoms in most cold atom experiments. MOT combines an atom cooling by dissipative light force and a position dependent force with a use of quadrupole magnetic field and circularly polarized light. In the configuration shown in Fig. 6-1, magnetic field shifts the energy level of Zeeman sublevels, and in a positive z position, the σ^- light that is sent towards the negative z direction is scattered more due to the energy shift. In a negative z position, $m_z = 1$

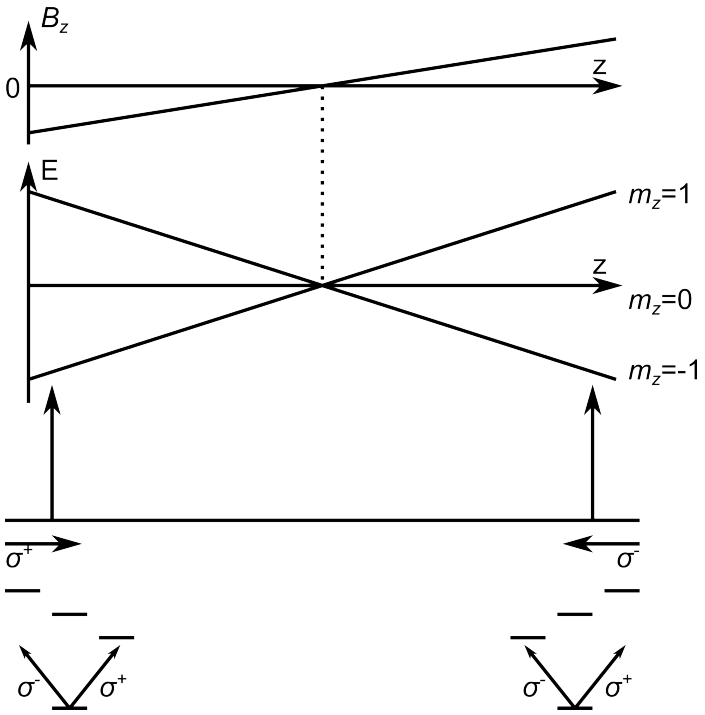

Figure 6-1: Mechanism of MOT: the configuration is that magnetic field $B_z = B_0 z$, and σ^+ light is sent to positive z direction, and σ^- light is sent to negative z direction. Frequency of light is red detuned relative to unperturbed transition frequency.

state has lower energy, and therefore the σ^+ light that is sent towards the positive z direction has more scattering. This means atoms in a $-z$ position gets more light force in the $+z$ direction, and atoms in a $+z$ position gets more light force in the $-z$ direction. Thus, atoms are confined at $z = 0$, and lose its energy due to a molasses effect due to the red detuned light. Type-I MOT have more Zeeman sublevels in the excited states than the ground state, using a $F \to F' = F + 1$ transition, and this is much more common than type-II MOT that uses a $F \to F' = F$ or $F \to F' = F - 1$ transition. [134, 135]

As for ytterbium, the ground state is the $6s^2 {}^1S_0$ state, which has $2I + 1$ Zeeman sublevels and no hyperfine structure, where I is a nuclear spin magnetic moment. $I = 0$ for bosonic isotopes, and $I = 1/2, 5/2$ for ^{171}Yb and ^{173}Yb, respectively. There are two suitable excited states for making a MOT. One is the $6s6p {}^1P_1$ state, whose decay linewidth is 28 MHz, and the other is the $6s6p {}^3P_1$ state, whose linewidth is 184 kHz. Because its total angular momentum $J = 1$ for these excited state, this gives

Table 6.1: Isotope shift for $^1S_0 \rightarrow^3 P_1$ transition [10]

mass number	F for the excited state	isotope shift
173	7/2	-1431.872(60)
171	1/2	− 1177.231(60)
176		0
174		954.832(60)
172		1954.852(60)
170		3241.177(60)
173	5/2	3266.243(60)
168		4609.960(80)
171	3/2	4759.440(80)
173	3/2	4762.110(120)

Table 6.2: Isotope shift for $^1S_0 \rightarrow^1 P_1$ transition [11]

mass number	F for the excited state	isotope shift
176		− 509.310(50)
173	5/2	− 253.418(50)
174		0
173	3/2	515.975(200)
172		533.309(53)
173	7/2	587.986(56)
171	3/2	832.436(50)
171	1/2	1153.696(61)
170		1192.393(66)
168		1887.400(50)

type-I MOT.[1] Parameters relavant to laser cooling with the $^1S_0 \rightarrow^1 P_1$ transition and the $^1S_0 \rightarrow^3 P_1$ transition are summarized in Table 6.3, and isotope shifts are summarized in Table 6.2 and Table 6.1. Also, the natural abundance of each isotope is summarized in Table 2.1.

[1]Particularly for the bosonic isotopes, the ground state has single Zeeman sublevel and the $^1P_1$ and $^3P_1$ excited state has three Zeeman sublevels, and therefore the level structure is identical to the situation depicted in Fig. 6-1

Table 6.3: Parameters for laser cooling: in addition to ${}^1S_0 \rightarrow {}^1P_1$ and ${}^1S_0 \rightarrow {}^3P_1$ transition, basic information on ${}^1S_0 \rightarrow {}^3P_0$ transition is also summarized, except for the Doppler limits.

transition		${}^1S_0 \rightarrow {}^1P_1$	${}^1S_0 \rightarrow {}^3P_1$	${}^1S_0 \rightarrow {}^3P_0$	Unit
wavelength	λ	398.9114	556.8024	578.4212	nm
lifetime	τ	5.70 ns	865 ns	22.6 s	
linewidth	$\Gamma/2\pi = 1/2\pi\tau$	27.9 MHz	184 kHz	7.0 mHz	
saturation intensity	$i_{\mathrm{sat}} = \frac{\pi hc}{3\lambda^3\tau}$	58	0.138	4.76×10^{-11}	mW/cm^2
Doppler limit temperature	$T_{\mathrm{D}} = \frac{\hbar\Gamma}{2k_{\mathrm{B}}}$	670	4.35		μK
Doppler limit velocity	$v_{\mathrm{D}} = \sqrt{\frac{k_{\mathrm{B}}T_{\mathrm{B}}}{m}}$	18	1.4		cm/s
electronic g-factor	g	1.04	1.49	0	
Recoil frequency	$\nu_{\mathrm{R}} = \frac{\hbar k^2}{4\pi m}$	7.2	3.7	3.5	kHz
Absorption cross section	$\sigma_{\mathrm{abs}} = \frac{3\lambda^2}{2\pi}$	76	147	157	10^{-15} m^2

MOT for ytterbium was first achieved with the ${}^1S_0 \rightarrow {}^1P_1$ transition [136]. This transition is broad, and therefore convenient to trap atoms in various velocity ranges. However, a decay from the $6s6p\,{}^1P_1$ state to the $6s6p\,{}^3P_2$ and $6s6p\,{}^3P_0$ metastable states limits the atom lifetime in the MOT up to ~ 600 ms, and the atom number up to $\sim 10^6$. To avoid this limit of atom number, the next thing achieved is to use the ${}^1S_0 \rightarrow {}^3P_1$ transition for a MOT transition. Directly loading atoms into a MOT with this transition after being slowed by a Zeeman slower achieved 10^8 atoms trapped. [137] The atom lifetime in this MOT is limited only by background gas collisions, and can be as long as 30 s. In addition to the trapped atom number, the temperature of the atoms is lower in the MOT with the ${}^1S_0 \rightarrow {}^1P_1$ transition, because of a narrower linewidth. The Doppler limit temperature of 4.4 μK is cold enough for atoms to be loaded into an optical lattice. Depending on their purpose, people used direct loading to a ${}^1S_0 \rightarrow {}^3P_1$ transition MOT, or first quickly trap atoms with a ${}^1S_0 \rightarrow {}^1P_1$ transition MOT and then transfer them to a ${}^1S_0 \rightarrow {}^3P_1$ transition MOT. [34] Recently, a new method of core-shell MOT achieved both quick loading and the large number of atoms trapped. [138] In this MOT, the centers of MOT beams for the ${}^1S_0 \rightarrow {}^1P_1$ transition are blocked and the ${}^1S_0 \rightarrow {}^3P_1$ transition light is sent there to avoid the decay to the metastable states, keeping the efficient gathering of atoms from the outskirt.

In our case, few thousands of atoms are needed in an optical lattice for a clock experiment, and a few seconds of lifetime is long enough. This means that we can put an oven close to the MOT region, removing a Zeeman slower, which is another technical complexity in experiment. Thus, we decided to put an oven to generate an atomic beam 2" away from the MOT region, and only send a counter-propagating beam for a longitudinal cooling. Based on the fact that we do not need a very large atom number, conventional two stage MOT, first with the ${}^1S_0 \rightarrow {}^1P_1$ transition and then transfer atoms into the ${}^1S_0 \rightarrow {}^3P_1$ transition MOT, is good enough. However, because of the configuration of the mirror MOT and the size of the MOT coil, we cannot have a large enough magnetic field to have the ${}^1S_0 \rightarrow {}^1P_1$ transition MOT, unless we send very large current to the MOT coils. This motivated us to develop a TCMOT.

6.2 Two-color MOT

The motivation of the TCMOT is to have a MOT with a low magnetic field gradient. For ytterbium, although ${}^1S_0 \rightarrow {}^1P_1$ transition MOTs typically use 50 G/cm magnetic field gradient, ${}^1S_0 \rightarrow {}^3P_1$ transition MOTs use only a few G/cm magnetic field gradient, and therefore a ${}^1S_0 \rightarrow {}^3P_1$ transition MOT is suitable for this purpose. However, a ${}^1S_0 \rightarrow {}^3P_1$ transition MOT has low capture velocity, and it is not likely that large number of atoms are trapped in the MOT without the help of a Zeeman slower. To avoid the problem of the small capture velocity, we superpose a ${}^1S_0 \rightarrow {}^1P_1$ transition laser to a ${}^1S_0 \rightarrow {}^3P_1$ transition laser, so that the ${}^1S_0 \rightarrow {}^1P_1$ transition laser works as molasses to slow down atoms. Once atoms are slowed down, the ${}^1S_0 \rightarrow {}^3P_1$ transition laser traps atoms.

This intuitive idea is confirmed by calculations. Description here is based on our paper [9], and notations are summarized in Fig. 6-2. First thing to confirm is if the ${}^1S_0 \rightarrow {}^1P_1$ transition laser works as a good molasses. To check this, we calculated acceleration $a = F/m$, where F is force and m is mass, on to an atom of velocity v by the following standard light force equation:

$$F_{\pm}(v,z) = \pm\frac{\hbar k\Gamma}{2}\frac{I_{\pm}(z)/I_{\mathrm{sat}}}{1 + I_{\pm}(z)/I_{\mathrm{sat}} + 4\left(\frac{\Delta \pm kv \mp \mu B' z}{\Gamma}\right)^2} \tag{6.1}$$

Here, $I_{\pm}$ is the intensity of two beams propagating to positive and negative directions, z is atom position, I_{sat} is the saturation intensity of a transition, k is wave number, μ is magnetic moment, and B' is magnetic field gradient. Fig. 6-3 shows the result of calculation. The ${}^1S_0 \rightarrow {}^1P_1$ transition laser makes significantly better molasses than the ${}^1S_0 \rightarrow {}^3P_1$ transition laser, and for atoms in most velocity ranges are mainly slowed down by the ${}^1S_0 \rightarrow {}^1P_1$ transition laser.

To calculate the trapping effect of the lasers, trapping potential is calculated by numerically integrating Eq. 6.1

$$U(z_0) = -\int_{-\infty}^{z_0} \left(F_+(0,z) + F_-(0,z)\right) dz \tag{6.2}$$

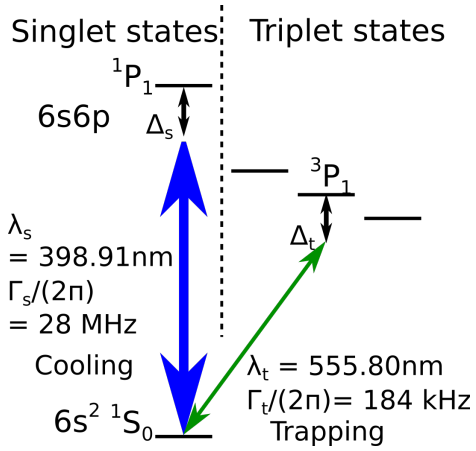

Figure 6-2: Transitions relevant to TCMOT and the definition of notation (Cited from [9])

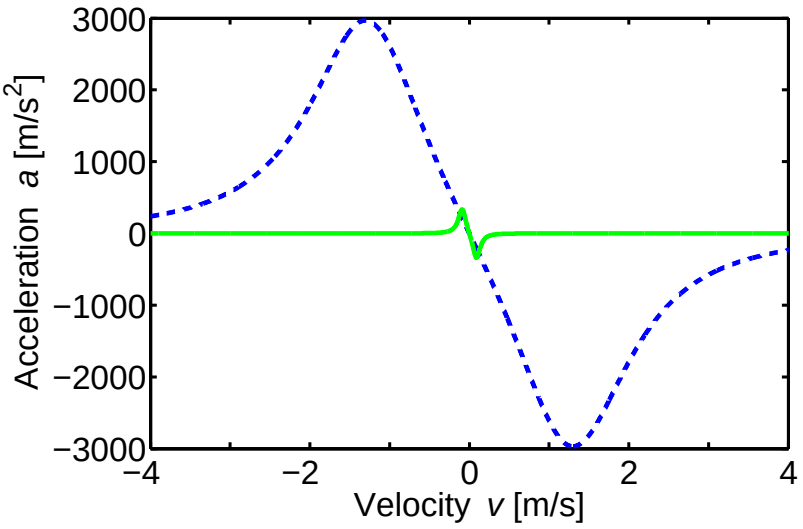

Figure 6-3: Calculated velocity dependence of the light-induced acceleration due to the singlet (blue dashed line) and triplet (green solid line) transitions (Cited from [9]): parameters were set as $\Delta_s = -0.7\Gamma_s$, $\Delta_t = -5.5\Gamma_t$, $I_s = 0.043 I_{sat,s}$, and $I_t = 27 I_{sat,t}$.

Fig. 6-4 shows potential depth for the $^1S_0 \rightarrow ^1P_1$ transition MOT and the $^1S_0 \rightarrow ^3P_1$ transition MOT. As expected from a broader linewidth, the $^1S_0 \rightarrow ^1P_1$ transition MOT has deeper trapping potential at large magnetic field gradient, but at lower magnetic field gradients of a few G/cm, the $^1S_0 \rightarrow ^3P_1$ transition MOT has deeper trapping potential. There are two important points here. One is that the potential depth by the $^1S_0 \rightarrow ^3P_1$ transition light is deeper than the Doppler limit temperature of the

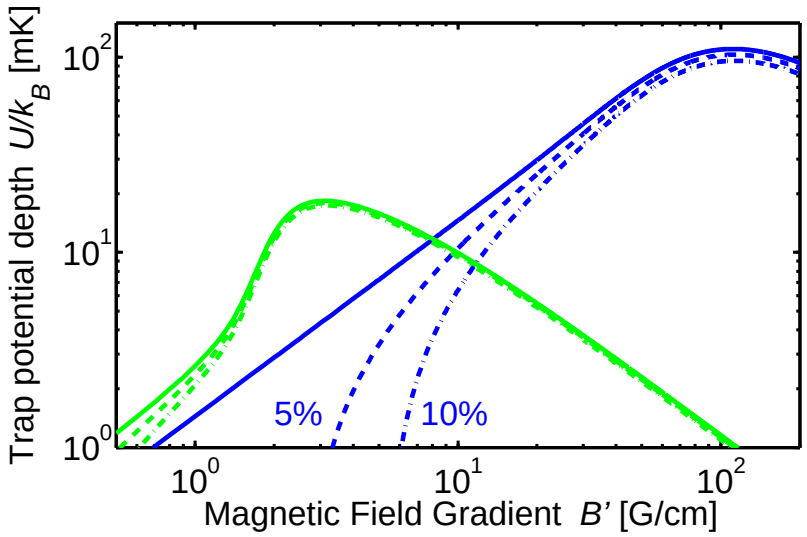

Figure 6-4: Calculated trapping potential depth for atoms at rest in the singlet MOT (blue lines) and the triplet MOT (green lines) versus B' (Cited from [9]): the solid lines, dashed lines, and dash-dotted lines are for an ideal MOT, and power imbalances of 5%, and 10% between the counter-propagating beams, respectively. Parameters were set as $\Delta_s = -0.7\Gamma_s$, $\Delta_t = -5.5\Gamma_t$, $I_s = 0.043 I_{sat,s}$, $I_t = 27 I_{sat,t}$, and beam size 1 cm.

$^1S_0 \rightarrow ^1P_1$ transition. This means that the atoms can be trapped by the $^1S_0 \rightarrow ^3P_1$ transition MOT even with the $^1S_0 \rightarrow ^1P_1$ transition light coexisting. Second thing is that the $^1S_0 \rightarrow ^3 P_1$ transition MOT is more robust against power imbalance than the $^1S_0 \rightarrow ^1P_1$ transition MOT, particularly at low magnetic field gradients. This is particularly important to our system, where we use a mirror MOT that has a certain phase shift at a reflection on the mirror, and the retroreflected beam does not have the same polarization purity as the incoming beam, which results in power imbalance.

To see how well TCMOT works, we perform some experiments. The experiments are performed before we put cavity structure in the chamber, so the MOT is not a mirror MOT but a standard MOT with 6 beams sent from outside of the chamber, which enables us to generate a magnetic field gradient as large as 50 G/cm. In the most experiments, we use ^{174}Yb, though we confirm that ^{171}Yb is also trapped in a TCMOT. Typical detuning for the 399 nm and 556 nm lasers, which correspond to the $^1S_0 \rightarrow ^1P_1$ transition and the $^1S_0 \rightarrow ^3P_1$ transition, respectively, is $\Delta_s = -0.7\Gamma_s$ and

$\Delta_t = -3.7\Gamma_t$, respectively. The beam intensity defined as the sum of six MOT beams are $I_s = 0.26 I_{sat,s}$ and $I_t = 160 I_{sat,t}$ for the 399 and 556 nm light respectively. We also send a longitudinal cooling beam counterpropagating to the atomic beam, whose power and detuning is $P_{CP} = 3$ mW and $\Delta_{CP} = -4.6\Gamma_s$. Atom number and the RMS radius of the cloud of trapped atoms are obtained from images taken by two Baumer Cameras. Atom number is calculated based on a transition rate, detuning from a resonance, and solid angle coverage, and the RMS radius is calculated from spatial distribution. Loading rate is measured by an APD. The measurement is performed by loading atoms to a TCMOT to the steady state, taking an image of a TCMOT, turning off 399 nm light, and taking a photo of a $^1S_0 \rightarrow ^3P_1$ transition MOT. Atom number counting is always done by atoms in this the $^1S_0 \rightarrow ^3P_1$ transition MOT, because it is difficult to estimate what kind of suppression of the scattering of each transition happens when two lights that are resonant on two different transitions are shined onto atoms. Error bars on graphs correspond to a standard deviation of five measurements.

Fig. 6-5 shows an experimental comparison bewteen the $^1S_0 \rightarrow ^1P_1$ transition MOT and the TCMOT. Our $^1S_0 \rightarrow ^1P_1$ transition MOT has maximum atom number of 4.0×10^5 at a relatively low magnetic field gradient of 13.5 G/cm, compared to a typical magnetic field gradient for the $^1S_0 \rightarrow ^1P_1$ transition MOT of 45 G/cm. This presumably is due to a good adjustment of the retroreflection, circular polarization, and beam intensity of the 399 nm light. At a magnetic field gradient lower than 13.5 G/cm, atom number in the MOT decreases quickly, and we did not see any atoms in the MOT below 6 G/cm. The TCMOT, on the other hand, had the largest atom number of 1.5×10^5 atoms at 6.75 G/cm, which is a bit smaller than that of $^1S_0 \rightarrow ^1P_1$ transition MOT at 13.5 G/cm, but still comparable amount. In addition, finite number of atoms are trapped at as small magnetic field gradient as 2 G/cm. The loading rate of TCMOT is comparable to the $^1S_0 \rightarrow ^1P_1$ transition MOT in Fig. 6-5. Relatively small atom number in our system is due to a small loading rate, and with a help of a Zeeman slower, it is expected to have comparable number of atoms trapped in the MOTs in other reports [137, 138].

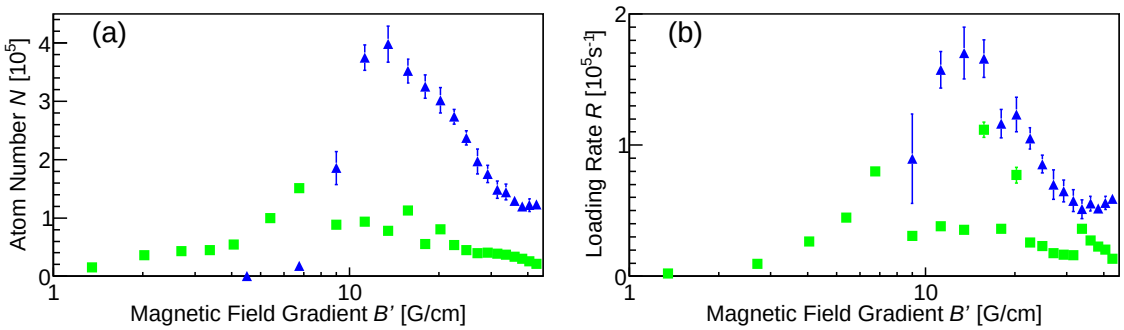

Figure 6-5: Comparison of the atom number (a) and the loading rate (b) in the singlet MOT (blue triangles) and the TCMOT (green squares) as a function of quadrupole field gradient B' (Cited from [9]): for $B' \leq 6$ G/cm, the singlet MOT does not trap any atoms. Other parameters were $\Delta_s = -0.7\Gamma_s$, $\Delta_t = -3.7\Gamma_t$, $I_s = 0.26I_{sat,s}$, and $I_t = 160I_{sat,t}$. We believe that major source of the error bar is the frequency instability of 399 nm laser.

Detailed properties of the TCMOT are shown in Fig. 6-6. These data is taken at the best magnetic field gradient of 6.75 G/cm, and tell us what values to choose for each parameter. Detunings of the 399 nm laser and the 556 nm laser should be around $-0.7\Gamma_s \simeq 20$ MHz and $-22\Gamma_t \simeq 4.0$ MHz, respectively. Atom number saturates at intensities around $0.2I_{sat,s}$ and $100I_{sat,t}$ for the 399 nm laser and the 556 nm laser, respectively. We observed finite number of atoms when we turned off the 399 nm laser, which proves that there are a few atoms that are below the capture velocity of the $^1S_0 \rightarrow ^3P_1$ transition MOT even without a Zeeman slower in an atomic beam. Temperature of the TCMOT is 1 mK, which is slightly above the Doppler limit of the $^1S_0 \rightarrow ^1P_1$ transition MOT.

To show our intuitive explanation of molasses by the $^1S_0 \rightarrow ^1P_1$ transition and a trapping potential by the $^1S_0 \rightarrow ^3P_1$ transition is correct, we make a MOT with different conditions, which are summarized in Table 6.4. First, we compare half power TCMOT and full power MOT that has the 399 nm laser and the 556 nm laser alternately turning on and off at 25 kHz frequency. We trap comparable number of atoms, and this shows that the enhancement of atom trapping in TCMOT compared to the $^1S_0 \rightarrow ^1P_1$ transition MOT is not due to a nonlinear effect of two lasers but their independent effects combined. Another test is to compare a TCMOT where the

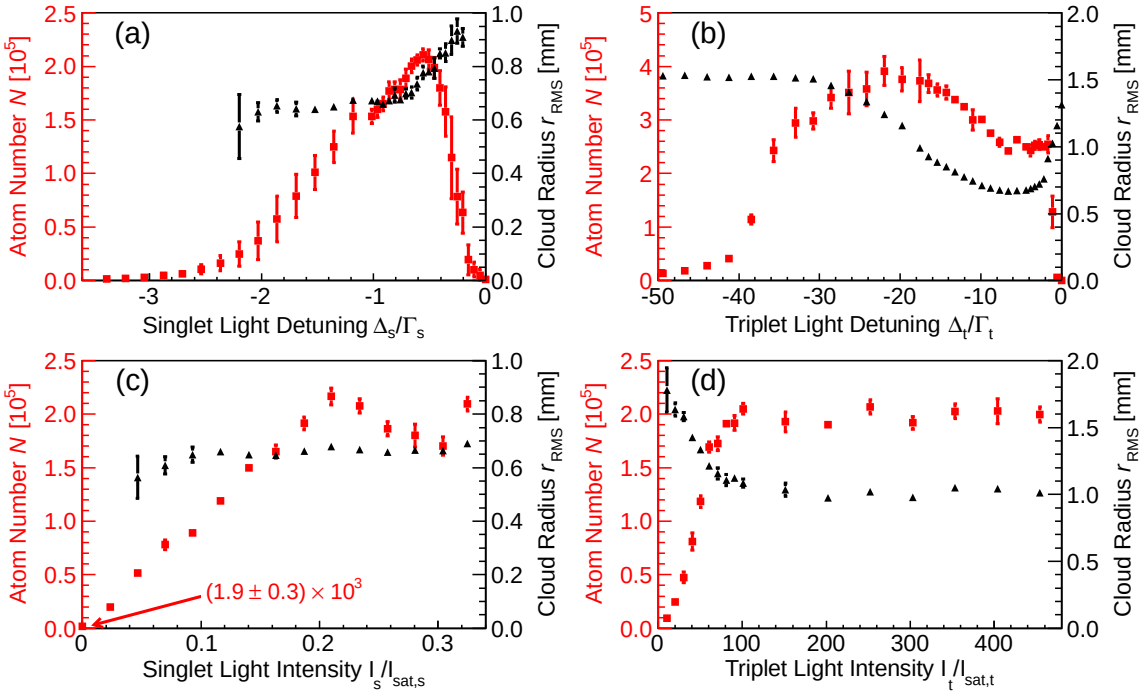

Figure 6-6: Characterization of the TCMOT (Cited from [9]): atom number N (red squares) and RMS cloud size r_{RMS} (black triangles) are plotted against (a) Δ_{s}, (b) Δ_{t}, (c) I_{s}, and (d)I_{t}. We varied only one parameter for each graph, shown on the horizontal axis. Fixed parameters were $\Delta_{\mathrm{s}} = -0.7\Gamma_{\mathrm{s}}$, $\Delta_{\mathrm{t}} = -3.7\Gamma_{\mathrm{t}}$, $I_{\mathrm{s}} = 0.26I_{\mathrm{sat,s}}$, $I_{\mathrm{t}} = 160I_{\mathrm{sat,t}}$, and $B' = 6.75$ G/cm. We believe that major source of the error bar is the frequency instability of 399 nm laser.

center of the 399 nm laser is blocked, a pure ${}^1S_0 \rightarrow {}^3P_1$ transition MOT, and a pure ${}^1S_0 \rightarrow {}^1P_1$ transition MOT. The number of atoms trapped in the blocked TCMOT is in the same order of magnitude as 1/2 power TCMOT, whereas it is an order of magnitude larger than the pure ${}^1S_0 \rightarrow {}^3P_1$ transition MOT and the pure ${}^1S_0 \rightarrow {}^1P_1$ transition MOT. This shows that the trapping potential is made by the ${}^1S_0 \rightarrow {}^3P_1$ transition, as there are no light force in the middle where 399 nm light is blocked, and the enhancement compared to the ${}^1S_0 \rightarrow {}^3P_1$ transition MOT happened with the 399 nm light only on the outskirt of MOT. Note that this configuration is the same as that of a core-shell MOT [138] except that we did not have any frequency broadening for 556 nm laser. These results show that the TCMOT is achieved indeed by the effect of the ${}^1S_0 \rightarrow {}^1P_1$ transition working as molasses and the ${}^1S_0 \rightarrow {}^3P_1$ transition making a trapping potential.

Table 6.4: N and r_{RMS} in the MOT in different conditions. Parameters are fixed at $\Delta_{\mathrm{s}} = -0.7\Gamma_{\mathrm{s}}$, $\Delta_{\mathrm{t}} = -3.7\Gamma_{\mathrm{t}}$, $I_{\mathrm{s}} = 0.26 I_{\mathrm{sat,s}}$, $I_{\mathrm{t}} = 160 I_{\mathrm{sat,t}}$, and $B' = 6.75$ G/cm. The errors shown are statistical errors; systematic errors are estimated to be 10%.

Condition	N ($\times 10^3$)	r_{RMS} [mm]
Full power TCMOT	243 ± 10	0.69 ± 0.01
1/2 power TCMOT	60 ± 8	0.69 ± 0.01
25 kHz singlet/triplet switching	25 ± 3	0.80 ± 0.09
Pure singlet MOT	5.4 ± 0.7	2.04 ± 0.03
Pure triplet MOT	1.1 ± 0.2	0.61 ± 0.02
Blocked TCMOT	16 ± 1	0.67 ± 0.01

There are some applications for the TCMOT. The criterion if the TCMOT works for other atomic species is whether the Doppler limited temperature of the broad transition MOT $k_B T_s \sim \hbar\Gamma_s$ is lower than the potential depth of narrow transition MOT $U_t \sim \Gamma_t^{3/2}$.[2] Checking this ratio in ytterbium, we get the lower bound of $\Gamma_t/(2\pi))$ to be 35 kHz, which gives $\Gamma_{\mathrm{s}}/\Gamma_{\mathrm{t}} \sim 800$. This number suggests that TCMOTs can be useful for cadmium [139], dysprosium [140, 141], erbium [142], and thulium [143, 144]. Regarding the technique, the original motivation was to have a MOT with a low magnetic field gradient, but this means that a large power is not necessary to keep the current on the MOT coil. This is useful when electrical power is limited, such as on a satellite or in a portable system. Also, small magnetic field gives less magnetization of the structure surrounding atoms, which leads to the smaller amount of uncertainty in Zeeman shift.

6.3 Mirror MOT

After we established the technique to make a TCMOT, we inserted cavity structure and obtained a TCMOT with mirror MOT configuration. We first found a MOT with ^{174}Yb, which has the largest natural abundance, and then changed parameters for ^{171}Yb. Following parameters are for ^{171}Yb. [3]

[2] This is derived as the force scales as Γ_t and the spatial range over which the transition is near resonant scales as $\Gamma_t^{1/2}$ because the saturation-broadened linewidth scales as $\Gamma_t^{1/2}$, assuming a constant laser intensity.

[3] As this is a summary of what we achieved, only the result is written and it looks quite easy to achieve a mirror MOT. However, it took a quite while to find the first mirror MOT. First of all,

Our mirror MOT is a combination of a standard mirror MOT and a TCMOT. Configuration of optics and cameras are described in Section 4.7 and 4.6. We typically send 18 mW of 399 nm light and 5.5 mW of 556 nm light, which corresponds to an intensity of $0.40 I_{\mathrm{sat,s}}$ and $51 I_{\mathrm{sat,t}}$, respectively.[4] Detunings of the lasers are $\Delta_{\mathrm{s}} = -0.7\Gamma_{\mathrm{s}} \simeq 20$ MHz, and $-38\Gamma_{\mathrm{t}} \simeq 7.0$ MHz. The power of the longitudinal cooling beam is 1.8 mW, and the magnetic field gradient is 9 G/cm. With this, we first generate a TCMOT, and transfer the atoms into a ${}^1S_0 \rightarrow {}^3P_1$ transition MOT by turning off the 399 nm light. Typical atom number trapped in the ${}^1S_0 \rightarrow {}^3P_1$ transition MOT is 10^4, and its lifetime is 3 s, limited by the background gas collisions.

The temperature and the size of the MOT are measured by absorption imaging with the 1 to 1 magnification Baumer camera. Fig. 6-7 shows the temperature and the cloud size of a green MOT for different combinations of the detuning and intensity of 556 nm laser. From this we set a detuning of 200 kHz and an intensity of 10 $I_{\mathrm{sat,t}}$ as the optimal parameters.

The distance of the green MOT from the mirror is measured by tilting the 1:2.2 magnification Baumer camera. With a certain tilt ($\sim$ 15 degrees), a reflected image of the MOT on the mirror is observed in the camera when the MOT is close enough to the mirror. With the camera magnification and the size of CCD pixels, the distance between the MOT and the mirror is calculated to be the half of the distance of the real and reflected image of the MOT. We measure atom lifetime at different MOT distances from the mirror. The lifetime is measured by taking many photos in a single

---

you need to be sure that you are sure that you have correct laser frequencies. It is more difficult for a TCMOT than a standard single color MOT, because you need to tune two lasers to correct frequencies. In our case, 399 nm laser was easy to tune, because we saw the fluorescence of the atomic beam by the laser on a camera. Regarding 556 nm laser, we had to rely on the stability of the ultrastable cavity, and to assume that ω_{bridge} did not change before and after the installation of the experimental cavity. After that, we tested various parameters, such as polarization, overlap of the atomic beam and the MOT region, and bias field, but what was most important was after all increasing the magnetic field gradient. We used two power supplies in parallel, sending 160 A current, whereas the current we need to get 9 G/cm is 115 A, and found the first sign of a ${}^1S_0 \rightarrow {}^1P_1$ transition MOT. After that, we searched the resonance of the ${}^1S_0 \rightarrow {}^3P_1$ transition in the ${}^1S_0 \rightarrow {}^1P_1$ transition MOT, and eventually we got a TCMOT. The lesson is that even you want to use the TCMOT, you need to have large enough magnetic field to generate a broad transition MOT at the beginning, and once you find a TCMOT, you can safely operate it with a low magnetic field gradient.

[4] Here, the beam size of two MOT beam is assumed to be 1 cm in diameter.

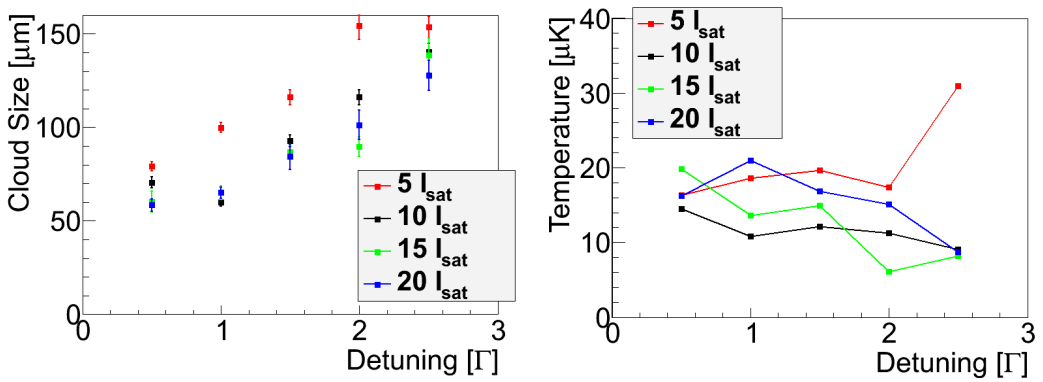

(a) Cloud size (b) Temperature

Figure 6-7: Cloud size and Temperature of the green MOT in mirror MOT configuration with different detuning and intensity: $\Gamma = 184$ kHz, and detuning is to the lower frequency compared to the atomic resonance.

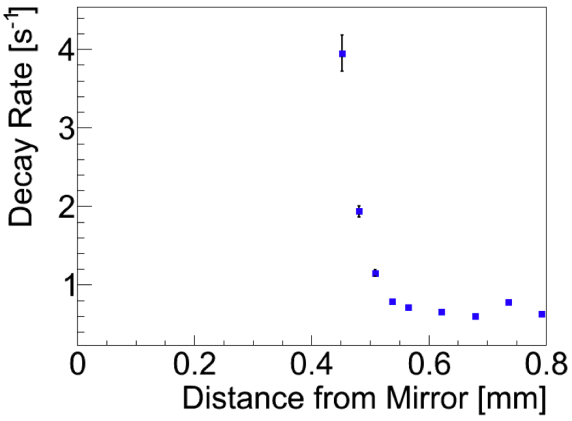

Figure 6-8: Decay rate of the MOT with different distance from mirror

run, and extracting total fluorescence from the MOT in each photo. The fluorescence is fitted by exponential function. Fig. 6-8 shows how green MOT lifetime changes according to the distance from the mirror. The decay rate increases at 0.5 mm away from the mirror, and decay is too fast to observe at 0.4 mm. This is reasonably consistent with [145], which becomes a double check of the validity of the MOT distance measurement by the camera.

6.4 Loading sequence to the optical lattice

To find an overlap of atoms and the cavity mode, we trap atoms in the ${}^1S_0 \rightarrow {}^3P_1$ transition MOT, and lock the experimental cavity resonant to probe laser of a frequency same as the MOT laser. We send a strong probe laser, move the MOT around and find a position where the MOT lifetime gets significantly shorter than other places. This is the position where the cavity light kicks atoms out of the MOT. Next, we turn off the probe light, keeping the cavity resonant to the MOT laser frequency. If the MOT overlaps the cavity mode, scattering from the MOT beam to the cavity mode happens, and a single-photon counter located at the output detects the scattered photons. Once we find this overlap, we tune the magnetic field around, and try to find the best position based on the scattering into the cavity. Typical signal is shown in Fig. 6-9. The feature is at the largest overlap, vacuum Rabi splitting is so large that the scattering into the cavity is suppressed. After figuring out this position, we move onto the off resonant probing with typically -10 MHz detuning (see Section 7.1.1) to see the cavity resonant frequency shift by the atoms. At this point, a finite number of atoms overlaps with the cavity mode, and moving the MOT around by tuning bias magnetic field provides fine alignment of the cavity mode and the MOT. Relative alignment does not change unless background magnetic field changes.

The lattice loading sequence is summarized in Fig. 6-10. At least 5 s is spent for loading the TCMOT prior to the start of the sequence shown in Fig. 6-10. We first gradually turn off the 399 nm laser, shifting bias magnetic field from the number for the TCMOT to the ${}^1S_0 \rightarrow {}^3P_1$ transition MOT. Note that we need to tune the longitudinal magnetic field regarding the cavity axis to tune the axial position of the MOT because of the tilted quadrupole field. Next, we tune 556 nm laser frequency up to $-1.1\Gamma_t$. Then we reduce the 556 nm laser intensity. After we wait for a while for the MOT to be thermalized, we move the MOT from far from the mirror to the point where we load atoms into the lattice. In the last 20 ms, we reduce 556 nm laser power further, in addition to making the detuning larger by another $1.1\Gamma_t$. This last 20 ms step is crucial for an efficient lattice loading, because the AC Stark shift by 759 nm

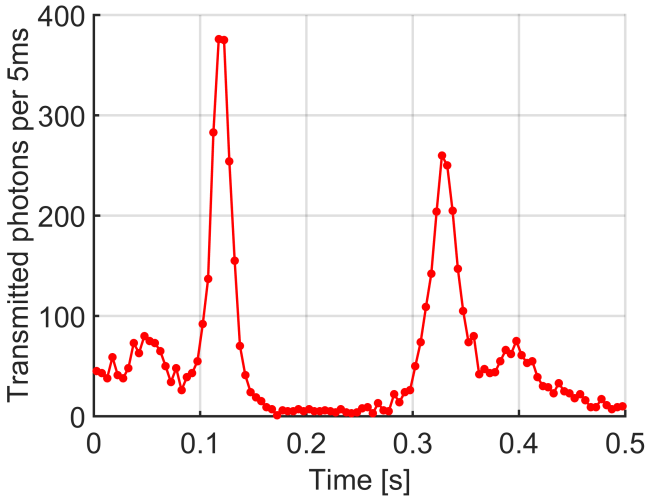

Figure 6-9: Scattering rate to experimental cavity from MOT atoms when atoms scan over cavity mode

light is larger for the $^3P_1$ state than for the ground state, and the optimal detuning for the MOT compression actually is blue detuned for atoms that overlap with the lattice. Thus, we need to cool those atoms down in the last moment. Quadrupole magnetic field is kept constant over all the time.

After we turn off the 556 nm laser instantaneously, we ramp the quadrupole magnetic field and radial bias field B_x, B_y to zero, and axial magnetic field B_z to a specific value, such as 7.1 G over 20 ms. This ramping time is finite because suddenly turning off the MOT coil kicks the cavity structure, and we have $\sim$ 100 ms of dark time of the transmission of probe beam through the experimental cavity.

6.5 Optical lattice properties

As described in Chapter 4, an optical lattice is made by the 759 nm magic wavelength along the cavity mode. Since the experimental cavity has a factor of 1000 enhancement in the trap laser power, we only need to send 6.7 mW to get 1.1 W intracavity power.[5] Loading of atoms into optical lattice is described in Section 6.4. The point related to the properties of the optical lattice is that we tune the x direction bias

[5]The coupling efficiency to TEM_{00} mode of the experimental cavity is not 100 %.

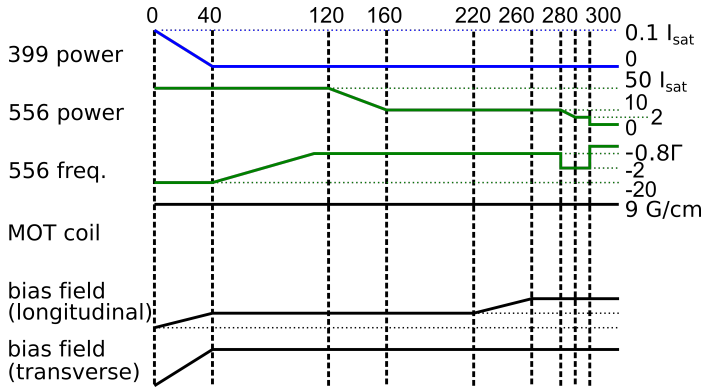

Figure 6-10: Sequence for loading atoms into optical lattice.

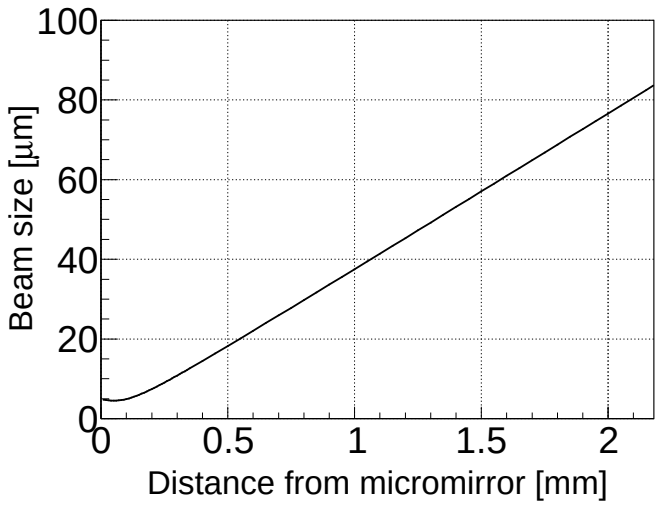

Figure 6-11: Beam size of one dimensional optical lattice against the distance from micromirror

magnetic field to tune the atom position along the one dimensional lattice along the experimental cavity axis.

The beam size of the optical lattice changes against the distance from the micromirror as shown in Fig. 6-11. As the green MOT size is 50 μm in radius, the MOT is larger than the optical lattice when atoms are 1.3 mm or less apart from the micromirror.

The trapping frequency of the lattice is measured by modulating the lattice power by modulating the RF power going into an AOM in the path from 759 nm slave laser to experimental cavity. When the modulation frequency of the lattice power matches

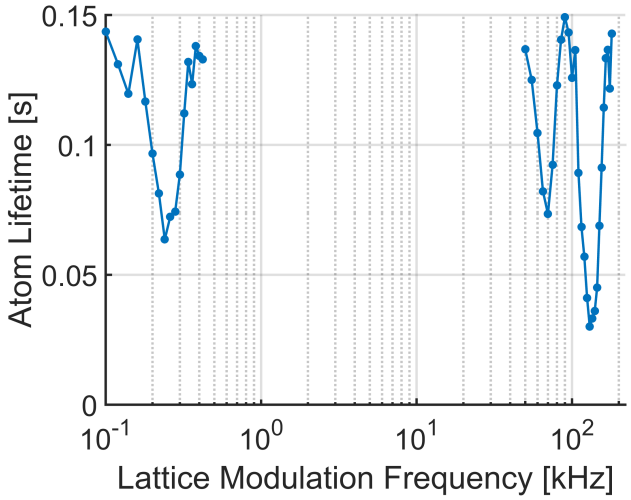

Figure 6-12: Atom lifetime in optical lattice against different modulation frequencies of intracavity power: the high frequency dip of doublet is twice the trapping frequency. The low frequency one is there because the modulation of the AOM diffraction was not purely sinusoidal, and therefore we had higher harmonics components.

twice the trapping frequency, atoms are parametrically heated in side the lattice and the lifetime decreases, according to the following formula [124].

$$\Gamma = \frac{1}{T} = \pi^2 \nu^2 S(2\nu) \tag{6.3}$$

The measurement is performed with atoms 1.99 mm away from the micromirror. Lifetime measurement is performed with the off resonant probe (see Section 7.1.1 for the detailed method), and lifetime is estimated by fitting the atom number decay by an exponential function. Fig. 6-12 shows the result, and this suggests a trapping frequency of 125 ± 5 Hz (radial) and 67 ± 2 kHz (axial) for 1.11 W intracavity power.

Because of the parametric heating effect by Eq. 6.3, atom lifetime in the lattice is limited by the intensity fluctuation of the intracavity light. Because our cavity linewidth is 1.9 MHz, which is larger than a typical trapping frequency of 100 kHz, the cavity does not work as a tool to remove the intensity noise. Rather, its relatively narrow resonant peak converts frequency fluctuation to power fluctuation, and

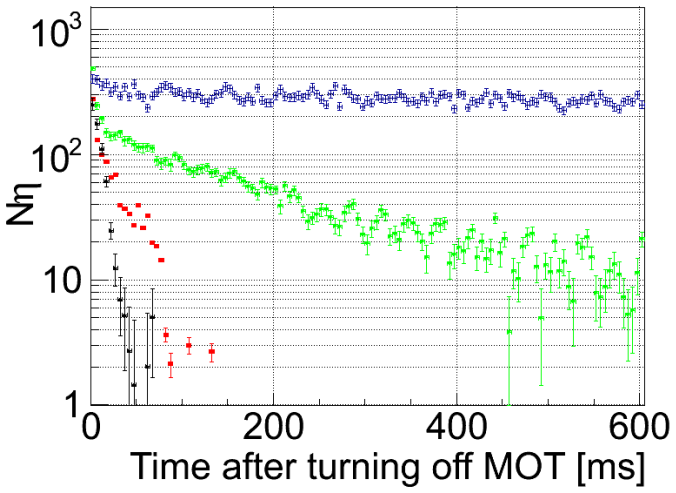

Figure 6-13: Atom lifetime with different stabilizations: black: initial trapping $\tau = 7.7 \pm 0.5$ ms, red: with last 20 ms cooling $\tau = 32.1 \pm 0.2$ ms, green: first atom trap $\tau = 188.9 \pm 1.7$ ms, blue: current best $\tau = 2951 \pm 89$ ms

therefore frequency stabilization is crucial for long atom lifetime in the optical lattice. This is the reason why we put a large amount of effort on stabilizing the 759 nm laser frequency (see Section 5.4, and intensity feedback for experimental cavity (see Section 4.3.4). Fig. 6-13 summarizes the lifetime of atoms in the optical lattice with different level of stabilization. Typically, we have around 1 s lifetime unless the probe light is too strong.

According to Eq. 6.3, the lifetime can change simply by changing the intracavity power, as this changes the trapping frequency of the lattice. We confirmed that the atom lifetime changes more or less in an expected way when we change the lattice depth, as shown in Fig. 6-14. At 100 kHz or more trapping frequency, measured lifetime has a reasonable match with th expected lifetime. Deviation at low frequency should be due to the too shallow lattice to trap atoms.

6.6 A MOT with high magnetic field gradient

All the properties of the MOT described so far is for 9.2 G/cm magnetic field gradient by 115 A current on the MOT coil. As described in Section 4.5.1, the magnetic field

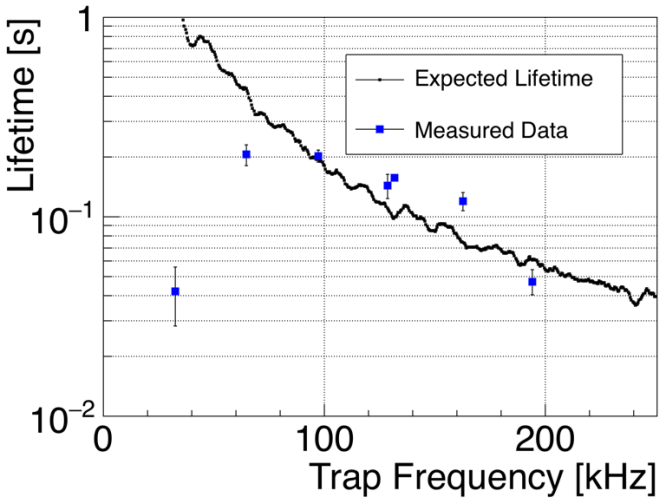

Figure 6-14: Expected (black) and measured (blue) atom lifetime in the optical lattice: expected lifetime is calculated from the spectral intensity noise of the 759 nm transmission through experimental cavity

gradient can be increased up to 14.4 G/cm by a higher current (180 A) on the MOT coil. Even with this configuration, the sequence to load atoms into the lattice is the same: the TCMOT, the green MOT, the last 20 ms cooling, and turning off the magnetic field. The difference is the time to turn off the MOT coil, lattice intensity, and optimal detuning for the 556 nm laser. It takes longer time to turn off the MOT coil, because when the slope of the current on the MOT coil goes beyond certain threshold, there appears long lasting $\approx$ 100 Hz oscillation in cavity resonant frequency. In the case of 180 A current, it turns down by 10.5 A in first 8 ms, 33.9 A in the next 10 ms, 101.6 A in the next 20 ms and 33.9 A to zero in the last 10 ms, where as in 115 A case we linearly turn it down to zero in 20 ms.

The optimal loading parameters for 9.2 G/cm and 14.4 G/cm magnetic field gradients are summarized in Table 6.5. When the magnetic field gradient B' is large, atom number increases by a factor of two or three at the same MOT position. Higher B' confines atoms tighter, and this allows loading to closer to the mirror. We observed twice as many initial $N\eta$ at 0.5 mm away from the mirror as 0.9 mm away. Here, we needed more trap laser intensity than 0.9 mm away case, and resulting atom lifetime is shorter. Even the loading to 0.25 mm away is observed, with estimated initial $N\eta$

of ~ 7000. At this position, average cooperativity η is 7.9, believing the number in Section 7.6. Based on this result, we guess that with $B' = 14.4$ G/cm, we have a MOT size smaller than cavity mode at all the distance down to 0.25 mm, and number of atoms loaded into the optical lattice is the same. The increase in $N\eta$ is due to the increase in η.

Table 6.5: Parameters and atom behaviors in different MOT magnetic field gradient B' and distance from micromirror d: note that the data on 0.25 mm away is not the optimized parameters but parameters when we observed this. I is intensity and P is power.

B' [G/cm]	d [mm]	green MOT		last 20 ms cooling		Trap laser		Initial $N\eta$	lifetime τ
		I/I_{sat}	$\Delta_{\mathrm{t}}/\Gamma$	I/I_{sat}	$\Delta_{\mathrm{t}}/\Gamma$	P [mW]	I [kW/cm^2]		[s]
9.2	2.0	10	-1.1	2	-2.2	6.7	6.2	500	1
9.2	0.9	10	-1.1	10	-2.2	6.7	29	500	1
14.4	0.9	10	-2.7	10	-3.3	6.7	29	1000	1
14.4	0.5	10	-2.2	10	-2.2	11	199	2000	0.24
14.4	0.25	10	-2.2	10	-3.3	5.7	298	7000	0.21

Chapter 7

Cavity QED experiments

This chapter describes experiments that lead to spin squeezing of ^{171}Yb ground state Zeeman sublevels. First I describe four different kinds of atom number counting we use to perform various measurements. All are methods to count the population of a specific spin state of the ground state. Next, I go through all the procedures to double check if the system works well, such as state preparation, Rabi and Ramsey spectroscopy, and noise estimates on atom number counting. In the end I describe our results on spin squeezing.

7.1 Measurement methods

The energy levels we use are shown in Fig. 7-1. We are interested in the ground state nuclear spin of ^{171}Yb. Since the magnetic moment is 1/2, we have two Zeeman sublevels, and the Bloch sphere picture in the following discussion is that for this nuclear spin 1/2 state.

To detect this spin 1/2 state, we use the 556 nm laser that is near resonant to the $^1S_0 \rightarrow ^3P_1$ transition and the experimental cavity. The $^3P_1$ excited state has two hyperfine levels, $F = 3/2$ and $F = 1/2$. In ^{171}Yb case, the hyperfine splitting is 5936.671(100) MHz. Because we have the closed transition between $m = \pm 1/2$ in ground state and the $m = \pm 3/2$ excited state of the $F = 3/2$ hyperfine level, we use

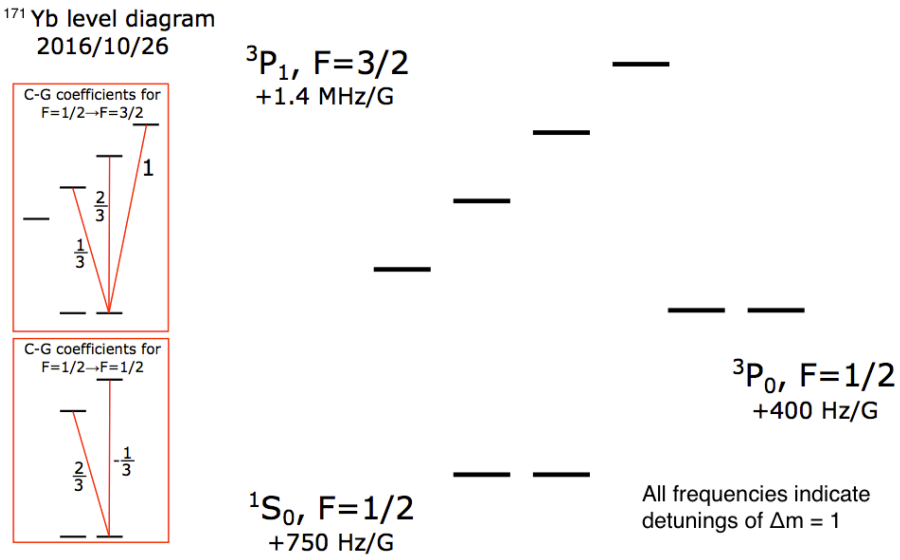

Figure 7-1: The system we used in the following experiments: Clebsch-Gordan coefficients and Zeeman shifts are summarized.

the $F = 3/2$ level for probing. [1]

We take the advantage of strong interactions between atoms and light enhanced by the experimental cavity that has high finesse at 556 nm. We have four different kinds of method. One is an off resonant probe, where a cavity resonance is far from the ${}^1S_0 \rightarrow {}^3P_1$ transition resonance. Three other methods use vacuum Rabi splitting when cavity resonance and atomic resonance of the ${}^1S_0 \rightarrow {}^3P_1$ transition are at the same frequency. One method is simply to scan the probe laser, which we call scan measurement. Another one is called chirp measurement, where we have two sidebands that are scanned from the bare atomic resonance to the blue and red directions in a symmetric way. The third one is a phase measurement-based on the chirp measurement. All the detections are done by a single photon counter into which transmitted 556 nm light goes (Fig. 7-2). The following subsections describe the details of each measurement scheme.

[1] Another technical reason would be that it is easier to use the same frequency as the laser used for ${}^1S_0 \rightarrow {}^3P_1$ transition MOT, not the one 6 GHz away.

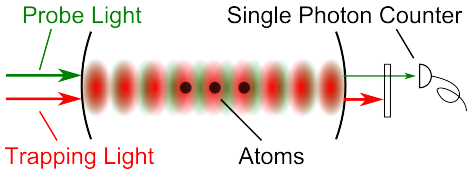

Figure 7-2: Setup for probing atom number

7.1.1 Off resonant probe

The off resonant probe uses the dispersive cavity resonance shift caused by the existence of atoms in the cavity mode. Eq. 3.15 shows the amount of the cavity resonance shift by atom number $N\eta$. Modifying this equation to

$$N\eta = \delta\omega_c \frac{4\delta}{\kappa\Gamma}, \tag{7.1}$$

we extract the atom number in the cavity mode. This measurement is non-destructive, in the sense that it does not kick atoms out of the lattice unless the probe light is too strong,[2] and therefore we can measure the atom number in the lattice continuously. This method is primarily used for adjustment of the MOT position to have the maximum overlap with the cavity mode, and lifetime measurement of atoms in the lattice. To have the same detuning of the cavity resonance from the atomic resonance for two spin states, we do not apply any magnetic field when performing this measurement. Thus, this measurement gives the atom number $N\eta$ as $(N_\uparrow + N_\downarrow/3)\eta$, due to the Clebsch-Gordan coefficients.

To extract the atom number precisely, we need to know four frequencies–$\delta\omega_c$, δ, κ, and Γ–precisely. The linewidth of the atomic transition Γ is known with less than 1 % precision from literature [71, 146], and we used 184 kHz, which is the latest measurement [71]. The cavity linewidth κ is measured by the ringdown finesse measurement with a precision less than 1 %. A typical number is 400 kHz, which corresponds to a finesse of 15000. Detuning of the probe light from the atomic transition δ is

[2] At the cooperativity $\eta = 0.6$ and photon detection rate of $\gtrsim 500$ kHz, we observe faster loss of atoms in the lattice, which is estimated to be due to the probe light kicking atoms out of lattice, but otherwise, there was no sign of atoms being disturbed by the probing.

easily extracted from the information about the RF frequency applied to the EOM to generate the probe beam. The fluctuation of this number is only due to that of VCO, which is typically 10 kHz out of the typical δ of 10 MHz. The number that requires careful measurement is $\delta\omega_c$, particularly because our cavity frequency drifts according to the frequency drift of the 759 nm laser due to the RAM in PDH lockings and the reference cavity performance. To calibrate $\delta\omega_c$, we turn on the 399 nm MOT beam to kick all the atoms out of the lattice at the end of off resonant probe sequence, followed by a scan of probe laser frequency over a cavity resonance. A comparison of the peak height of the scanned cavity resonance and an average of the amount of the transmission at the empty cavity gives a frequency detuning of the bare cavity from the probe beam, and comparison of the amount of the transmission relative to the peak height gives the atom number at each time.

Typical raw data are shown in Fig. 7-3. At $t = 0.4$ s, the MOT is turned off, and the atom number in the lattice starts to decay. According to Eq. 3.15, the cavity shift gets smaller, and the transmission gets larger. At the end, peak due to the calibration scan is shown. Converting this data into the atom number $N\eta$, we get Fig. 7-4. Typically, we use $\delta = -10$ MHz detuning, and this δ gives $\delta\omega_c = 920$ kHz$= 2.3\kappa$ for $N\eta = 500$. We set the photon counting rate of 1 MHz at a cavity resonance, and use 1 ms binning to get photon number of a few hundred in each bin. With this δ, we can resolve up to $N\eta \sim 1500$, and if we need to measure more $N\eta$, we increase δ. We typically fit this atom number decay with an exponential function and extract the atom lifetime in the lattice and the initial atom number.

7.1.2 Scan

The scan measurement and the following two measurements use vacuum Rabi splitting. As described in Section 3.1 and Eq. 3.14, the amount of vacuum Rabi splitting is proportional to the square root of $N\eta$, and therefore we can extract the atom number from the amount of vacuum Rabi splitting in the following way:

$$N\eta = \frac{4f^2}{\Gamma\kappa} \tag{7.2}$$

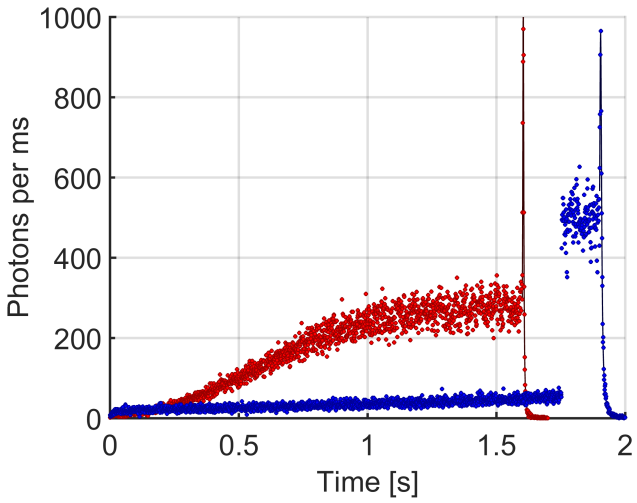

Figure 7-3: Raw data for the off resonant probing

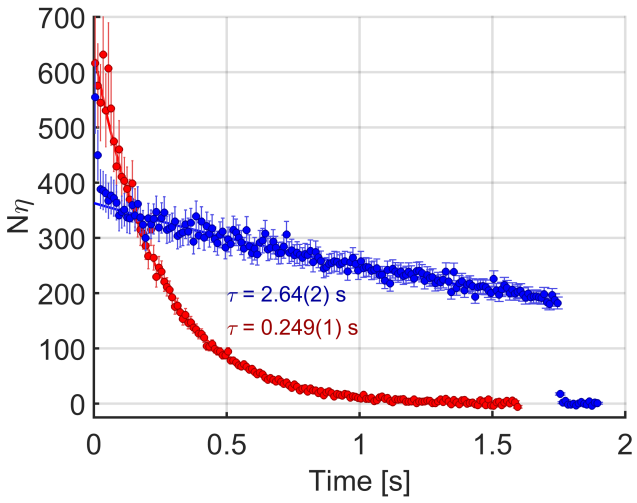

Figure 7-4: Atom number decay in the cavity mode derived from Fig. 7-3

The easiest way to see vacuum Rabi splitting is to scan the probe laser frequency linearly over the resonance, and see two resonant peaks. We call this measurement "scan measurement." We linearly ramp the voltage of the VCO that drives the EOM for the probe light, and scan the probe light frequency. Acquired data is the time dependent transmission. We use calibration information on the VCO voltage to frequency conversion to change the time information to frequency, as the VCO output frequency is slightly nonlinear to the input voltage.

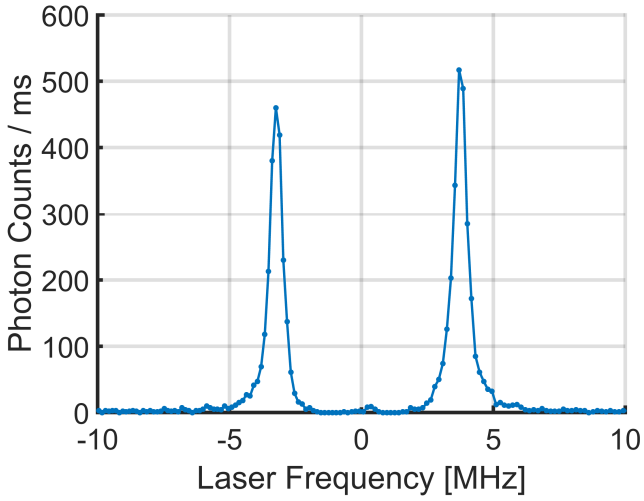

Figure 7-5: Typical signal by scan measurement

To separate Zeeman sublevels of the $^3P_1$ excited state by a larger amount than the vacuum Rabi splitting, a bias magnetic field in $+z$ direction is applied. We typically apply 7.1 G, which generates a 10 MHz frequency shift between two adjacent Zeeman sublevels. Because of a difficulty in tuning the cavity resonant frequency quickly, we fix the cavity frequency in an experimental sequence. To measure the atom number in the $m_z = 1/2$ state in the ground state, we use +15 MHz detuning of the cavity resonance frequency from the atomic resonance frequency of the $^1S_0 \rightarrow ^3P_1$ transition without any magnetic field, and a σ^+ polarization light. For measuring the atom number in the $m_z = -1/2$ state, we use -15 MHz detuning of the cavity frequency, and a σ^- polarization probe light.

A typical transmission signal whose x axis is converted into a frequency unit is shown in Fig. 7-5. We spend 20 ms to scan over 20 MHz. From this we convert the frequency splitting to the atom number. We fit this with Eq. 3.10 multiplied by a normalization factor. A typical number with $\Gamma = 184$ kHz, $\kappa = 400$ kHz, and $N\eta = 1000$ gives 8.58 MHz vacuum Rabi splitting. A single scan gives one piece of information on the atom number, and the uncertainty of the atom number comes from the uncertainty of the fitting. Also, the cavity resonant frequency fluctuation during two peaks and atom loss due to the probe add uncertainty.

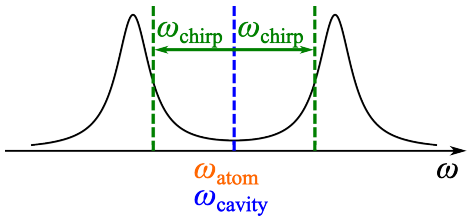

Figure 7-6: Concept of the chirp measurement in the frequency space

7.1.3 Chirp measurement

The scan measurement has an advantage of being conceptually easy, and robust against the cavity frequency drift. However, because of the time difference of a few ms between two peaks, it is affected by a fast cavity frequency change due to mechanical vibrations that cannot be suppressed by locking. To solve this problem, we use another measurement scheme called chirp measurement. The idea of chirp measurement is to have two probe beam frequencies scanning over the two vacuum Rabi splitting peaks at the same time in opposite directions, as shown in Fig. 7-6. Because the fluctuation of the resonant frequency of the vacuum Rabi splitting peaks due to the cavity frequency fluctuation is a common mode, scanning over them at the same time in the opposite directions cancels the fast fluctuation. In addition, the effect of change in atom number or the frequency shift of the cavity over the few ms in the scan measurement is removed, thanks to the simultaneous scanning over two peaks.

To generate these sideband frequencies of $\omega_{\text{p}} \pm \omega_{\text{chirp}}$, we mix an RF signal of ω_{chirp} with a VCO signal driving the EOM for the probe beam, and chirp ω_{chirp}. The signal obtained by the single photon counter is shown in Fig. 7-7. The peak position derived from this data is f in Eq. 3.14, and we get $N\eta$ from Eq. 7.2. We typically perform a single measurement in 1 ms, with ~ 100 and ~ 40 photons transmitted in a chirp for measurement-based squeezing and cavity feedback squeezing, respectively, and perform this again and again if we need a large number of photons for a precise measurement of the atom number.

To have a precise peak frequency estimate, we perform a single parameter maxi-

mum likelihood fitting with a Lorentzian function. Typically, the Lorentzian function has three parameters of center ω_0, peak height AN_γ, where N_γ is the number of detected photons, and width γ, as shown in Eq. 7.3

$$f(\omega) = \frac{A}{1 + (2(\omega - \omega_0)/\gamma)^2} \tag{7.3}$$

To reduce the number of parameters, we use the average of cavity and atomic resonance width $\gamma = (\Gamma + \kappa)/2$ as the linewidth γ, and peak height per photon A is estimated by a Lorentzian fit we did in advance with a large detected photon number. Then the function $f(\omega)$ has a single parameter of ω_0 to be estimated.

The crucial part of this chirp measurement is whether the atomic resonance ω_{at} and the cavity resonance ω_{c} are precisely the same. If these frequencies are different, we see two peaks at slightly different frequencies, because we set the probe laser frequency relative to ω_{at}, whereas the vacuum Rabi splitting resonance shifts according to the shift of ω_{c}. Because we do a single parameter fit for the peak position search, the frequency difference of the peaks more than a FWHM of the Lorentzian resonance $(\kappa + \Gamma)/2$ deteriorates the quality of fitting significantly. To avoid this, we first run 100 scan measurements to see the frequency difference between the cavity resonance and the atomic resonance. This frequency difference is obtained by fitting each scan to Eq. 3.10, and averaging 100 data. According to the frequency difference, we tune the cavity resonance frequency, and if necessary, run another 100 scan measurements to see if the frequency is modified in a good way. Next, we run chirp measurements with different probe frequency to see if the start frequency of the chirp ω_{p} matches $\omega_{\mathrm{at}} = \omega_{\mathrm{c}}$. Once the correct center frequency is obtained, the frequency calibration is performed by a two light pulses that are on the opposite slope of the cavity resonance. As the frequency that has largest drift is ω_{c}, when the amount of transmission photons by these two pulses gets imbalanced, we tune ω_{c} for the two pulses to have better balancing. [3]

[3]The majority of drift is monotonic drift of more than 10 MHz over a few hours during the oven running. It turned out that this is due to the change in thermal balance for experimental cavity by heat from MOT coil. Once this drift is removed, it is desired to have an upgrade of the reference cavity, and RAM stabilization for 759 nm laser locking and experimental cavity locking.

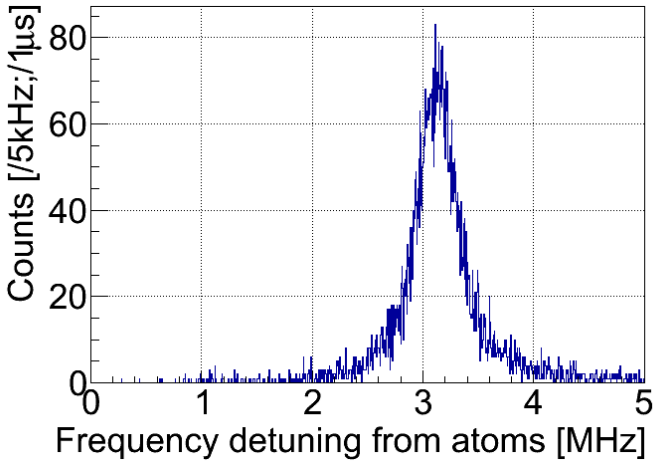

Figure 7-7: Typical signal of chirp measurement

7.1.4 Phase measurement

According to Eq. 3.16, the phase shift is an odd function of a detuning from $\omega_c = \omega_0$ (i.e. $\delta = \Delta$), and behaves as shown in Fig. 7-9. When $N\eta$ is large enough, the function is approximately an arctangent function whose origin is at two vacuum Rabi splitting peaks. The electric field of the transmitted light at the chirp measurement is calculated as

$$\begin{aligned} E &= E_0 \left(e^{i\left(kz - \left(\omega_\mathrm{p} + \omega_\mathrm{chirp}\right)t + \phi_\mathrm{ph}\right)} + e^{i\left(kz - \left(\omega_\mathrm{p} - \omega_\mathrm{chirp}\right)t - \phi_\mathrm{ph}\right)} \right) \\ &= E_0 e^{i(kz - \omega_\mathrm{p} t)} \left(e^{-i\left(\omega_\mathrm{chirp} t + \phi_\mathrm{ph}\right)} + e^{i\left(\omega_\mathrm{chirp} t + \phi_\mathrm{ph}\right)} \right). \end{aligned} \tag{7.4}$$

Therefore we obtain

$$P \propto \cos^2\left(\omega_\mathrm{chirp} t + \phi_\mathrm{ph}\right) \tag{7.5}$$

as the power. This means that we can extract phase information as a shift of the photon arrival time relative to the chirp frequency's phase reference, which is easily obtained by a function generator we use for the chirp (SRS DS345). We implemented this phase measurement in addition to the transmission peak measurement of the chirp measurement.

The raw data of the phase is shown in Fig. 7-8. The phase changes as ω_chirp is

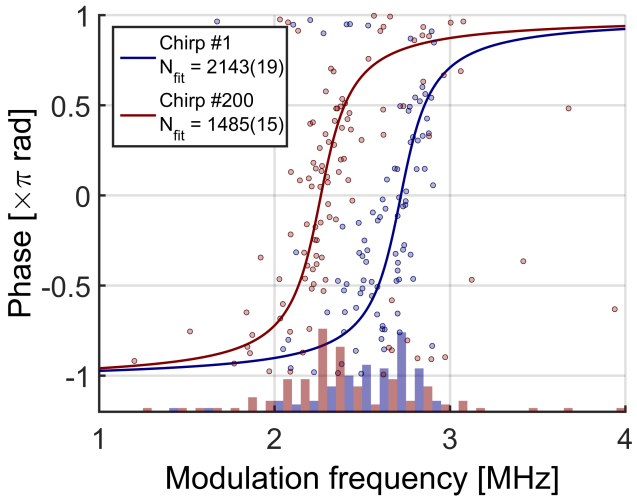

Figure 7-8: Typical signal of phase measurement

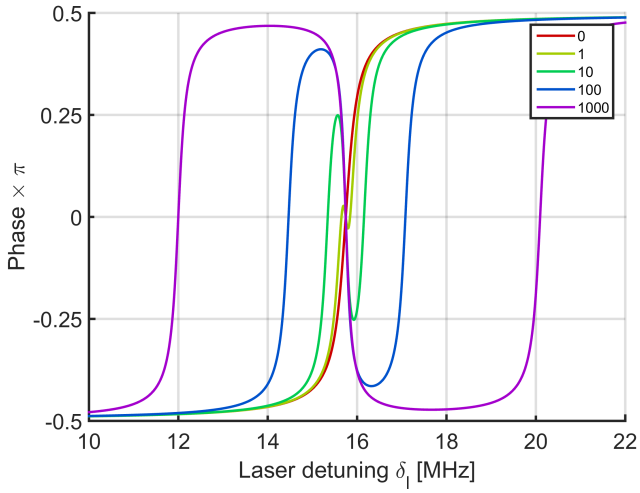

Figure 7-9: The phase of the light that is transmitted through experimental cavity: it is assumed that $\omega_{\mathrm{at}} = \omega_{\mathrm{c}}$

scanned, and fitting this with Eq. 3.16 gives the position of the resonant frequency of the transmission. The phase measurement is effective when the contrast of the beat note is more than 85%. Because the contrast gets high when ω_{p} is well tuned to $\omega_{\mathrm{at}} = \omega_{\mathrm{c}}$, this contrast is used for a frequency calibration for ω_{c}.

7.2 Optical pumping

The first thing to do after trapping atoms into an optical lattice is state preparation for spin squeezing: optical pumping to a single state. To perform an optical pumping to the $m_F = 1/2$ ground state, we use a transition from the $m_F = -1/2$ sublevel of the $^1S_0$ ground state to the $m_F = 1/2$ sublevel of the $^3P_1$ $F = 3/2$ level, as shown in Fig. 7-10. We send a pumping beam through the experimental cavity.

Fig. 7-11 shows the quality of the optical pumping with different detunings of the pump beam from the resonant frequency between the $m_F = -1/2$ ground state and the $m_F = 1/2$ excited state. The measurement is performed by the sequence shown in Fig. 7-12. Since the scan measurement is performed for only one of the $m_F = \pm 1/2$ states, a single sequence obtains the number of atoms remaining after the pumping. The atom number is normalized by the twice the initial atom number in the state we probe. The ratio of the atom number in the $m_F = 1/2$ state and the $m_F = -1/2$ state after the pumping is obtained by dividing the remaining atom numbers, and the sum is obtained by adding them. The pumping is most effective when the frequency detuning of the pump beam is zero from the atomic resonance. At the blue detuned side, we observe a certain amount of atom loss, which is presumably due to heating by the pumping light. As this graph is a relatively early result, we still had 2 % of atoms remaining in the $m_F = -1/2$ state, and the loss at the resonance is 40 %, but currently, we typically have less than 0.5 % of atoms remaining in the $m_F = -1/2$ state, and the loss due to the heating is more or less zero.[4] Particularly when we apply a larger B_z magnetic field, the quality of optical pumping improves, and we see only a few atoms remaining in $m = -1/2$ state out of ~ 2000 total $N\eta$.

[4] we only see the atom number increase in the $m_F = 1/2$ state by 80 %. The reason we regard that the loss due to the heating is zero is that atoms are initially polarized, as the number in $\omega_{\rm pump} - \omega_{1/2} = \pm 1$ MHz data shows.

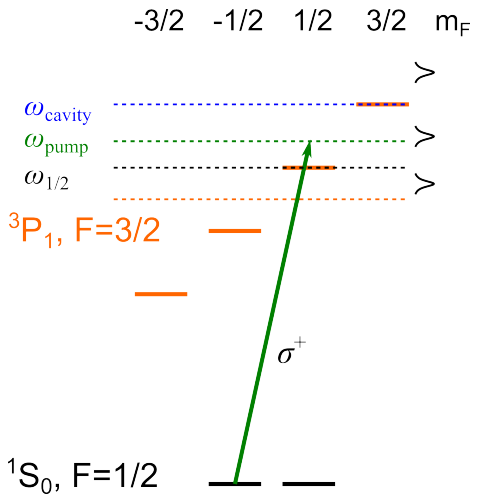

Figure 7-10: Energy level and relevant laser frequencies for optical pumping

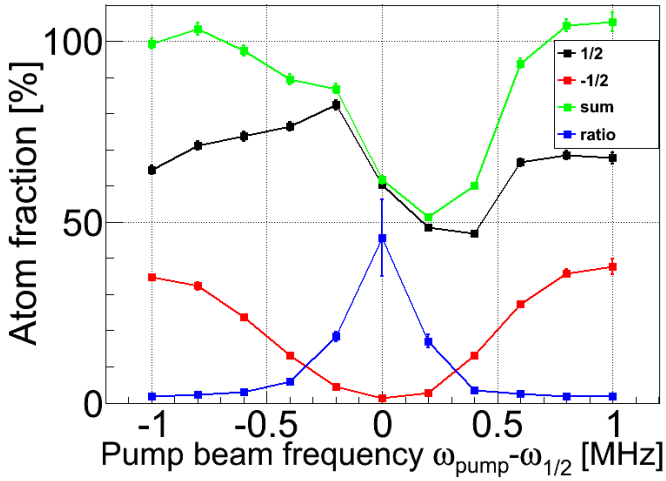

Figure 7-11: Quality of optical pumping for different pump laser frequency

7.3 Rabi pulse and coherence

Once all atoms are pumped into the $m_F = 1/2$ state, we want to put the state into a superposition state between the $m_F = \pm 1/2$ states coherently. To do this and other rotations on the Bloch sphere, we need to have good Rabi pulses, such as a $\pi/2$ pulse and a π pulse. These pulses are first achieved by applying an oscillating magnetic field with the x direction bias coil, and later the coil for Rabi pulse is replaced by the AC coil. The $m_F = \pm 1/2$ states are regarded to be a two-level state, and to have decent

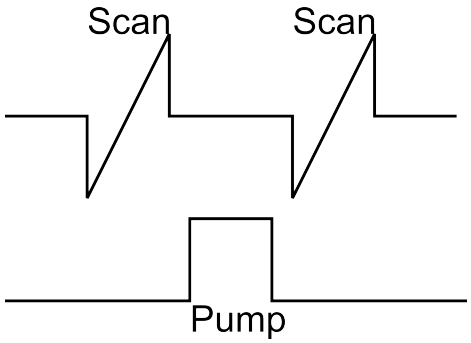

Figure 7-12: Sequence for optical pumping experiment

energy shift between them, we applied 7.06 G magnetic field, which corresponds to a Larmor frequency of 5296 Hz. Note that this is a two-level state that is truly a spin 1/2 system.

It is important for coherence to be maintained over the whole manipulation of the states during a sequence. To check this coherence, we have a sequence shown in Fig. 7-13, and take a ratio of atom number before and after the Rabi pulse measured by scan measurements. We change the length of the Rabi pulse, and check if the coherence is maintained. Fig. 7-14 shows a result with the x bias coil. Half of the coherence remains after 500 ms. The data points are fitted with the following fit function.

$$f(t) = \frac{1}{2}\left(1 + \cos\left(2\pi\frac{t}{p_0}\right)e^{-t/p_2}\right)e^{-t/p_1}, \tag{7.6}$$

where $1/p_0$ is Rabi frequency, which is 17 Hz, and p_1 is the loss of coherence due to the atom lifetime in the lattice, which is 846 ms, according to the fit, which is the limiting factor of the coherence. The loss of the coherence except for the loss of atoms in the lattice is more than 2 s.

Although this coherence time is long enough to do manipulations, the length of the $\pi/2$ pulse is as long as 14.66 ms. A long Rabi pulse has a danger of being susceptible to the possible fluctuations of background magnetic fields, and a shorter pulse is desired. Thus, we implement the AC coil. Fig. 7-15 shows a result of a coherence measurement for the AC coil. The lengths of $\pi/2$ and π pulses are 1.8 ms and 3.6 ms, respectively, which corresponds to a Rabi frequency of 139 Hz. Beyond 15 ms,

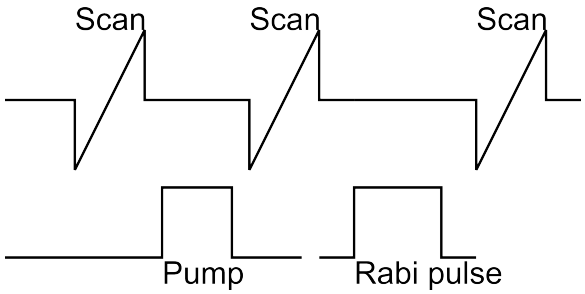

Figure 7-13: Sequence for Rabi pulse coherence test

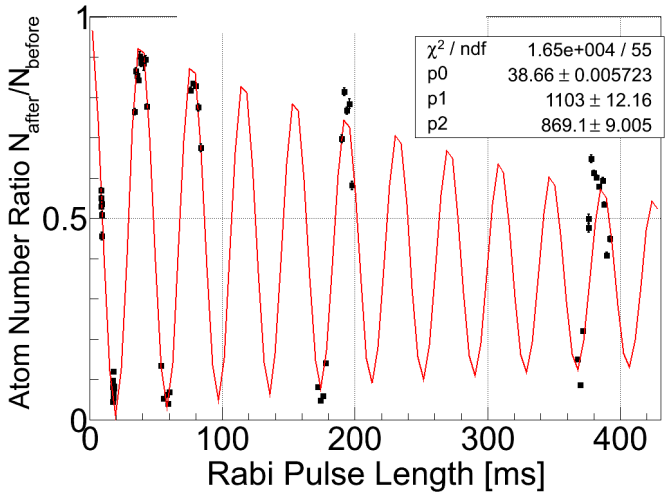

Figure 7-14: Coherence of Rabi pulse with x direction bias coil: fitting function is $0.5(1+\cos(2\pi x/p_0)\exp(-x/p_2))\exp(-x/p_1)$.

we don't see any oscillating feature, because the capacitor is completely discharged and the power supply turned to a constant current operation to supply the DC offset current. The length of the Rabi oscillation can be increased by reducing the DC offset voltage. Note that this data is measured with a $B_z = 13.77$ G magnetic field, which corresponds to a Larmor frequency of 10.295 kHz.

7.4 Ramsey spectroscopy and coherence

With the Rabi oscillation confirmed, another useful tool for us to see the coherence of the state is the Ramsey sequence. This can give us information on the coherence of the state after any kind of procedure in between two $\pi/2$ pulse of the standard

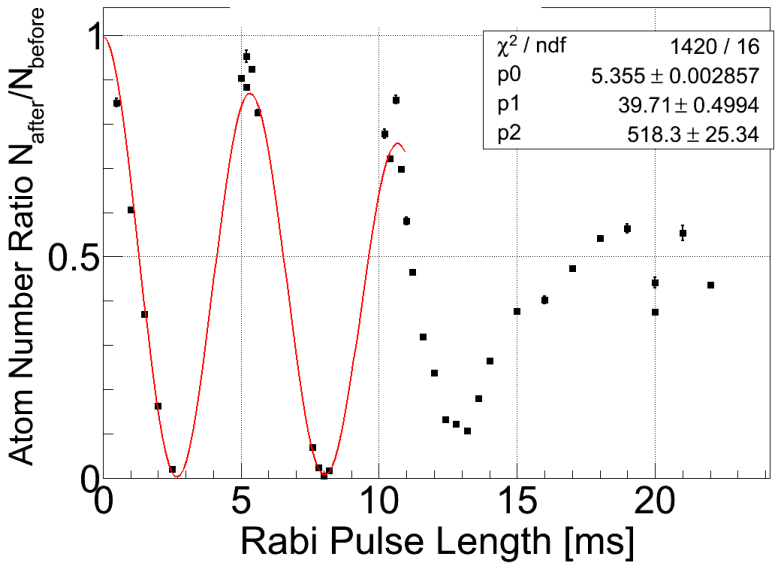

Figure 7-15: Coherence of Rabi pulse with AC coil: fit is misleading and should not be believed too much. The fitting function is $0.5(1+\cos(2\pi x/p_0)\ \exp(-x/p_2))\ \exp(-x/p_1)$.

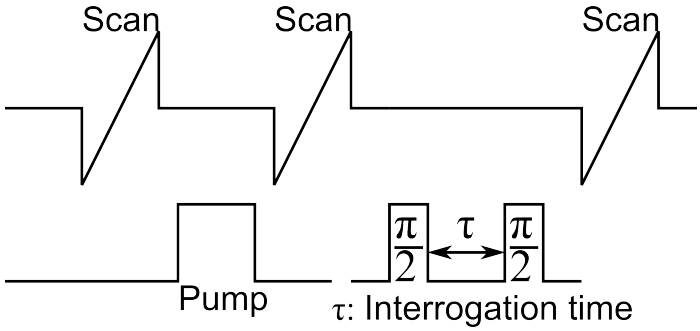

Figure 7-16: Ramsey sequence

Ramsey sequence. The basic Ramsey sequence we performed is shown in Fig. 7-16. After the optical pumping to the $m_F = 1/2$ state, we measure the atom number in the $m_F = 1/2$ state with a scan measurement, and send two $\pi/2$ pulses separated by an interrogation time of τ. The second pulse has a different phase from the first one.

We first change frequency of the AC field, setting the phase difference between two $\pi/2$ pulses zero and interrogation time $\tau = 10$ ms. This gives a good Ramsey fringe, as shown in Fig. 7-17. The fitting function is the standard Ramsey sequence

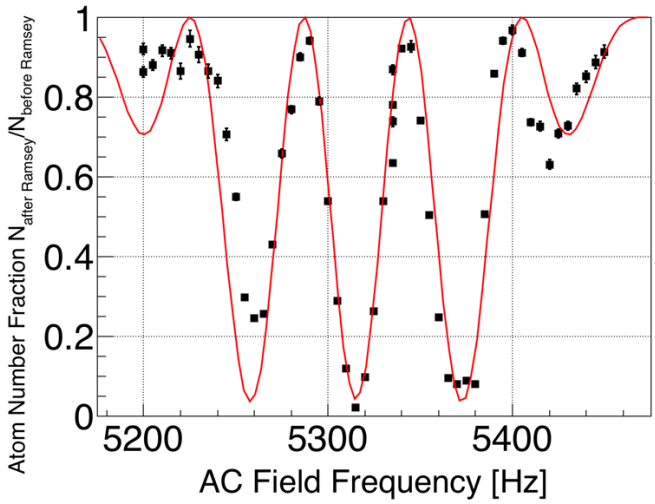

Figure 7-17: Ramsey fringe fitting function is the standard Ramsey sequence transition probability $1 - \frac{4p_0^2}{\Omega_g^2}\sin^2\left(\frac{\Omega_g p_2}{2}\right)(\cos\left(\frac{\Omega_g p_2}{2}\right)\cos\left(\frac{\delta T}{2}\right) - \frac{\delta}{\Omega_g}\sin\left(\frac{\Omega_g p_2}{2}\right)\sin\left(\frac{\delta T}{2}\right))^2$, where $\Omega_g = 2\pi\sqrt{p_0^2 + (x-p_1)^2}$, $\delta = 2\pi(x - p_1)$ and $T = 10$ ms.The fitted parameters are $p_0 = 49.41 \pm 0.09$ Hz, $p_1 = 5315.00 \pm 0.03$ Hz, and $p_2 = 5.726 \pm 0.008$ ms.

population, and this gives the precise Larmor frequency of 5315 Hz. [5]

Next, we set the interrogation time $\tau = 10$ and 100 ms, and changed the phase of the second pulse from zero to 2π. As shown in Fig. 7-18, the coherence is more than 95 % in the $\tau = 10$ ms case. When $\tau = 100$ ms, the coherence decays by a certain amount, but still 60 % of it remains. This is good enough for us to perform spin squeezing and observe the effect without being limited by the coherence of the state itself.

With the AC coil, we first perform the standard Ramsey sequence with different interrogation times. The fraction of atoms in the $m_F = 1/2$ state is fit with $y = A\cos(2\pi f x - \phi_0)\exp(-x/T_2) + y_0\exp(x/T_1)$. This fit gives coherence time $T_2^* = 130 \pm 2$ ms, as shown in Fig. 7-19. The experiment is also performed with a Larmor frequency of 10.380 kHz, and the fitted oscillation frequency gives a precise Larmor frequency of 10.295 kHz. A Ramsey sequence with echo, which means a π pulse is applied when half of the interrogation time has passed, is also performed. Fig. 7-20 shows the result. The decay time of the contrast is $T_2 = 1.80 \pm 0.30$ s, which is limited by the

[5] At this time, magnetic field was slightly different from 7.06 G

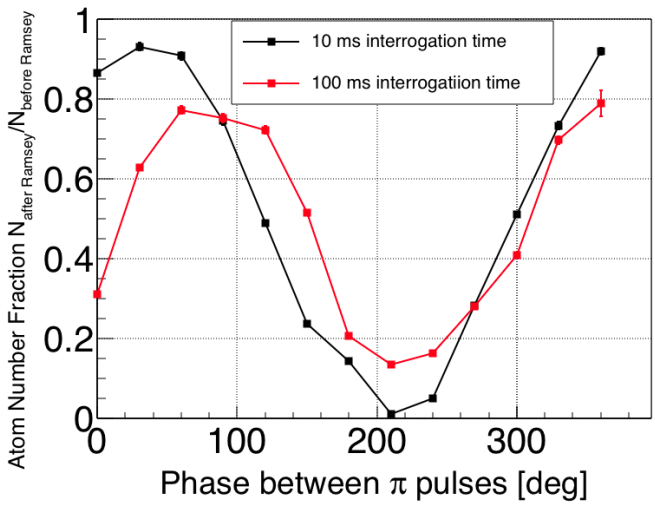

Figure 7-18: Measurement of Ramsey coherence with x direction bias coil

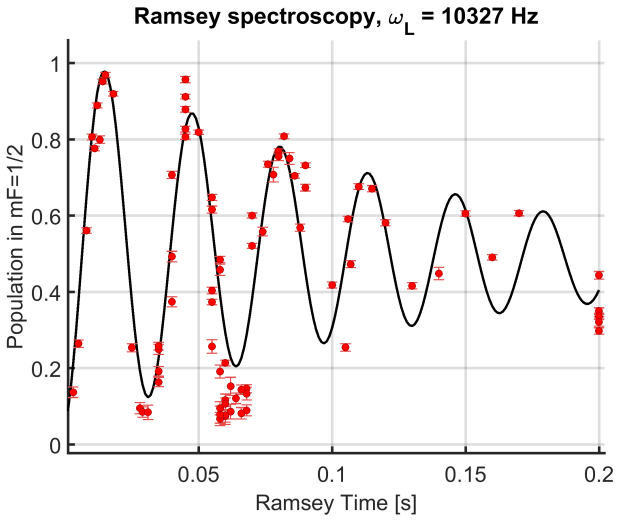

Figure 7-19: Coherence decay in Ramsey sequence: Larmor frequency is 10.327 kHz. Fit function is $y = A\cos(2\pi f x - \phi_0)\exp(-x/T_2) + y_0\exp(x/T_1)$, and fitted parameters are $y_0 = 0.5308 \pm 0.0142$, $\phi_0 = 2.838 \pm 0.077$, $A = 0.5073 \pm 0.0453$, $f = 30.4074 \pm 0.2569$, $T_2 = 0.1295 \pm 0.0240$, and $T_1 = 1.9780 \pm 2.3646$.

lifetime of atoms in the lattice.

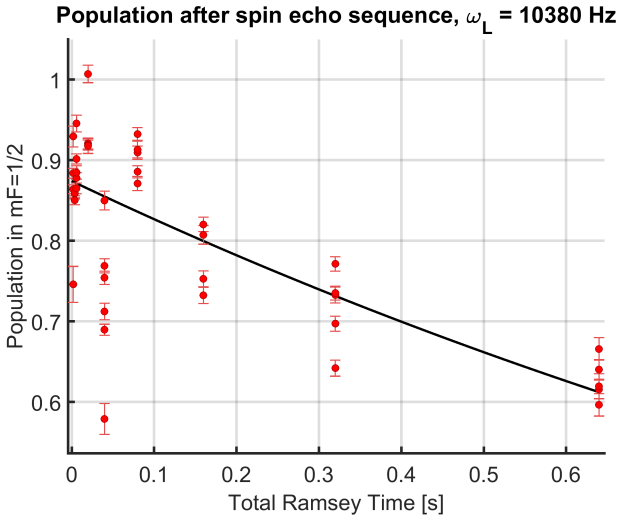

Figure 7-20: Coherence decay in Ramsey sequence with echo: Fit function is $y_0 \exp(-x/\Gamma)$, and fit result is $y_0 = 0.8743 \pm 0.0105$ and $\Gamma = 1.7964 \pm 0.3034$.

7.5 Atom number counting

The precision of atom number counting is crucial for a large amount of squeezing, because to confirm 20 dB squeezing, we need to have a measurement of the atom number 20 dB more precise than the SQL. We first tried to do this with scan measurement. For the scan measurement, we can perform this test without using actual atoms. We generated two probe frequencies 3 MHz apart by mixing a 1.5 MHz RF signal with a VCO frequency, and scanned the VCO frequency. This told us that there is a $\sim$ 30 kHz fluctuation in the frequency measurement, no matter how many photons we use for detection.

The sequence for the test with the chirp measurement is shown in Fig. 7-21. Because we use the vacuum Rabi splitting for the chirp measurement, we have to use actual atoms with this measurement. The chirp measurement is performed multiple times in a single sequence, and we get a series of atom numbers in a sequence, which decrease over time, because of the atom number decay in the lattice induced by the probe light. To have the best estimate of the atom number in a certain time in a sequence, we perform a linear fit, and to assure that the linear fit is good enough, and that we don't have to use more complicated fit function, such as exponential fit,

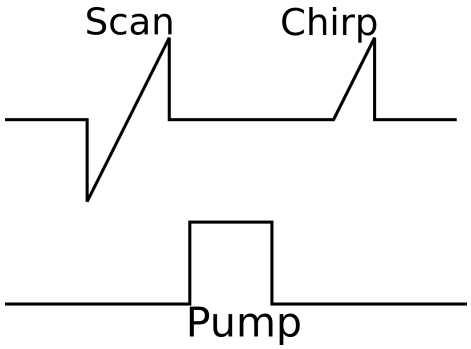

Figure 7-21: The sequence for atom number counting precision test

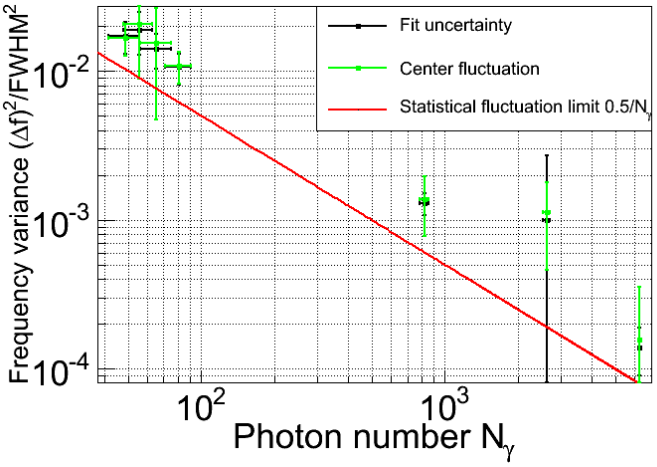

Figure 7-22: Precision of the peak position estimate for different transmission photon number

we only use the data where atom number stays with in 20 % of the initial number. We calculate the atom number fluctuation as the deviation from this fit, and plot it against different photon numbers. Fig. 7-22 and 7-23 show the result. Note that the frequency fluctuation is estimated in the same way as atom number fluctuation, and the linear fit is good enough for both of them.

The results suggest that our frequency estimate with the chirp measurement is as good as the theoretical limit of the Lorentzian fitting. Theoretically, the typical width of the Lorentzian fit uncertainty should be described by a unit of FWHM, as the Lorentzian curve does not have a finite variance. With the FWHM, the theoretical upper bound of the fitting precision is calculated to be $\Delta f/\mathrm{FWHM} = 0.5/N_\gamma$,

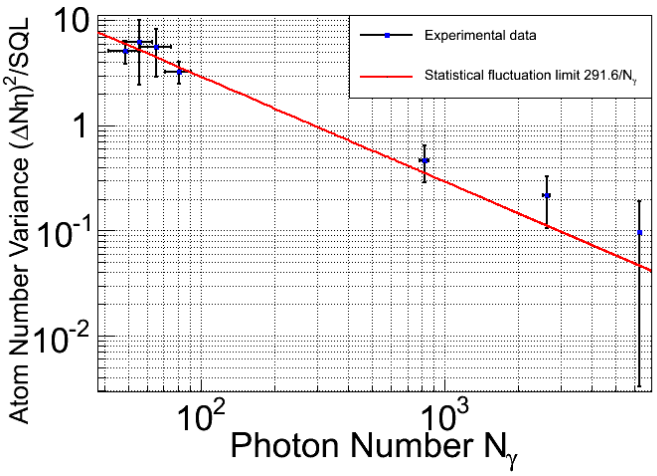

Figure 7-23: Precision of the atom number estimate for different transmission photon number

where N_γ is the number of photons used for the peak frequency estimate. Data points are above this theoretical limit within the errorbar, and the fitting uncertainty and the actual fluctuation of atom number match well. This suggests that we hit the theoretical limit, and our fitting does not have any problems regarding the uncertainty estimate. When we convert the theoretical limit according to Eq. 7.2 and the error propagation for it, we get the theoretical limit for an atom number estimate of $\Delta(N\eta) = 291.6/N_\gamma$. Because $N\eta$ is not proportional to f, $\Delta(N\eta)$ is much larger than the SQL at the small number of photons, but still Fig. 7-23 implies that with sufficiently large number of photons, we still can measure well below the SQL. Note that this analysis is done only with the transmission photon number. With the phase information, we also can go 3 dB higher precision than only with transmission. However, uncertainty due to the atom loss due to the probe beam comes in, and the maximum precision is estimated to be -13 dB of SQL.

7.6 Measurement of cooperativity

To correctly estimate the amount of squeezing, we need to know the cooperativity η precisely, as what we can measure through the cavity is only $N\eta$, whereas the spin squeezing is always described by the variance of N. One way to estimate η is to use

the information of geometry. As we know the radii of curvature and the distance between two mirrors, and the distance of atoms from the micromirror substrate, we can estimate η. However, direct measurement of η is always more reliable. To do this, we first optically pump the population to the $m_F = 1/2$ state, and we transfer a specific number of atoms from the $m_F = 1/2$ state to the empty $m_F = -1/2$ state by a short Rabi pulse. The normalized variance of the number of atoms transferred is

$$\frac{\langle \Delta N\eta^2 \rangle}{\langle N\eta \rangle} = \frac{\langle \eta^2 \rangle}{\langle \eta \rangle} \approx \eta, \tag{7.7}$$

as all the fluctuation in $N\eta$ comes from that of N, and if we do this measurement with different $N\eta$ and plot $(\Delta N\eta)^2$ against N, the slope is η. There are two reasons we prefer small N; one is that only in this region, is the relation of $(\Delta N\eta)^2$ and $N\eta$ linear, as described in the next section. The other is that with small N, the relative quantum noise is larger than large N, and we are more sure that the noise is dominated by the quantum noise.

The experiment is done with a sequence shown in Fig. 7-13, where the length of the Rabi pulse is very short. We measure the population in the $m_F = -1/2$ state by a scan measurement. After the optical pumping, we send a short Rabi pulse to transfer atoms from the $m_F = 1/2$ state to the $m_F = -1/2$ state, whose length is changed to take data for different $N\eta$. The atoms are 0.9 mm away from the micromirror substrate. Fig. 7-24 shows the result. Here, N on x axis is not the total atom number but the final atom number in the $m_F = -1/2$ state. To get the total atom number, we use the information of the atom number measured before optical pumping, and the typical number of the initial atom polarization, where 3/8 is in $m_F = -1/2$ state, and 5/8 is in $m_F = 1/2$ state, and get $\eta = 0.613 \pm 0.037$. η for different atom positions is derived from this number and the geometry of the cavity mode.

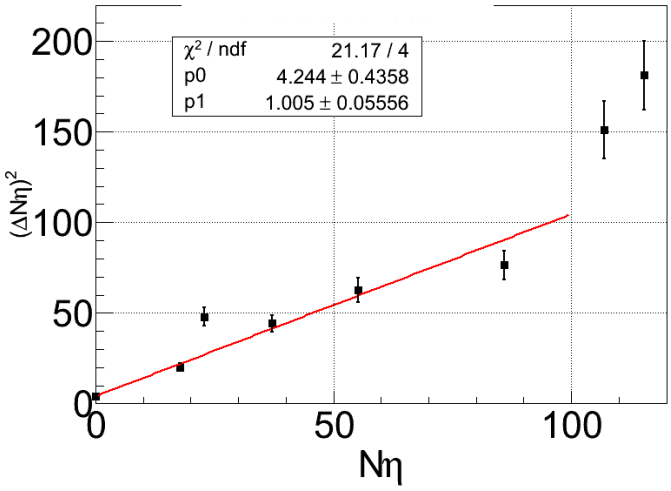

Figure 7-24: Result of cooperativity measurement: note that N here is the initial atom number in -1/2 state, not the total atom number in the trap.

7.7 Estimate of classical noise

Eq. 7.7 only holds for $N \ll N_{\mathrm{tot}}$, where N is the atom number transferred, and N_{tot} is the total atom number in the lattice. For arbitrarily large N, the correct formula is the variance for the binomial distribution $\Delta N = Np(1-p)$, which is $N/4$ at $p = 1/2$. Here, because N is large, the quantum noise is suppressed, and it is easier to see the effect of the classical noise. This is the case of the $\pi/2$ pulse, and the stability here is very important to have a reproducible transfer of atoms to the equator of the Bloch sphere. To estimate the effect of the classical noise, we perform the stability measurement of the $\pi/2$ pulse.

The sequence for the experiment is the following; we optically pump the population to the $m_F = 1/2$ state, send a $\pi/2$ pulse, and measure the population in the $m_F = 1/2$ state by a scan measurement. We repeat this ~ 100 times, and put the final population normalized by the population after the optical pumping into a histogram. Fig. 7-25 shows the result with a Gaussian fit. Based on the average $N\eta = 806 \pm 71$ and $\eta = 0.613 \pm 0.037$, we get an SQL of 329 ± 34, whereas measured variance $(N\sigma)^2 = 714 \pm 148$. The measured variance is 2.17 times larger than the SQL. Part of the reason why the variance is more than the SQL is because the initial atom number

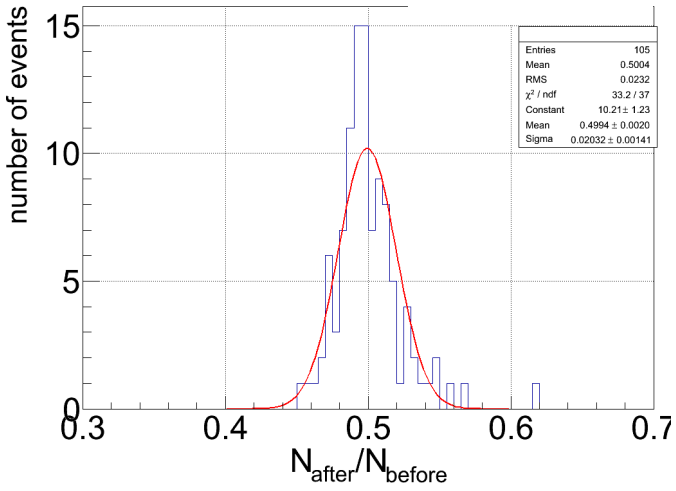

Figure 7-25: Histogram for the atom fraction after a $\pi/2$ pulse

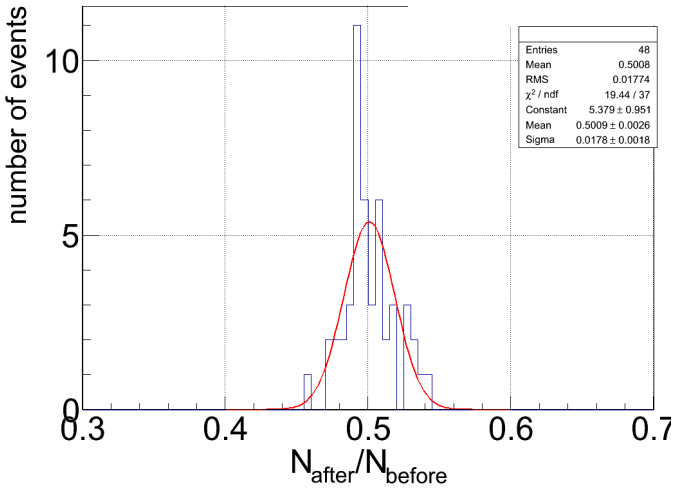

Figure 7-26: Histogram for the atom fraction after a $\pi/2$ pulse with the post selection of $765 \leq N\eta \leq 845$

fluctuates as 806 ± 71, where ± 71 is standard deviation. When we post-select the data of $765 \leq N\eta \leq 845$, the histogram becomes Fig. 7-26. This gives $(N\sigma)^2 = 548 \pm 114$, which is only 1.67 times worse than than the SQL. We conclude that this is not too noisy for performing a spin squeezing measurement.

The same measurement is performed with a Rabi pulse by the AC coil. Here, the average $N\eta$ is $N_{\text{ave}}\eta = 1433.66$ before a post selection, and together with the standard deviation of $\sigma = 0.01276 \pm 0.00315$ in Fig. 7-27, variance is calculated to be 1.526

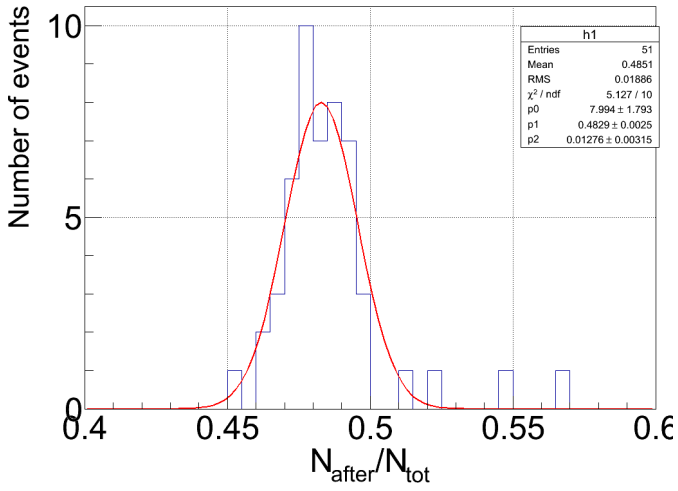

Figure 7-27: Histogram for the atom fraction after a $\pi/2$ pulse by AC coil

times larger than SQL. When we post-select the data with the condition of $0.9N_{\rm ave}\eta < N\eta < 1.1N_{\rm ave}$, the histogram becomes Fig. 7-28. This gives $\sigma = 0.00863 \pm 0.00144$, resulting in the variance of only 0.698 times larger than the SQL. The latter suggests that actual cooperativity might be a bit smaller; it should be 0.43 instead of 0.613 for the variance to be the same as the SQL. The most likely explanation for a poor estimate of η in Section 7.6 is that the estimate of the initial polarization of atoms is wrong. In any case, this shows that the $\pi/2$ pulse by the AC coil is free from classical noise.

7.8 Measurement-based spin squeezing

To perform the simplest squeezing, we first perform a measurement-based squeezing. The idea is described in Section 3.4.1. The sequence is shown in Fig. 7-29. We make a relatively weak chirp measurement 200 times, where each chirp has N_γ of ~ 100, after putting the state onto the equator of the Bloch sphere. We regard first n_1 measurements of this 200 chirps as a squeezing measurement, and the next n_2 pulses as a strong measurement. This sequence is run more than 100 times for the purpose of taking an average and a standard deviation. Defining the measured population in the $m_F = 1/2$ state with the first and the second measurement as $N_1\eta$ and $N_2\eta$,

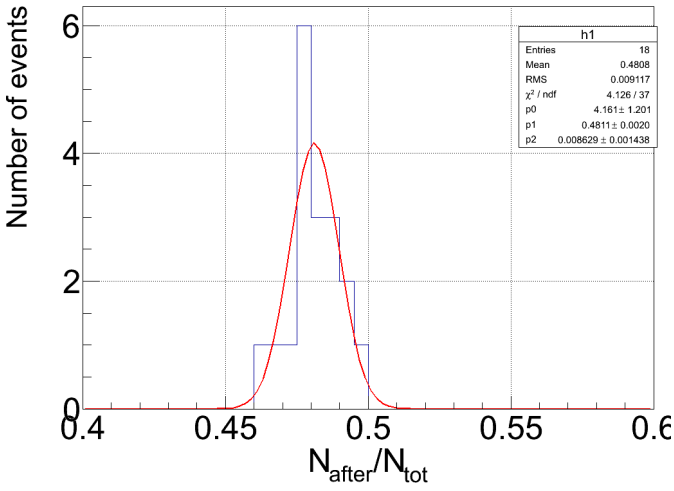

Figure 7-28: Histogram for the atom fraction after a $\pi/2$ pulse by AC coil with the post selection of $0.9N_{\text{ave}}\eta \leq N\eta \leq 1.1N_{\text{ave}}\eta$

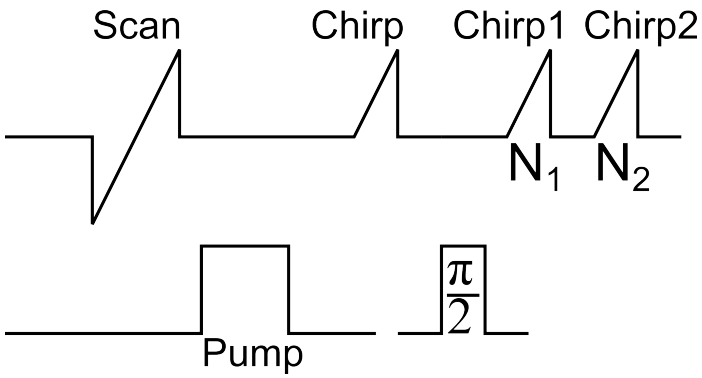

Figure 7-29: Sequence for measurement-based squeezing

we take the variance of $N_2 - N_1$ to get $(\Delta N_\uparrow)$. Total atom number N_0, which is on average 6800, is derived by doubling the average of N_2 and $\eta = 0.125$ at 1.99 mm away from the micromirror. From these numbers, we get the measurement variance $4\left(\Delta N_\uparrow\right)/N_0$, shown by the green dots in Fig. 7-30. Apparently, this variance gets smaller as the squeezing measurement gets stronger. To get the amount of useful squeezing, we need to incorporate the effect of coherence loss.

The contrast measurement is performed separately with a sequence described in Fig. 7-31. This is the Ramsey coherence measurement in Fig. 7-16, except that the interrogation time τ is replaced by n_1 chirp measurements. The extracted coherence

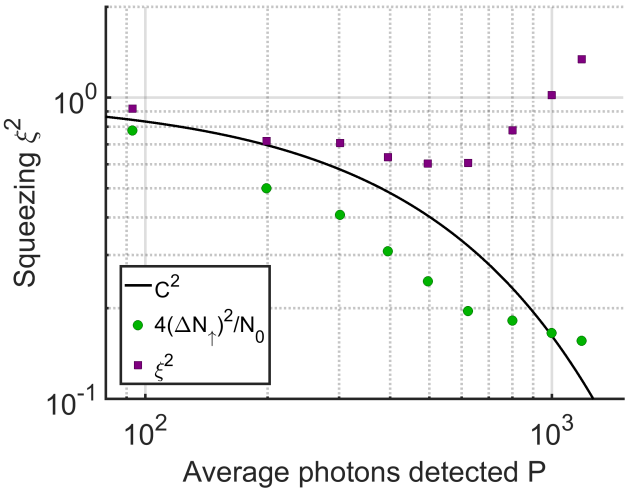

Figure 7-30: Result of the measurement-based squeezing

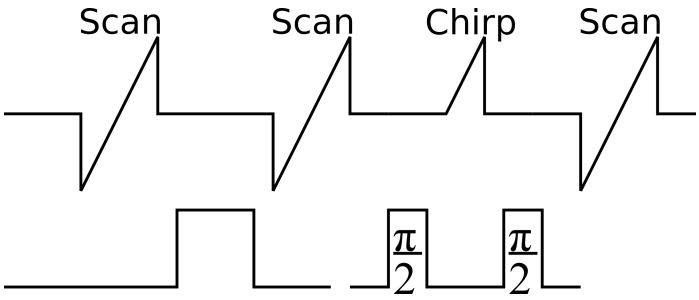

Figure 7-31: Sequence for measuring the contrast for the measurement-based squeezing

is fitted in Fig. 7-32, and the fitted coherence is plotted on Fig. 7-30. According to the graph, we get the largest amount of squeezing of 2.1 dB in the language of Wineland criterion (Eq. 3.24) at 500 or 600 detected photons.

This amount of squeezing matches to the theoretical calculation well. Based on Eqs. 3.36, 3.40, and measured $N_1\eta = 425 \pm 35$, total amount of squeezing is $\xi^2_{\mathrm{W,tot}} = 0.569$. This is 2.45 dB of squeezing, which is quite close to the measured value of 2.1 dB. Eqs. 3.35, 3.37, and 3.39 imply some possible ways to improve the amount of squeezing. First of all, increasing the number of atoms linearly increases the amount of squeezing. There is room for a better measurement by parking the probe frequency at the top of a peak of the Lorentzian. This should double the amount of squeezing.

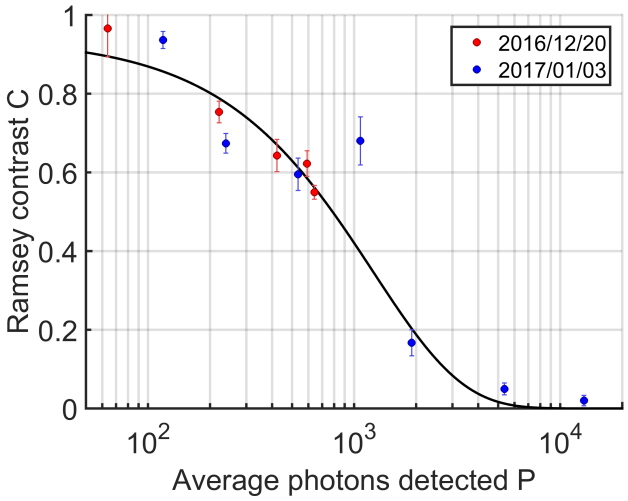

Figure 7-32: Contrast measurement for the measurement-based squeezing

If we have better light collection efficiency, such as better coupling of the cavity transmission to a fiber by a multimode fiber and a single photon counter with better quantum efficiency, this also improves the amount of squeezing.

7.9 Phase shift by probe light

To estimate if the cavity feedback squeezing works, a good starting point is to test if the phase shift is the same amount as the prediction by Eq. 3.42. To test this, we perform phase shift measurements. The sequence is to send a phase shift pulse after bringing the state into the 1:1 superposition state of the $m_f = 1/2$ state and the $m_f = -1/2$ state, and then measure the atomic phase shift due to a phase shift pulse by changing the phase of the second $\pi/2$ pulse, as shown in Fig. 7-33. The result is shown in Fig. 7-34. First, we scan the frequency of the probe beam while we send the phase shift pulse. (Fig. 7-34 (a), (b)) As most of the photons are transmitted through the cavity when the frequency is resonant to a peak of vacuum Rabi splitting, this is effectively a phase shift with on resonant light. Next, we set the phase shift light frequency $\sim$ 1 MHz off from a peak of vacuum Rabi splitting. (Fig. 7-34 (c), (d)) Here, the atom number is $N\eta \approx 630$.

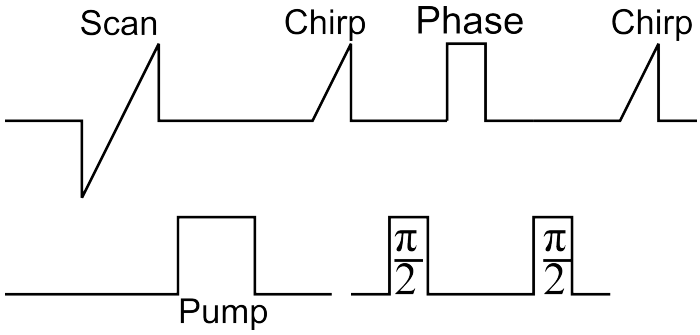

Figure 7-33: Sequence for phase shift measurement

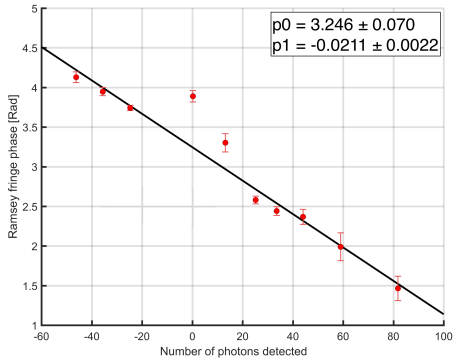

(a) Phase shift by an on resonant pulse

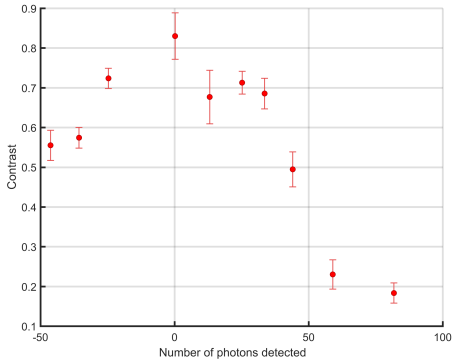

(b) Contrast by an on resonant pulse

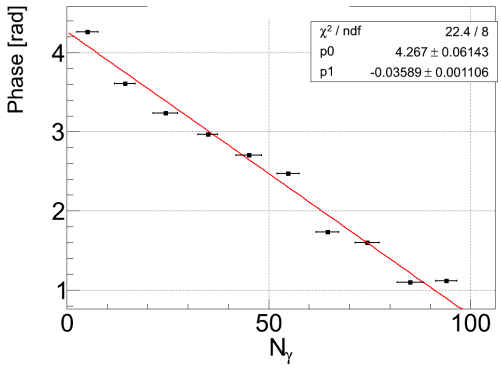

(c) Phase shift by an off resonant pulse

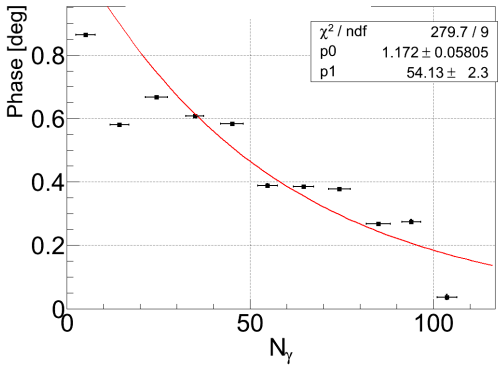

(d) Contrast by an off resonant pulse

Figure 7-34: Phase shift measurements: The fit function for (a) and (c) is $y = p_0 + p_1 x$, and the fit function for (d) is $y = p_0 \exp(-x/p_1)$. The negative photon numbers in (a) and (b) correspond to sending red detuned photons.

The phase shift is linear to the photon number, as predicted by Eq. 3.42. For

$y \gg 1$ and $q \ll 1$, Eq. 3.42 becomes

$$\varphi_{\mathrm{at,tot}} = -\eta \frac{1}{2y} T, \tag{7.8}$$

and the amount of the phase shift per photon is calculated as -8.489×10^{-3} rad/γ^6, plugging in $N\eta = 630$, $\eta = 0.613$, $q_1 = 31$ ppm, and $q_2 = 196$ ppm. This does not include a factor of quantum efficiency of the detector. Including this detection efficiency, the expected phase shift is -0.0679 rad/γ for the resonant case. For the off resonant case, $y = 48$ instead of 37, and this gives -0.0523 rad/γ. These numbers are too large to explain the result in Fig. 7-34, particularly the on resonant case. A possible explanation is the estimate of η mentioned in Section 7.7; if we use $\eta = 0.43$ instead of 0.613, the phase shifts become 0.0476 and 0.0367 rad/γ for the on and off resonant cases, respectively, and this matches well, at least to the off resonant case. Potentially, the steeper slope for three points around [0,20] is the true phase shift rate for the on resonant case.

The contrast decay is faster than expected from Fig. 7-32; although the atom number decreased only by a factor of 10, the decay constant decreased from ~ 1300 to 54. This raises a question of whether nonuniform coupling of each atom to the probe light can decohere the state faster than a coherence loss by scattering light into free space, and therefore we perform a phase shift measurement with spin echo. The sequence is to have two phase shift pulses, and in the middle a π pulse is sent to flip the spin, as shown in Fig. 7-35.

The result of the phase shift measurement with spin echo is shown in Figs. 7-36 and 7-37. Although there remains slope at a small number of photons, the phase shift flattens out at a large number of photons. This suggests the phase echo works well. Later, we once more do the measurement, only with two data points, and at this measurement, the slope is 0.00055 rad/γ, which is effectively zero. Also, given that the cavity feedback squeezing works well, spin echo cancels the phase shift in a desirable way. The contrast decay shown in Fig. 7-37 has an order-of-magnitude

[6]Here, γ means photon.

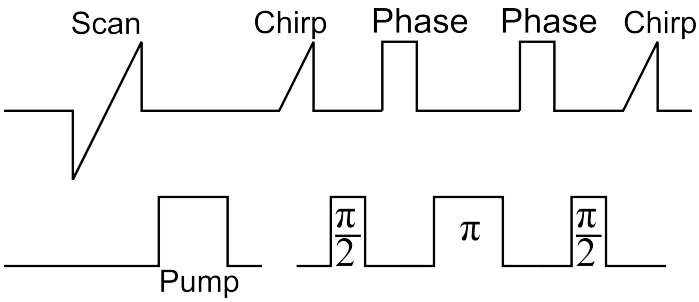

Figure 7-35: Sequence for phase shift measurement

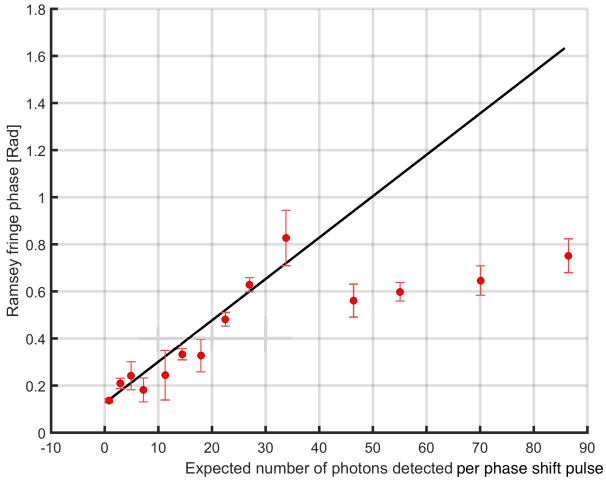

Figure 7-36: Phase shift with spin echo: the linear fit is $y = (0.126 \pm 0.015) + (0.0176 \pm 0.0081)x$.

larger decay constant compared to a single pulse phase shift. This supports the idea that nonuniform couplings dephase the state more quickly. Also, this implies that with spin echo, we can send a much larger number of photons for cavity feedback squeezing.

7.10 Cavity feedback squeezing

7.10.1 Theoretical estimate

The amount of squeezing we obtained from the measurement squeezing is relatively small without any further improvement in a few parameters. One of the major limiting

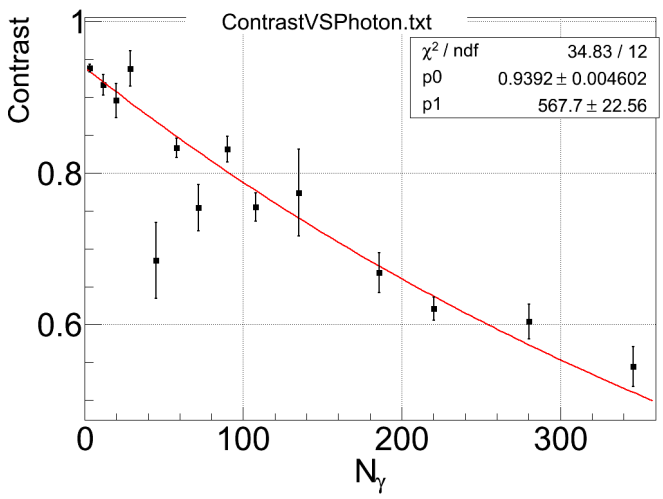

Figure 7-37: Contrast for phase shift measurement

factors is the light collection efficiency, which is only 12 %. This can be overcome by using cavity feedback squeezing, which does not require any measurement for squeezing.

Our system for the cavity feedback squeezing is the same as measurement-based squeezing; we use spin 1/2 Zeeman sublevels of the ground state of ^{171}Yb for the spin to squeeze, and squeezing is performed by the interaction between the $m_F = 1/2$ state of the ground state and $m_F = 3/2$ of the $F = 3/2$ hyperfine level of the $^3P_1$ excited state via 556 nm laser (see Fig. 3-11). As we have total atom number of $N_{\rm tot}\eta \sim 2000$, which is larger than the measurement-based squeezing experiment case thanks to the high magnetic field configuration for the MOT, we applied 14.3 G magnetic field to separate Zeeman sublevels of the $F = 3/2$ hyperfine level of the $^3P_1$ state. [7] The method is to send some phase shift pulses in a way to cancel technical noises to generate the nonlinear phase shift induced squeezing, as described in Chapter 3.

To determine the parameters and estimate the amount of squeezing we can achieve, a theoretical calculation is performed as described in Section 3.9 and Appendix A.5. It is convenient to estimate the amount of squeezing for a specific number of scatter photons $p_{\rm sc}$, because $p_{\rm sc}$ is directly connected to the contrast of the atomic system.

[7] At this magnetic field, separation of adjacent Zeeman sublevels is 20 MHz, and vacuum Rabi splitting for $N\eta \sim 2000$ is $2g = 12$ MHz.

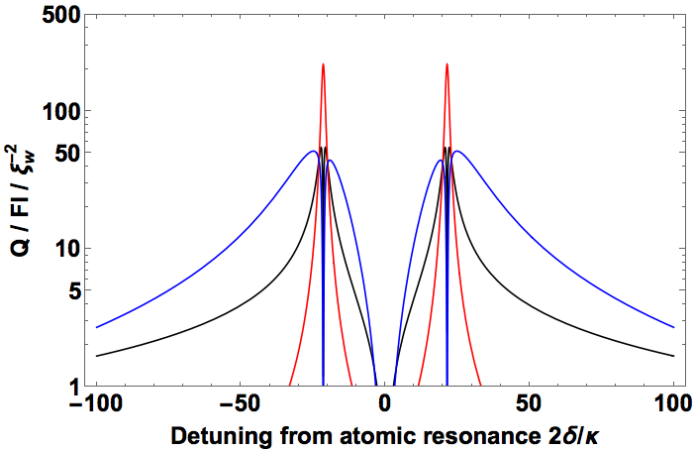

Figure 7-38: Shearing Q (black), Fisher information FI (red) and squeezing parameter ξ_w^-2 (blue) for scattered photon number of 2500/e: horizontal axis is in frequency normalized by the half linewidth of cavity resonance. Cavity resonance ω_c is assumed to be the same as atomic resonance ω_a.

Assuming $N_1 = 2500$ and $\eta = 0.4$ for $N_1\eta = 1000$, the typical p_{sc} for the most useful squeezing is $p_{sc} = N_1/e \simeq 920$. Fig. 7-38 shows the shearing Q (Eq. 3.44), Fisher information FI (Eq. 3.45), and Wineland squeezing parameter ξ_w^-2 (Eq. 3.46) for $p_{sc} = 920$ as a function of detuning from the cavity resonance δ, where the cavity resonance is parked at the same frequency as atomic resonance ($\omega_c = \omega_a$). The amount of squeezing takes maximum at a few linewidths away from the resonances of vacuum Rabi splitting $\delta = \pm g$. When the detuning is close to the resonances of vacuum Rabi splitting, the amount of squeezing reduces because of sharply increasing Fisher information and reduction in the shearing. When $|\delta| > g$, the decrease of the amount of squeezing is slower than $|\delta| < g$. An important feature is when $\delta - g \gg \kappa/2$ for $\delta > 0$ or $\delta - (-g) \gg \kappa/2$ for $\delta < 0$, where the Fisher information is so small that the squeezing is unitary.

In the actual experiment, a photon number parameter easy to observe is the number of transmitted photons through the experimental cavity p_{tr}. Fig. 7-39 shows the amount of squeezing $(1 + Q^2)/F$ against δ for different p_{tr}, based on Eq. 3.46. Note that it is not the case that the amount of squeezing ξ_w^-2 increases significantly as the detuning of the phase shift pulse gets smaller, because the probability for an

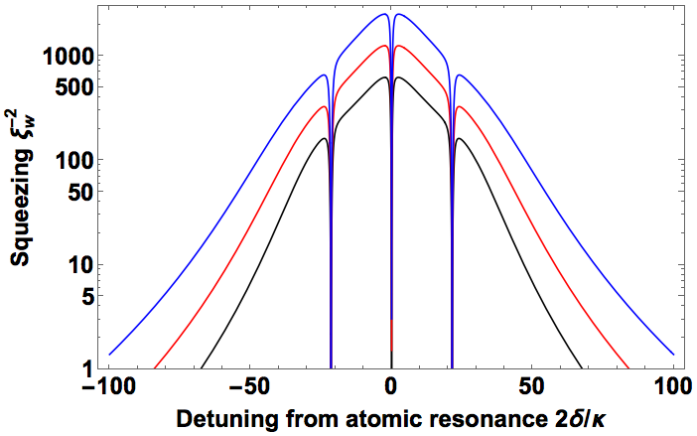

Figure 7-39: Amount of squeezing ξ_w^2 for different transmitted photon number: black, red, and blue lines correspond to 1000, 2000, and 4000 detected photons at a single photon counter.

atom to scatter a photon into free space increases as the frequency of the squeezing light gets closer to the atomic resonance.

7.10.2 Antisqueezing

The experiment consists of three parts: antisqueezing, unsqueezing, and phase sensitivity gain. To show that we can get a squeezed state, we first measured the antisqueezing by the phase shift pulse.

The experimental sequence is shown in Fig. 7-40. After the optical pumping, a $\pi/2$ pulse is sent to put the state on the one to one superposition state of spin up and down. Then the phase shift pulses are sent. This is a 556 nm laser with a detuning from atomic resonance of $\Delta = 12.8$ MHz. Because the phase shift pulse has linear term regarding S_z, as well as nonlinear term, we send this the phase shift pulse twice to cancel the linear phase shift by a spin echo technique. This also makes sure that atoms in both the $m_F = 1/2$ state and the $m_F = -1/2$ state interact with the light. The last $\pi/2$ pulse is sent only when we want to see the amount of antisqueezing in the phase direction, and without it, we can check how noisy the state becomes in the population difference direction after the sequence. As for the atom number counting, all initial detection is removed, as we established a way to reliably estimate the atom

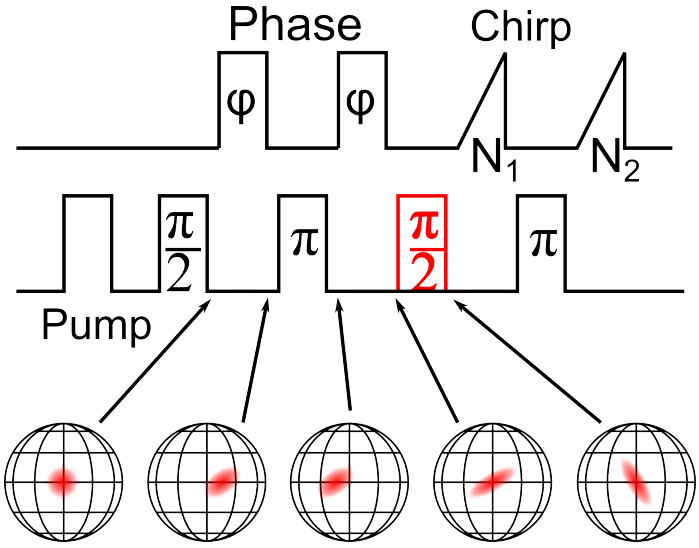

Figure 7-40: Sequence for antisqueezing experiment: the picture below the sequence shows the change from a coherent state in the ideal system. The last $\pi/2$ pulse is sent only for measuring phase direction uncertainty. The first π pulse and the second $\pi/2$ pulses have $\pi/2$ phase relative to the first $\pi/2$ pulse and the last π pulse.

number ratio of $N_1/N_{\rm tot}$ as $N_1/(N_1+N_2)$. To avoid effects from the 60 Hz background magnetic field, from the beginning of the first $\pi/2$ pulse to the middle of the π pulse for spin echo and from the middle of the π pulse for the echo to the end of 2nd $\pi/2$ pulse are set to be 16.67 ms.

The result is shown in Fig. 7-41 and 7-42. In each condition, ~ 100 data points are taken, and post selected by the contrast of the phase measurement ($C > 0.8$), the atom number N_1+N_2 (typically 2000 ± 200), and detected photon number N_γ (target number$\pm$10%). Fig. 7-41 shows the uncertainty of an antisqueezed state in phase and population difference direction. Atom number $N_{\rm tot}\eta$ is 2020 ± 228, and detected photon number N_γ is 2403 ± 107. This clearly shows the state has larger uncertainty than the SQL in the phase direction, whereas there is no significant additional noise onto the population difference direction. This is one of the things expected for a squeezed state generated by cavity feedback squeezing.[8]

Fig. 7-42 shows the dependence of the uncertainty in the phase direction on the

[8]This itself does not prove that the state is squeezed, as we have not observed anything that implies the narrower distribution than SQL. The unsqueezing measurement is necessary to be sure that the state is squeezed.

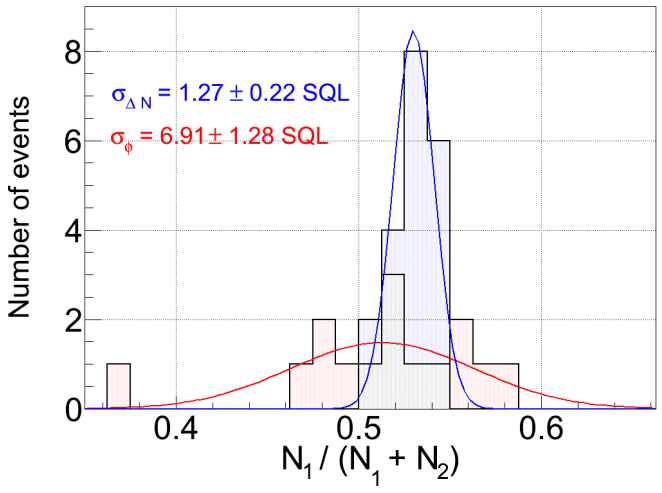

Figure 7-41: Noise distribution of an antisqueezed state

strength of phase shift pulse strength. This pulse strength is always described by the photon number detected by a single photon detector, whose overall detection efficiency of the photon coming out of the cavity is 12 %. Here, the average atom number is 2183 ± 119. What is measured here is the uncertainty of a state in the phase direction, and for the cavity feedback squeezing, this is basically the shearing Q, which is proportional to the transmitted photon number p_{tr}. In Fig. 7-42, uncertainty is well proportional to N_γ up to $N_\gamma = 2000$, but for $N_\gamma = 4000$, Q is smaller compared to this linear behavior. This should be explained by a good antisqueezing and an exponential decay of the contrast due to the phase shift pulses, and the data points were fitted by a fitting function $y = p_0 + p_1 x \exp(-x/8662)$. The decay constant of the contrast is obtained by the contrast measurement for unsqueezing (Fig. 7-46). This model explains the behavior of the antisqueezing well, and the slope $(2.42 \pm 0.23) \times 10^{-3}$ is reasonably close to the theoretical calculation of 0.001850 by Eq. 3.47. The larger slope than the theoretical estimate might mean that our overall coupling efficiency is smaller than the typical value of 12 %. Although the sequence has the echo feature, we had a residual phase shift, which is 0.01 degree/N_γ.

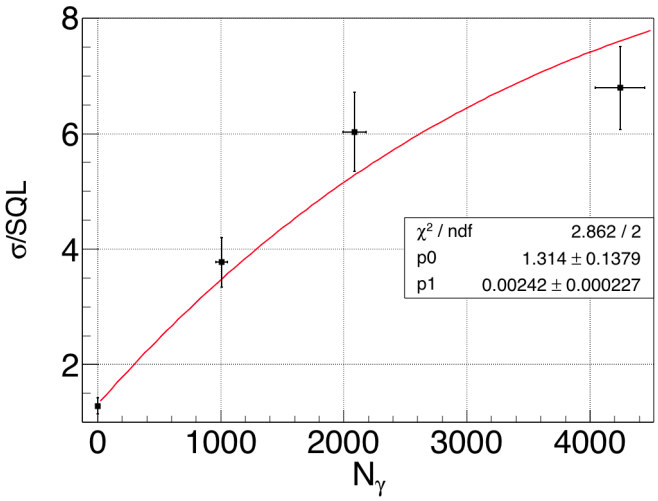

Figure 7-42: The amount of antisqueezing for different photon number N_γ for phase shift pulse: the fitting function is $y = p_0 + p_1 N_\gamma \exp(-N_\gamma/8662)$, where the decay constant of the exponential function comes from the contrast measurement Fig. 7-46.

7.10.3 Unsqueezing

The unsqueezing is defined as a process to put a squeezed state back to a coherent spin state, as shown in the bottom half of Fig. 7-43. To do this we first squeeze the state in the same way as antisqueezing. To put the state back to the coherent spin state, we first make a small rotation on the squeezed state to flip it against the equator. Then we send two other phase shift pulse that has a spin echo π pulse in between. Since the state is flipped in the way that the part closer to the north pole has negative phase compared to its center, the phase shift pulse that shifted the northern part of the state more to the positive direction now undo the shearing, as shown in the figure. This results in a state going back to its original distribution after the same procedure as the antisqueezing. In the end we rotate the state by $\pi/2$ to measure the uncertainty in the phase direction.

The basic structure of the sequence is the same as antisqueezing sequence. After the optical pumping, a $\pi/2$ pulse is sent to put the state onto the equator. Then two phase shift pulses between which a π pulse is located for the spin echo are sent. So far the procedure is the same as antisqueezing. Next, an ε pulse is sent to flip the state. Here, ε is regarded as a variable, and we experimentally change this between $-\pi/2$ and

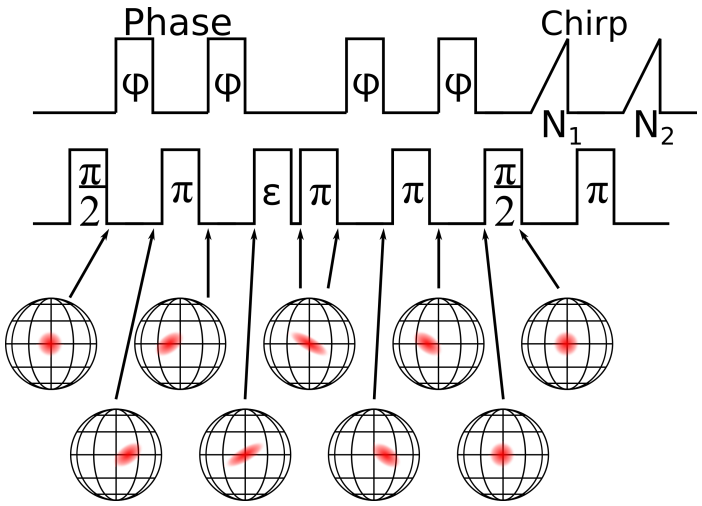

Figure 7-43: Sequence for unsqueezing experiment: the picture below the sequence shows the change from a coherent state in the ideal system. The first three π pulses and the second $\pi/2$ pulse is along S_y, and the first $\pi/2$ pulse and the last π pulse is along S_x. The ε pulse has the rotation axis that matches to the residual phase shift observed in antisqueezing measurement.

π to find the best rotation angle. The rotation axis for this ε pulse is chosen according to the residual phase shift observed in antisqueezing measurement to minimize the deviation of the state from the equator of the Bloch sphere. Theoretically, the best ε is twice as much as the angle θ between the long axis of the state and the equator, as shown in Fig. 7-44. To have another spin echo feature, we then send another π pulse along the rotation axis same as the first π pulse. The second half of the sequence is the same as antisqueezing part: a phase shift pulse, π pulse and another phase shift pulse. The timing of the sequence is matched to 60 Hz in the same way as the antisqueezing sequence; it takes 16.67 ms from the beginning of first $\pi/2$ pulse to the middle of first π pulse, between the middle of each π pulse, and from the second last π pulse to the end of the last $\pi/2$ pulse. The last π pulse is for flipping the population to measure N_2.

Fig. 7-45 shows the result of unsqueezing, and Fig. 7-46 is the constrast measurement with the same N_γ. The graph shows the ε dependence of the uncertainty in resulting state. Each data point is obtained by post selection from ~ 50 runs by the contrast of the phase measurement ($C > 0.8$), the atom number $N_1 + N_2$ (typi-

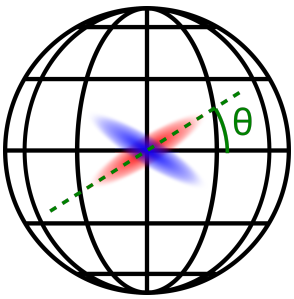

Figure 7-44: Squeezed state after antisqueezing sequence and its flipping

cally 2000 ± 200), and detected photon number N_γ (target number$\pm$10%). The basic behaviors that are common to all of different N_γ is a sharp dip at a relatively small $\varepsilon \sim 0.2\pi$ and dull peak around $\varepsilon \sim 0.7\pi$. These features as well as y intercept match to the following intuitive understanding of unsqueezing.

- At $\varepsilon = 0$, we have the uncertainty of $2Q$ at the end of unsqueezing sequence, because the squeezed state is sheared by another shearing of Q in the second half of unsqueezing sequence, where Q is the amount of shearing in an antisqueezing sequence.

- At $\varepsilon = 2\theta$, where θ is defined in Fig. 7-44, the state is flipped in the way that the unsqueezing process puts the state back to original coherent spin state. The expected θ is $\tan^{-1}(1/Q)$.

- At $\varepsilon = \theta \pm \pi/2$, the state is rotated for the long axis of the sheared state to be along population difference direction. This means during the unsqueezing, it has a factor of Q leverage for the shearing by Q, and therefore resulting uncertainty in phase direction is Q^2. Note that this state is the most sensitive to the contrast loss.

The solid line in the figure is based on a theoretical calculation with $N_{\mathrm{tot}} = 600$. The $Q = 4.00$ used for the theoretical calculation reasonably matches the experimental result. The unsqueezing strongly suggests that the antisqueezing we observed in Fig. 7-42 is not due to some classical noise but spin squeezing, because the classical noise

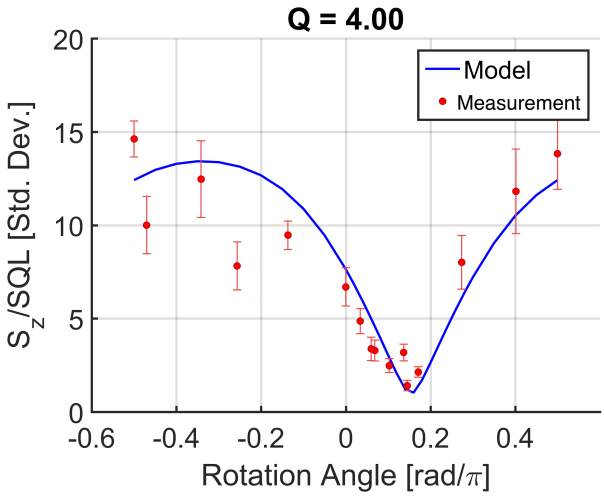

Figure 7-45: Result of unsqueezing for $N_\gamma \sim 4000$: the uncertainty of unsqueezed state in phase direction is plotted for different rotation angle ε. Red dots are experimental results, and blue solid line is a numerical fit of the experimental results to a theoretical model with $N_{\text{tot}} = 600$.

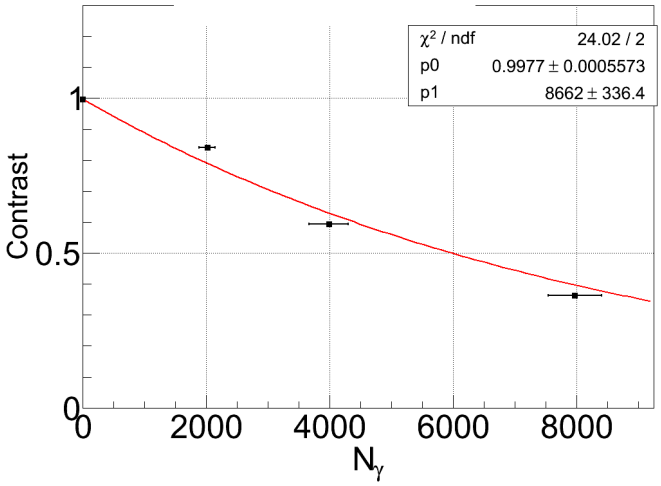

Figure 7-46: Contrast Measurement for Unsqueezing: the fit function is $y = p_0 \exp(-N_\gamma/p_1)$.

simply adds up when the same sequence is repeated.[9]

[9]It is true that certain kind of classical noise can behave in the similar way to unsqueezing, like the state's narrowing down to original coherent spin state in spin echo. This is another reason we need to show the gain in phase sensitivity to show that the phenomena we are observing here is not classical but quantum.

7.10.4 Gain in phase sensitivity

To see if this squeezing and unsqueezing by cavity feedback squeezing is useful for metrology, the gain in phase sensitivity is the direct thing to show. The gain in phase sensitivity by the one axis squeezing comes from the fact that the point 1 SQL away from the equator in population difference direction has a factor of Q shearing. If two states are δ radian apart in the population difference direction on the Bloch sphere, after one axis squeezing that generates the shearing of Q, the shift in the phase direction is $Q\delta$. [116, 147]

To demonstrate this in our system and measure the amount of gain, we run experiments with the sequence shown in Fig. 7-47. This sequence is exactly the same as the unsqueezing sequence shown in Fig. 7-43, except for the δ pulse after the ε pulse and a π pulse. To have the best resolution at the final state, we set $\varepsilon = 2\theta$ derived from the unsqueezing experiment. The δ pulse is for rotating the state by angle δ radian along the rotation axis same as the first $\pi/2$ pulse to shift the state in population difference direction. We chose a few different δ. The experiment is performed in the same way as antisqueezing and unsqueezing experiments; we run the sequence ~ 100 times for each data point, and post select the data by the contrast of the phase measurement ($C > 0.8$), the atom number $N_1 + N_2$ (typically 2000 ± 200), and detected photon number N_γ (target number$\pm$10%).

Fig. 7-48 shows the result of the gain in phase sensitivity. The graph shows that the slope $(N_1/N_{\rm tot})/\delta$ with the unsqueezing sequence is 2.10 times larger than that of a Ramsey sequence with full contrast, and 3.45 times larger than that of a Ramsey sequence with reduced contrast by $N_\gamma \sim 4000$ unsqueezing process. This shows that the unsqueezing process increased the phase sensitivity by factor of 3.45 in the unit of standard deviations. The theory predicts that this number should match with Q obtained by the unsqueezing measurement, and the gain of 3.45 is reasonably close to $Q = 4.00$ described in Fig. 7-45. This proves that the state after the antisqueezing process is broadened by the quantum mechanical effect of the cavity

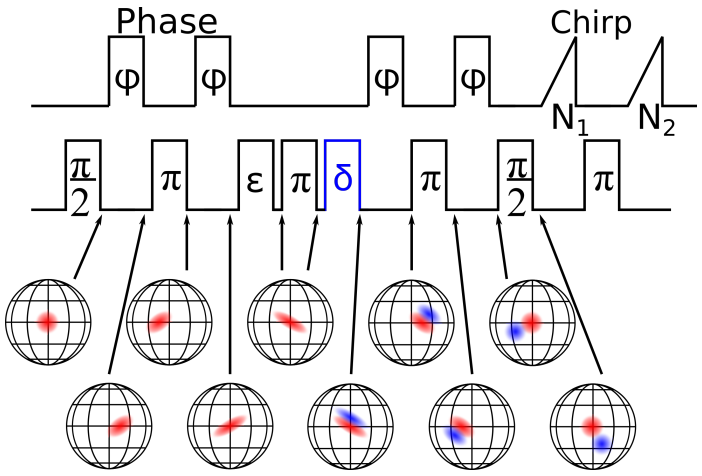

Figure 7-47: Sequence for phase sensitivity gain experiment: the picture below the sequence shows the change from a coherent state in the ideal system. The blue distribution is the sequence with the δ rotation pulse, and the red distribution is the case without the rotation pulse for comparison. The first three π pulses and the second $\pi/2$ pulse is along S_y, and the first $\pi/2$ pulse, the δ pulse, and the last π pulse are along S_x. The ε pulse has the rotation axis that matches to the residual phase shift observed in antisqueezing measurement.

feedback squeezing. Assuming that $Q = 3.45$, the inferred amount of squeezing is

$$\xi_W^2 = \frac{1}{C^2}\frac{1}{Q^2} = 0.138 = -8.6 \text{ dB} \tag{7.9}$$

Here, Fisher information is assumed to be much smaller than 1, based on the theoretical calculation shown in Fig. 7-38, and only slightly broadened state ($\sigma = 1.41 \pm 0.28SQL$) at the bottom of the dip in Fig. 7-45, and $C = 0.783$ based on the half of the photon number in overall unsqueezing process and Fig. 7-46.

7.10.5 Discussion

Three measurements, antisqueezing, unsqueezing, and gain in phase sensitivity for $N_\gamma = 4000$ reasonably matches to the amount of shearing $Q = 3.45$, and thus the state after the antisqueezing process is inferred to be squeezed by 8.6 dB. This number has reasonable agreement with the theoretical prediction shown in Fig. 7-39 (red curve, $2\delta/\kappa = 64$).

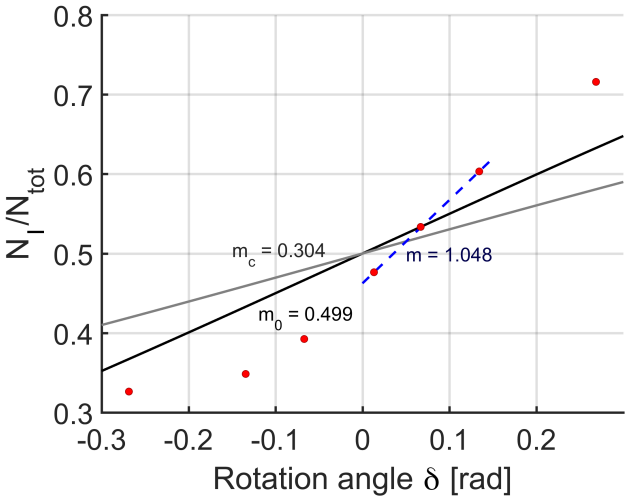

Figure 7-48: Gain in phase sensitivity for detected photon number $N_\gamma \sim 4000$: red dots are the experimental results of the gain in phase sensitivity measurement. m_0, m_c and m are the slope for Ramsey sequence without any phase shift pulses, Ramsey sequence with phase shift pulses with total $N_\gamma \sim 4000$, and with the gain in phase sensitivity experiment. The average N_γ and $N_{\rm tot}$ are 4191 ± 23 and 1916 ± 18. Average here is the simple average of the average N_γ and $N_{\rm tot}$ obtained in each data point, which includes different number of runs.

According to the theory, this squeezing scheme gives Fisher information that is much smaller than 1, and thus the squeezing is unitary. Experimentally, the sign of unitary squeezing is observed, but it is not as reproducible as it should be. In Fig. 7-45, data point at $\epsilon = 0.145\pi$ rad is 1.41 ± 0.28 SQL wide, but $\epsilon = 0.137\pi$ rad point is as wide as 3.17 ± 0.45 SQL. This is probably due to some technical noise that is not well controlled. Possible sources are asymmetry in the sequence regarding ϵ pulse, slightly imperfect $\pi/2$ and π pulse, not fully cancelled transverse magnetic field, and drift in B_z.

To remove the possible source of the noise further, we carefully measure the correct length of π and $\pi/2$ pulse, and make the sequence more symmetric by placing $\varepsilon/2$ pulse before and after the π pulse in the middle, as shown in Fig. 7-49. This have certain benefit on reducing the noise at the best unsqueezing point, and with narrower post selection of the center value ± 5 %, we reproducibly obtained the width of distribution close enough to 1 SQL. Fig. 7-50 compares the result in Fig. 7-45

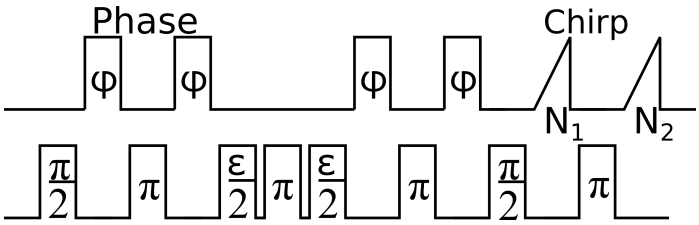

Figure 7-49: More symmetric sequence for unsqueezing experiment: the first three π pulses and the second $\pi/2$ pulse is along S_y, and the first $\pi/2$ pulse and the last π pulse is along S_x. With the fine tuning of RF frequency to the Larmor frequency, and precise pulselength for π and $\pi/2$ pulse, $\varepsilon/2$ pulses have the rotation axis along S_y.

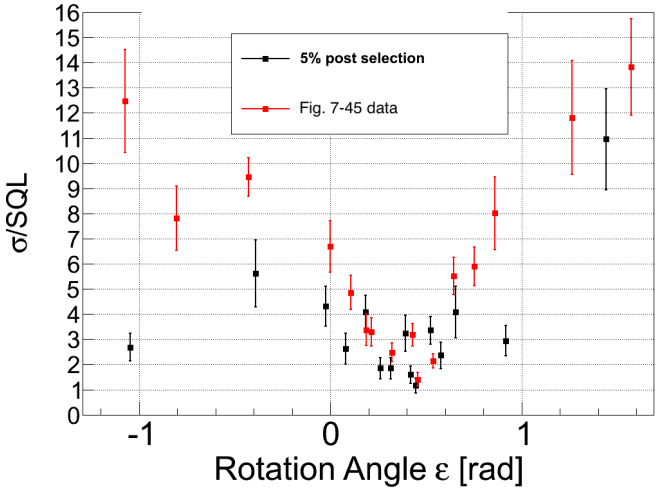

Figure 7-50: Result of unsqueezing for $N_\gamma \sim 4000$: the uncertainty of unsqueezed state in phase direction is plotted for different rotation angle ε.

and the result with symmetric sequence. The symmetric sequence and narrower post selection criterion reduced the noise on the state, which made the result close to the intuitive understanding with $Q = 4$ and contrast $C = 0.61$, and here the bottom of the dip is 1.16 ± 0.29 SQL, which is 1 within the error bar. Thus, the unitary squeezing is demonstrated.

The same problem on the noise also applies to the gain in phase sensitivity measurement. Although the average makes a larger slope than without squeezing and unsqueezing process, the uncertainty of the state is ~ 4 SQL. This actually means this unsqueezing method is not useful for the actual metrology, and the reduction of the noise is desired. The sequence is symmetrized in the similar way as the sym-

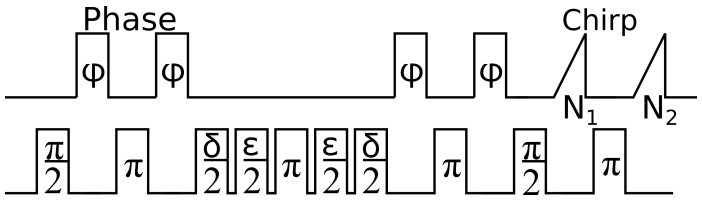

Figure 7-51: Symmetrized sequence for phase sensitivity gain experiment: rotation axis for each pulse is the same as that in Fig. 7-47 with $\delta/2$ pulses and $\epsilon/2$ pulses having same rotation axes as δ pulse and ϵ pulse, respectively.

metric unsqueezing sequence, as shown in Fig. 7-51. This together with narrower post selection reduces the uncertainty down to below 2 SQL. This opens the way to metrological gain in the phase sensitivity, but further reduction of the noise is desired.

Another important thing on these three experiments is that no measurement precision beyond SQL is necessary to do these experiments. 9.0 dB of squeezing has been proved without having as precise atom number measurement as 9.0 dB below SQL. This benefits implementations of this method into actual metrology, as one technical complexity of precise measurement far beyond SQL is removed from the system.

Some possible applications of this method are for atomic clocks or magnetometers. Here, let's take an atomic clock as an example. The basic idea is to have the phase sensitivity gain experiment by the phase drift of the local oscillator from the atomic system. We first prepare the squeezed state by the antisqueezing sequence, and instead of sending a δ rotation pulse, we send $\pi/2$ pulse to make the state elongated in population difference direction. This $\pi/2$ pulse is the start of the interrogation time in the Ramsey sequence. At the end of the interrogation time, we send another $\pi/2$ pulse to rotate the accumulated phase drift to the population difference direction. Then we unsqueeze the state, and the resulting offset at the end of last $\pi/2$ pulse is Q times more than the accumulated phase drift.[10] In a sense, this kind of enhancement in phase detection is possible if you simply make the interrogation time longer. In this sense, the spin squeezing becomes powerful for atomic clocks when it is necessary

[10]This method does not work for the symmetric sequence for the gain in phase sensitivity, because the second $\delta/2$ pulse has opposite rotation axis. Further development of the sequence is desired.

to detect drifts over a relatively short time, or when the interrogation time is limited by some other factors, such as atom lifetime in the optical lattice, in a fountain clock, or laser coherence due to broad linewidth.

Chapter 8

Towards a spin squeezed atomic clock: future directions

8.1 Clock transition search

The search for the ${}^1S_0 \rightarrow {}^3P_0$ transition of ^{171}Yb in our system is performed with the 578 nm laser. The method is to shine the 578 nm laser onto the green MOT and scan the frequency of the 578 nm laser to see a faster decay of atoms in the MOT due to the 578 nm laser's exciting atoms into the metastable state. The laser frequency tuning is performed by locking the laser to the ultrastable cavity and tuning ω_{bridge} of the locking.

To estimate the search range for ω_{bridge}, we first measure the absolute frequency of the cavity mode to which we lock the laser by using the stable axis of the ultrastable cavity, the ${}^1S_0 \rightarrow {}^3P_1$ atomic transition, and the 556 nm laser. The FSR of the cavity is measured by generating sidebands by an EOM with kHz precision. It is 3155.8282(4) MHz for 1157 nm light, and 3155.827(1) MHz for 1112 nm light. This FSR and the frequency difference between the ${}^1S_0 \rightarrow {}^3P_1$ transition and the ${}^1S_0 \rightarrow {}^3P_0$ transition reported in Ref. [148] tells that the frequencies of the undoubled light of two transitions are different by 3342 FSR and 509.3(4.4) MHz. When we lock the 556 nm laser to the atomic resonance of the ${}^1S_0 \rightarrow {}^3P_1$ transition, the cavity resonance of the stable axis is 1130.48 MHz above the atomic transition. This information

indicates that the ${}^1S_0 \rightarrow {}^3P_0$ transition is 1516.0 MHz above the 518299114.7(4.4) MHz cavity resonance. This cavity resonance is proved to exist by a measurement with a wavemeter (Toptica WS7). Thus, the search region has been narrowed down to ~ 2 MHz prior to the search.

The search is performed with ~ 10 mW 578 nm laser focused down to ~ 50 μm. $\omega_{\mathrm{bridge}} = \omega_{\mathrm{AOM}} + \omega_{\mathrm{synth}}$ is found to be 1508.37 MHz, where the frequency shift by AOM $\omega_{\mathrm{AOM}} = 40$ MHz and the synthesizer frequency $\omega_{\mathrm{synth}} = 1468.37$ MHz.[1]

8.2 Future directions

8.2.1 Spin squeezed atomic clock

As we have observed a certain amount of squeezing, the next step for the spin squeezed atomic clock is to put this squeezed state into the 6s6p ${}^3P_0$ excited state via the clock transition. Coherent excitation should be possible simply by shining the 578 nm laser resonant to the ${}^1S_0 \rightarrow {}^3P_0$ transition. To prevent unnecessary decoherence due to the excitation of both Zeeman sublevels, a nonzero magnetic field in z direction should be applied, and pure circularly polarized light should be sent. This makes it possible to excite $m = \pm 1/2$ ground state to $m = \mp 1/2$ state in the excited state, resulting in a superposed state $(|g, \mp 1/2\rangle + |e, \pm 1/2\rangle)/\sqrt{2}$.

To perform this, the 578 nm laser has to be reliable. The locking quality is acceptable, but the ultrastable cavity performance is critical for a stable operation. Because the ultrastable cavity's temperature changes by 50 mK temperature per 1 $^\circ$ room temperature change, a more sophisticated way of stabilizing the ultrastable cavity is desired, such as a temperature stabilization of the inside of the enclosure. To perform a good Rabi spectroscopy, long and weak interrogation pulse is used [4], but typically such a pulse reduces the contrast of Rabi oscillation. [149] At the beginning, a strong but short Rabi pulse is more suitable for transferring atoms from ground state

[1] This measurement was performed before we noticed that the zero crossing of the reference cavity is not 32.5 °C but 2.5 °C. This is why we could not find the transition at the same frequency the next time, and ω_{synth} has to be changed according to the temperature change.

to excited state in a coherent way.

The 578 nm laser has to be shone from the side for a few reasons. First of all, it is almost impossible to get all of the ${}^1S_0 \rightarrow {}^3P_1$ transition, the ${}^1S_0 \rightarrow {}^3P_0$ transition and the magic wavelength of the 759 nm laser to be on resonant to the experimental cavity. Also, we want to excite whole atoms to the excited state without any difference between atoms; therefore we need to have a uniform coupling to the atoms, which is impossible in the magic wavelength lattice. To do the interrogation from the radial direction of the one-dimensional lattice in a recoil-free way, we need to make this lattice at least two-dimensional, so that the trapping in the direction of propagation of the 578 nm laser is in the Lamb-Dicke regime. To achieve this, a tapered amplifier (TA) (Toptica, BoosTA PRO 765) for the 759 nm laser is being built. This will give ~ 1.5 W output, which makes a deep enough lattice in the radial direction.

8.2.2 Cavity QED in the strongly coupled regime

Another direction of the experiment is to generate more sophisticated states for the metrological gain. The unique feature of our experimental cavity can give average cooperativity up to ~ 33, and this enables us to get non-gaussian states through atom light interaction. One example is that, when we send two frequencies, each of which is resonant to one of two resonances of vacuum Rabi splitting and detect a single photon, we can conditionally generate a non-Gaussian state that is a coherent superposition of two CSS that is farther than SQL. The intuitive understanding is that we cannot tell what the frequency of the detected photon is, and the two frequencies induce opposite phase shifts to atoms. Thus atoms are in the superposition state between positive phase shift and negative phase shift. If the cooperativity η is larger than the Fisher information, two blobs are separated to generate a kitten state, and the interference fringe between them gives better phase resolution than the SQL. Key technology here is to have large enough η. So far, we have achieved $\eta \approx 8$, and if we need to achieve higher η we need to establish a way to load atoms very close to micromirrors, such as 50 μm away. Also, a long enough lifetime in the lattice is important. This can be achieved by further reducing the intensity noise of the trapping laser.

Conclusion

We have built an apparatus to spin squeeze an optical lattice clock with ^{171}Yb, and performed spin squeezing on the ground state Zeeman sublevels by nuclear magnetic moment of $I = 1/2$. The spin squeezing is performed by two different methods. Measurement-based squeezing gave 2.1 dB of spin squeezing. Cavity feedback squeezing demonstrated 8.6 dB of squeezing. The cavity feedback squeezing is performed in a unitary way, and this does not involve any measurement more precise than SQL. By transferring the population in one sublevel in the ground state to the 6s6p $^3P_0$ excited state, a squeezed state of a pseudospin system with an electronic excited state is expected to be achieved, and this will lead to an optical lattice clock whose stability is enhanced by spin squeezing.

Appendix A

Derivation of formulae related to spin squeezing

In this section, the details of the derivation of formulae appearing in Chapter 3 are described.

A.1 Strong atom-photon interaction through optical cavity

The starting point of a classical description of atom light behavior in an optical cavity is a Lorentz model with complex polarizability

$$\alpha = 6\pi\varepsilon_0 c^3 \frac{\Gamma/\omega_0^2}{\omega_0^2 - \omega^2 - i(\omega^3/\omega_0^2)\Gamma}, \tag{A.1}$$

for a two level system and light field

$$E(z_0, t) = \frac{\mathcal{E}}{\sqrt{\varepsilon_0 c A}} e^{i(kz_0 - \omega t)}. \tag{A.2}$$

Here, ω is the frequency of the light field, k is the wave number, z_0 is the position of atoms, and $A = \pi w^2/2$ is the effective mode area. $\mathcal{E}$ is a beam size independent electric field that satisfies $P = |\mathcal{E}|^2/2$, where P is the power of a laser beam. Assuming

that an atom is at the waist of a free space Gaussian beam, the coherent scattering into the Gaussian beam direction of this light field is calculated to be

$$\mathcal{E}_{\mathcal{M}} = i\beta\mathcal{E} \tag{A.3}$$

$$\beta = \frac{k}{\pi w^2}\frac{\alpha}{\varepsilon_0} \tag{A.4}$$

by integrating the far field of the dipole radiation field

$$\mathcal{E}_{\mathcal{M}} = \sqrt{\varepsilon_0 c}\int e_{\mathcal{M}} E_{\mathrm{rad}} 2\pi\rho d\rho, \tag{A.5}$$

where cavity mode $e_{\mathcal{M}}$ and field radiated by the atoms E_{rad} are

$$e_{\mathcal{M}}(\rho, z) \approx \left(\frac{2}{\pi w(z)^2}\right)^{1/2} \exp\left(-\frac{\rho^2}{w(z)^2} + ikz + ik\frac{\rho^2}{2z} - i\frac{\pi}{2}\right) \tag{A.6}$$

$$E_{\mathrm{rad}} = \frac{k^2 \sin\theta}{4\pi\varepsilon_0}\frac{e^{ikR}}{R}\alpha E_{\mathrm{in}} \tag{A.7}$$

$$w(z) = w_0\sqrt{1 + \left(\frac{z}{z_R}\right)^2} \approx \frac{wz}{z_R} \tag{A.8}$$

A property of α

$$|\alpha|^2 = \frac{6\pi\varepsilon_0}{k^3}\mathrm{Im}(\alpha), \tag{A.9}$$

gives the following optical theorem for β:

$$|\beta|^2 = \frac{6}{k^2 w^2}\mathrm{Im}(\beta), \tag{A.10}$$

With Eq. A.10 and the integral of Eq. A.7 over a 4π solid angle, the following relation is derived for the total scattering power of an atom driven by a free space Gaussian beam:

$$P_{4\pi} = \frac{ck^4}{12\pi\varepsilon_0}|\alpha E|^2 = \frac{k^2 w^2}{6}|\beta\mathcal{E}|^2 = \mathrm{Im}(\beta)|\mathcal{E}|^2 \tag{A.11}$$

Now, suppose the configuration in Fig. 3-2. With this configuration, intracavity

electric field satisfies following equation.

$$\mathcal{E}_{\rm c} = r_1 r_2 e^{2ikL}\mathcal{E}_{\rm c} + iq_1\mathcal{E}_{\rm in} + 2\mathcal{E}_{\mathcal{M}} \tag{A.12}$$

With the definition of transmission and Eq. A.3, Eq. A.12 is solved as

$$\begin{aligned}
\mathcal{E}_{\rm c} &= \frac{2iq_1\mathcal{E}_{\rm in}}{q_1^2+q_2^2}\frac{1}{1-2i\delta/\kappa - 8i\beta/(q_1^2+q_2^2)} && \text{(A.13)}\\
&= \frac{2iq_1\mathcal{E}_{\rm in}}{q_1^2+q_2^2}\frac{1}{\left(1+{\rm Im}\left(\frac{8\beta}{q_1^2+q_2^2}\right)\right) - \left(\frac{2\delta}{\kappa}+{\rm Re}\left(\frac{8\beta}{q_1^2+q_2^2}\right)\right)i} && \text{(A.14)}
\end{aligned}$$

where detunings are defined as $\delta = \omega - \omega_c$, and $\Delta = \omega - \omega_0$. Using the RWA, we get the following from Eqs. A.1, A.4, and A.13.

$$\mathcal{E}_{\rm c} = \frac{2iq_1\mathcal{E}_{\rm in}}{q_1^2+q_2^2}\frac{1}{\left[1+\eta\mathcal{L}_a(\Delta)\right] - \left[\frac{2\delta}{\kappa}+\eta\mathcal{L}_d(\Delta)\right]i}, \tag{A.15}$$

where

$$\begin{aligned}
\mathcal{L}_a(\Delta) &= \frac{\Gamma^2}{4\Delta^2+\Gamma^2} && \text{(A.16)}\\
\mathcal{L}_d(\Delta) &= \frac{-2\Delta\Gamma}{4\Delta^2+\Gamma^2} && \text{(A.17)}\\
\eta &= \frac{24\mathcal{F}}{\pi w^2 k^2} && \text{(A.18)}
\end{aligned}$$

are the dispersive Lorentzian, absortive Lorentzian, and single atom cooperativity, respectively.

From Eq. A.14, $\mathcal{E}_t$ is calculated as

$$\begin{aligned}
\mathcal{E}_{\rm t} &= iq_2\mathcal{E}_{\rm c}\\
&= \frac{2iq_1q_2\mathcal{E}_{\rm in}}{q_1^2+q_2^2}\frac{1}{\left(1+{\rm Im}\left(\frac{8\beta}{q_1^2+q_2^2}\right)\right) - \left(\frac{2\delta}{\kappa}+{\rm Re}\left(\frac{8\beta}{q_1^2+q_2^2}\right)\right)i} && \text{(A.19)}
\end{aligned}$$

The scattering into free space is calculated by Eq. A.11 with $\mathcal{E} = 2\mathcal{E}_c$:

$$P_{4\pi} = \frac{k^2 w^2}{6}|\beta|^2|2\mathcal{E}_c|^2 \tag{A.20}$$

$$= \frac{2q_1^2}{q_1^2+q_2^2}\mathrm{Im}\left(\frac{16\beta}{q_1^2+q_2^2}\right)\frac{1}{\left(1+\mathrm{Im}\left(\frac{8\beta}{q_1^2+q_2^2}\right)\right)^2+\left(\frac{2\delta}{\kappa}+\mathrm{Re}\left(\frac{8\beta}{q_1^2+q_2^2}\right)\right)^2} \tag{A.21}$$

Dividing by the incident light and using the RWA, the following simple form is obtained.

$$\frac{P_{4\pi}}{P_{in}} = \frac{2q_1^2}{q_1^2+q_2^2}\frac{2\eta\mathcal{L}_a(\Delta)}{\left[1+\eta\mathcal{L}_a(\Delta)\right]^2+\left[\frac{2\delta}{\kappa}+\eta\mathcal{L}_d(\Delta)\right]^2} \tag{A.22}$$

From Eq. A.19, the transmission power is calculated as

$$\frac{P_{tr}}{P_{in}} = \frac{4q_1^2q_2^2}{(q_1^2+q_2^2)^2}\frac{1}{\left[1+\eta\mathcal{L}_a(\Delta)\right]^2+\left[\frac{2\delta}{\kappa}+\eta\mathcal{L}_d(\Delta)\right]^2} \tag{A.23}$$

The phase shift due to the atoms in the cavity is calculated as the phase of $\mathcal{E}_\mathrm{c}/\mathcal{E}_\mathrm{in}$. From Eq. A.19, the phase shift ϕ_ph is

$$\phi_\mathrm{ph} = \tan^{-1}\left(\frac{\frac{2\delta}{\kappa}+\mathrm{Re}\left(\frac{8\beta}{q_1^2+q_2^2}\right)}{1+\mathrm{Im}\left(\frac{8\beta}{q_1^2+q_2^2}\right)}\right) \tag{A.24}$$

$$= \tan^{-1}\frac{\frac{2\delta}{\kappa}+\eta\mathcal{L}_d(\Delta)}{1+\eta\mathcal{L}_a(\Delta)} \tag{A.25}$$

In the second line, the RWA is used. This phase measurement is performed with a homodyne measurement with some reference light.

A.2 Coherent spin state in Ref. [2]

The coherent spin state is defined is Eq. 3.17, but the original definition in the first proposal in Ref. [2] is different. There, it is defined as

$$|\mu\rangle = \frac{1}{(1+|\mu|^2)^S}\exp\left(\mu\hat{S}_-\right)|0\rangle = \frac{1}{(1+|\mu|^2)^S}\sum_{k=0}^{2S}\left(\frac{2S!}{k!\,(2S-k)!}\right)^{1/2}\mu^k|k\rangle, \tag{A.26}$$

where μ is a complex number, $k = 2S$ corresponds to a state where all the atoms are in the $|\downarrow\rangle$ state, and $k = 0$ corresponds to a state where all spins are in the $|\uparrow\rangle$ state. [2] When θ and ϕ are defined as $\mu = \tan\frac{\theta}{2}e^{i\phi}$, Eq. A.26 becomes

$$|\theta,\phi\rangle = \left(\cos\frac{\theta}{2}\right)^{2S} \exp\left(\tan\frac{\theta}{2}e^{i\phi}\hat{S}_-\right)|0\rangle, \tag{A.27}$$

which is easier to understand as the spin state oriented to the direction of the polar coordinates (θ,ϕ). Note that this is an approximation for large S with a small number of $|\downarrow\rangle$ components, which is a good way to describe solid state magnetic system in a magnetic field.

A.3 Amount of squeezing by one axis squeezing

Unitary squeezing makes use of a unitary transformation $\hat{U}(t) = \exp[-itF(\hat{S}_z)]$ generated by the Hamiltonian $H = \hbar F(\hat{S}_z)$. This transforms the ladder operator $\hat{S}_+$ as follows:

$$\hat{S}_+(t) = \hat{U}^\dagger\hat{S}_+\hat{U} = \hat{S}_+(0)\exp\left[itf(\hat{S}_z)\right] \tag{A.28}$$

$$f(\hat{S}_z) = F(\hat{S}_z+1) - F(\hat{S}_z) \tag{A.29}$$

When the Hamiltonian is the lowest order nonlinear Hamiltonian

$$\hat{H} = \hbar\chi\hat{S}_z^2 \tag{A.30}$$

$f(\hat{S}_z) = 2\chi(\hat{S}_z + 1/2)$. Substituting this into Eq. A.28, we get the ladder operators at time t. Rotating this distribution around the x axis with $\exp(i\nu\hat{S}_x)\hat{S}\exp(-i\nu\hat{S}_x)$ and starting with a coherent state

$$|\theta,\phi\rangle = |\frac{\pi}{2},0\rangle = \frac{1}{2^S}\sum_{m=0}^{2S}\binom{2S}{m}^{1/2}|S,m\rangle \tag{A.31}$$

as an initial state, the following distribution is obtained.

$$\langle \hat{S}_x \rangle = S \cos^{2S-1} \frac{\mu}{2},\ \langle \hat{S}_y \rangle = 0,\ \langle \hat{S}_z \rangle = 0 \tag{A.32}$$

$$\langle \Delta \hat{S}_x^2 \rangle = \frac{S}{2} \left[2S \left(1 - \cos^{2(2S-1)} \frac{\mu}{2} \right) - \left(S - \frac{1}{2} \right) A \right] \tag{A.33}$$

$$\langle \Delta \hat{S}_{y,z}^2 \rangle = \frac{S}{2} \left[1 + \frac{1}{2} \left(S - \frac{1}{2} \right) \left(A \pm \sqrt{A^2 + B^2} \cos(2\nu + 2\delta) \right) \right], \tag{A.34}$$

where $A = 1 - \cos^{2S-2} \mu$, $B = 4 \sin \frac{\mu}{2} \cos^{2S-2} \frac{\mu}{2}$, $\mu = 2\chi t$, $\delta = \frac{1}{2} \tan^{-1} \frac{B}{A}$. $\langle \Delta \hat{S}_y^2 \rangle$ is minimized, and $\langle \Delta \hat{S}_z^2 \rangle$ is maximized at $\nu = \frac{\pi}{2} - \delta$. The increased and reduced variances are

$$V_{\pm} = \frac{S}{2} \left[1 + \frac{1}{2} \left(S - \frac{1}{2} \right) A \pm \left(S - \frac{1}{2} \right) \sqrt{A^2 + B^2} \right] \tag{A.35}$$

Here, we are particularly interested in the reduced variance V_-. For $S \gg 1$ and $|\mu| \ll 1$,

$$V_- \approx \frac{S}{2} \left(\frac{1}{S^2 \mu^2 + \frac{1}{24} S^2 \mu^4} \right), \tag{A.36}$$

where $\alpha = \frac{1}{2} S\mu$ and $\beta = \frac{1}{4} S\mu^2$. The minimum value for V_- is

$$V_{\min} \approx \frac{1}{2} \left(\frac{S}{3} \right)^{1/3} \sim S^{1/3} \tag{A.37}$$

at $|\mu| = 24^{1/6} S^{-2/3}$.

A.4 Amount of measurement-based squeezing in our system

First, we think of the atom number measurement by transmission power of the vacuum Rabi splitting. The transmission photon is detected by a single photon counter of quantum efficiency of c including all the coupling efficiency. The definition of N, N_1 and N_2 gives

$$S_z = N_1 - \frac{1}{2} N_0 \tag{A.38}$$

From Eq. 3.24 and Eq. A.38,

$$\xi_W^2 = \frac{1}{C^2}\frac{2\left(\Delta N_1\right)^2}{N_1} \tag{A.39}$$

The uncertainty of N_1 is evaluated by Eq. 3.14:

$$\frac{\left(\Delta N_1\right)^2}{N_1} = 16\frac{(\Delta f)^2}{\eta\gamma_{\rm g}^2}, \tag{A.40}$$

where $\gamma_{\rm g} = \sqrt{\kappa\Gamma}$. As the scattering of the probe photon only happens for the $|\uparrow\rangle$ state, assuming the state is initially $Sz = 0$, the following probabilities are true.

$$\begin{aligned}
p(s|\uparrow) &= 1 - e^{-\gamma t} && \text{(A.41)}\\
p(ns|\uparrow) &= e^{-\gamma t} && \text{(A.42)}\\
p(s) &= \frac{1}{2} = \frac{1}{2}\left(1 - e^{-\gamma t}\right),\ p(ns) = 1 - p(s) && \text{(A.43)}\\
p(\uparrow|ns) &= \frac{p(ns|1)p(1)}{p(ns)} = \frac{e^{-\gamma t}}{1 + e^{-\gamma t}}, && \text{(A.44)}
\end{aligned}$$

where s and ns stand for scattering and no scattering. Because the contrast for the state $\sqrt{p_1}|\uparrow\rangle + \sqrt{1-p_1}|\downarrow\rangle$ is $C = 2\sqrt{p_1(1-p_1)} = \sqrt{p_1 p_2}$, the remaining contrast is

$$C^2 = C_{\rm ns}^2 p(ns) = \frac{2e^{-\gamma t}}{1 + e^{-\gamma t}} \tag{A.45}$$

Define $m = p/N_1$, a relation $p_{\rm sc} = (\Gamma/\kappa)p$ between the transmitted photon number p and the scattered photon number $p_{\rm sc}$, and a quantum efficiency including all coupling constants c. A peak center estimate with cp detected photons is

$$(\Delta f)^2 = \frac{0.5}{cp}\gamma_{\rm av}^2 \tag{A.46}$$

From Eqs. A.39, A.40, A.45, A.46, the following expression is obtained with $x = m\Gamma/\kappa$:

$$\xi_{W,\rm tr}^2 = \frac{32}{N_1\eta}\frac{0.5}{c}\frac{\gamma_{\rm av}}{\gamma_{\rm g}}\frac{\Gamma}{\kappa}\frac{1}{2xe^{-x}/(1+e^{-x})} \tag{A.47}$$

The maximum of $2xe^{-x}/(1+e^{-x})$ is 0.5569 at $x = 1.278$. Thus, the final expression is

$$\xi^2_{W,\mathrm{tr}} = \frac{32}{N_1\eta}\frac{0.8978}{c}\frac{\gamma_{\mathrm{av}}}{\gamma_{\mathrm{g}}}\frac{\Gamma}{\kappa} \tag{A.48}$$

Next, we estimate the amount of squeezing by phase measurement. The basic formula is the same as the transmission case, and only the precision of the peak center estimate is different. Substituting $\beta = 0$ into Eq. A.13, the phase shift of the output light is $2\delta/\kappa$. In the vacuum Rabi splitting case, $\Delta\phi = 2\Delta f/\gamma_{\mathrm{av}}$. This gives

$$\left(\frac{\Delta f}{\gamma_{\mathrm{g}}}\right) = \frac{1}{4}\left(\frac{\gamma_{\mathrm{av}}}{\gamma_{\mathrm{g}}}\right)(\Delta\phi)^2 \tag{A.49}$$

If the phase measurement is by homodyne detection, the noise of the signal is $(\Delta n_{\mathrm{hom}})^2 = 4(cp)^2(\Delta\phi)^2$, because the signal is $cp(\sin^2(\Delta\phi+\pi/2)-\cos^2(\Delta\phi+\pi/2))= cp\sin(2\Delta\phi) = 2cp\Delta\phi$. The noise of heterodyne detection is twice as bad, and assuming the signal equals the shot noise,

$$(\Delta\phi)^2 = \frac{1}{2cp} \tag{A.50}$$

From Eqs. A.39, A.40, A.45, and with a treatment to maximize the contrast factor the same as the transmission case, the following expression is obtained.

$$\xi^2_{W,\mathrm{ph}} = \frac{8}{N_1\eta}\frac{0.8978}{c}\frac{\gamma_{\mathrm{av}}}{\gamma_{\mathrm{g}}}\frac{\Gamma}{\kappa} \tag{A.51}$$

This assumes that the probe light is parked on the peak of the vacuum Rabi splitting. An easier situation is when the probe frequency is scanned over a peak. In this case, the Fisher information of the phase $\phi = \tan^{-1} x$ is $1/(1+x^2)$, and the probability of a photon to be transmitted is another Lorentzian, and therefore the overall efficiency drops to

$$\int_{\infty}^{\infty}\frac{1}{\pi}\frac{1}{1+x^2}\frac{1}{(1+x^2)}dx = \frac{3}{8} \tag{A.52}$$

Thus, the Wineland parameter for the phase measurement when the probe frequency

is scanned is

$$\xi^2_{W,\mathrm{ph}} = \frac{64}{3N_1\eta}\frac{0.8978}{c}\frac{\gamma_{\mathrm{av}}}{\gamma_{\mathrm{g}}}\frac{\Gamma}{\kappa}, \tag{A.53}$$

A.5 Amount of cavity feedback squeezing in our system

The system for the cavity feedback squeezing is also the same as that for measurement-based squeezing. The difference is that the probe laser frequency is off resonance, i.e. off from both the bare atomic resonance and the resonance of the vacuum Rabi splitting. The estimation of the atomic phase shift starts from the following relation between the atomic phase per transmission photon and the light phase:

$$\varphi_{\mathrm{at,t}} = \frac{d\phi_{\mathrm{ph,t}}}{dS_z} = \frac{d\phi_{\mathrm{ph,t}}}{dN_1} \tag{A.54}$$

The phase of transmitted light described in Eq. A.25 gives

$$\varphi_{\mathrm{at,t}} = -\eta\frac{x+y}{1+y^2}T_{\mathrm{s}}, \tag{A.55}$$

where T_s is the transmission coefficient $P_{\mathrm{tr}}/P_{\mathrm{in}}$ of a symmetric cavity. From A.23,

$$T_s = |t_s|^2 = \frac{1}{\left[1+N_1\eta\mathcal{L}_a(y)\right]^2+\left[x+N_1\eta\mathcal{L}_d(y)\right]^2} \tag{A.56}$$

$$= \frac{1+y^2}{y^2+x^2(1+y^2)-2N_1\eta xy+(1+N_1\eta)^2} \tag{A.57}$$

Based on the argument of a dipole transition, the phase of scattered light is the same as that of transmitted light. Thus, the atomic phase due to the scattered light is the same as that due to the transmission. To discuss the reflection light, the following relation is useful, where $q = q_1/q_2$:

$$t = \frac{2q_1q_2}{q_1^2+q_2^2}t_s = \frac{2q}{1+q^2}t_s = \frac{\varepsilon}{q}t_s \tag{A.58}$$

The electric field of the reflected light is given by $r_1\mathcal{E}_{\rm in} - q_1\mathcal{E}_{\rm c} = \mathcal{E}_{\rm in} - \frac{q_1}{q_2}\mathcal{E}_{\rm t} = \mathcal{E}_{\rm in}(1 - \frac{q_1}{q_2}t)$. Therefore

$$\begin{aligned} r &= 1 - \frac{2q^2}{1+q^2}t_s \\ &= \frac{\left[1+N_1\eta\mathcal{L}_a(y)\right]^2 + \left[x+N_1\eta\mathcal{L}_d(y)\right]^2 - \varepsilon\left(\left[1+N_1\eta\mathcal{L}_a(y)\right] + i\left[x+N_1\eta\mathcal{L}_d(y)\right]\right)}{\left[1+N_1\eta\mathcal{L}_a(y)\right]^2 + \left[x+N_1\eta\mathcal{L}_d(y)\right]^2} \end{aligned} \tag{A.59}$$

This gives

$$\phi_{\rm ph,r} = \tan^{-1}\frac{-\varepsilon\left[x+N_1\eta\mathcal{L}_d(y)\right]}{\left[1+N_1\eta\mathcal{L}_a(y)\right]^2 + \left[x+N_1\eta\mathcal{L}_d(y)\right]^2 - \varepsilon\left[1+N_1\eta\mathcal{L}_a(y)\right]} \tag{A.60}$$

and therefore

$$\begin{aligned} \varphi_{\rm at,r} &= \frac{d\phi_{\rm ph,r}}{dN_1} \\ &= \frac{\eta(x+y-\varepsilon y)}{-2N_1\eta(\varepsilon-1+xy) + ((\varepsilon-1)^2+x^2)(1+y^2) + N_1^2\eta^2} + \varphi_{\rm at,t} \qquad \text{(A.61)} \\ &= \varphi_{\rm at,r0} + \varphi_{\rm at,t} \qquad \text{(A.62)} \end{aligned}$$

The total atomic phase per incoming photon is

$$\varphi_{\rm at,tot} = R\left(\varphi_{\rm at,r0} + \varphi_{\rm at,t}\right) + (T+\rho)\,\varphi_{\rm at,t} = \varphi_{\rm at,t} + R\varphi_{\rm at,r0}, \tag{A.63}$$

where ρ is the scattering probability, and $R+T+\rho = 1$. Eqs. A.22 and A.23 give

$$\rho = 2\varepsilon N\eta\mathcal{L}_a(y)T_s = \frac{1+q^2}{2}2N\eta\mathcal{L}_a(y)T \tag{A.64}$$

From Eqs. A.63, A.55, A.61, A.23, A.64, and $R = 1-T-\rho$, a final expression of

$$\varphi_{\rm at,tot} = -\eta\frac{y}{1+y^2}\frac{2q^2}{1+q^2}T_s = -\eta\frac{y}{1+y^2}\frac{1+q^2}{2}T \tag{A.65}$$

is obtained.

The shearing per incoming photon is calculated as

$$Q_1 = \frac{\varphi_{\mathrm{at,tot}}(S_z = \sqrt{S/2}) - \varphi_{\mathrm{at,tot}}(S_z = 0)}{(\Delta\phi)_{\mathrm{SQL}}} = \sqrt{2S}\frac{d\varphi_{\mathrm{at,tot}}}{dS_z}\sqrt{\frac{S}{2}} = S\frac{d\varphi_{\mathrm{at,tot}}}{dS_z} \quad \text{(A.66)}$$

From Eq. A.65, we obtain

$$Q = p_{\mathrm{in}} N_1 \frac{d\varphi_{\mathrm{at,tot}}}{dN_1} = -\eta p_{\mathrm{sc}} \frac{1+q^2}{2} \frac{y(xy - N_1\eta - 1)}{1+y^2} T \quad \text{(A.67)}$$

$$= -2p_{\mathrm{in}} N_1 \eta^2 \frac{1+q^2}{2} \frac{y(xy - N\eta - 1)}{(1+y^2)^2} T^2 \quad \text{(A.68)}$$

So far our discussion has been limited to the phase shift. To estimate the amount of squeezing, the antisqueezing due to the Fisher information needs to be calculated. To estimate it, let us start from a coherent state for cavity transmission:

$$\alpha = t\alpha_{\mathrm{in}} \quad \text{(A.69)}$$

Here, t can be written as $t = \sqrt{T}e^{-i\phi}$. Regarding the atom number estimate, t should be differentiated by atom number N.

$$\frac{\partial t}{\partial N} = \frac{1}{2\sqrt{T}}\frac{\partial T}{\partial N}e^{i\phi} + i\sqrt{T}\frac{\partial \phi}{\partial N}e^{i\phi} \quad \text{(A.70)}$$

$$\left|\frac{\partial t}{\partial N}\right|^2 = \frac{1}{4T}\left(\frac{\partial T}{\partial N}\right)^2 + T\left(\frac{\partial \phi}{\partial N}\right)^2 \quad \text{(A.71)}$$

As each quadrature of the coherent state has variance of 1/4,

$$\frac{1}{4} = p_{\mathrm{in}}\frac{1}{4T}\left(\frac{\partial T}{\partial N}\right)^2 (\Delta N)^2 \quad \text{(A.72)}$$

$$\frac{1}{4} = p_{\mathrm{in}} T\left(\frac{\partial \phi}{\partial N}\right)^2 (\Delta N)^2 \quad \text{(A.73)}$$

Therefore

$$\frac{1}{(\Delta N)^2} = p_{\text{in}} \frac{1}{4T} \left(\frac{\partial T}{\partial N} \right)^2 \tag{A.74}$$

$$\frac{1}{(\Delta N)^2} = 4 p_{\text{in}} T \left(\frac{\partial \phi}{\partial N} \right)^2 \tag{A.75}$$

Note that this means that the cavity feedback squeezing has an effect due to the phase shift (Eq. A.75) in addition to the transmission change (Eq. A.74), as explained in Section 3.5. Naively, the atom number uncertainty is

$$\frac{1}{(\Delta N)^2} = 2 p_{\text{in}} \left| \frac{\partial t}{\partial N} \right|^2, \tag{A.76}$$

but when the polar angle of a state is known, the fluctuation along the radial direction does not come into the measurement, and the measurement is twice as precise. Because $r = 1 - t$ and $s_i = \sqrt{2\eta \mathcal{L}_a(y)} t$, where the subscript i is the scattering due to the ith atom.

$$\left| \frac{\partial t}{\partial N} \right|^2 = \left| \frac{\partial r}{\partial N} \right|^2 \tag{A.77}$$

$$\left| \frac{\partial s_i}{\partial N} \right|^2 = 2\eta \mathcal{L}_a(y) \left| \frac{\partial t}{\partial N} \right|^2 \tag{A.78}$$

Thus,

$$\frac{1}{(\Delta N)_t^2} = \frac{1}{(\Delta N)_r^2} = 4 p_{\text{in}} \left| \frac{\partial t}{\partial N} \right|^2 \tag{A.79}$$

$$\frac{1}{(\Delta N)_s^2} = 8 p_{\text{in}} N \eta \mathcal{L}_a(y) \left| \frac{\partial t}{\partial N} \right|^2 \tag{A.80}$$

Note that the effect of N atoms is summed for the scattering component. Summing these three terms, the total atom number uncertainty is

$$\frac{1}{(\Delta N)_{\text{tot}}^2} = 8 p_{\text{in}} (1 + N \eta \mathcal{L}_a(y)) \left| \frac{\partial t}{\partial N} \right|^2 \tag{A.81}$$

As

$$\left|\frac{\partial t}{\partial N}\right|^2 = \left(\frac{4q_1q_2}{q_1^2+q_2^2}\right)^2 \eta^2 \frac{1+y^2}{(y^2+x^2(1+y^2)-2N_1\eta xy+(1+N_1\eta)^2)^2} \tag{A.82}$$

The Fisher information is

$$\begin{aligned} F_{\rm tot} &= \frac{2N_1}{(\Delta N_1)^2} = 4\left(\frac{2q_1q_2}{q_1^2+q_2^2}\right)^2 p_{\rm in}N_1\eta^2\frac{1+y^2+N_1\eta}{(1+y^2)^2}T_s^2 &\text{(A.83)}\\ &= 2\eta p_{\rm sc}\frac{\varepsilon^2}{q^2}\frac{1+y^2+N_1\eta}{1+y^2}T_s &\text{(A.84)}\end{aligned}$$

The overall squeezing for large Q is

$$\xi_W^2 = \frac{1+F}{Q^2} = \left(\frac{2}{1+q^2}\right)^2 \frac{(1+y^2)^2+8\eta p_{\rm sc}(1+y^2+N_1\eta)(1+y^2)T}{\eta^2 p_{\rm sc}^2 y^2(xy-N_1\eta-1)^2T^2} \tag{A.85}$$

Appendix B

Modified current controller

The standard laser current controller in our lab is a Libbrecht-Hall type controller [130] designed by a former group member. The low noise feature of this current controller comes from temperature stabilized voltage reference LM399, as well as capacitors and inductors for cutting off high frequency noise. The controller has a main current source regulated by a FET, and it also has a modulation input that can apply a small amount of modulation current proportional to an input voltage, which is used for scanning laser frequency, or as an input for a negative feedback to stabilize a laser frequency. This modulation input is commonly used for the input signal from a lockbox in our lab, and in our design, this modulation signal is split into two paths: an output for piezo modulation, and that for laser current modulation, as shown in the left half of Fig. B-1.

For the lasers with optical feedback, which are 759 nm and 1157 nm master lasers, the piezo modulation goes to the piezo in the path of the optical feedback, and both paths have modulation by the input signal at low frequency.[1] Because the main low frequency drift is the drift of path length of the optical feedback path, this should be compensated only by the piezo tuning, and current tuning at the same time increases a danger of mode hopping. To prevent this current tuning at low frequency, we put a high pass filter in the current modulation path, as shown in the right half of Fig. B-1.

[1] At high frequency, the piezo path has a low pass filter in addition to the capacitance of the piezo itself.

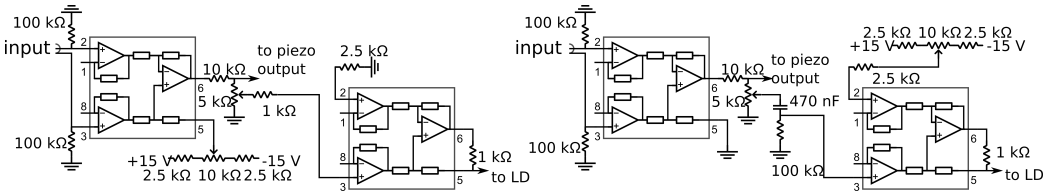

Figure B-1: Schematics for the modified current controller: original design (left)) and modified design (right). Only the modulation input path is written.

The feature of this modification is that the DC offset feature by a voltage divider between ±15 V is changed from common tuning for both piezo and current to the tuning only for current. This enables the precise tuning of the current by a POT in the voltage divider even with an AC coupling from input. The DC offset of the piezo tuning is performed by a DC offset in input signal, which is typically provided by an output offset feature in the lockbox.

Bibliography

[1] Boris Braverman. Cavity quantum electrodynamics with ensembles of ytterbium-171. *Doctoral Thesis, Massachusetts Institute of Technology*, 2017.

[2] J M Radcliffe. Some properties of coherent spin states. *Journal of Physics A: General Physics*, 4(3):313, 1971.

[3] https://www.nist.gov/pml/time-and-frequency-division/primary-standard-nist-f1.

[4] N. Hinkley, J. A. Sherman, N. B. Phillips, M. Schioppo, N. D. Lemke, K. Beloy, M. Pizzocaro, C. W. Oates, and A. D. Ludlow. An atomic clock with 10^{-18} instability. *Science*, 341(6151):1215–1218, 2013.

[5] N. Huntemann, B. Lipphardt, Chr. Tamm, V. Gerginov, S. Weyers, and E. Peik. Improved limit on a temporal variation of m_p/m_e from comparisons of Yb^+ and Cs atomic clocks. *Phys. Rev. Lett.*, 113:210802, Nov 2014.

[6] Monika H. Schleier-Smith, Ian D. Leroux, and Vladan Vuletić. Squeezing the collective spin of a dilute atomic ensemble by cavity feedback. *Phys. Rev. A*, 81:021804, Feb 2010.

[7] L. Pezzè, A. Smerzi, M. K. Oberthaler, R. Schmied, and P. Treutlein. Non-classical states of atomic ensembles: fundamentals and applications in quantum metrology. *arXiv*, 1609.01609, Sep 2016.

[8] André Heinz. Frequency stabilization of lasers in an optical clock experiment. *Master Thesis in Physics, Friedrich-Alexander University Erlangen-Nuremberg*, 2015.

[9] Akio Kawasaki, Boris Braverman, QinQin Yu, and Vladan Vuletic. Two-color magneto-optical trap with small magnetic field for ytterbium. *Journal of Physics B: Atomic, Molecular and Optical Physics*, 48(15):155302, 2015.

[10] Kanhaiya Pandey, Alok K. Singh, P. V. Kiran Kumar, M. V. Suryanarayana, and Vasant Natarajan. Isotope shifts and hyperfine structure in the 555.8-nm $^1S_0 \rightarrow {}^3P_1$ line of yb. *Phys. Rev. A*, 80:022518, Aug 2009.

[11] Dipankar Das, Sachin Barthwal, Ayan Banerjee, and Vasant Natarajan. Absolute frequency measurements in yb with 0.08 ppb uncertainty: Isotope shifts and hyperfine structure in the 399−nm $^1s_0 \rightarrow ^1 p_1$ line. *Phys. Rev. A*, 72:032506, Sep 2005.

[12] D.B. Sullivan. Time and frequency measurement at nist: The first 100 years. *Proc. 2001 IEEE International Frequency Control Symposium and PDA Exhibition*, pages 4–17, 2001.

[13] H. Lyons. The atomic clock. *Instruments*, 22:133–135, Dec 1949.

[14] Harold Lyons. Spectral lines as frequency standards. *Annals of the New York Academy of Sciences*, 55(5):831–871, 11 1952.

[15] J. V. L. Parry L. Essen. Atomic and astronomical time. *Nature*, 177:744, Apr 1956.

[16] W. Markowitz, R. Glenn Hall, L. Essen, and J. V. L. Parry. Frequency of cesium in terms of ephemeris time. *Phys. Rev. Lett.*, 1:105–107, Aug 1958.

[17] J. Guena, M. Abgrall, D. Rovera, P. Laurent, B. Chupin, M. Lours, G. Santarelli, P. Rosenbusch, M. E. Tobar, R. Li, K. Gibble, A. Clairon, and S. Bize. Progress in atomic fountains at lne-syrte. *IEEE Transactions on Ultrasonics, Ferroelectrics, and Frequency Control*, 59(3):391–409, March 2012.

[18] Thomas P Heavner, Elizabeth A Donley, Filippo Levi, Giovanni Costanzo, Thomas E Parker, Jon H Shirley, Neil Ashby, Stephan Barlow, and S R Jefferts. First accuracy evaluation of nist-f2. *Metrologia*, 51(3):174, 2014.

[19] V Gerginov, N Nemitz, S Weyers, R Schröder, D Griebsch, and R Wynands. Uncertainty evaluation of the caesium fountain clock ptb-csf2. *Metrologia*, 47(1):65, 2010.

[20] Krzysztof Szymaniec, Sang Eon Park, Giuseppe Marra, and Witold Chałupczak. First accuracy evaluation of the npl-csf2 primary frequency standard. *Metrologia*, 47(4):363, 2010.

[21] Steven Peil, Thomas B Swanson, James Hanssen, and Jennifer Taylor. Microwave-clock timescale with instability on order of 10 — 17. *Metrologia*, 54(3):247, 2017.

[22] J. C. Bergquist, Wayne M. Itano, and D. J. Wineland. Recoilless optical absorption and doppler sidebands of a single trapped ion. *Phys. Rev. A*, 36:428–430, Jul 1987.

[23] Warren Nagourney, Nan Yu, and Hans Dehmelt. High resolution ba+ monoion spectroscopy with frequency stabilized color-center laser. *Optics Communications*, 79(3):176 – 180, 1990.

[24] E Peik, G Hollemann, and H Walther. Double resonance spectroscopy of a single trapped indium ion. *Physica Scripta*, 1995(T59):403, 1995.

[25] G. P. Barwood, C. S. Edwards, P. Gill, H. A. Klein, and W. R. C. Rowley. Observation of the 5s2s1/2-4d2d5/2 transition in a single laser-cooledtrapped sr+ ion by using an all-solid-state system oflasers. *Opt. Lett.*, 18(9):732–734, May 1993.

[26] S. Urabe, M. Watanabe, H. Imajo, K. Hayasaka, U. Tanaka, and R. Ohmukai. Observation of doppler sidebands of a laser-cooled ca+ ion by using a low-temperature-operated laser diode. *Applied Physics B*, 67(2):223–227, 1998.

[27] M. Roberts, P. Taylor, G. P. Barwood, P. Gill, H. A. Klein, and W. R. C. Rowley. Observation of an electric octupole transition in a single ion. *Phys. Rev. Lett.*, 78:1876–1879, Mar 1997.

[28] E Träbert, A Wolf, J Linkemann, and X Tordoir. Measurement of the b + and al + intercombination and sc 12+ forbidden transition rates at a heavy-ion storage ring. *Journal of Physics B: Atomic, Molecular and Optical Physics*, 32(2):537, 1999.

[29] T. Rosenband, D. B. Hume, P. O. Schmidt, C. W. Chou, A. Brusch, L. Lorini, W. H. Oskay, R. E. Drullinger, T. M. Fortier, J. E. Stalnaker, S. A. Diddams, W. C. Swann, N. R. Newbury, W. M. Itano, D. J. Wineland, and J. C. Bergquist. Frequency ratio of al+ and hg+ single-ion optical clocks; metrology at the 17th decimal place. *Science*, 319(5871):1808–1812, 2008.

[30] C. W. Chou, D. B. Hume, J. C. J. Koelemeij, D. J. Wineland, and T. Rosenband. Frequency comparison of two high-accuracy al^+ optical clocks. *Phys. Rev. Lett.*, 104:070802, Feb 2010.

[31] N. Huntemann, C. Sanner, B. Lipphardt, Chr. Tamm, and E. Peik. Single-ion atomic clock with 3×10^{-18} systematic uncertainty. *Phys. Rev. Lett.*, 116:063001, Feb 2016.

[32] Hidetoshi Katori, Masao Takamoto, V. G. Pal'chikov, and V. D. Ovsiannikov. Ultrastable optical clock with neutral atoms in an engineered light shift trap. *Phys. Rev. Lett.*, 91:173005, Oct 2003.

[33] Masao Takamoto, Feng-Lei Hong, Ryoichi Higashi, and Hidetoshi Katori. An optical lattice clock. *Nature*, 435:321–324, May 2005.

[34] N. D. Lemke, A. D. Ludlow, Z. W. Barber, T. M. Fortier, S. A. Diddams, Y. Jiang, S. R. Jefferts, T. P. Heavner, T. E. Parker, and C. W. Oates. Spin-1/2 optical lattice clock. *Phys. Rev. Lett.*, 103:063001, Aug 2009.

[35] J. J. McFerran, L. Yi, S. Mejri, S. Di Manno, W. Zhang, J. Guéna, Y. Le Coq, and S. Bize. Neutral atom frequency reference in the deep ultraviolet with fractional uncertainty $= 5.7 \times 10^{-15}$. *Phys. Rev. Lett.*, 108:183004, May 2012.

[36] T. L. Nicholson, S. L. Campbell, R. B. Hutson, G. E. Marti, B. J. Bloom, R. L. McNally, W. Zhang, M. D. Barrett, M. S. Safronova, G. F. Strouse, W. L. Tew, and J. Ye. Systematic evaluation of an atomic clock at $2 \times 10 - 18$ total uncertainty. *Nature Communications*, 6:6896 EP –, 04 2015.

[37] Kazuhiro Yamanaka, Noriaki Ohmae, Ichiro Ushijima, Masao Takamoto, and Hidetoshi Katori. Frequency ratio of ^{199}Hg and ^{87}Sr optical lattice clocks beyond the si limit. *Phys. Rev. Lett.*, 114:230801, Jun 2015.

[38] Nils Nemitz, Takuya Ohkubo, Masao Takamoto, Ichiro Ushijima, Manoj Das, Noriaki Ohmae, and Hidetoshi Katori. Frequency ratio of yb and sr clocks with $5 \times 10 - 17$ uncertainty at 150 seconds averaging time. *Nat Photon*, 10(4):258–261, 04 2016.

[39] D. W. Allan. Statistics of atomic frequency standards. *Proceedings of the IEEE*, 54(2):221–230, Feb 1966.

[40] SchioppoM., BrownR. C., McGrewW. F., HinkleyN., FasanoR. J., BeloyK., YoonT. H., MilaniG., NicolodiD., ShermanJ. A., PhillipsN. B., OatesC. W., and LudlowA. D. Ultrastable optical clock with two cold-atom ensembles. *Nat Photon*, 11(1):48–52, 01 2017.

[41] R. Le Targat, L. Lorini, Y. Le Coq, M. Zawada, J. Guéna, M. Abgrall, M. Gurov, P. Rosenbusch, D. G. Rovera, B. Nagórny, R. Gartman, P. G. Westergaard, M. E. Tobar, M. Lours, G. Santarelli, A. Clairon, S. Bize, P. Laurent, P. Lemonde, and J. Lodewyck. Experimental realization of an optical second with strontium lattice clocks. *Nature Communications*, 4:2109 EP –, 07 2013.

[42] Ian D. Leroux, Monika H. Schleier-Smith, and Vladan Vuletić. Orientation-dependent entanglement lifetime in a squeezed atomic clock. *Phys. Rev. Lett.*, 104:250801, Jun 2010.

[43] Onur Hosten, Nils J. Engelsen, Rajiv Krishnakumar, and Mark A. Kasevich. Measurement noise 100 times lower than the quantum-projection limit using entangled atoms. *Nature*, 529(7587):505–508, 01 2016.

[44] Ichiro Ushijima, Masao Takamoto, Manoj Das, Takuya Ohkubo, and Hidetoshi Katori. Cryogenic optical lattice clocks. *Nat Photon*, 9(3):185–189, 03 2015.

[45] H Hachisu, M Fujieda, M Kumagai, and T Ido. Absolute frequency measurement at 10 -16 level based on the international atomic time. *Journal of Physics: Conference Series*, 723(1):012042, 2016.

[46] Ali Al-Masoudi, Sören Dörscher, Sebastian Häfner, Uwe Sterr, and Christian Lisdat. Noise and instability of an optical lattice clock. *Phys. Rev. A*, 92:063814, Dec 2015.

[47] Takehiko Tanabe, Daisuke Akamatsu, Takumi Kobayashi, Akifumi Takamizawa, Shinya Yanagimachi, Takeshi Ikegami, Tomonari Suzuyama, Hajime Inaba, Sho Okubo, Masami Yasuda, Feng-Lei Hong, Atsushi Onae, and Kazumoto Hosaka. Improved frequency measurement of the 1s0-3p0 clock transition in 87sr using a cs fountain clock as a transfer oscillator. *Journal of the Physical Society of Japan*, 84(11):115002, 2015.

[48] Y Lin, Q Wang, Y Li, F Meng, B Lin, E Zang, Z Sun, F Fang, T Li, and Z Fang. The nim sr optical lattice clock. *Journal of Physics: Conference Series*, 723(1):012021, 2016.

[49] Huidong Kim, Myoung-Sun Heo, Won-Kyu Lee, Chang Yong Park, Hyun-Gue Hong, Sang-Wook Hwang, and Dai-Hyuk Yu. Improved absolute frequency measurement of the 171 yb optical lattice clock at kriss relative to the si second. *Japanese Journal of Applied Physics*, 56(5):050302, 2017.

[50] Marco Pizzocaro, Pierre Thoumany, Benjamin Rauf, Filippo Bregolin, Gianmaria Milani, Cecilia Clivati, Giovanni A Costanzo, Filippo Levi, and Davide Calonico. Absolute frequency measurement of the ^{1}s$_0$ - ^{3}p$_0$ transition of 171 yb. *Metrologia*, 54(1):102, 2017.

[51] Masami Yasuda, Hajime Inaba, Takuya Kohno, Takehiko Tanabe, Yoshiaki Nakajima, Kazumoto Hosaka, Daisuke Akamatsu, Atsushi Onae, Tomonari Suzuyama, Masaki Amemiya, and Feng-Lei Hong. Improved absolute frequency measurement of the 171 yb optical lattice clock towards a candidate for the redefinition of the second. *Applied Physics Express*, 5(10):102401, 2012.

[52] A. P. Kulosa, D. Fim, K. H. Zipfel, S. Rühmann, S. Sauer, N. Jha, K. Gibble, W. Ertmer, E. M. Rasel, M. S. Safronova, U. I. Safronova, and S. G. Porsev. Towards a mg lattice clock: Observation of the $^1S_0{-}^3P_0$ transition and determination of the magic wavelength. *Phys. Rev. Lett.*, 115:240801, Dec 2015.

[53] C.-Y. Xu, J. Singh, J. C. Zappala, K. G. Bailey, M. R. Dietrich, J. P. Greene, W. Jiang, N. D. Lemke, Z.-T. Lu, P. Mueller, and T. P. O'Connor. Measurement of the hyperfine quenching rate of the clock transition in ^{171}Yb. *Phys. Rev. Lett.*, 113:033003, Jul 2014.

[54] Sergey G. Porsev, Andrei Derevianko, and E. N. Fortson. Possibility of an optical clock using the $6^1S_0 \rightarrow 6^3P_0^o$ transition in ^{171,173}Yb atoms held in an optical lattice. *Phys. Rev. A*, 69:021403, Feb 2004.

[55] Anpei Ye and Guangfu Wang. Dipole polarizabilities of $ns^2\ ^1S_0$ and $nsnp\ ^3P_0$ states and relevant magic wavelengths of group-iib atoms. *Phys. Rev. A*, 78:014502, Jul 2008.

[56] Andrew D. Ludlow, Martin M. Boyd, Jun Ye, E. Peik, and P. O. Schmidt. Optical atomic clocks. *Rev. Mod. Phys.*, 87:637–701, Jun 2015.

[57] L. Yi, S. Mejri, J. J. McFerran, Y. Le Coq, and S. Bize. Optical lattice trapping of ^{199}Hg and determination of the magic wavelength for the ultraviolet $^1s_0 \leftrightarrow ^3 p_0$ clock transition. *Phys. Rev. Lett.*, 106:073005, Feb 2011.

[58] Martin M. Boyd, Andrew D. Ludlow, Sebastian Blatt, Seth M. Foreman, Tetsuya Ido, Tanya Zelevinsky, and Jun Ye. ^{87}Sr. *Phys. Rev. Lett.*, 98:083002, Feb 2007.

[59] T. L. Nicholson, M. J. Martin, J. R. Williams, B. J. Bloom, M. Bishof, M. D. Swallows, S. L. Campbell, and J. Ye. Comparison of two independent sr optical clocks with 1×10^{-17} stability at 10^3 s. *Phys. Rev. Lett.*, 109:230801, Dec 2012.

[60] A. D. Ludlow, X. Huang, M. Notcutt, T. Zanon-Willette, S. M. Foreman, M. M. Boyd, S. Blatt, and J. Ye. Compact, thermal-noise-limited optical cavity for diode laser stabilization at 1×10^{-15}. *Opt. Lett.*, 32(6):641–643, Mar 2007.

[61] S.L. Campbell, R.B. Hutson, G.E. Marti, A. Goban, N. Darkwah Oppong, R.L. McNally, L. Sonderhouse, J.M. Robinson, W. Zhang, B.J. Bloom, and J. Ye. A fermi-degenerate three-dimensional optical lattice clock. *arXiv*, 1702.01210, Feb 2017.

[62] Tomoya Akatsuka, Masao Takamoto, and Hidetoshi Katori. Three-dimensional optical lattice clock with bosonic ^{88}Sr atoms. *Phys. Rev. A*, 81:023402, Feb 2010.

[63] Yosuke Takasu, Kenichi Maki, Kaduki Komori, Tetsushi Takano, Kazuhito Honda, Mitsutaka Kumakura, Tsutomu Yabuzaki, and Yoshiro Takahashi. Spin-singlet bose-einstein condensation of two-electron atoms. *Phys. Rev. Lett.*, 91:040404, Jul 2003.

[64] K. Tsigutkin, D. Dounas-Frazer, A. Family, J. E. Stalnaker, V. V. Yashchuk, and D. Budker. Observation of a large atomic parity violation effect in ytterbium. *Phys. Rev. Lett.*, 103:071601, Aug 2009.

[65] C. W. Hoyt, Z. W. Barber, C. W. Oates, T. M. Fortier, S. A. Diddams, and L. Hollberg. Observation and absolute frequency measurements of the $^1s_0$-$^3p_0$ optical clock transition in neutral ytterbium. *Phys. Rev. Lett.*, 95:083003, Aug 2005.

[66] Z. W. Barber, C. W. Hoyt, C. W. Oates, L. Hollberg, A. V. Taichenachev, and V. I. Yudin. Direct excitation of the forbidden clock transition in neutral ^{174}Yb atoms confined to an optical lattice. *Phys. Rev. Lett.*, 96:083002, Mar 2006.

[67] Meng-Jiao Zhang, Hui Liu, Xi Zhang, Kun-Liang Jiang, Zhuan-Xian Xiong, Bao-Long Lü, and Ling-Xiang He. Hertz-level clock spectroscopy of 171 yb atoms in a one-dimensional optical lattice. *Chinese Physics Letters*, 33(7):070601, 2016.

[68] N. D. Lemke, J. von Stecher, J. A. Sherman, A. M. Rey, C. W. Oates, and A. D. Ludlow. p- wave cold collisions in an optical lattice clock. *Phys. Rev. Lett.*, 107:103902, Aug 2011.

[69] A. D. Ludlow, N. D. Lemke, J. A. Sherman, C. W. Oates, G. Quéméner, J. von Stecher, and A. M. Rey. Cold-collision-shift cancellation and inelastic scattering in a yb optical lattice clock. *Phys. Rev. A*, 84:052724, Nov 2011.

[70] J. A. Sherman, N. D. Lemke, N. Hinkley, M. Pizzocaro, R. W. Fox, A. D. Ludlow, and C. W. Oates. High-accuracy measurement of atomic polarizability in an optical lattice clock. *Phys. Rev. Lett.*, 108:153002, Apr 2012.

[71] K. Beloy, J. A. Sherman, N. D. Lemke, N. Hinkley, C. W. Oates, and A. D. Ludlow. Determination of the $5d6s\ ^3D_1$ state lifetime and blackbody-radiation clock shift in yb. *Phys. Rev. A*, 86:051404, Nov 2012.

[72] K. Beloy, N. Hinkley, N. B. Phillips, J. A. Sherman, M. Schioppo, J. Lehman, A. Feldman, L. M. Hanssen, C. W. Oates, and A. D. Ludlow. Atomic clock with 1×10^{-18} room-temperature blackbody stark uncertainty. *Phys. Rev. Lett.*, 113:260801, Dec 2014.

[73] Hidetoshi Katori, V. D. Ovsiannikov, S. I. Marmo, and V. G. Palchikov. Strategies for reducing the light shift in atomic clocks. *Phys. Rev. A*, 91:052503, May 2015.

[74] Bureau International des Poids et Mesures. Si brochure: The international system of units (si) [8th edition, 2006; updated in 2014]. 2014.

[75] S. Kolkowitz, I. Pikovski, N. Langellier, M. D. Lukin, R. L. Walsworth, and J. Ye. Gravitational wave detection with optical lattice atomic clocks. *Phys. Rev. D*, 94:124043, Dec 2016.

[76] J. K. Webb, J. A. King, M. T. Murphy, V. V. Flambaum, R. F. Carswell, and M. B. Bainbridge. Indications of a spatial variation of the fine structure constant. *Phys. Rev. Lett.*, 107:191101, Oct 2011.

[77] R. M. Godun, P. B. R. Nisbet-Jones, J. M. Jones, S. A. King, L. A. M. Johnson, H. S. Margolis, K. Szymaniec, S. N. Lea, K. Bongs, and P. Gill. Frequency ratio of two optical clock transitions in $^{171}yb^{+}$ and constraints on the time variation of fundamental constants. *Phys. Rev. Lett.*, 113:210801, Nov 2014.

[78] A. Derevianko and M. Pospelov. Hunting for topological dark matter with atomic clocks. *Nat Phys*, 10(12):933–936, 12 2014.

[79] C. W. Chou, D. B. Hume, T. Rosenband, and D. J. Wineland. Optical clocks and relativity. *Science*, 329(5999):1630–1633, 2010.

[80] Tetsushi Takano, Masao Takamoto, Ichiro Ushijima, Noriaki Ohmae, Tomoya Akatsuka, Atsushi Yamaguchi, Yuki Kuroishi, Hiroshi Munekane, Basara Miyahara, and Hidetoshi Katori. Geopotential measurements with synchronously linked optical lattice clocks. *Nat Photon*, 10(10):662–666, 10 2016.

[81] S. Kolkowitz, S. L. Bromley, T. Bothwell, M. L. Wall, G. E. Marti, A. P. Koller, X. Zhang, A. M. Rey, and J. Ye. Spin–orbit-coupled fermions in an optical lattice clock. *Nature*, 542(7639):66–70, 02 2017.

[82] A. Dareau, M. Scholl, Q. Beaufils, D. Döring, J. Beugnon, and F. Gerbier. Doppler spectroscopy of an ytterbium bose-einstein condensate on the clock transition. *Phys. Rev. A*, 91:023626, Feb 2015.

[83] E. T. Jaynes and F. W. Cummings. Comparison of quantum and semiclassical radiation theories with application to the beam maser. *Proceedings of the IEEE*, 51(1):89–109, Jan 1963.

[84] J. J. Sanchez-Mondragon, N. B. Narozhny, and J. H. Eberly. Theory of spontaneous-emission line shape in an ideal cavity. *Phys. Rev. Lett.*, 51:550–553, Aug 1983.

[85] G. S. Agarwal. Vacuum-field rabi splittings in microwave absorption by rydberg atoms in a cavity. *Phys. Rev. Lett.*, 53:1732–1734, Oct 1984.

[86] A. Boca, R. Miller, K. M. Birnbaum, A. D. Boozer, J. McKeever, and H. J. Kimble. Observation of the vacuum rabi spectrum for one trapped atom. *Phys. Rev. Lett.*, 93:233603, Dec 2004.

[87] H J Kimble. Strong interactions of single atoms and photons in cavity qed. *Physica Scripta*, 1998(T76):127, 1998.

[88] Haruka Tanji-Suzuki, Ian D. Leroux, Monika H. Schleier-Smith, Marko Cetina, Andrew T. Grier, Jonathan Simon, and Vladan Vuletić. Chapter 4 - interaction between atomic ensembles and optical resonators: Classical description. In P.R. Berman E. Arimondo and C.C. Lin, editors, *Advances in Atomic, Molecular, and Optical Physics*, volume 60 of *Advances In Atomic, Molecular, and Optical Physics*, pages 201 – 237. Academic Press, 2011.

[89] P. Drummond. Optical bistability in a radially varying mode. *IEEE Journal of Quantum Electronics*, 17(3):301–306, Mar 1981.

[90] Christian Gross. Spin squeezing, entanglement and quantum metrology with bose-einstein condensates. *Journal of Physics B: Atomic, Molecular and Optical Physics*, 45(10):103001, 2012.

[91] Masahiro Kitagawa and Masahito Ueda. Squeezed spin states. *Phys. Rev. A*, 47:5138–5143, Jun 1993.

[92] D. J. Wineland, J. J. Bollinger, W. M. Itano, and D. J. Heinzen. Squeezed atomic states and projection noise in spectroscopy. *Phys. Rev. A*, 50:67–88, Jul 1994.

[93] Kevin C. Cox, Graham P. Greve, Joshua M. Weiner, and James K. Thompson. Deterministic squeezed states with collective measurements and feedback. *Phys. Rev. Lett.*, 116:093602, Mar 2016.

[94] Monika H. Schleier-Smith, Ian D. Leroux, and Vladan Vuletić. States of an ensemble of two-level atoms with reduced quantum uncertainty. *Phys. Rev. Lett.*, 104:073604, Feb 2010.

[95] J. Appel, P. J. Windpassinger, D. Oblak, U. B. Hoff, N. Kjærgaard, and E. S. Polzik. Mesoscopic atomic entanglement for precision measurements beyond the standard quantum limit. *Proceedings of the National Academy of Sciences*, 106(27):10960–10965, 2009.

[96] Zilong Chen, Justin G. Bohnet, Shannon R. Sankar, Jiayan Dai, and James K. Thompson. Conditional spin squeezing of a large ensemble via the vacuum rabi splitting. *Phys. Rev. Lett.*, 106:133601, Mar 2011.

[97] R. J. Sewell, M. Koschorreck, M. Napolitano, B. Dubost, N. Behbood, and M. W. Mitchell. Magnetic sensitivity beyond the projection noise limit by spin squeezing. *Phys. Rev. Lett.*, 109:253605, Dec 2012.

[98] R. J. Sewell, M. Napolitano, N. Behbood, G. Colangelo, F. Martin Ciurana, and M. W. Mitchell. Ultrasensitive atomic spin measurements with a nonlinear interferometer. *Phys. Rev. X*, 4:021045, Jun 2014.

[99] T. Takano, M. Fuyama, R. Namiki, and Y. Takahashi. Spin squeezing of a cold atomic ensemble with the nuclear spin of one-half. *Phys. Rev. Lett.*, 102:033601, Jan 2009.

[100] A. Sorensen, L. M. Duan, J. I. Cirac, and P. Zoller. Many-particle entanglement with bose-einstein condensates. *Nature*, 409(6816):63–66, 01 2001.

[101] J. Esteve, C. Gross, A. Weller, S. Giovanazzi, and M. K. Oberthaler. Squeezing and entanglement in a bose-einstein condensate. *Nature*, 455(7217):1216–1219, 10 2008.

[102] C. Gross, T. Zibold, E. Nicklas, J. Estève, and M. K. Oberthaler. Nonlinear atom interferometer surpasses classical precision limit. *Nature*, 464(7292):1165–1169, 04 2010.

[103] Max F. Riedel, Pascal Böhi, Yun Li, Theodor W. Hänsch, Alice Sinatra, and Philipp Treutlein. Atom-chip-based generation of entanglement for quantum metrology. *Nature*, 464(7292):1170–1173, 04 2010.

[104] B. Lücke, M. Scherer, J. Kruse, L. Pezzé, F. Deuretzbacher, P. Hyllus, O. Topic, J. Peise, W. Ertmer, J. Arlt, L. Santos, A. Smerzi, and C. Klempt. Twin matter waves for interferometry beyond the classical limit. *Science*, 334(6057):773–776, 2011.

[105] C. D. Hamley, C. S. Gerving, T. M. Hoang, E. M. Bookjans, and M. S. Chapman. Spin-nematic squeezed vacuum in a quantum gas. *Nat Phys*, 8(4):305–308, 04 2012.

[106] T. Berrada, S. van Frank, R. Bücker, T. Schumm, J. F. Schaff, and J Schmiedmayer. Integrated mach–zehnder interferometer for bose–einstein condensates. *Nature Communications*, 4:2077 EP –, 06 2013.

[107] Caspar F. Ockeloen, Roman Schmied, Max F. Riedel, and Philipp Treutlein. Quantum metrology with a scanning probe atom interferometer. *Phys. Rev. Lett.*, 111:143001, Oct 2013.

[108] Helmut Strobel, Wolfgang Muessel, Daniel Linnemann, Tilman Zibold, David B. Hume, Luca Pezzè, Augusto Smerzi, and Markus K. Oberthaler. Fisher information and entanglement of non-gaussian spin states. *Science*, 345(6195):424–427, 2014.

[109] W. Muessel, H. Strobel, D. Linnemann, D. B. Hume, and M. K. Oberthaler. Scalable spin squeezing for quantum-enhanced magnetometry with bose-einstein condensates. *Phys. Rev. Lett.*, 113:103004, Sep 2014.

[110] W. Muessel, H. Strobel, D. Linnemann, T. Zibold, B. Juliá-Díaz, and M. K. Oberthaler. Twist-and-turn spin squeezing in bose-einstein condensates. *Phys. Rev. A*, 92:023603, Aug 2015.

[111] Y. C. Liu, Z. F. Xu, G. R. Jin, and L. You. Spin squeezing: Transforming one-axis twisting into two-axis twisting. *Phys. Rev. Lett.*, 107:013601, Jun 2011.

[112] Wen Huang, Yan-Lei Zhang, Chang-Ling Zou, Xu-Bo Zou, and Guang-Can Guo. Two-axis spin squeezing of two-component bose-einstein condensates via continuous driving. *Phys. Rev. A*, 91:043642, Apr 2015.

[113] Yong-Chang Zhang, Xiang-Fa Zhou, Xingxiang Zhou, Guang-Can Guo, and Zheng-Wei Zhou. Cavity-assisted single-mode and two-mode spin-squeezed states via phase-locked atom-photon coupling. *Phys. Rev. Lett.*, 118:083604, Feb 2017.

[114] I. Kruse, K. Lange, J. Peise, B. Lücke, L. Pezzè, J. Arlt, W. Ertmer, C. Lisdat, L. Santos, A. Smerzi, and C. Klempt. Improvement of an atomic clock using squeezed vacuum. *Phys. Rev. Lett.*, 117:143004, Sep 2016.

[115] Ian D. Leroux, Monika H. Schleier-Smith, and Vladan Vuletić. Implementation of cavity squeezing of a collective atomic spin. *Phys. Rev. Lett.*, 104:073602, Feb 2010.

[116] O. Hosten, R. Krishnakumar, N. J. Engelsen, and M. A. Kasevich. Quantum phase magnification. *Science*, 352(6293):1552–1555, 2016.

[117] Anne Louchet-Chauvet, Jürgen Appel, Jelmer J Renema, Daniel Oblak, Niels Kjaergaard, and Eugene S Polzik. Entanglement-assisted atomic clock beyond the projection noise limit. *New Journal of Physics*, 12(6):065032, 2010.

[118] Kevin C. Cox, Graham P. Greve, Baochen Wu, and James K. Thompson. Spatially homogeneous entanglement for matter-wave interferometry created with time-averaged measurements. *Phys. Rev. A*, 94:061601, Dec 2016.

[119] Klaus Mølmer and Anders Sørensen. Multiparticle entanglement of hot trapped ions. *Phys. Rev. Lett.*, 82:1835–1838, Mar 1999.

[120] D Hunger, T Steinmetz, Y Colombe, C Deutsch, T W Hänsch, and J Reichel. A fiber fabry-perot cavity with high finesse. *New Journal of Physics*, 12(6):065038, 2010.

[121] Dorian Gangloff, Molu Shi, Tailin Wu, Alexei Bylinskii, Boris Braverman, Michael Gutierrez, Rosanna Nichols, Junru Li, Kai Aichholz, Marko Cetina, Leon Karpa, Branislav Jelenković, Isaac Chuang, and Vladan Vuletić. Preventing and reversing vacuum-induced optical losses in high-finesse tantalum (v) oxide mirror coatings. *Opt. Express*, 23(14):18014–18028, Jul 2015.

[122] Thomas P. Purdy. Cavity qed with ultracold atoms on an atom chip. *Doctoral Thesis*, 2009.

[123] Grace H. Zhang, Boris Braverman, Akio Kawasaki, and Vladan Vuletić. Note: Fast compact laser shutter using a direct current motor and three-dimensional printing. *Review of Scientific Instruments*, 86(12):126105, 2015.

[124] T. A. Savard, K. M. O'Hara, and J. E. Thomas. Laser-noise-induced heating in far-off resonance optical traps. *Phys. Rev. A*, 56:R1095–R1098, Aug 1997.

[125] Kristan L. Corwin, Zheng-Tian Lu, Carter F. Hand, Ryan J. Epstein, and Carl E. Wieman. Frequency-stabilized diode laser with the zeeman shift in an atomic vapor. *Appl. Opt.*, 37(15):3295–3298, May 1998.

[126] Jae Ihn Kim, Chang Yong Park, Jin Yong Yeom, Eok Bong Kim, and Tai Hyun Yoon. Frequency-stabilized high-power violet laser diode with an ytterbium hollow-cathode lamp. *Opt. Lett.*, 28(4):245–247, Feb 2003.

[127] R. W. P. Drever, J. L. Hall, F. V. Kowalski, J. Hough, G. M. Ford, A. J. Munley, and H. Ward. Laser phase and frequency stabilization using an optical resonator. *Applied Physics B*, 31(2):97–105, 1983.

[128] Qian Lin, Mackenzie A. Van Camp, Hao Zhang, Branislav Jelenković, and Vladan Vuletić. Long-external-cavity distributed bragg reflector laser with subkilohertz intrinsic linewidth. *Opt. Lett.*, 37(11):1989–1991, Jun 2012.

[129] Z. W. Barber, J. E. Stalnaker, N. D. Lemke, N. Poli, C. W. Oates, T. M. Fortier, S. A. Diddams, L. Hollberg, C. W. Hoyt, A. V. Taichenachev, and V. I. Yudin. Optical lattice induced light shifts in an yb atomic clock. *Phys. Rev. Lett.*, 100:103002, Mar 2008.

[130] K. G. Libbrecht and J. L. Hall. A low - noise high - speed diode laser current controller. *Review of Scientific Instruments*, 64(8):2133–2135, 1993.

[131] David R. Leibrandt, Michael J. Thorpe, Mark Notcutt, Robert E. Drullinger, Till Rosenband, and James C. Bergquist. Spherical reference cavities for frequency stabilization of lasers in non-laboratory environments. *Opt. Express*, 19(4):3471–3482, Feb 2011.

[132] J. Reichel, W. Hänsel, and T. W. Hänsch. Atomic micromanipulation with magnetic surface traps. *Phys. Rev. Lett.*, 83:3398–3401, Oct 1999.

[133] E. L. Raab, M. Prentiss, Alex Cable, Steven Chu, and D. E. Pritchard. Trapping of neutral sodium atoms with radiation pressure. *Phys. Rev. Lett.*, 59:2631–2634, Dec 1987.

[134] A. M. L. Oien, I. T. McKinnie, P. J. Manson, W. J. Sandle, and D. M. Warrington. Cooling mechanisms in the sodium type-ii magneto-optical trap. *Phys. Rev. A*, 55:4621–4624, Jun 1997.

[135] V. B. Tiwari, S. Singh, H. S. Rawat, and S. C. Mehendale. Cooling and trapping of ^{85}Rb atoms in the ground hyperfine $f = 2$ state. *Phys. Rev. A*, 78:063421, Dec 2008.

[136] K. Honda, Y. Takahashi, T. Kuwamoto, M. Fujimoto, K. Toyoda, K. Ishikawa, and T. Yabuzaki. Magneto-optical trapping of yb atoms and a limit on the branching ratio of the $^1P_1$ state. *Phys. Rev. A*, 59:R934–R937, Feb 1999.

[137] T. Kuwamoto, K. Honda, Y. Takahashi, and T. Yabuzaki. Magneto-optical trapping of yb atoms using an intercombination transition. *Phys. Rev. A*, 60:R745–R748, Aug 1999.

[138] Jeongwon Lee, Jae Hoon Lee, Jiho Noh, and Jongchul Mun. Core-shell magneto-optical trap for alkaline-earth-metal-like atoms. *Phys. Rev. A*, 91:053405, May 2015.

[139] K.-A. Brickman, M.-S. Chang, M. Acton, A. Chew, D. Matsukevich, P. C. Haljan, V. S. Bagnato, and C. Monroe. Magneto-optical trapping of cadmium. *Phys. Rev. A*, 76:043411, Oct 2007.

[140] Seo Ho Youn, Mingwu Lu, Ushnish Ray, and Benjamin L. Lev. Dysprosium magneto-optical traps. *Phys. Rev. A*, 82:043425, Oct 2010.

[141] Mingwu Lu, Nathaniel Q. Burdick, Seo Ho Youn, and Benjamin L. Lev. Strongly dipolar bose-einstein condensate of dysprosium. *Phys. Rev. Lett.*, 107:190401, Oct 2011.

[142] A. Frisch, K. Aikawa, M. Mark, A. Rietzler, J. Schindler, E. Zupanič, R. Grimm, and F. Ferlaino. Narrow-line magneto-optical trap for erbium. *Phys. Rev. A*, 85:051401, May 2012.

[143] J. J. McClelland and J. L. Hanssen. Laser cooling without repumping: A magneto-optical trap for erbium atoms. *Phys. Rev. Lett.*, 96:143005, Apr 2006.

[144] D D Sukachev, E S Kalganova, A V Sokolov, S A Fedorov, G A Vishnyakova, A V Akimov, N N Kolachevsky, and V N Sorokin. Secondary laser cooling and capturing of thulium atoms in traps. *Quantum Electronics*, 44(6):515, 2014.

[145] J. Reichel. Microchip traps and bose-einstein condensation. *Applied Physics B*, 74(6):469–487, 2002.

[146] J. E. Golub, Y. S. Bai, and T. W. Mossberg. Radiative and dynamical properties of homogeneously prepared atomic samples. *Phys. Rev. A*, 37:119–124, Jan 1988.

[147] Emily Davis, Gregory Bentsen, and Monika Schleier-Smith. Approaching the heisenberg limit without single-particle detection. *Phys. Rev. Lett.*, 116:053601, Feb 2016.

[148] L Nenadović and J J McFerran. Clock and inter-combination line frequency separation in 171 yb. *Journal of Physics B: Atomic, Molecular and Optical Physics*, 49(6):065004, 2016.

[149] M. J. Martin, M. Bishof, M. D. Swallows, X. Zhang, C. Benko, J. von Stecher, A. V. Gorshkov, A. M. Rey, and Jun Ye. A quantum many-body spin system in an optical lattice clock. *Science*, 341(6146):632–636, 2013.